

Bangor University

DOCTOR OF PHILOSOPHY

The application of Biot's theory to sea-bed sediments.

Hurley, Michael Thomas

Award date:
1989

Awarding institution:
Bangor University

[Link to publication](#)

General rights

Copyright and moral rights for the publications made accessible in the public portal are retained by the authors and/or other copyright owners and it is a condition of accessing publications that users recognise and abide by the legal requirements associated with these rights.

- Users may download and print one copy of any publication from the public portal for the purpose of private study or research.
- You may not further distribute the material or use it for any profit-making activity or commercial gain
- You may freely distribute the URL identifying the publication in the public portal ?

Take down policy

If you believe that this document breaches copyright please contact us providing details, and we will remove access to the work immediately and investigate your claim.

Download date: 28. Apr. 2024

THE APPLICATION OF BIOT'S THEORY TO SEA-BED SEDIMENTS

MICHAEL THOMAS HURLEY B.Sc

January 1989

**A thesis submitted to the University of Wales
for the degree of Philosophiae Doctor**

**School of Ocean Sciences
University College of North Wales
Menai Bridge, Gwynedd**

To my Mother and Father

SUMMARY

Biot's theory - which explains how sediments respond to stresses - has been applied to different sea-bed sediments. To successfully use Biot's theory as a predictive tool, sensitivity studies showed the following experimental measurements are required: the frame bulk modulus, the shear modulus, the tortuosity, the permeability and the porosity. These properties were determined for turbidite sediments from the North Atlantic Ocean (Site 1), and carbonates from the Western Indian Ocean - (Site 2).

The following experimental observations were made: the permeability varies over 7 orders of magnitude for turbidites from Site 1 due to technique dependent and intrinsic reasons; in-situ shear moduli are 4 times greater than values determined from samples in the laboratory; shear modulus results from resonant column and bender element transducer techniques agree well; experiments designed for obtaining the frame bulk modulus are problematic, and it is difficult to determine pore size / geometry parameters apart from the tortuosity.

Biot's theory was used to predict the response of sea-bed sediments to hydrodynamic and ultrasonic stresses. A new low frequency hydrodynamic boundary-value solution was developed from Biot's theory, allowing predictions of tidally-induced pore-pressures. Comparisons between predictions and in-situ measurements at Site 1 were favourable, verifying Biot's theory at low frequencies.

At ultrasonic frequencies, Biot predictions of the velocity and attenuation of fast and slow compressional waves were compared to experimental measurements. The slow wave was argued to be induced at free-flow boundaries, and was found to be very difficult to detect in soft water-saturated sediments. A qualitative agreement was shown between Biot fast wave attenuation predictions and new experimental attenuation measurements on a bar of sandstone.

For Sites 1 and 2, Biot predictions for the increases in the fast wave velocity for high porosity - permeability sediments agreed with experimental measurements. Elsewhere in the literature, this behaviour has been linked to an increase of the frame bulk modulus with increases in porosity. Alternatively, it was argued such increases in fast wave velocity can be attributed to Biot's dispersion mechanism, and hence are a verification of his theory at high frequencies.

ACKNOWLEDGEMENTS

This work could not have been achieved without the excellent supervision of Prof Denzil Taylor Smith and Dr Peter Schultheiss. I am additionally grateful to Peter, who has spent much time with me, helping transform abstract ideas into coherent scientific rationale.

I am grateful to colleagues of the University College North Wales, the Institute of Oceanographic Sciences, the Ocean Drilling Program and the University of Hawaii, who have either assisted with experimental work, engaged in enlightening discussions or who have given vital moral support. I would like to thank especially, Mr Richard Babbs, Dr Jan Backman, Dr Jim Bennell, Dr Angela Davies, Dr Tim Francis, Mr Dave Gunn, Mr Peter Hempel, Mr Quentin Huggett, Dr Barry Lienert, Prof Murli Manghnani, Dr Peter Schultheiss, Dr Elliot Taylor, Prof. Denzil Taylor Smith and Dr Sharon Webb.

This work was funded by a Natural Environmental Research Council CASE studentship. I am additionally grateful to NERC, who provided support for participation in RRS Discovery Cruise 153, ODP Leg 115, and post-cruise research at Texas A and M University. I would also like to thank Prof Murli Manghnani, Prof Denzil Taylor Smith and Dr Peter Schultheiss, who made possible a period of research at the University of Hawaii.

CONTENTS

Title Page

Dedication

Declaration

Summary

Acknowledgements

Contents

List of symbols

1	INTRODUCTION	1
1.1	Background	1
1.2	Sound waves in relation to Biot's theory	3
1.3	Aims of this thesis	4
1.4	The structure of this thesis	5
2	BIOT'S THEORY OF POROELASTICITY	7
2.1	Introduction	7
2.2	Quasi-static poroelasticity	8
2.2.1	A poroelastic medium and its state variables	8
2.2.2	The governing equations for quasi-static poroelasticity	9
2.2.3	The constants characterising a poroelastic medium	10
2.2.4	Problems of quasi-static poroelasticity	10
2.3	Dynamic poroelasticity	11
2.3.1	A model of a poroelastic medium for dynamic deformations	11
2.3.2	Governing equations for dynamic poroelasticity	12
2.3.3	Constants for dynamic poroelasticity and the viscodynamic operator	12
2.3.4	The problem of dynamic poroelasticity: the characteristic equation	13

2.4	Solutions to the characteristic equation	14
2.4.1	Exact solutions	14
2.4.2	Asymptotic velocity limits	15
2.4.3	Approximate velocity solutions	16
2.5	Summary	17
3	GENERAL SOLUTIONS TO BIOT'S THEORY AND A BOUNDARY VALUE PROBLEM	19
3.1	Introduction	19
3.2	General solutions of poroelasticity	20
3.2.1	Quasi-static formulation	20
3.2.2	Dynamic formulation	22
3.3	Boundary value problems	25
3.3.1	Tidal loading of the sea-bed	25
3.3.2	Numerical examples for the tidally-induced pore pressure	28
3.4	Summary	31
4	THE PERMEABILITY OF DEEP-SEA SEDIMENTS	33
4.1	Introduction	33
4.2	Laboratory permeability: consolidation and direct flow tests	34
4.2.1	Samples, the sample cell and sample preparation	34
4.2.2	The consolidation and permeability system	35
4.2.3	Consolidation and permeability test procedure	36
4.3	Method 1: Permeability from consolidation (k_{a1})	37
4.3.1	Procedure for analysis of test data	37
4.3.2	Permeability analysis for samples from Site 1	38
4.4	Analysis and results for method 2: Permeability from direct-flow tests (k_{a2})	40

4.5	In-situ permeability: piezometer experiments	40
4.5.1	In-situ pore pressure instrument PUPPI	40
4.5.2	Description of in-situ pore pressure data	42
4.6	Method 3: Permeability from pore-pressure decay (k_{a3})	42
4.6.1	Procedure for analysis of PUPPI data	42
4.6.2	Permeability analysis for Site 1	43
4.7	Method 4: Permeability from tidal cycles (k_{a4})	44
4.7.1	Procedure for analysis of PUPPI data	44
4.7.2	Permeability analysis for Site 1	44
4.8	Method 5: Permeability from grain size (k_{a5})	46
4.8.1	The Kozeny-Carman equation	46
4.8.2	Permeability results for Site 1	47
4.9	Method 6: Permeability from dispersion (k_{a6})	48
4.9.1	Use of Biot's poroelastic theory to predict permeability	48
4.9.2	Permeability results for Site 1	48
4.10	Discussion	50
4.10.1	A comparison of the results from the six methods used to determine the permeability of the turbidite sediments from Site 1	50
4.10.2	Permeability from laboratory consolidation analysis (method 1)	50
4.10.3	Permeability from laboratory direct flow analysis (method 2)	51
4.10.4	Permeability from piezometer insertion pressure (method 3)	52
4.10.5	Permeability from tidal cycle analysis (method 4)	53
4.10.6	Permeability from grain size analysis (method 5)	54
4.10.7	Permeability from compressional wave dispersion (method 6)	54
4.11	Definition and uses of "large-scale", "small scale" and "micro" permeability	55
4.12	Summary	57

5	THE ELASTIC CONSTANTS OF DEEP-SEA SEDIMENTS	59
5.1	Introduction	59
5.2	Resonant column method for obtaining E and G	61
5.2.1	The principle of the resonant column	61
5.2.2	The resonant column system	62
5.2.3	Samples, sample preparation and resonant column test procedure	65
5.3	Bender element method for obtaining G_{\max}	66
5.3.1	Mounting bender elements in soil testing devices	66
5.3.2	Driving / measuring system	67
5.3.3	Factors affecting received bender signals	67
5.3.4	Interpretation of received bender signals: problems	68
5.3.5	Benefits of signal conditioning	69
5.3.6	Characterisation of received bender signals in different media	69
5.3.7	Criteria for interpreting received bender signals to obtain V_s and G_{\max}	71
5.3.8	Samples tested using bender elements	72
5.4	G_{\max} and E_{\max} results for sediments from Sites 1, 2 and 4	72
5.4.1	Failure of E_{\max} experiments on samples from Site 1	72
5.4.2	Comparision of G_{\max} from resonant column and bender techniques: Sites 1 and 4	73
5.4.3	G_{\max} versus effective stress and sub-bottom depths at Sites 1 and 4	76
5.4.4	G_{\max} versus effective stress at Site 2	78
5.5	Anelastic behaviour of sediments: Q and shear modulus dispersion	80
5.5.1	Band limited constant Q model of sediments	80
5.5.2	Shear modulus dispersion analysis at Site 1	82

5.6	Determining a second elastic constant E or ν_b for Sites 1 and 4	84
5.6.1	E results for Sites 1 and 4: degradation and experimental problems	84
5.6.2	Calculating the elastic constant ν_b for samples from Sites 1, 2 and 4	88
5.7	Summary	92
6	CHARACTERISATION OF BIOT'S SLOW WAVE	95
6.1	Introduction	95
6.2	Previous studies involving Biot's slow wave in unconsolidated fluid saturated natural sediments	95
6.2.1	Features of Biot's slow wave	96
6.2.2	Experimental observations of the slow wave in unconsolidated sediments?	97
6.3	Experimental attempts to detect Biot's slow wave	99
6.3.1	Design of a new compressional mode bender transducer	99
6.3.2	Experimental set-up for using the new compressional wave transducer in sand at different effective stresses	100
6.3.3	Some initial results using the new transducer in saturated sand at different effective stresses	102
6.3.4	Experimentals using the compressional mode bender transducer in different media	103
6.3.5	Problems with attempts to detect Biot's slow wave in unconsolidated sediments	105
6.4	General solutions and a boundary value problem for a propagating slow wave	106
6.4.1	Explicit form of a general solution for propagating slow waves	106

6.4.2	Boundary problem of a fluid-filled porous medium subjected to a transient input	107
6.4.3	On the question: is Biot's slow wave a fluid or frame wave?	110
6.5	Summary	110
7	DISPERSION OF BIOT'S FAST WAVE	112
7.1	Introduction	112
7.2	Parameters affecting the magnitude of fast wave dispersion	113
7.2.1	The effect of tortuosity	113
7.2.2	The effect of shear modulus on dispersion in surficial sediments	116
7.3	Parameters affecting the location of fast wave dispersion in the frequency band	118
7.3.1	Inferences from the characteristic equation	118
7.3.2	Effect of permeability	119
7.3.3	Effect of grain size	119
7.3.4	Effect of pore-radius	123
7.3.5	Effect of fluid viscosity	125
7.4	Dispersion predictions using variations of Biot's theory	128
7.4.1	The approximate theory of Geertsma and Smit (1961)	128
7.4.2	The non-tortuous viscous flow theory of Hovem and Ingram (1979)	129
7.4.3	The variable pore-size theory of McCann and McCann (1985)	131
7.5	A discussion on the applicability of Biot's theory for accounting for fast wave dispersion in sediments	133
7.6	Summary	138

8	ATTENUATION OF BIOT'S FAST WAVE	140
8.1	Introduction	140
8.2	Extensional wave attenuation in porous rods	141
8.2.1	Low-frequency attenuation/modulus experimental set-up	141
8.2.2	The Biot-Gardner theory of extensional waves in porous rods	142
8.2.3	White's (1986) analysis of Spencer's (1981) results	144
8.2.4	Calibration of the low frequency attenuation apparatus	146
8.2.5	Preliminary results for attenuation in wet and dry Berea sandstone samples	149
8.3	Factors affecting the magnitude and location of fast wave attenuation in the frequency band	151
8.3.1	Inferences from the characteristic equation	151
8.3.2	Effect of shear modulus, tortuosity and porosity	152
8.3.3	Effect of permeability and pore radius	153
8.3.4	Effect of fluid viscosity	156
8.4	A discussion on the applicability of Biot's theory for accounting for fast wave attenuation in sediments	157
8.5	Summary	159
9	COMPONENTS OF GEOACOUSTIC AND HYDRODYNAMIC MODELS OF THE SEA-BED	162
9.1	Introduction	162
9.2	Practical constraints on possible components of geoacoustic and hydrodynamic models	163
9.2.1	Permeability	163
9.2.2	Elastic constants	164
9.2.3	The slow wave	164
9.2.4	Fast wave and fast wave dispersion	166
9.2.5	Fast wave attenuation	167

9.3	The components of geoacoustic and hydrodynamic models	168
9.3.1	A geoacoustic model for use with Biot's theory	168
9.3.2	A hydrodynamic model for use with Biot's theory	171
9.4	Sensitivity of predictions from Biot's theory to the uncertainties in the parameters of geoacoustic and hydrodynamic models	173
9.4.1	Sensitivity analysis for a geoacoustic model	173
9.4.2	A numerical example for a geoacoustic model of a carbonate sea-bed	175
9.4.3	Sensitivity analysis for a hydrodynamic model	178
9.5	Summary	180
10	A CASE STUDY: BIOT'S THOERY APPLIED TO HYDRODYNAMIC AND GEOACOUSTIC MODELS OF THE SEA-BED OF THE NORTH EAST ATLANTIC OCEAN	182
10.1	Introduction	182
10.2	Background information for Site 1	183
10.2.1	The geology of Site 1	183
10.2.2	Results from geotechnical / geophysical experiments on sediments recovered from Site 1	184
10.2.3	In-situ geotechnical / geophysical experiments at Site 1	189
10.3	A hydrodynamic model of Site 1 and comparisons between measured and predicted tidal pore-pressure responses	192
10.4	A geoacoustic model of Site 1 and comparisons between predicted and measured compressional wave velocities	194
10.5	Summary	201

11	A CASE STUDY: BIOT'S THEORY APPLIED TO GEOACOUSTIC MODELS OF THE SEA-BED OF THE WESTERN INDIAN OCEAN	203
11.1	Introduction	203
11.2	Background information for Site 2	204
11.2.1	The geology of Site 2	204
11.2.2	Results from ship-board laboratory physical properties measurements on sediments recovered from Site 2	205
11.2.3	Results from post-cruise laboratory geotechnical and acoustical experiments on sediments recovered from Site 2	210
11.3	A geoacoustical model of Site 2 based on ship-board measurements and comparisons between measured and predicted values of V_p	212
11.4	A geoacoustical model of Site 2 based on post-cruise measurements and comparisons between measured and predicted values of V_p	218
11.5	A discussion on the usefulness of geoacoustic models of Site 2 and whether or not Biot-type dispersion is verified by them	221
11.6	Summary	223
12	THE APPLICATION OF BIOT'S THEORY TO SEA-BED SEDIMENTS	226
12.1	The findings of this thesis	226
12.2	Applications of the findings of this thesis	227
12.3	A statement on the problems involved with successful application of Biot's theory to sea-bed sediments	228
12.4	The way forward	230

Appendix 1	Elasticity theory	233
Appendix 2	Anelastic theory	238
Appendix 3	Description and geographical location of data sets and samples	244
Appendix 4	BASIC computer code BIOT_FRQ.BAS	247
Appendix 5	BASIC computer code BIOT_ERR.BAS	256
References		267

LIST OF SYMBOLS WITH THE PAGE WHICH THEY ARE INTRODUCED

a	capillary tube / pore aperture radius	12
a_1	Biot predicted fast compressional wave attenuation coefficient	14
a_2	Biot predicted slow compressional wave attenuation coefficient	14
a_b	elastic constant: frame constrained compressibility	9
a_I	infinite frequency limit of a_1	151
a_p	fast wave attenuation coefficient	153
A_1	area	240
A_t	area	240
A_n	displacement amplitude after n cycles	241
A_{n+1}	displacement amplitude after n+1 cycles	241
b	damping coefficient	130
ber	real part of the Kelvin function first kind, zero order	13
bei	imaginary part of the Kelvin function first kind, zero order	13
C	shape / dimension constant	236
C_h	horizontal coefficient of consolidation	42
C_v	vertical coefficient of consolidation	37
d_m	average grain diameter	46
D	elastic constant: constrained modulus	235
\hat{D}	complex anelastic constrained modulus	241
D_c	constrained modulus from consolidation tests	37
D_i	imaginary part of \hat{D}	242
D_r	real part of \hat{D}	242
D_E	extensional-mode damping ratio	65

D_S	shear-mode damping ratio	65
e	void ratio	37
e_0	initial void ratio	37
$[e_{ij}]$	antisymmetric strain tensor ($i, j = 1, 2, 3$)	234
E	elastic constant: Young's modulus	60
E_i	imaginary part of E	142
E_r	real part of E	142
\hat{E}	complex anelastic Young's modulus	81
E_{\max}	low strain amplitude determination of E	65
f	frequency	12
f_0	reference frequency	81
f_c	characteristic frequency	96
f_r	resonant frequency	61
f_t	transitional frequency	12
$\hat{F}(\kappa)$	complex frequency correction function	12
F_a	dynamic driving force	236
F_i	imaginary part of $\hat{F}(\kappa)$	130
F_r	real part of $\hat{F}(\kappa)$	130
F_s	restoring force	236
FF	formation factor	189
g	acceleration due to gravity	33
G	elastic constant: shear modulus	10
\hat{G}	complex anelastic shear modulus	81
G_0	reference shear modulus	81
G_{\max}	low strain amplitude determination of G	65
h	sample height	37
i	$\sqrt{-1}$	13
I	mass polar inertia of sample	62
I_0	mass polar inertia of additional mass	62

\hat{k}	complex wave number	12
$\hat{k}_{1,3}$	fast compressional wave numbers	15
$\hat{k}_{2,4}$	slow compressional wave numbers	15
k_a	intrinsic permeability	9
k_{a1}	k_a from consolidation tests	37
k_{a2}	k_a from direct flow tests	40
k_{a3}	k_a from piezometer insertion pore pressure decay	42
k_{a4}	k_a from tidal cycle analysis	44
k_{a5}	k_a from grain size analysis	46
k_{a6}	k_a from fast wave dispersion	48
k_{eff}	effective flow permeability of a laminar material	55
\bar{k}_{eff}	effective acoustic permeability of a laminar material	56
k_i	imaginary part of \hat{k}	241
k_j	permeability of a thin layer	56
k_r	real part of \hat{k}	241
k_s	permeability of burrowed sediment	193
k_v	hydraulic conductivity	33
K	elastic constant: bulk modulus	89
\bar{K}	elastic constant	143
K_b	elastic constant: frame bulk modulus	10
\hat{K}_b	complex anelastic frame bulk modulus	84
K_f	elastic constant: fluid bulk modulus	10
K_f'	elastic constant: gas affected fluid bulk modulus	30
K_g	elastic constant: gas bulk modulus	30
K_s	elastic constant: solid bulk modulus	10
l	length of element of sediment	11
l_e	length of tortuous path through sediment	11
l_j	thickness of thin layer	55

L	thickness of sample	62
L_s	thickness of sea-bed	25
m	inertial coupling factor	12
$\hat{m}(\omega)$	complex dynamic anelastic modulus	239
m_a	additional mass	62
m_i	imaginary part of $\hat{m}(\omega)$	239
m_r	real part of $\hat{m}(\omega)$	239
m_s	mass of sample body	62
$M(t)$	time dependent anelastic modulus	238
M_{ijkl}	elastic constant: fourth rank modulus tensor	234
M_r	relaxed state of $M(t)$	238
M_u	unrelaxed state of $M(t)$	238
n	number of layers in lamina	55
n_b	number of worm burrows per cm^2	193
p	pore fluid pressure	9
$p(z)$	variation of pore pressure with depth	26
p_0	pore pressure at surface of sea-bed	25
p_i	PUPPI insertion pressure	42
p_p	tidal induced differential pore pressure	43
p_t	tidal pressure	43
$P_{1,3}$	maximum fast compressional wave pore pressure amplitudes	22
$P_{2,4}$	maximum slow compressional wave pore pressure amplitudes	22
q	hydrodynamic tidal pressure	25
q_0	maximum amplitude of q	26
Q	elastic constant	9
$1/Q_E$	specific extensional attenuation	144
$1/Q_s$	specific shear attenuation	80

r	radius of porous rod	144
r_0	radius of probe	42
r_b	radius of worm burrows	193
R	reflection coefficient	199
S	fraction of gas in fluid	30
t	time	9
t_{50}	time for 50% consolidation	42
T	tortuosity	11
$\hat{T}(\kappa)$	complex dimensionless argument	13
u	solid displacement	9
u_i	solid displacement in three dimensions ($i = 1,2,3$)	233
U	fluid displacement	9
$U_{1,3}$	maximum fast wave solids displacement amplitude	22
$U_{2,4}$	maximum slow wave solids displacement amplitude	22
U_G	normalised uncertainty in G	174
U_{Kb}	normalised uncertainty in K_b	174
U_{Kf}	normalised uncertainty in K_f	174
U_{Ks}	normalised uncertainty in K_s	174
U_{Vz}	normalised uncertainty in V_z	174
U_ϕ	normalised uncertainty in ϕ	174
U_p	normalised uncertainty in p	174
$U_{\rho f}$	normalised uncertainty in ρ_f	174
$U_{\rho s}$	normalised uncertainty in ρ_s	174
$V_{1,3}$	Biot fast wave velocity predictions at frequency f	14
$V_{2,4}$	Biot slow wave velocity predictions at frequency f	14
V_e	experimental fast wave velocity	198
V_{frame}	velocity of "frame" wave	102
V_G	Gassmann theory fast wave velocity prediction	15
V_I	infinite frequency Biot fast wave velocity prediction	16

V_{2I}	infinite frequency Biot slow wave velocity prediction	16
V_{in-sit}	in-situ velocity of sea-water	170
V_{lab}	laboratory velocity of sea-water	170
V_p	fast wave velocity	49
V_r	rod (extensional) wave velocity	62
V_s	shear wave velocity	62
V_t	total volume of pore space	131
V_x	volume of pore space occupied by pores of specific pore radius	131
V_z	zero frequency Biot fast wave velocity prediction	15
V_{2Z}	zero frequency Biot slow wave velocity prediction	15
w	relative displacement of fluid to solid	9
$W_{1,3}$	maximum fast wave relative motion amplitude	22
$W_{2,4}$	maximum slow wave relative motion amplitude	22
x_i	Cartesian co-ordinate ($i = 1,2,3$)	233
X	elastic constant	143
Y	elastic constant	143
z	depth displacement co-ordinate	9
$\hat{z}_{1,3}$	fast wave complex characteristic roots	14
$\hat{z}_{2,4}$	slow wave complex characteristic roots	14
Z_1	predicted fast wave impedance	198
α	elastic constant	9
β	constant	62
γ_w	unit weight of water	33
δ_E	extensional logarithmic decrement	241
δ_{ij}	Kronecker's delta	234
ΔG	uncertainty in G	174
ΔK_b	uncertainty in K_b	174

ΔK_f	uncertainty in K_f	174
ΔK_s	uncertainty in K_s	174
Δp	uncertainty in prediction of p	178
Δp_p	differential pore pressure measured by PUPPI	41
ΔV_z	uncertainty in prediction of V_z	174
$\Delta \rho_f$	uncertainty in ρ_f	174
$\Delta \rho_s$	uncertainty in ρ_s	174
$\Delta \phi$	uncertainty in ϕ	174
$\Delta \omega$	width of resonance peak	241
ϵ	dilatational strain	9
$[\epsilon_{ij}]$	symmetric strain tensor ($i, j = 1, 2, 3$)	233
η	dynamic viscosity	9
θ	constant	62
$\hat{\theta}$	complex boundary correction function	143
θ_i	imaginary part of $\hat{\theta}$	143
θ_r	real part of $\hat{\theta}$	143
κ	dimensionless argument of operator $\hat{F}(\kappa)$	12
λ	elastic constant	235
$\hat{\lambda}$	complex anelastic coefficient	241
λ_t	wavelength of tidal stress	25
ν	Poisson's ratio	89
ν_b	frame Poisson's ratio	88
ρ	bulk density (wet)	10
ρ_{12}	mass coupling coefficient	130
$\hat{\rho}_{12}$	complex mass coupling coefficient	130
ρ_{bh}	electrical resistivity of bore-hole sediments	206
ρ_f	fluid density	10
ρ_{pf}	electrical resistivity of pore-fluid in sediments	206
ρ_s	solids density	11

σ	total vertical stress	9
σ_{eff}	effective stress	170
σ_{pc}	pre-consolidation effective stress	210
$[\sigma_{ij}]$	stress tensor	233
$\Sigma_{1,3}$	maximum fast wave total stress amplitude	22
$\Sigma_{2,4}$	maximum slow wave total stress amplitude	22
τ	relaxation time	238
ϕ	porosity	9
ϕ	loss angle	239
ϕ_E	extensional-mode loss angle	240
ω	angular frequency	13
ω_r	resonant angular frequency	61
Ω_{ij}	rotation	237
$\partial/\partial t$	temporal differential operator	9
$\partial/\partial z$	one dimensional spatial differential operator	9
∇	three dimensional spatial differential operator	237

1 INTRODUCTION

1.1 Background

Between the years 1941 and 1962, M.A. Biot developed a theory relating the propagation velocity of sound waves at different frequencies, to various physical and geotechnical properties of sea-bed sediments. The importance of understanding this link between the propagation of sound through sea-bed sediments and the properties of those sediments are shown by four different examples from areas as diverse as defence, oil exploration, engineering design and environmental pollution control.

The ability to track and communicate to submarines relies upon sound transmission through the sea. The manner in which sound waves interact with sea-bed sediments considerably affects the efficiency of naval surveillance systems. The important aspects of sound transmission through sea-bed sediments (of the ocean floor) which are of interest to the United States Office of Naval Research are given by Malahoff (1974): "Particular emphasis is directed toward studies of ocean floor acoustical processes, namely the physics of high frequency reflectivity of the ocean floor; the physics of low frequency acoustical propagations through the sea floor; the formation of ocean floor acoustic reflectors; and the areal variations in these acoustic phenomena".

Both offshore and onshore oil exploration depend upon identifying buried geological structures which hold the promise of trapping oil. Large scale mapping of structures can be achieved by the seismic reflection method, where sound waves are reflected by the boundaries between different layers of sedimentary rocks. However, with the depletion of oil resources and the expense of offshore investigations, greater attention is being focussed on the fine detail of seismic reflection records and attempts to completely define these data through geological and

geophysical borehole results (McQuillan et al., 1984). From borehole or laboratory studies, the propagation velocity and attenuative properties of sedimentary rocks can reveal much diagnostic information, such as the lithology, physical state, and degree of saturation (Toksoz and Johnson, 1981). The transition from large scale seismic reflection surveys to small scale borehole and laboratory work requires a move to higher frequency sound wave sources; so the frequency dependence of velocity and attenuation also becomes important.

The successful design of offshore structures relies on a knowledge of the geotechnical properties of sea-bed sediments and an understanding of how they deform under static and dynamic stresses (Muir-Wood, 1980). The shear strength, the bearing capacity, the permeability and the dynamic shear modulus of sea-bed sediments are all required by the design engineer. Conventional high strain amplitude geotechnical tests often do not capture the dynamic elastic behaviour of sea-bed sediments at low strain amplitudes (Taylor-Smith, 1974). A better understanding of (low strain amplitude) sound wave propagation through sea-bed sediments may allow prediction of desired geotechnical parameters (Taylor-Smith, 1986).

Searle et al. (1985) describe contributions to a feasibility study into the containment of heat emitting radio-active waste beneath sea-bed sediments. Central to this work is the determination of the geotechnical properties of sea-bed sediments and characterisation of pore-water advection within the sea-bed. The shear strength and shear moduli need to be known so the feasibility of burial of waste canisters within the sea-bed sediments can be assessed. The permeability and excess pore pressure need to be measured so that the time taken for any radio-nuclides (which might escape from the canisters) to reach the water column can be calculated. If this seepage time is greater than the decay time of the waste (to environmentally safe levels), no pollution will occur.

1.2 Sound waves in relation to Biot's theory

"Sound" is the name given to small amplitude stress waves which propagate through media, and which are audible to the human ear. "Sound" is used to describe compressional stress waves; although there are other types of stress waves including shear, rod and interface waves, which are not audible. Compressional waves can propagate within three frequency bands; below 10 Hz in the infra-sonic range; between 20 Hz and 20 kHz in the acoustic range and above 20 kHz in the ultrasonic range. The velocity of compressional waves varies with frequency - a phenomenon called velocity dispersion - as does its attenuation.

Biot's (1956 a,b) theory gives relationships for the velocity and attenuation of compressional and shear waves as a function of the physical constants of the medium through which the waves propagate, and also the frequency of the stress waves. Biot's theory predicts two kinds of compressional stress wave: the fast wave, which is the usual sound wave, and the slow wave which is more obscure in character.

If the appropriate physical constants of sea-bed sediments are measured, then Biot's theory can be used to predict the frequency variation of velocity and attenuation of compressional waves travelling through those sediments. If velocity and attenuation measurements are collected at various frequencies, then Biot's theory can be used in an inverse sense allowing predictions of various physical constants of the sediment.

Biot's full (1962 a,b) theory requires 12 physical constants which describe the sediment (the input parameters) and gives predictions of the velocity and attenuation of fast and slow compressional waves (the output parameters). The task of determining the input and output parameters is complicated by many factors: retrieving representative samples of sediment from the sea-bed with minimal disturbance; the extreme variability of

sea-bed sediments both laterally and vertically within the sea-bed; anisotropy within the sediments themselves; lastly, the technical difficulties in accurately measuring many of the 12 input parameters, measuring the fast wave dispersion and attenuation over a wide frequency band, and of course, measuring the slow wave at all.

1.3 Aims of this thesis

In this thesis, the validity of the following hypothesis is examined: a numerical model of the sea-bed (based on measurements of sediment physical properties) can be used as input for Biot's theory to allow predictions of the response of the sea-bed when it is subjected to dynamic stresses. The strategy adopted can be outlined as follows:

1. The importance of the input and output parameters to Biot's theory are assessed in the light of their ease of experimental determination.

2. The impracticable aspects of Biot's theory are eliminated allowing simplified models of the sea-bed sediments to be defined.

3. Data are collected to create appropriate numerical models of the sea-bed.

4. Using the models as input for a practical version of Biot's theory, predicted and measured responses are compared.

Models are constructed for two different parts of the compressional wave frequency spectrum. The geacoustic models which are used lie in the acoustic to ultrasonic frequency range, where sound wave propagation velocities and attenuations can be measured on samples in the laboratory. A hydrodynamic model is used at a much lower frequency value (in the infra-sonic range) to study the deformation of sea-bed sediments under tidally-induced stresses.

For the hydrodynamic model of the sea-bed, it is not the velocity of compressional waves which are of interest, but the spatial variation of the in-situ pore-pressure response induced by the tide.

The models are based on measurements of the physical properties of sediments from two areas of sea-bed. Site 1, which is a sequence of turbidite sediments from Great Meteor East in the Northern Atlantic Ocean, and Site 2, a sequence of thick carbonate sediments from the Western Indian Ocean. Data from Site 3, a deep-sea carbonate area from the Pacific Ocean and Site 4, a marine beach area in the UK, are used for background information.

1.4 The structure of the thesis

Chapters 2 and 3 introduce Biot's (1956 a,b,c) theory of poroelasticity and give the necessary analysis which lead to expressions for pore-pressures and velocities developed as a consequence of deformation of sea-bed sediments.

Chapters 4 and 5 focus on techniques and experiments involved in evaluating the permeability and elastic constants of sea-bed sediments; as both are identified as key parameters in geoacoustic and hydrodynamic models.

Chapters 6, 7 and 8 cover aspects of compressional wave propagation in sediments, concentrating on identifying the physical properties which influence the velocity and attenuation of these waves. The experimental difficulties involved in measuring both the physical properties and the waves are assessed.

Chapter 9 uses the major results obtained from Chapters 3 to 8 to allow the definition of simplified and practical geoacoustic and hydrodynamic models which can be analysed using Biot's (1956 a,b,c) theory.

Chapters 10 and 11 describe the geoacoustic models (based on experimental data) for Sites 1 and 2, and the hydrodynamic model for Site 1. Biot's theory is applied to these models allowing comparisons between predicted and measured deformations of sea-bed sediments.

Chapter 12 gives a discussion on the validity of the hypothesis (given in 1.3), based on the results of the previous chapters and ends with some conclusions and recommendations for future work.

2.1 Introduction

Biot's theory of poroelasticity is an extension of the classical theory of elasticity (Appendix 1). Biot developed his theory over a number of years, directing his attentions to fluid saturated porous systems. The initial work (Biot, 1941) concentrated upon establishing the governing equations relating the following primary variables: stress, strain, pore-pressure, solid and fluid displacement. Biot (1941) applied these equations to the problem of predicting the pore pressure and settlement, as functions of time and space, within a sediment column which had a static stress applied to it.

Later, inertial terms were added to the governing equations (Biot 1956 a,b) allowing an extension of the earlier theory to cover dynamic stresses. In these papers, the governing equations were used to obtain wave equations for compressional and shearing deformations. The solutions to these wave equations yielded compressional and shear wave velocities and attenuations as functions of frequency. These results led to the interesting discovery that two different types of compressional waves could propagate within a porous saturated medium; the fast and the slow waves.

This poroelastic theory (Biot, 1956 a,b,c) was later improved and extended to the case of poro-anelastic materials (Biot 1962 a,b). However, experimental methods had not improved enough to make full use of this more generalised formulism. A simplified more practical version of Biot's (1962a) theory for poro-anelastic deformations was offered by Stoll and Bryan (1970). The simplified form of Biot's theory of poro-anelasticity (which is still complex!) is often called the Biot-Stoll theory. This version of the theory has been further developed by other workers (e.g.

Berryman and Thigpen, 1987) gaining in sophistication, but lacking in practicality.

The Biot-Stoll theory represents one of the most complex forms of poro-anelastic theory used in the literature to characterise the behaviour of sediments and rocks under dynamic stresses. However, it is often more useful to use less complex versions of Biot's theory, as the number of experimental measurements required are greatly reduced. A useful approximate version of Biot's (1956 a,b) theory was obtained by Geertsma and Smit (1961).

There are numerous examples in the literature where Biot's theories of quasi-static poroelasticity (Biot 1941), dynamic poroelasticity (Biot 1956 a,b) and dynamic poro-anelasticity (Biot 1962 a,b), have been used to successfully characterise the behaviour of sediments and rocks under different applied stresses. The case of quasi-static poroelasticity is the most appropriate to consider first as it is straightforward to extend it to the dynamic poroelastic and poro-anelastic cases. For simplicity the theories will be presented in their one-dimensional form.

2.2 Quasi-static poroelasticity

2.2.1 A poroelastic medium and its state variables

A poroelastic medium is an elastic medium containing voids or pores which are fluid filled. The fluid may be a gas. Porous sediments or rocks can be treated as special cases of poroelastic media. In a porous sediment the grains are bonded or pressed together to form an elastic "frame", which can be fluid saturated. However, the grains or solid materials making up the frame themselves can be treated as elastic, as can the pore fluid. The elasticity of the frame, the solids and the fluids, are all important in controlling how the sediment behaves under the application of stresses.

Biot's (1941) theory of quasi-static poroelasticity does not imply a frame of sedimentary grains surrounded by a fluid. However, to use Biot's theory it is conceptually useful to visualise the sediments in this way. Biot's (1941) theory relates the following state variables of a fluid saturated porous elastic medium: the total vertical stress (σ), the pore fluid pressure (p), the solid displacement (u), the fluid displacement (U), the vertical strain component (ϵ) and the relative motion of fluid to solid (w). The latter is simply related to U and u by the fractional porosity (ϕ):

$$w = \phi \cdot (U - u) \quad 2.1$$

2.2.2 The governing equations for quasi-static poroelasticity

Biot's theory relates the poroelastic state variables through the four governing equations. The constitutive relationship is a modified version of the constitutive relationship for elasticity (Appendix 1), accounting for the effect of pore pressures. It is a sophisticated version of the Terghazi effective stress principle. The equilibrium of stress field is the same as for classical elasticity (Appendix 1). The equilibrium of fluid flow is given by Darcy's law. Lastly, Biot (1941) expressed the continuity of fluid flow in a new way. These equations are:

$$\sigma = \frac{\partial u}{\partial z} \cdot \frac{1}{a_b} - \alpha p \quad 2.2$$

$$\frac{\partial \sigma}{\partial z} = 0 \quad 2.3$$

$$-\frac{\partial p}{\partial z} = \frac{\eta}{k_a} \cdot \frac{\partial w}{\partial t} \quad 2.4$$

$$\alpha \cdot \frac{\partial^2 u}{\partial z \partial t} + \frac{\partial^2 w}{\partial z \partial t} = - \frac{\partial p}{\partial t} \cdot \frac{1}{Q} \quad 2.5$$

2.2.3 The constants characterising a poroelastic medium

Nine physical parameters of a poroelastic medium are required for Biot's quasi-static governing equations. These are: the frame bulk modulus (K_b), the frame shear modulus (G), the solids bulk modulus (K_s), the fluid bulk modulus (K_f), the fractional porosity (ϕ), the intrinsic permeability (k_a), the dynamic viscosity (η), the fluid density (ρ_f) and the total density (ρ). Biot and Willis (1957) showed that the first five of these parameters are related to the elastic constants α , Q and a_b in a simple way:

$$a_b = (K_b + 4G/3)^{-1} \quad 2.6$$

$$\alpha = 1 - \frac{K_b}{K_s} \quad 2.7$$

$$\frac{1}{Q} = \frac{\phi}{K_f} - \frac{\phi}{K_s} + \frac{1}{K_s} - \frac{K_b}{K_s} \cdot \frac{1}{K_s} \quad 2.8$$

2.2.4 Problems of quasi-static poroelasticity

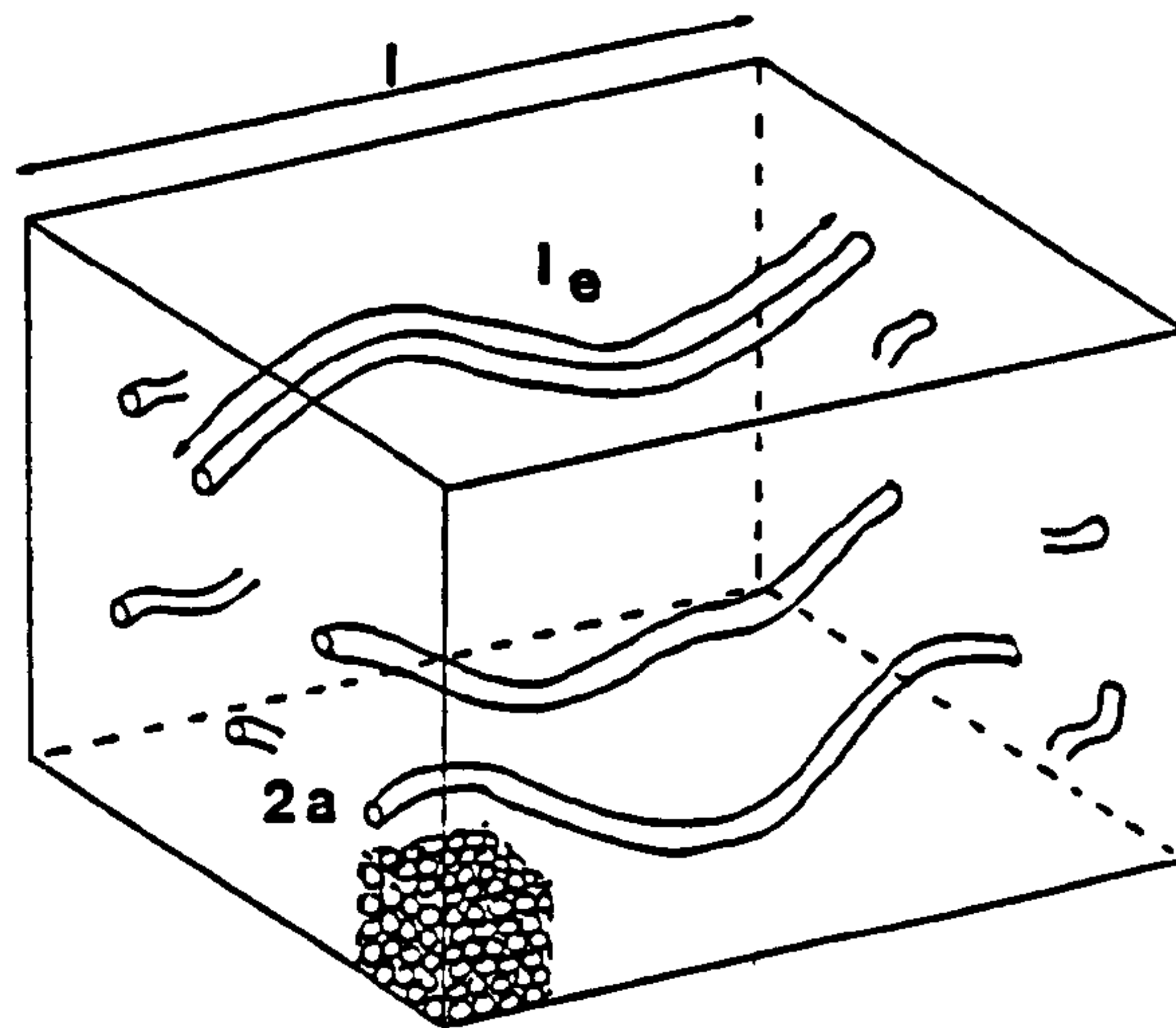
Various practical problems of quasi-static poroelasticity can be addressed by using equations 2.1 to 2.8. Biot (1941) solves the boundary value problem of one dimensional soil consolidation, finding expressions for the pore pressure and solid displacement as functions of time and space. He also showed that the consolidation problem solution consists of two components: a component given by classical elasticity theory and an additional component satisfying a heat conduction type equation. Later, Biot (1956c) obtained the general solution for quasi-static poroelasticity in a more formal fashion. Using this general solution it is possible to solve appropriate boundary value problems.

2.3 Dynamic poroelasticity

2.3.1 A model of a poroelastic medium for dynamic deformations

It is useful to extend the conceptual model of a sediment used in the quasi-static analysis to cover Biot's (1956 a,b) dynamic theory. For the new model it is assumed that the pore-space, which occurs as a result of the packing arrangement of the solid grains, can be represented by a series of capillary tubes. The tubes are assumed to be of a constant radius (a) and follow a tortuous path through the sediment, characterised by a tortuosity (T). This idealised poroelastic medium is shown in Figure 2.1.

Figure 2.1 The physical parameters for an idealised poroelastic medium



GRAIN AND PORE-FLUID PROPERTIES : K_s, ρ_s
 K_f, ρ_f, η

PORE SPACE PROPERTIES : $T = (l_e / l)^2$
 $a, k_a = \phi a^2 / 8T$

BULK PROPERTIES : K_b, G, ρ
 $\phi = (\rho_s - \rho) / (\rho_s - \rho_f)$

2.3.2 Governing equations for dynamic poroelasticity

Biot (1956 a,b) extended his theory of quasi-static poroelasticity to cover dynamic deformations by adding inertial terms to the governing equations. Later, Biot (1962a) recast these new equations in a more manageable form. The equations for the equilibrium of the stress field and equilibrium of the fluid flow became:

$$\frac{\partial \sigma}{\partial z} = \rho \cdot \frac{\partial^2 u}{\partial t \partial t} + \rho_f \cdot \frac{\partial^2 w}{\partial t \partial t} \quad 2.9$$

$$-\frac{\partial p}{\partial z} = \rho_f \cdot \frac{\partial^2 u}{\partial t \partial t} + \left[m \cdot \frac{\partial^2 w}{\partial t \partial t} + \frac{\eta}{k_a} \cdot \frac{\partial w}{\partial t} \right] \cdot \hat{F}(\kappa) \quad 2.10$$

In equation 2.10, m is an inertial coupling factor, η/k_a is a viscous damping factor and $\hat{F}(\kappa)$ is a complex frequency correction factor which allows for the deviation from Poisseuille flow at frequencies (f) above a "transitional frequency (f_t)" (Biot, 1956b). At frequencies below f_t , $\hat{F}(\kappa)$ is equal to unity. The quantity within the square brackets multiplied by $\hat{F}(\kappa)$ is Biot's (1962b) viscodynamic operator - which is the key to Biot's (1956 a,b, 1962 a,b) theory of dynamic poroelasticity. Note, all the primary variables (u , U , σ and p) are assumed to be harmonic with time and space, having a frequency f , an angular frequency ω and a complex wave number \hat{k} (Appendix 2).

2.3.3 Constants for dynamic poroelasticity and the viscodynamic operator

To calculate the viscodynamic operator and, hence, to use Biot's theory of dynamic poroelasticity two further material parameters are required in addition to those used for the quasi-static formulism (2.2.3). The tortuosity (T) is required to calculate the inertial coupling factor (m) and an average pore-radius / shape value (a) is needed for the frequency correction $\hat{F}(\kappa)$:

$$\mathbf{u} = \frac{\mathbf{T} \cdot \rho}{\phi} \mathbf{f} \quad 2.11$$

$$\hat{\mathbf{P}}(\kappa) = \frac{\kappa \cdot \hat{\mathbf{T}}(\kappa)}{4 - [8 \cdot \hat{\mathbf{T}}(\kappa) / i\kappa]} \quad 2.12$$

$$\hat{\mathbf{T}}(\kappa) = \frac{\text{ber}'(\kappa) + i\text{bei}'(\kappa)}{\text{ber}(\kappa) + i\text{bei}(\kappa)} \quad 2.13$$

$$\kappa = a \cdot \left[\frac{\omega \rho}{\eta} \mathbf{f} \right]^{1/2} \quad 2.14$$

$$\mathbf{f}_t = \frac{\pi \eta}{\rho_f 4a} 2 \quad 2.15$$

There still remains some controversy over the exact nature of the viscodynamic operator. Cleary (1980) derives an alternative version which accounts for the aspect-ratio of the capillary-like pores. Johnson et al. (1987) introduce a new constant which is related to the ratio of the wetted surface area of pores to the pore volume. However, in both these cases additional information to T and a is required to further define the microgeometry of the pore-space. There are considerable practical difficulties in extracting this type of information for natural sediments and rocks, and it is these experimental short-comings which limit the usefulness of these more sophisticated versions of Biot's theory.

2.3.4 The problem of dynamic poroelasticity: the characteristic equation

As for classical elasticity (Appendix 1) and classical anelasticity (Appendix 2), it is possible to construct an equation which has harmonic plane wave solutions. Biot (1956a, 1962a) obtains the characteristic equation for dynamic poroelasticity by combining the dynamic governing equations (equations 2.2, 2.5, 2.9, 2.10) assuming harmonic plane wave solutions. Thus, combining these, one obtains the coupled equations:

$$\left[\frac{1}{a_b} + \alpha^2 Q \right] \cdot \frac{\partial^2 u}{\partial z \partial z} + \alpha Q \cdot \frac{\partial^2 w}{\partial z \partial z} = \rho \cdot \frac{\partial^2 u}{\partial t \partial t} + \rho_f \cdot \frac{\partial^2 w}{\partial t \partial t} \quad 2.16$$

$$\alpha Q \cdot \frac{\partial^2 u}{\partial z \partial z} + Q \cdot \frac{\partial^2 w}{\partial z \partial z} = \rho_f \cdot \frac{\partial^2 u}{\partial t \partial t} + \left[m \cdot \frac{\partial^2 w}{\partial t \partial t} + \frac{\eta}{k_a} \cdot \frac{\partial w}{\partial t} \right] \cdot \hat{F}(\kappa) \quad 2.17$$

If the state variables u and w are allowed to become harmonic in time and space, characterised by a complex wave number \hat{k} and an angular frequency ω (see Appendix 2), then the coupled equations can be combined to form the characteristic equation, which is a fourth order polynomial in \hat{k}/ω , with complex coefficients:

$$\begin{aligned} & \left[\frac{\hat{k}}{\omega} \right]^4 \cdot \frac{Q}{a_b} + \left[\frac{\hat{k}}{\omega} \right]^2 \cdot \left[2\alpha Q \rho_f - Q \rho - \hat{F}(\kappa) \cdot \left[\frac{1}{a_b} + \alpha^2 Q \right] \cdot \left[m - \frac{i\eta}{\omega k_a} \right] \right] \\ & + \left[\rho m \cdot \hat{F}(\kappa) - \rho_f^2 - \frac{i\eta \rho}{\omega k_a} \cdot \hat{F}(\kappa) \right] = 0 \end{aligned} \quad 2.18$$

2.4 Solutions to the characteristic equation

2.4.1 Exact solutions

The characteristic equation can be re-expressed as a quadratic in $(\hat{k}/\omega)^2$ which can be simply solved using the quadratic solution formula. Therefore, the four roots of the characteristic equation ($\hat{z}_1 = -\hat{z}_3$, $\hat{z}_2 = -\hat{z}_4$) can be determined. Unfortunately, these exact solutions are very lengthy and not suitable for explicit expression, but they can be obtained by using the computer coding shown in Appendix 4.

The roots \hat{z}_1 and \hat{z}_3 represent fast compressional waves travelling in negative and positive directions; \hat{z}_2 and \hat{z}_4 represent slow compressional waves. The real and imaginary components of these roots are simply related to the velocity (V_j) and specific attenuation coefficient (a_j) of each wave ($j = 1, 2$), see Appendix 2:

$$[\hat{z}_j]^2 = \left[\frac{\hat{k}_j}{\omega_j} \right]^2, \quad j = 1 \text{ (fast)}, j = 2 \text{ (slow)} \quad 2.19$$

$$v_j = \left[\frac{\omega}{\text{Re}(\hat{k}_j)} \right] \quad j = 1, 2, \quad \text{Re}(k) = \text{Real part of } \hat{k} \quad 2.20$$

$$a_j = \text{Im}(k_j), \quad j = 1, 2, \quad \text{Im}(k) = \text{Imag part of } \hat{k} \quad 2.21$$

2.4.2 Asymptotic velocity limits

The exact solutions to the characteristic equation allow the velocity and attenuation coefficients of the fast and slow wave to be determined as a function of angular frequency (ω). Low-frequency asymptotic expressions for the fast and slow wave velocities (V_Z and V_{2Z}) may be obtained by making the viscous damping factor much larger than the inertial coupling factor in the viscodynamic operator, and then expanding the characteristic equation:

$$\hat{z}_1 = -\hat{z}_3 = \left[\frac{a_b \cdot \rho}{1 + Q a_b \alpha^2} \right]^{1/2} \quad 2.22$$

$$\hat{z}_2 = -\hat{z}_4 = \left[-\frac{i\gamma\omega}{k_a} \cdot \left[\frac{1}{Q} + a_b \alpha^2 \right] \right]^{1/2} \quad 2.23$$

Gassmann (1951) independently obtained an expression for the (fast) compressional wave velocity in an undrained poroelastic medium (V_G). The undrained or "closed" pore condition means that no fluid flow takes place within the poroelastic medium. According to Biot's theory, the closed pore condition is almost equivalent to the low-frequency fast wave velocity asymptote (V_G), where the viscous drag is so large that little relative flow occurs between the fluid and solid components. Therefore it is possible to write $V_Z \approx V_G$ where Gassmann's equation is:

$$v_G = \left[\frac{1/a_b + \alpha^2/Q}{\rho} \right]^{1/2} \quad 2.24$$

High frequency asymptotic expressions can be obtained by making the damping factor much less than the inertial coupling factor; however these results are still complex. An alternative method for obtaining an approximate high frequency asymptote has been given by Geertsma and Smit (1961).

2.4.3 Approximate velocity solutions

Geertsma and Smit (1961) obtained high frequency approximate velocity solutions to the characteristic equation for the fast (V_I) and slow (V_{2I}) waves. They first assumed that the (imaginary) viscous damping terms could be neglected at this limit and also that the quadratic equation in $(\hat{k}/\omega)^2$ has simple roots:

$$v_I^2 \approx \frac{Q\rho + (1/a_b + \alpha^2 Q) \cdot m - 2\alpha Q\rho_f}{\rho m - \rho_f \rho_f} \quad 2.25$$

$$v_{2I}^2 \approx \frac{Q/a_b}{m \cdot (1/a_b + \alpha Q \alpha) + Q\rho - 2\alpha Q\rho_f} \quad 2.26$$

The approximate solutions (equations 2.25 and 2.26) will hold providing that:

$$\frac{Q\rho + m \cdot (1/a_b + \alpha^2 Q) - 2\alpha Q\rho_f}{\rho m - \rho_f \rho_f} \gg \left[\frac{4Q/a_b}{\rho m - \rho_f \rho_f} \right]^{1/2} \quad 2.27$$

Geertsma and Smit (1961) also recognised that the frequency dependence of the fast compressional wave (V_1), between the infinite frequency velocity limit (V_I), and the low-frequency limit (V_Z , which is given by equations 2.19, 2.20 and 2.22, or equation 2.24), can be approximated by the following relationship:

$$V_1 \approx \frac{V_I^4 \cdot [(k_a \omega \cdot (\rho_m - \rho_f \rho_f))]^2 + V_Z^4 \cdot [\eta \rho]^2}{V_I^2 \cdot [(k_a \omega \cdot (\rho_m - \rho_f \rho_f))]^2 + V_Z^2 \cdot [\eta \rho]^2} \quad 2.28$$

2.4 Summary

Biot's theory introduces the governing equations for poroelasticity which relate the four primary variables (total stress, pore pressure, fluid displacement and solid displacement) through eleven physical constants of the poroelastic medium.

For dynamic problems (where inertial terms are important), a characteristic equation can be developed from the governing equations. The solution of the characteristic equation gives the propagation velocity and attenuation constants of compressional waves travelling through the poroelastic medium. Two compressional waves are predicted, one fast and the other slow. At the low frequency limit, Biot's fast wave velocity (V_Z) is equivalent to that given by Gassmann (1951). At the infinite frequency limit, an approximate equation for the fast wave velocity (V_I) is provided by Geertsma and Smit (1961). The velocity dispersion between V_Z and V_I can be given by an approximate solution of the characteristic equation (Geertsma and Smit, 1961).

The equations presented in Chapter 2 are important for all subsequent chapters. Of particular significance is the characteristic equation, which can be solved to give fast and slow wave velocities and attenuation coefficients as a function of frequency (computer coding given

in Appendix 4). In Chapter 3, the low frequency general solution to Biot's theory will be developed using some of the results from Chapter 2. Boundary conditions can be applied to this general solution, resulting in a particular solution. The particular solution gives expressions for the primary variables as a function of time and space and of the physical constants of the poroelastic medium. The boundary value problem of tidal-loading of the sea-bed will be presented in Chapter 3.

3.1 Introduction

The solutions of Chapter 2 allow the velocity and attenuation of compressional waves to be determined at various frequencies. These solutions do not offer a complete description of the variation of the primary variables as functions of time and space. In order to do this, the general solutions of poroelasticity need to be developed. These general solutions can then be applied to suitable boundary value problems.

Biot (1956c) developed the general solutions for poroelasticity using the Biot (1941) quasi-static formulation of the governing equations. Later, Rice and Cleary (1976) obtained similar expressions and applied them to problems of crack propagation in poroelastic media. Yamamoto et al. (1978), Zienkiewicz et al. (1980), Mei and Foda (1981) and Okusa (1985), amongst other authors, derived general solutions of poroelasticity from quasi-static or dynamic formulations. These authors then applied their solutions to problems such as wave loading of the sea-bed and the earthquake response of the footings of dams. In many of these cases the analysis is more complex than necessary, introducing slight errors in some results.

It is of interest to illustrate the equivalence of the general solutions obtained from quasi-static and dynamic formulations of Biot's (1941, 1956a) theory in a simple and clear fashion. Once this equivalence has been shown, the simplified results can be used to solve various boundary value problems, such as predicting pore pressures developed in the sea-bed due to stresses imposed on it by tidal forces. This particular problem is of significance as experimental data, recording the variation of dynamic pore-pressures developed in the sea-bed due to tidal pressures, have recently become available (Schultheiss and McPhail, 1985).

If the simplified general solutions can be successfully applied to the boundary value problem of tidal loading of the sea-bed, then the magnitude of the sea-bed parameters which control these deformations can be inferred. This is of great interest, as any (inverse) in-situ determination of a particular property of the sea-bed is valuable for comparative purposes with laboratory measurements of that property. In-situ determinations of geotechnical parameters are especially valuable for civil engineering design purposes.

3.2 General solutions of poroelasticity

3.2.1 Quasi-static formulation

The general solutions to poroelasticity give expressions for the primary variables u , w , p and σ , as functions of time and space. To obtain these general solutions, the (1 dimensional) governing equations (2.2 to 2.5) are combined to form a characteristic equation, which can be simply solved. Superimposition of the roots of this equation gives the general solutions. Combining equations 2.2 to 2.5 gives:

$$\frac{\partial^2 p}{\partial z^2} \cdot \frac{k}{\eta} a = \frac{\partial p}{\partial t} \cdot \left[\frac{1}{Q} + \alpha^2 a_b \right] + \alpha a_b \cdot \frac{\partial \sigma}{\partial t} \quad 3.1$$

Operating on equation 3.1 with $\frac{\partial^2}{\partial z^2}$ and rearranging gives:

$$\frac{\partial^2}{\partial z^2} \cdot \left[\frac{\partial^2 p}{\partial z^2} - \frac{\partial p}{\partial t} \cdot \frac{\eta}{k_a} \cdot \left[\frac{1}{Q} + \alpha^2 a_b \right] \right] = 0 \quad 3.2$$

The solution to equation 3.2 is given by the sum of the solutions of the following two equations (Biot, 1956c):

$$\frac{\partial^2 p}{\partial z \partial z} = 0 \quad 3.3$$

$$\frac{\partial^2 p}{\partial z \partial z} = \frac{\partial p}{\partial t} \cdot \frac{\eta}{k_a} \cdot \left[\frac{1}{Q} + \alpha^2 a_b \right] \quad 3.4$$

Equation 3.3 is Laplace's equation and is associated with the fast wave, whilst 3.4 is a diffusion equation which is associated with the slow wave. Assuming a harmonic solution gives:

$$\hat{k}_1 \approx (-\hat{k}_3) \approx 0, \quad 3.5$$

$$\hat{k}_2 \approx (-\hat{k}_4) \approx \left[\frac{i\omega\eta}{k_a} \cdot \left[\frac{1}{Q} + \alpha^2 a_b \right] \right]^{1/2} \quad 3.6$$

with, $p = p_0 \exp[i(\omega t + \hat{k}z)]$

The wave numbers \hat{k}_1 and \hat{k}_3 represent fast compressional waves travelling in opposite directions with infinite phase velocity and zero attenuation. (In practice the fast wave velocity is finite at the low frequency limit and is given by equation 2.24, but it can be considered instantaneous with respect to the slow wave velocity). The wave numbers \hat{k}_2 and \hat{k}_4 represent slow waves travelling in opposite directions.

Biot (1941 and 1956a) noted that it takes some finite time for fluid flow to occur (equation 2.4) and therefore there is no fluid flow (hence viscous attenuation) for the effectively instantaneous fast wave. If $\frac{\partial w}{\partial t}$ is set equal to zero in the governing equations 2.4 and 2.5, the following relationship for the ratio of pore-pressure to the total stress can be found:

$$\frac{p}{\sigma} = - \frac{a_b \alpha Q}{1 + Q a_b \alpha^2} \quad (= P_1 = - P_3) \quad 3.7$$

Note, equation 3.7 is equivalent to the expression obtained by Biot (1941) for the instantaneous pore pressure developed in a sediment which has a static load applied to it. Now adding together the pore-pressure contributions from equations 3.5 and 3.6 gives the general pore-pressure solution for harmonic deformations of a poroelastic medium obtained from the quasi-static formulation of Biot's theory of poroelasticity:

$$p = \sum_{j=1}^{j=4} P_j \exp[i(\omega t + \hat{k}_j z)] \quad 3.8$$

Here, P_2 and P_4 are constants which are determined by the boundary conditions of the particular problem for which the general solution is used. and P_1 and P_3 are set by equation 3.7. There are similar relationships to equation 3.8 for the other primary variables u , w , and σ , with constants U_{1-4} , W_{1-4} , and Σ_{1-4} , which can be determined by using equations 2.2 to 2.5, 2.16, 2.17 and 3.8 along with the boundary conditions of the problem in question.

3.2.2 Dynamic formulation

The general solutions for poroelasticity can also be obtained from the dynamic governing equations (2.2, 2.5, 2.9 and 2.10). These solutions would be expected to be more useful than those obtained from the quasi-static formulation as they would be applicable over the entire frequency range, accounting for the dispersive and attenuation behaviour of both fast and slow waves.

Deresiewicz and Rice (1962) and Geertsma and Smit (1961) use general solutions obtained from the Biot's (1956 a,b) dynamic governing equations to study the reflection and transmission of compressional waves

at different porous / non-porous boundaries at both low and infinite frequency asymptotes. Zienkiewicz et al. (1980) and Mei and Foda (1981) use general solutions obtained from simplified dynamic governing equations (which are taken in the low-frequency range - hence μ is set to zero and $\hat{P}(\kappa)$ to unity in equation 2.10) to study the transmission of low-frequency compressional vibrations on land and the sea-bed.

The same approach to obtaining the general solution for the pore pressure, as used for the quasi-static formulation (3.2.1), is used for the dynamic formulation. Simply, the solutions to the dynamic characteristic equation (2.18, 2.19) are used to define the wave numbers \hat{k}_{1-4} , which are combined as in equation 3.8.

To check that the quasi-static and dynamic formulations give similar results, the low frequency asymptote solution of the dynamic characteristic equation is compared with the quasi-static solution. The equivalence of the \hat{k}_2 and \hat{k}_4 solutions from quasi-static and dynamic characteristic equations can be observed by comparing equation 3.6 to 2.23 and 2.19. However, if equation 3.5 is compared to 2.22 and 2.19 the deficiencies of the quasi-static analysis becomes apparent. The quasi-static analysis suggests that the fast wave travels with infinite velocity with $\hat{k}_1 \approx \hat{k}_3 \approx 0$, which is clearly not true. The fast wave velocity is virtually instantaneous with respect to the slow wave velocity, but the fast wave velocity is finite and is given by equation 2.24.

The next step to show the equivalence between the two formulations is to obtain a relationship similar to equation 3.7 from the dynamic governing equations. This is achieved by first obtaining a relationship between the constants U_{1-4} and W_{1-4} at low frequencies. Therefore, equation 2.16 can be rewritten (using equation 2.19):

$$\frac{W_j}{U_j} = \frac{[1/a_b + \alpha^2 Q] \cdot \hat{z}_j^2 - \rho}{\rho_f - \alpha Q \cdot \hat{z}_j^2} \quad j = 1, 2, 3, 4 \quad 3.9$$

(assuming $u = u_0 \exp[i(\omega t + k z)]$ and $w = w_0 \exp[i(\omega t + k z)]$)

Using the low-frequency solution for the fast wave (equation 2.22) in equation 3.9 ($j = 1, 3$), gives the following relationship between the ratio of the relative fluid motion and solid motion amplitudes for the fast wave:

$$\frac{W_1}{U_1} \approx \frac{W_3}{U_3} \approx 0 \quad 3.10$$

Equation 3.10 shows that for this low-frequency limit there is virtually no relative motion between the solids and fluids $\left[\frac{\partial w}{\partial t} = 0 \right]$ for the fast wave. This is proof of Biot's (1941) intuitive observation (see 3.2.1) and is a result which was used by Geertsma and Smit (1961) in their analysis of reflection of compressional waves at boundaries. Next, the result $\frac{\partial w}{\partial t} = 0$ for fast wave deformations is substituted back into the governing equations (2.2, 2.5, 2.9, 2.10) which gives:

$$\frac{p}{\sigma} = - \left[\frac{Q \alpha a_b}{1 + Q a_b \alpha^2} \right] = - \frac{\rho}{\rho_f} \quad 3.11$$

This equation is essentially the same as equation 3.7, which again backs up the agreement between quasi-static and dynamic analyses. However, there is the additional result in equation 3.11, which relates the elastic constants Q , a_b and α to the density components ρ and ρ_f . Cleary (1980) identifies this as the much misunderstood Biot (1956a) compatibility relationship, which allows for the propagation of the fast and slow

compressional waves without any relative motion between fluid and solid $\left[\frac{\partial w}{\partial t} = 0\right]$. Also, it can be verified that $\frac{\partial w}{\partial t} = 0$, by obtaining a similar equation to 3.9 from 2.17, substituting in the low-frequency fast wave solution (2.22) and finally using 3.11.

In summary, the results given in equations 2.22, 2.23 and 3.11, obtained from the dynamic analysis, agree favourably with their counterparts, 3.5, 3.6 and 3.7, obtained from the quasi-static analysis. This agreement gives an equivalent general solution for the pore pressure (as shown in equation 3.8) obtained from both formulations. This agreement is valid only at low-frequencies. As the frequency approaches f_t (equation 2.15) the inertial terms of the viscodynamic operator and the frequency correction factor $\hat{F}(\kappa)$ affect the general solution obtained from the dynamic formulation.

3.3 Boundary value problem

3.3.1 Tidal loading of the sea-bed

The general solution for the variation of the pore-pressure as a function of time and space, obtained for a poroelastic medium which is subjected to harmonic stresses (3.2), can be used to solve the simple boundary value problem of tidal loading of the sea-bed. The boundary conditions assumed for this problem are shown in Figure 3.1.

The tide is assumed to exert a uniaxial harmonic hydrostatic stress on the sea-bed, of magnitude q , angular frequency ω and wavelength λ_t . The sea-bed is assumed to comprise a layer of elastic sediments of thickness L_s ($\ll \lambda_t$), overlying a rigid, impermeable basement. The single important boundary condition is that the effective stress at the surface of the sea-bed is zero, i.e. the pore pressure at the surface of the sea-bed (p_0) is equal and opposite to the tidal pressure (q). These boundary conditions are used, along with the general solution for the pore

pressure, to obtain an expression giving the dependence of pore pressure with depth $p(z)$, in the sediment. As $L_s \ll \lambda_t$, only the downward components of the pore-pressure general solution are required. Therefore, the following simplification of equation 3.8 is obtained:

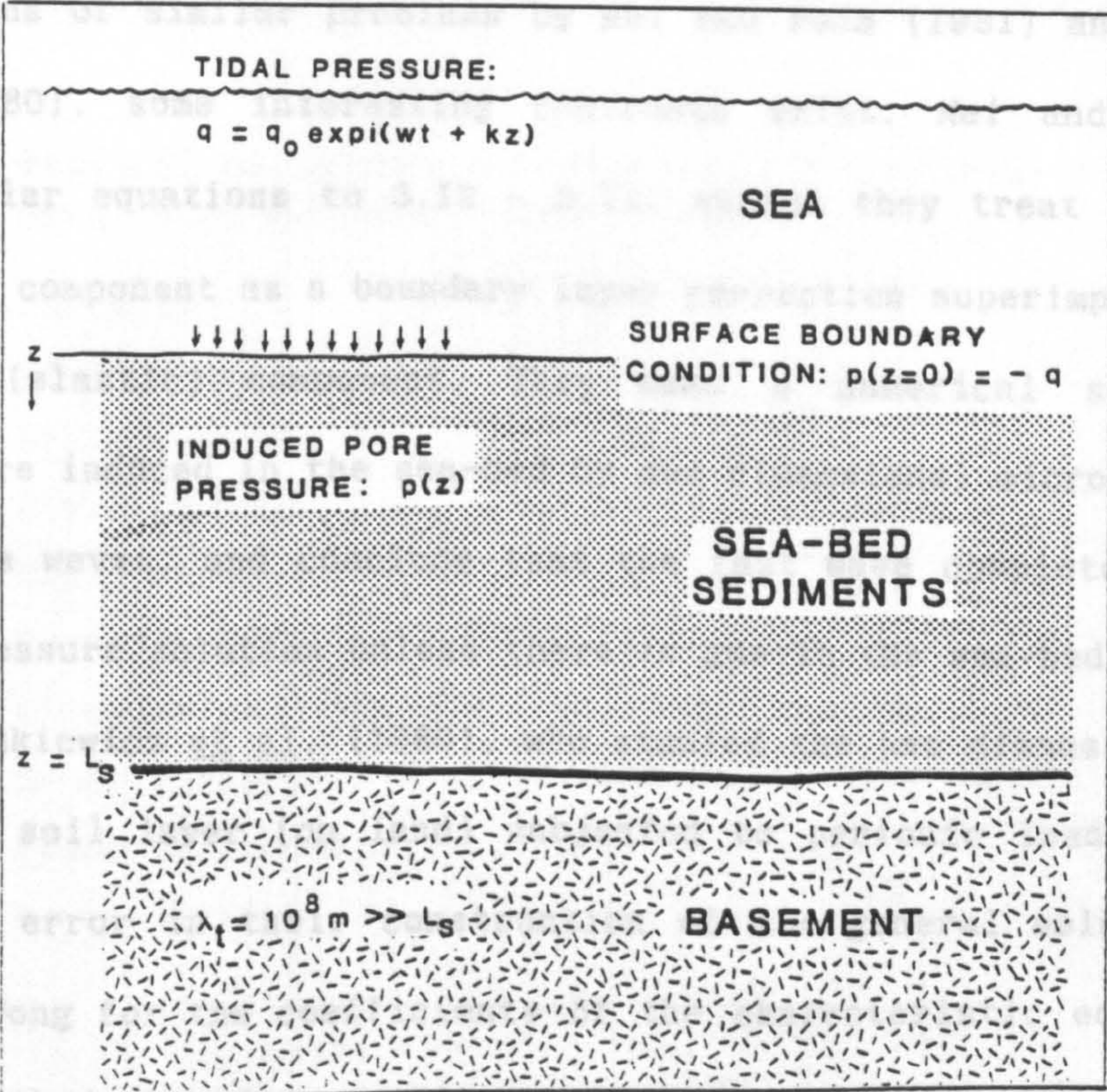
$$p(z) \cdot \exp(i\omega t) = \left[P_1 + P_2 \cdot \exp \left[-z \cdot \left[\frac{\omega \gamma}{k_a} \cdot \left[\frac{1}{Q} + \alpha^2 a_b \right] \right]^{1/2} \right] \right] \cdot \exp(i\omega t) \tag{3.12}$$

Using the boundary condition at the surface of the sea-bed, $p(z=0) = -q$:

$$P_1 = \left[\frac{a_b \alpha Q}{1 + a_b \alpha \alpha Q} \cdot (-q) \right] \tag{3.13}$$

$$P_2 = -q \cdot \left[1 - \frac{a_b \alpha Q}{1 + a_b \alpha \alpha Q} \right] \tag{3.14}$$

Figure 3.1 Boundary conditions for tidal loading of the sea-bed



The solution of the problem is given by equations 3.12 to 3.14. Physically this solution has a simple interpretation. The driving force (amplitude q) can be thought of as a very low frequency compressional wave which travels through the water column as a fast wave. On impinging on the sea-bed surface, this wave generates fast and slow pore pressure waves (amplitudes P_1 and P_2). The fast wave component has an amplitude P_1 which is only slightly smaller than q , and travels through the sediment layer without attenuation. The slow wave has a much smaller initial amplitude (P_2), which equalises the pressure between the water column and the top of the sea-bed. However, the amplitude of the slow wave attenuates rapidly with depth, with an attenuation factor which depends on the elastic constants (α , Q and a_b), the permeability (k_a) and the angular frequency of the wave (ω). The total pore-pressure developed in the sea-bed at any depth $p(z)$ is the sum of the fast and slow pore-pressure components. This pressure will be dominated by the fast wave component (P_1) at all depths.

If the results of equations 3.12, 3.13 and 3.14 are compared to the solutions of similar problems by Mei and Foda (1981) and Zienkiewicz et al. (1980), some interesting contrasts exist. Mei and Foda (1981) obtain similar equations to 3.12 - 3.14, except they treat the slow wave (diffusion) component as a boundary layer correction superimposed upon the fast wave (elastic) component. They make a numerical study of the pore-pressure induced in the sea-bed by one dimensional microseisms due to standing sea waves, and conclude that the fast wave completely dominates the pore-pressure solution unless there is gas in the sea-bed.

Zienkiewicz et al. (1980), who studied the one dimensional case of a saturated soil layer (on land) subjected to periodic loading, make an unfortunate error in their construction of the general solution getting the signs wrong for the coefficients of the characteristic equation. This invalidates their boundary problem analysis for the pore pressures induced

in the soil layer (which appear suspicious at first sight as the magnitude of the induced pore pressures are greater than the applied stress).

3.3.2 Numerical examples for the tidally-induced pore pressure

The solutions given in equations 3.12 - 3.14, along with the equations defining the elastic constants a_b , α and Q (equations 2.6 to 2.8), can be easily coded on a computer and the pore pressure profiles for various values of the parameters generated. Two numerical examples of predicted tidally-induced pore-pressure profiles are given: the first is for surficial turbidite sediments in a deep-water environment (Table 3.1): the second is for muddy surficial sediments in a shallow water environment where free gas is likely to be present in the sea-bed.

The values shown in Table 3.1 are used in equations 2.6 - 2.8 and 3.12 - 3.14 to calculate pore-pressure profiles (Figure 3.2). The predicted pore pressures are expressed as a percentage of the hydrodynamic pressure exerted on the surface of the sea-bed. It can be seen that well over 99% of the hydrodynamic pressure is transferred to the sea-bed.

Table 3.1 Physical parameters characterising a surficial turbidite deep-water sediment - data set TURB_M1

1. Porosity	0.7
2. Fluid density	1030 kg/m ³
3. Grain density	2650 kg/m ³
4. Fluid modulus	(2.25).10 ⁹ Pa
5. Grain modulus	(3.6).10 ¹⁰ Pa
6. Dynamic viscosity	10 ⁻³ Pa.s
7. Circular frequency	(1.454).10 ⁻⁴ Hz
8. Shear modulus	10 ⁷ Pa
9. Frame bulk modulus	10 ⁷ Pa
10. Permeability	10 ⁻¹⁶ to 10 ⁻¹³ m ²

1,10	Schultheiss and Gunn (1985)
2-6	Ogushwitz (1985)
7	Diurnal tidal frequency
8 and 9	Arbitrary estimates

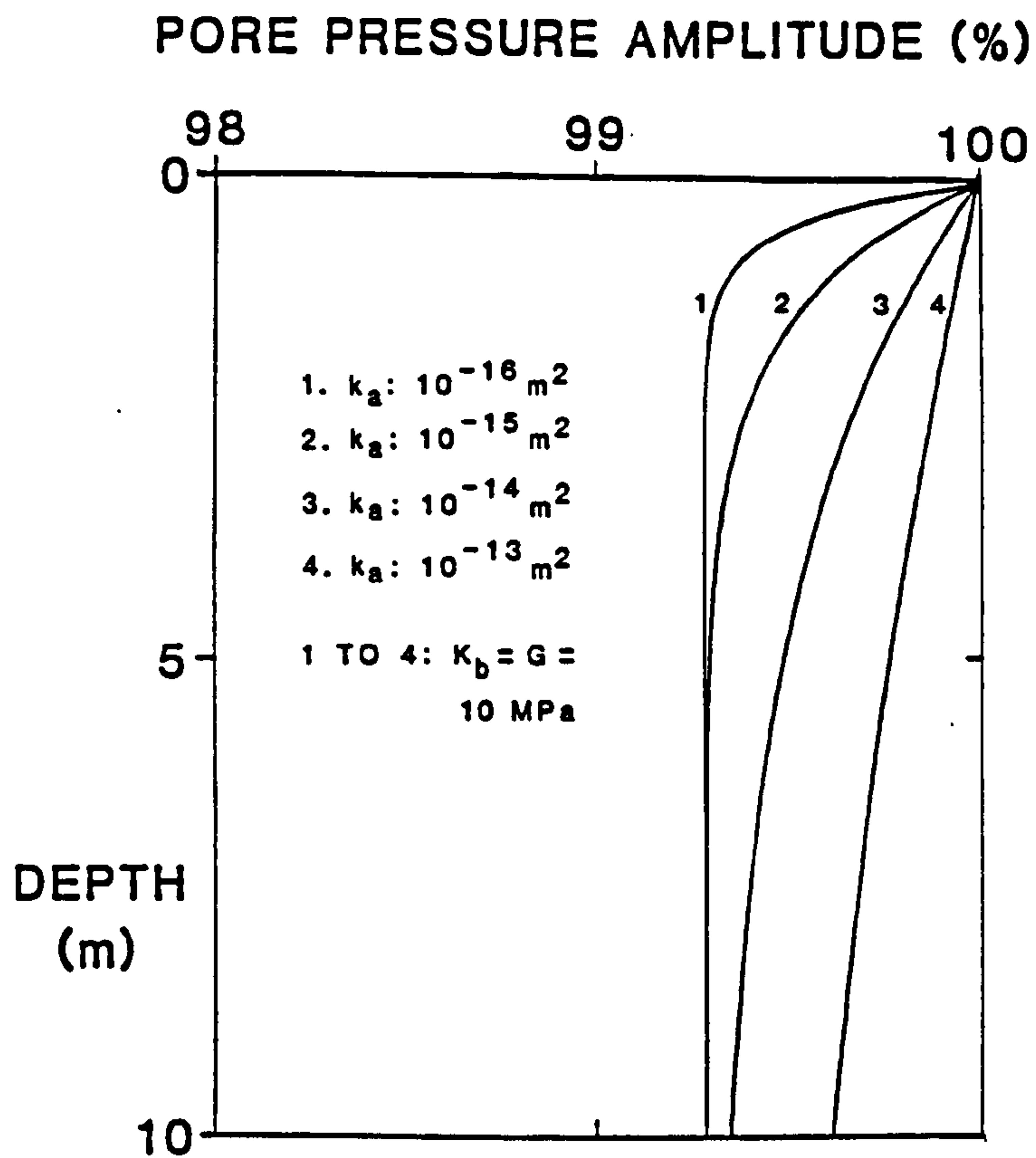


Figure 3.2 Predicted tidally-induced pore-pressure profiles for a deep-water soft turbidite sea-bed

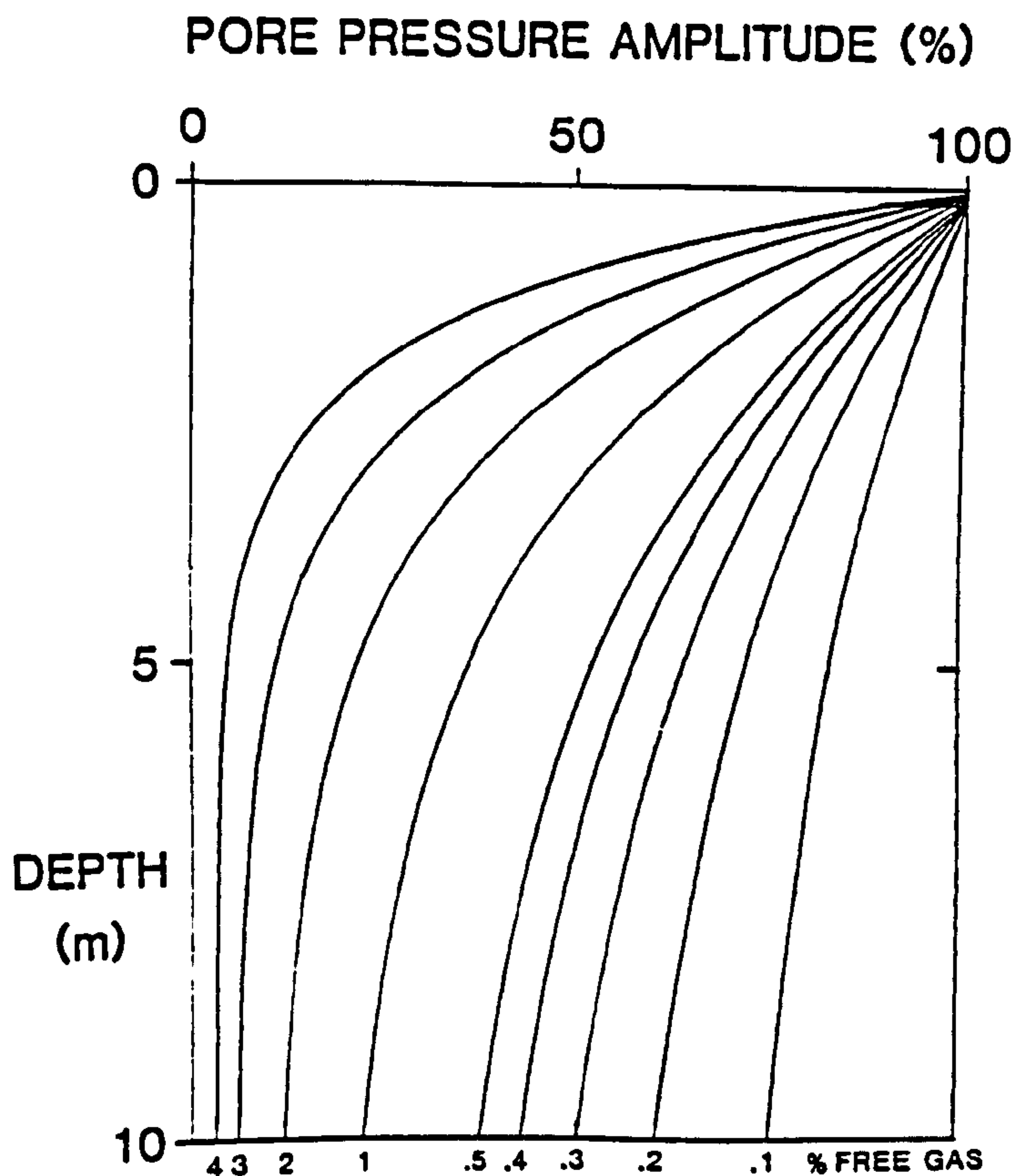


Figure 3.3 Predicted tidally-induced pore-pressure profiles for a gassy shallow water muddy sea-bed

The four different pore-pressure profiles shown in Figure 3.2, representing four different values of the permeability of the sea-bed, consist of two components: P_1 and $P_2 \cdot \exp[]$ in equation 3.12. The P_1 component primarily depends upon the "stiffness" of the sea-bed and dictates the asymptotic value to which the four curves tend to at depth. The $P_2 \cdot \exp[]$ component is the slow wave boundary correction component and only affects the upper few metres of the sea-bed. The magnitude of the slow wave pore-pressure component depends upon the magnitude of the permeability; for larger permeabilities more (slow wave) fluid diffusion occurs near the sea-bed interface - hence the pore-pressure induced near the sea-bed surface is greater than for smaller permeabilities.

The second numerical example is for a shallow water muddy sea-bed with gas present in the surficial sediments. The numerical values given in Table 3.1 are used again, except a constant permeability of $(3.0) \cdot 10^{-14} \text{ m}^2$, constant shear and frame bulk moduli of 20 MPa, and a range of fluid bulk moduli (K_f) are used. Allowing K_f to vary has the same effect upon the induced pore-pressure profile as changing G and K_b , which dictate the stiffness of the sea-bed. The new value for K_f (denoted K_f') accounting for various saturations of gas is given by equation 3.15, where $K_g = 10^5 \text{ Pa}$ = the bulk modulus of the gas, and S = the fraction of gas present in the fluid:

$$\frac{1}{K_f'} = \left[\frac{1}{K_f} + \frac{S}{K_g} \right] \quad 3.15$$

Calculating a range of values for K_f' for different S , and using K_f' instead of K_f in equation 3.12, with the other parameters as shown in Table 3.1, gives the pore pressure profiles shown in Figure 3.3. These curves show the dramatic effect that a tiny percentage of free gas has upon the pore pressure developed in the sea-bed. With increasing gas

content, less of the tidal pressure is transferred directly to the pore pressure (the P_1 component in equation 3.12 becomes less significant). The pore pressure becomes entirely due to the "slow wave" diffusive flow (also see Chandler and Johnson, 1981).

3.4 Summary

The general solutions of poroelasticity give expressions for each of the primary variables (pore-pressure, total stress, fluid and solid displacements) as functions of time, space and the material constants of the poroelastic medium. Only the general solution for the pore-pressure is of interest. For one dimensional deformations travelling in one direction, the general solution has a fast and a slow wave component. The velocity of the fast wave deformations can be considered instantaneous with respect to slow wave deformations.

At low frequencies, there is no fluid flow for the fast wave deformations. This means the poroelastic medium will act in an undrained way for the fast wave, and the fast wave pore pressure component induced in the medium will be a simple fraction of the stress applied to the porous medium. This leaves a residual pore-pressure difference between the inside and the outside of the poroelastic medium. This difference is dissipated by the slow wave, depending upon the boundary conditions at the interface. If no drainage is allowed across the boundary ("closed pore condition") then no slow wave will result. If drainage is allowed ("open pore condition"), then close to the boundary, there will be an additional slow wave component to the total pore-pressure developed in the medium.

These results are applied to the boundary value problem of tidal loading of the sea-bed. For this case, a simple expression is obtained for the variation of (tidally induced) pore-pressure with depth in the sea-bed, which is expressed as a ratio of the amplitude of the applied

tidal stress. Two simple numerical examples are considered using this equation, one for a deep-sea soft sea-bed and one for a shallow water soft sea-bed containing gas. In the first case, the permeability of the sea-bed is shown to vary the shape of the pore-pressure versus depth curve somewhat. In the second case, the presence of the gas greatly affects the shape of the pore-pressure versus depth profile. In the deep-sea environment, where no free gas is present, increasing the frame moduli of the sea-bed would similarly affect the pore-pressure versus depth profile.

The numerical examples for the hydrodynamic problem of tidally-induced pore-pressures in the sea-bed isolate the permeability and frame moduli as being important parameters. It transpires (Chapters 6 to 8) that these parameters are of equal importance to (higher frequency dynamic studies of) acoustic and ultrasonic compressional wave propagation in sea-bed sediments. In Chapters 4 and 5 various experimental and laboratory techniques for evaluating the permeability and frame bulk moduli of sediments are assessed. In Chapters 9 and 10, the hydrodynamic tidal boundary value problem is returned to; after a better characterisation of the permeability and frame moduli of deep-sea sediments have been made.

4.1 Introduction

In this thesis "permeability" will be used as an abbreviation of intrinsic permeability (k_a - with units of area). This must not be confused with the hydraulic conductivity (k_v), which has units of velocity, but elsewhere is often called the permeability. If the dynamic fluid viscosity (η), the fluid density (ρ_f) and the acceleration due to gravity (g) are known, the intrinsic permeability and hydraulic conductivity are simply related by:

$$k_a = \frac{k_v \cdot \eta}{\rho_f \cdot g} \quad 4.1$$

The intrinsic permeability of deep-sea sediments is a fundamental sediment parameter for Biot's dynamic theory of poroelasticity. The permeability is usually measured by laboratory tests on deep-sea sediment samples recovered from the sea-bed. There are a few data for the permeability of deep-sea sediments in the literature. Recent reports on new laboratory measurements are given by Schultheiss and Gunn (1985) and Silva et al. (1981). However, it is questionable whether such laboratory tests, carried out on small discrete samples, give true representations of the in-situ permeability of the sea-bed.

Two methods for obtaining the in-situ permeability - which use pore-pressure data from a piezometer buried in the sea-bed - have recently been developed. The first in-situ technique uses the decay of the pore pressure transient caused by insertion of the probe (Bennett et al., 1985). The second technique uses the dynamic pore pressure signal in the sediment which is induced by the tide, along with the boundary problem solution developed in Chapter 3.

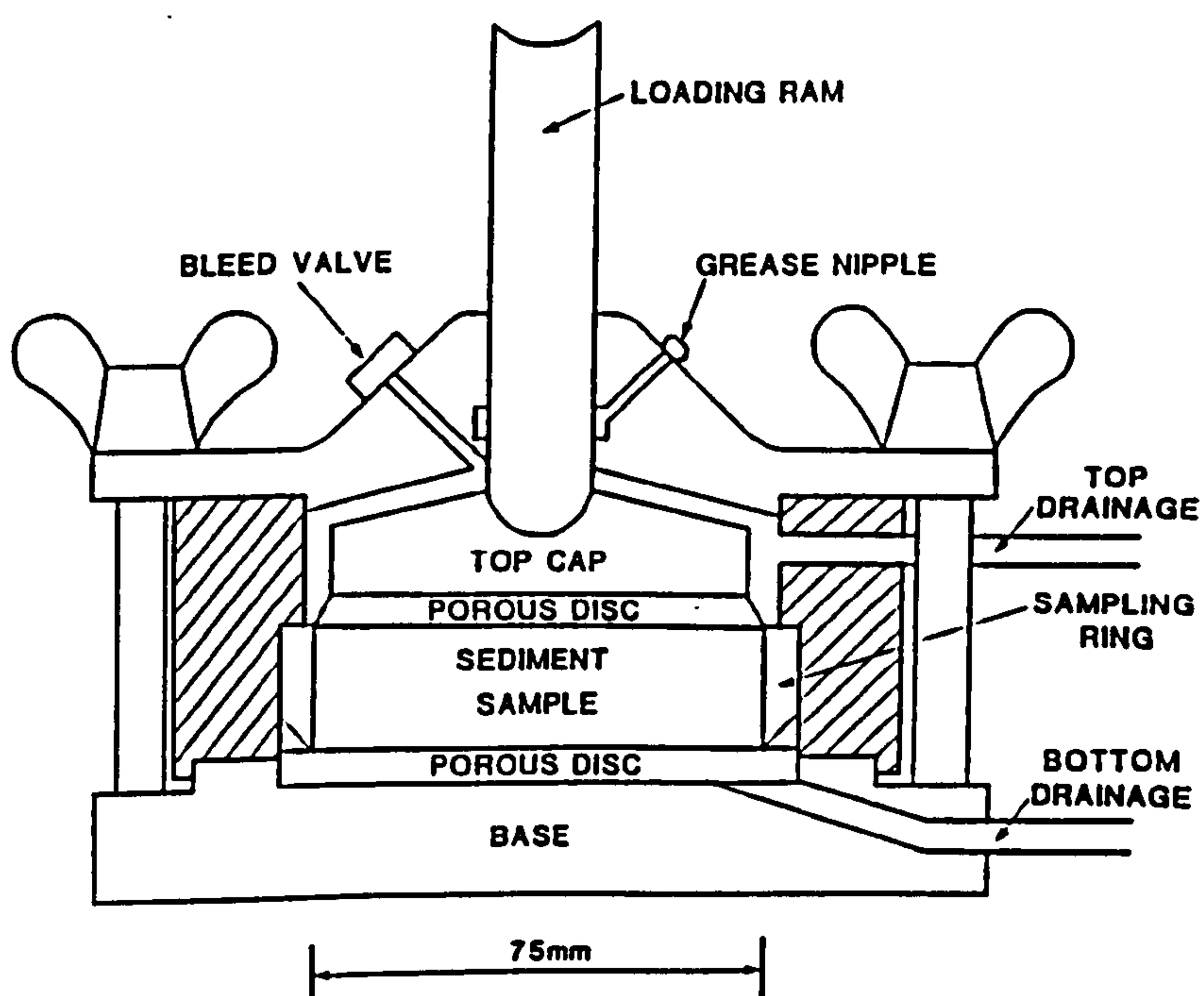
In order to compare laboratory and in-situ determinations of permeability, various unpublished raw data from Site 1 (Schultheiss, personal communication) are used. After a description of the experimental test procedures, the raw data are analysed using the appropriate theories. The disparities between permeability, evaluated from the different techniques, are then discussed.

4.2 Laboratory permeability: consolidation and direct flow tests

4.2.1 Samples, the sample cell and sample preparation

Laboratory experiments on eight samples from Site 1 (see 4.3.2, 4.4) were performed by Schultheiss and Gunn (1985) using the sample cell shown in Figure 4.1. A further six experiments were carried out on samples using a modified version of this cell (5.3.1) on samples from Site 2 (see 11.2.3). Both cells had a back pressure facility to ensure full saturation.

Figure 4.1 Schematic diagram of the back-pressured consolidation cell



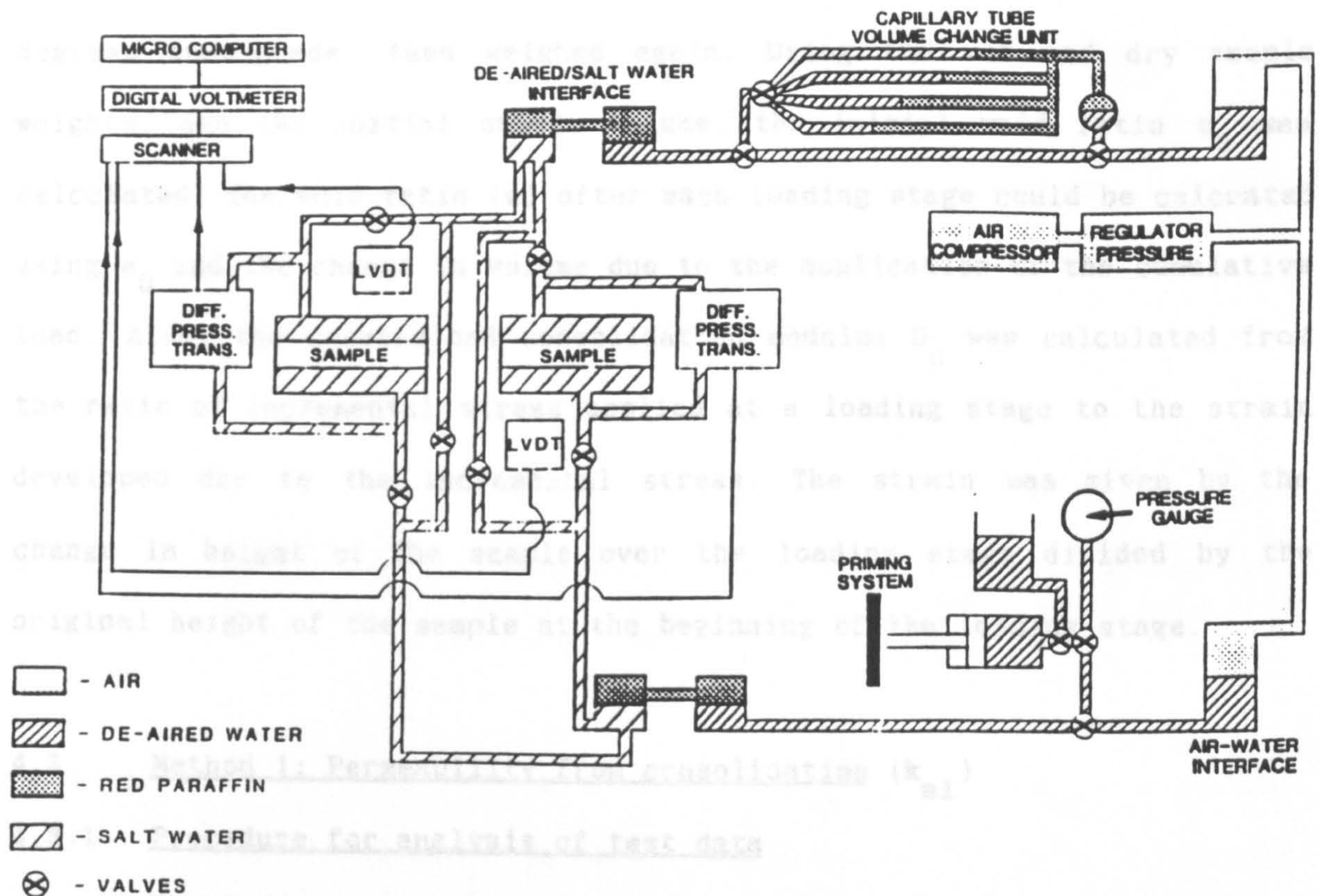
The samples from Site 1 were taken from whole-round 65 mm diameter gravity core-sections. For each sample, 6 cm lengths of core were cut and the sediment extruded from the liner. Sample rings of 50 mm diameter and 20 mm in length were gently pushed into the extruded sediment. Excess sediment was trimmed off with an electro-osmotic knife. The trimmed samples were stored in their rings under water at 4 degrees centigrade, until they were weighed then loaded into the cell. A similar sample preparation procedure was used for the samples from Site 2, which were obtained using advanced hydraulic piston coring techniques (Mayer, 1982), from the drilling ship JOIDES RESOLUTION (ODP Leg 115).

4.2.2 The consolidation and permeability system

To perform consolidation and direct-flow permeability tests the sample cell, containing a sample, was set-up in the system shown in Figure 4.2. Samples were placed under a back pressure of 30 kPa using the air compressor. This ensured full saturation as any free gas would be forced into solution at this pressure. The hydraulic conductivity (converted to intrinsic permeability using equation 4.1) of the sediment in the cell could be determined by applying a hydraulic gradient across the sample and measuring the rate of flow of water through the sample under this known gradient. The hydraulic gradient was applied by varying the heights of the air-water interfaces, and the rate of flow was measured by timing the discharge through a capillary tube of known volume.

Using a cantilevered loading arrangement, axial stresses were applied in increments to the samples. On the application of each stress increment the sample consolidates, resulting in a reduction in the height of the sample and the build-up and dissipation of a differential pore pressure across the sample. Variations in displacement and pore pressure were monitored automatically using transducers connected to a scanner and a micro-computer (Figure 4.2).

Figure 4.2 Laboratory consolidation/permeability system



4.2.3 Consolidation and permeability test procedure

After each sediment sample had been weighed and loaded into the consolidation system, it was left for a day to equilibrate and settle under a small load, before testing began. The test procedure consisted of a number of consolidation stages, at successively greater stress increments, with a direct-flow permeability test at the end of each consolidation stage. Each consolidation stage was started by the application of an incremental stress, and the settlement and pore-pressures were monitored until primary consolidation was completed. This was indicated by a zero differential pore pressure across the sample and a levelling out of the displacement.

The loading increments usually followed the pattern 12.5, 25, 50, 100, 200, 400, 800, 1600, 3000, 25 kPa. After all loading stages had been completed the sample was weighed, dried in an oven for 24 hours at 105 degrees centigrade, then weighed again. Using the wet and dry sample weights, and the initial sample volume, the initial void ratio e_0 was calculated. The void ratio (e) after each loading stage could be calculated using e_0 and the change in volume due to the application of the cumulative load. Also, the constrained consolidation modulus D_c was calculated from the ratio of incremental stress applied at a loading stage to the strain developed due to the incremental stress. The strain was given by the change in height of the sample over the loading stage divided by the original height of the sample at the beginning of the loading stage.

4.3 Method 1: Permeability from consolidation (k_{a1})

4.3.1 Procedure for analysis of test data

The hydraulic conductivity can be calculated in a straightforward way from consolidation data. Standard Casagrande interpretation of settlement data from each loading stage of the consolidation test (e.g. Vickers, 1978) gives the time taken for 50% consolidation, which is known as t_{50} . Using t_{50} and the height of the sample h , the vertical coefficient of consolidation C_v can be calculated using the Terzaghi relationship (equation 4.2). Then, the hydraulic conductivity can be calculated by using C_v , the unit weight of water (γ_w) and the constrained consolidation modulus D_c :

$$C_v = 0.197 \frac{h^2}{t_{50}} \quad 4.2$$

$$k_v = \frac{C_v \cdot \gamma_w}{D_c} \quad 4.3$$

4.3.2 Permeability analysis for samples from Site 1

Consolidation and direct-flow permeability tests were carried out on eight samples from Site 1 by Schultheiss and Gunn (1985). Test results for void ratio and direct-flow permeability are presented in their report. Using the raw data from these tests (Schultheiss, personal communication), permeabilities were evaluated from the consolidation method (4.3.1). A summary of the results for the permeabilities obtained from the consolidation data are presented in Table 4.1.

Table 4.1 Summary of data from laboratory permeability / consolidation tests on samples from Site 1, (based on analysis of data from Schultheiss and Gunn, 1985)

Sample no.	e_0	D_c (kPa)	C_v (m^2/s)	k_{a1} (m^2)	k_{a2} (m^2)	Porosity rebound (%/MPa)
D10695/6/28	3.86	440	$(3.6) \cdot 10^{-6}$	$(8.6) \cdot 10^{-16}$	$(8.0) \cdot 10^{-15}$	1.03
D10695/2/14	3.65	400	$(1.2) \cdot 10^{-7}$	$(3.1) \cdot 10^{-15}$	$(2.8) \cdot 10^{-15}$	2.51
D10695/3/28	3.00	400	$(1.7) \cdot 10^{-6}$	$(4.5) \cdot 10^{-14}$	$(6.0) \cdot 10^{-16}$	1.23
D10325/7	2.54	300	$(2.3) \cdot 10^{-6}$	$(8.1) \cdot 10^{-16}$	$(9.0) \cdot 10^{-16}$	4.85
S126/4-5	5.20	100	$(7.0) \cdot 10^{-6}$	$(7.4) \cdot 10^{-15}$	$(1.5) \cdot 10^{-14}$	1.71
S126/4-4	4.76	200	$(1.2) \cdot 10^{-6}$	$(6.5) \cdot 10^{-16}$	$(1.5) \cdot 10^{-14}$	1.85
S126/4-10	3.72	800	$(6.0) \cdot 10^{-6}$	$(7.8) \cdot 10^{-16}$	$(3.5) \cdot 10^{-15}$	0.90
S126/2-3	2.43	340	$(6.8) \cdot 10^{-6}$	$(2.1) \cdot 10^{-15}$	$(1.7) \cdot 10^{-15}$	2.48

Averages

$$\bar{D}_c = 370 \text{ kPa}$$

$$\bar{k}_{a1} = (2.24) \cdot 10^{-15} \text{ m}^2$$

$$\bar{k}_{a2} = (4.5) \cdot 10^{-15} \text{ m}^2$$

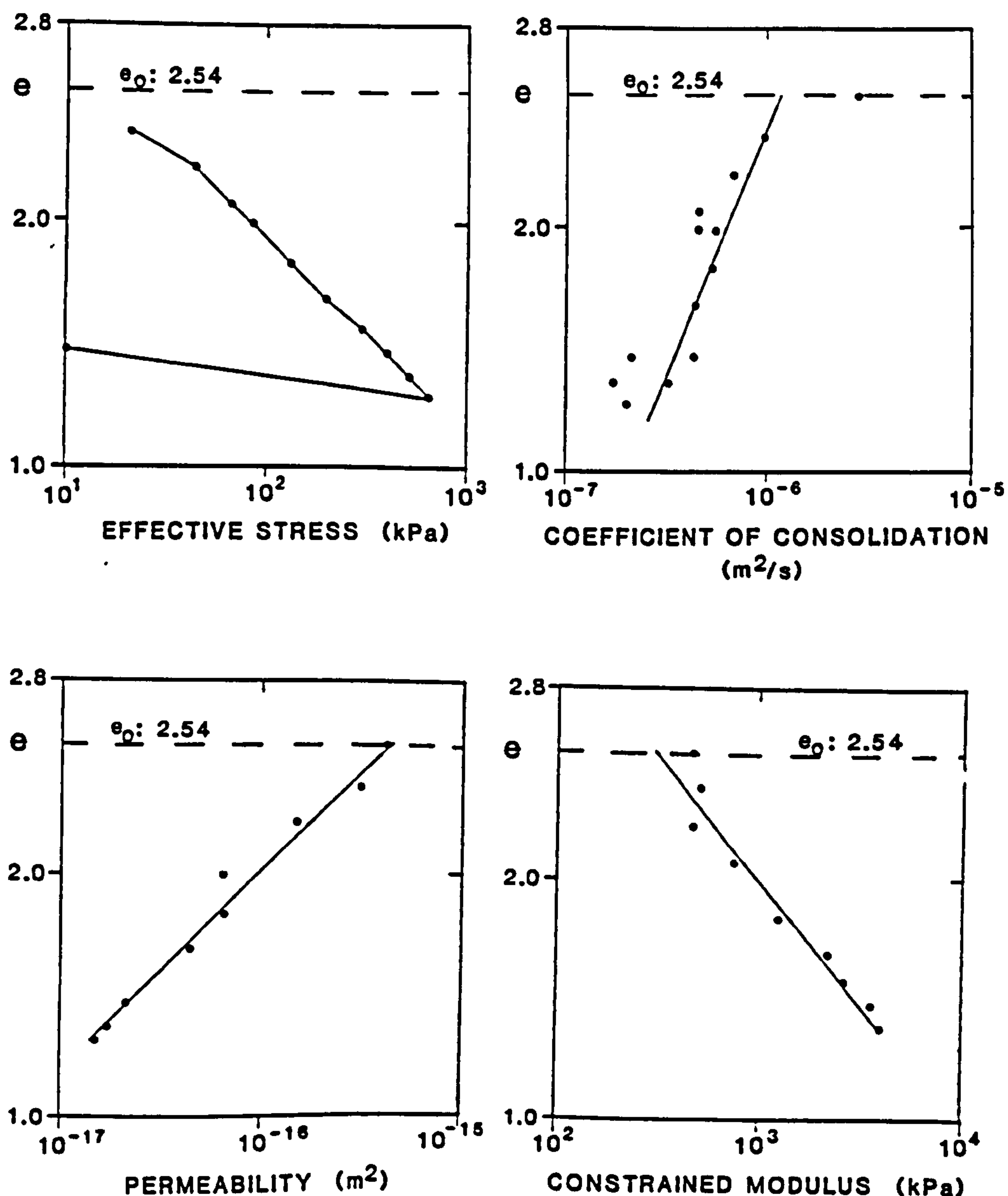
Ranges

$$(6) \cdot 10^{-16} \text{ to } (8) \cdot 10^{-15} \text{ m}^2$$

$$(6) \cdot 10^{-16} \text{ to } (1.5) \cdot 10^{-14} \text{ m}^2$$

For each sample, the permeability at the initial void ratio was calculated from C_v and D_c values extrapolated from a best line fit through the data from all the stages of the consolidation test. An example of the C_v and D_c values for sample D10325/7 obtained from this method is shown in Figure 4.3. This method was adopted as it best used the data from all of the stages of the consolidation test, and also because the C_v and D_c values obtained over the first few loading increments were typically erratic.

Figure 4.3 Consolidation data for sample D10325/7



4.4 Analysis and results for method 2: Permeability from direct-flow tests (k_{a2})

The hydraulic conductivity (converts to intrinsic permeability using Equation 4.1) can be simply determined from the direct-flow raw data using Darcy's law (equation 2.4). Direct-flow permeability results from Schultheiss and Gunn (1985) are shown in Table 4.1.

4.5 In-situ permeability: piezometer experiments

4.5.1 In-situ pore pressure instrument PUPPI

The in-situ permeability of the sea-bed can be determined by analysing measurements from piezometers such as PUPPI (Pop Up Pore Pressure Instrument). PUPPI is a simple device which measures the differential pore-pressure between the surface of the sea-bed, and a point up to 6 metres below the surface. PUPPI consists of a probe (which penetrates the sea-bed) with a pore-pressure port at its tip, another port open to the sea, a pore-pressure transducer between the ports and a logging / buoyancy assembly (Figure 4.4). The instrument free-falls to the sea-bed, the probe penetrates, and complete burial is prevented by a retarding cone. The logger records the output of the differential pore-pressure transducer at a pre-determined count-rate. When the transient pore-pressures induced by the insertion of the probe have equilibrated, the pipe joining the tip-port to the sea is opened. This acts as a calibration as it exposes both sides of the differential pressure transducer to the same pressure, and any differential pressures existing across the transducer before opening the pipe will cause an equal and opposite signal to be registered. The measurements are then complete and the logging/buoyancy assembly is returned to the sea-surface after it has been separated from the probe by a remote controlled release. Full details are given in McPhail and Schultheiss (1986).

Figure 4.4 Schematic diagram of the piezometer PUPPI

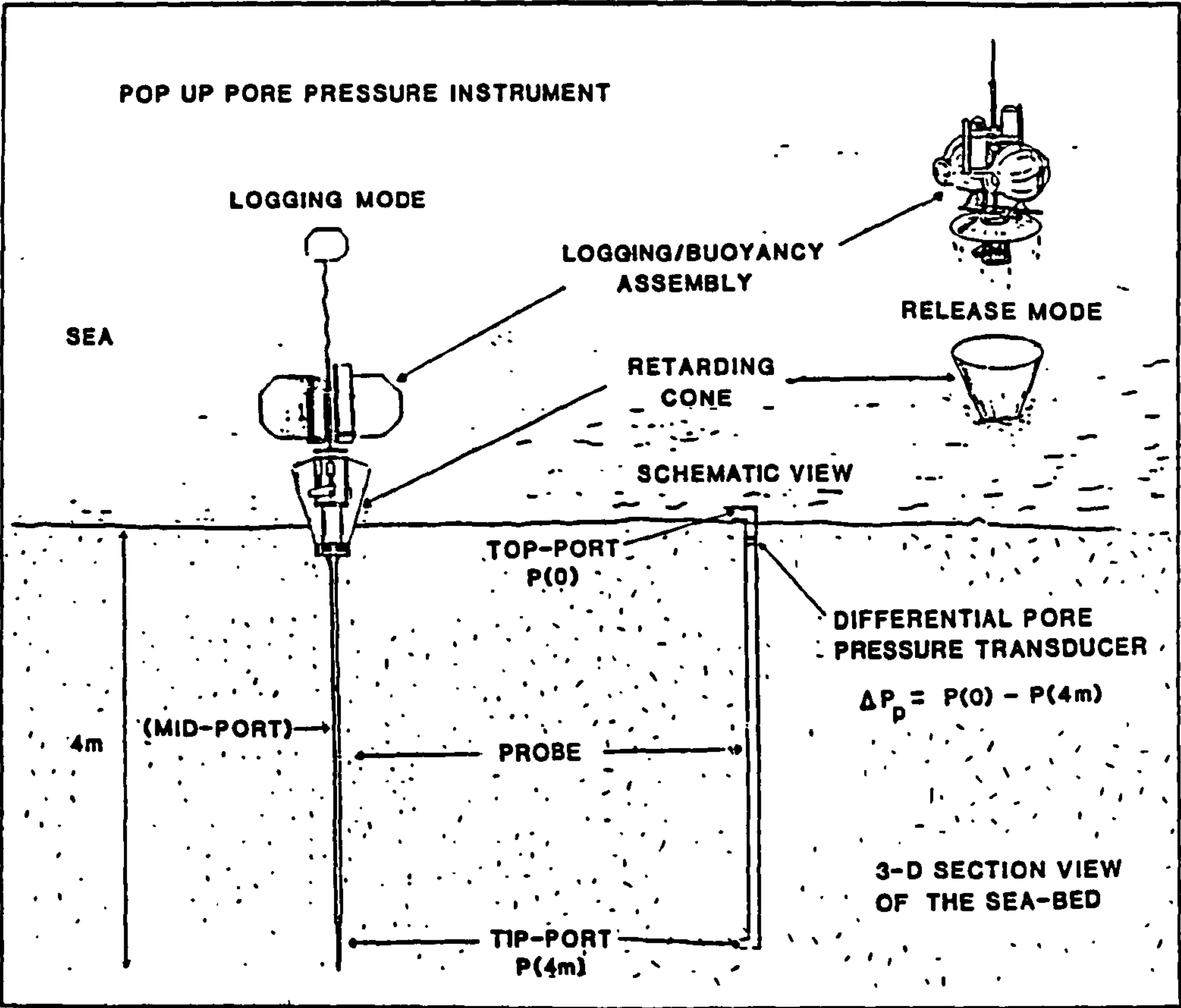
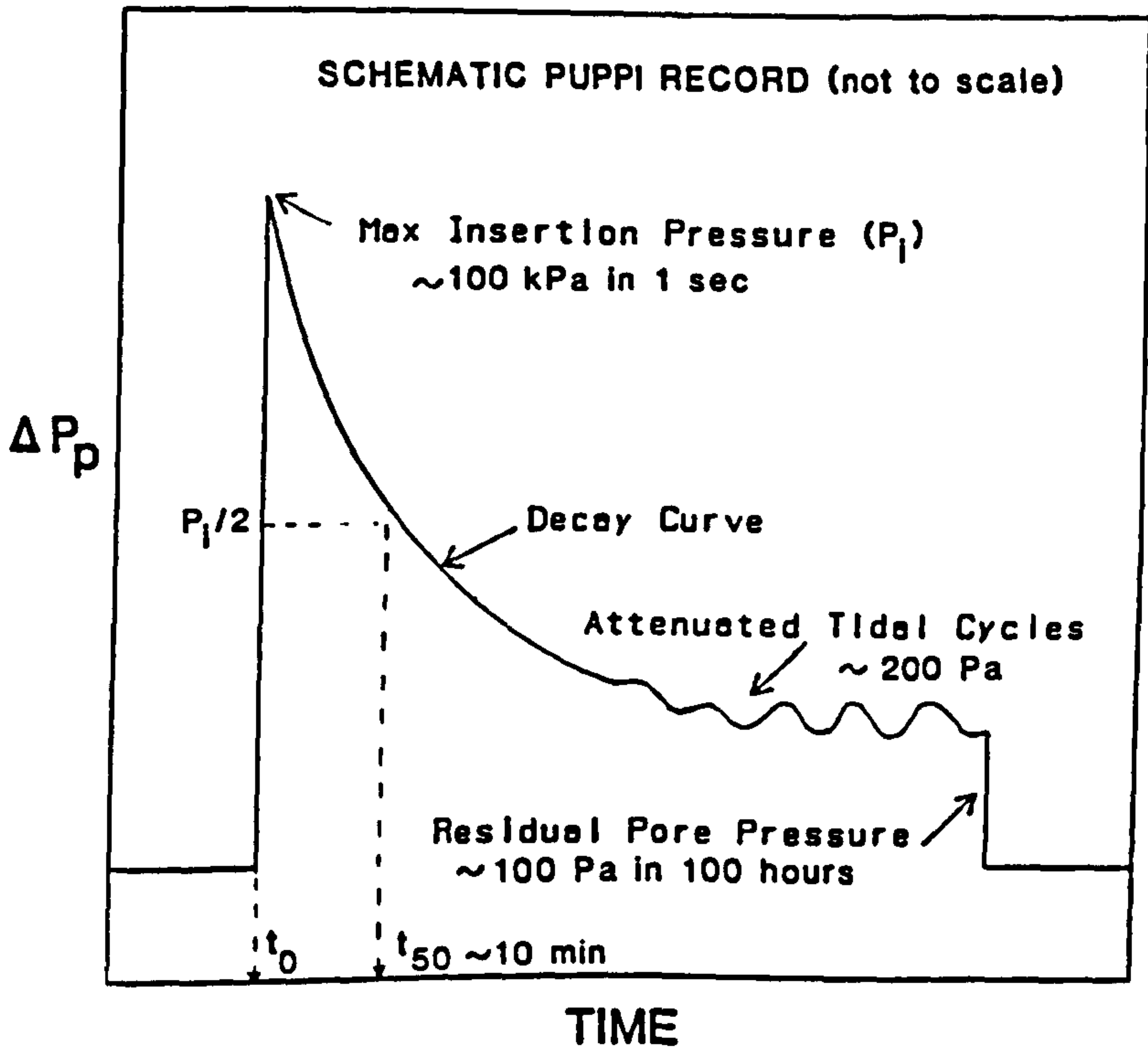


Figure 4.5 Schematic in-situ PUPPI differential pore-pressure record



4.5.2. Description of in-situ pore pressure data

PUPPI has been deployed more than 20 times at Site 1 in the N. Atlantic Ocean, giving a comprehensive data set for the variation of pore-pressures over time scales of seconds to months at this site (Schultheiss and McPhail, 1985). The instrument, which was designed to measure differential pore pressures in the sea-bed, proved to be sensitive enough to detect cyclic tidal pore pressures after the transient insertion pressure had decayed. A typical set of data from one deployment is shown in Figure 4.5. Analysis of these data (4.6, 4.7) gives the in-situ permeability, as well as other sea-bed sediment parameters.

4.6 Method 3: permeability from pore-pressure decay (k_{a3})

4.6.1 Procedure for analysis of PUPPI data

Bennett et al. (1985) have shown it is possible to calculate the in-situ permeability of the sea-bed by analysing piezometer insertion pressure decay transients using radial consolidation theory (Soderberg, 1962). A similar principle is used as for calculating the permeability from uni-axial consolidation tests (4.3.1). The rapid insertion of the probe into the sea-bed causes a radial stress to be applied to the sediment around the probe. This stress is translated to the pore-fluid and an insertion pressure p_i is measured by the piezometer. This pore-pressure decays exponentially as the sediment undergoes radial consolidation, and the time for 50% consolidation (t_{50}) is given at $p_i/2$ (Figure 4.5). Using t_{50} and the radius of the probe (r_o), the horizontal and vertical coefficients of consolidation (C_h , C_v) are given by the approximate equation 4.4. Using the value of C_v obtained in this way along with the (high strain) constrained modulus obtained from laboratory consolidation tests (D_c , see 4.3), the permeability can be calculated from equation 4.3.

$$C_h \approx C_v \approx r_o^2 / t_{50}$$

4.4

4.6.2 Permeability analysis for Site 1

PUPPI piezometer data for fourteen deployments at Site 1 (Schultheiss, personal communication) were analysed using the procedure outlined in 4.6.1. The results for t_{50} , C_h and k_{a3} are presented in Table 4.2. In calculating k_{a3} an average value of $D_c = 340$ kPa was used (from the results shown in Table 4.1).

Table 4.2 Summary of data from PUPPI deployments at Site 1 (analysis of data from Schultheiss, personal communication)

Station number	Probe depth (m)	Probe radius (m)	t_{50} (s)	C_h (m^2/s)	k_{a3} (m^2)	p_p/p_t %
CD6/1	4.0	0.01	180	$(5.6) \cdot 10^{-7}$	$(1.73) \cdot 10^{-16}$	1.0
CD6/2	4.25	0.01	202	$(5.0) \cdot 10^{-7}$	$(1.54) \cdot 10^{-16}$	0.8
CD6/3	4.0	0.01	--	--	--	1.0
CD9B/8	2.5?	0.01	1665?	$(6.0) \cdot 10^{-8}$	$(1.86) \cdot 10^{-17}$	0.4
CD9B/11	2.0	0.025	675	$(9.5) \cdot 10^{-7}$	$(2.49) \cdot 10^{-16}$	0.3
	4.0	0.01	158	$(6.3) \cdot 10^{-7}$	$(1.95) \cdot 10^{-16}$	1.2
CD9B/28	2.0	0.025	180	$(3.6) \cdot 10^{-6}$	$(1.11) \cdot 10^{-15}$	0.3
	4.0	0.01	1260	$(7.9) \cdot 10^{-8}$	$(2.54) \cdot 10^{-17}$	0.8
D11317	6.1	0.01	720	$(1.4) \cdot 10^{-7}$	$(4.33) \cdot 10^{-16}$	0.4
D11320	4.3	0.01	45?	$(2.2) \cdot 10^{-6}$	$(6.81) \cdot 10^{-16}$?
D11329	4.0	0.01	202	$(5.0) \cdot 10^{-7}$	$(1.54) \cdot 10^{-16}$	0.3
D11381	2.25	0.025	--	--	--	1.0
	4.25	0.01	180	$(5.6) \cdot 10^{-7}$	$(1.73) \cdot 10^{-16}$	0.9
D11382	4.0	0.025	1260	$(5.1) \cdot 10^{-7}$	$(1.57) \cdot 10^{-16}$	0.2?
	6.0	0.01	1485	$(6.7) \cdot 10^{-8}$	$(2.08) \cdot 10^{-16}$?
D11388	2.33	0.025	945	$(6.8) \cdot 10^{-7}$	$(2.10) \cdot 10^{-16}$	0.3
	4.33	0.01	1710	$(5.8) \cdot 10^{-8}$	$(1.79) \cdot 10^{-17}$	0.3?
D11391	2.0	0.025	1417	$(4.6) \cdot 10^{-7}$	$(1.42) \cdot 10^{-16}$	0?
	4.0	0.01	200	$(5.00) \cdot 10^{-7}$	$(1.54) \cdot 10^{-16}$	0.2
Average				Range		
$\bar{k}_{a3} = (2.28) \cdot 10^{-16}$				$(1.79) \cdot 10^{-17}$ to $(1.11) \cdot 10^{-15} \text{ m}^2$		
p_p/p_t @4m = 0.7 %				0.3 to 1.2 %		
p_p/p_t @2m = 0.3 %				0.4 to 0.0 %		

4.7 Method 4: permeability from tidal cycles (k_a)

4.7.1 Procedure for analysis of PUPPI data

The solution for the boundary value problem of tidal loading of the sea-bed developed in Chapter 3 can be used to analyse the dynamic tidal pore-pressure signals recorded by PUPPI. The solution can be used to predict the pore-pressure induced in the sea-bed due to the tidal forcing function. By assuming various physical constants for the sea-bed at Site 1 (Table 4.3), the shear modulus (G) and the intrinsic permeability of the sea-bed can be found by a process of adjustment such that the best fit is obtained between the experimental and predicted pore-pressures.

Table 4.3 Physical parameters characterising Site 1 used to calculate (tidal) permeability and shear modulus - data set TURB_M2

1. Porosity	0.8
2. Fluid density	1024 kg/m ³
3. Grain density	2670 kg/m ³
4. Fluid modulus	(2.4).10 ⁹ Pa
5. Grain modulus	(3.6).10 ¹⁰ Pa
6. Dynamic viscosity	10 ⁻³ Pa.s
7. Circular frequency	(1.454).10 ⁻⁴ Hz
8. Shear modulus	(10) to (50).10 ⁶ Pa
9. Frame bulk modulus	2.17 G
10. Permeability	10 ⁻¹⁵ to 10 ⁻¹² m ²

Best fit G = 17 MPa

Best fit $k_a = (2).10^{-13}$ m²

1-6 Schultheiss (personal communication)

7 Diurnal tidal frequency

8,9,10 Possible range of values from inverse theory

4.7.2 Permeability analysis for Site 1

The PUPPI tidal differential pressure results shown in Table 4.2 are expressed as a percentage of the absolute tidal pressure ($100p_p/p_t$) which was recorded by a tide-gauge. Typical PUPPI and tide-gauge records are shown in Figure 4.6.

Figure 4.6 Tide gauge and tidally-induced in-situ pore-pressure PUPPI records at Site 1

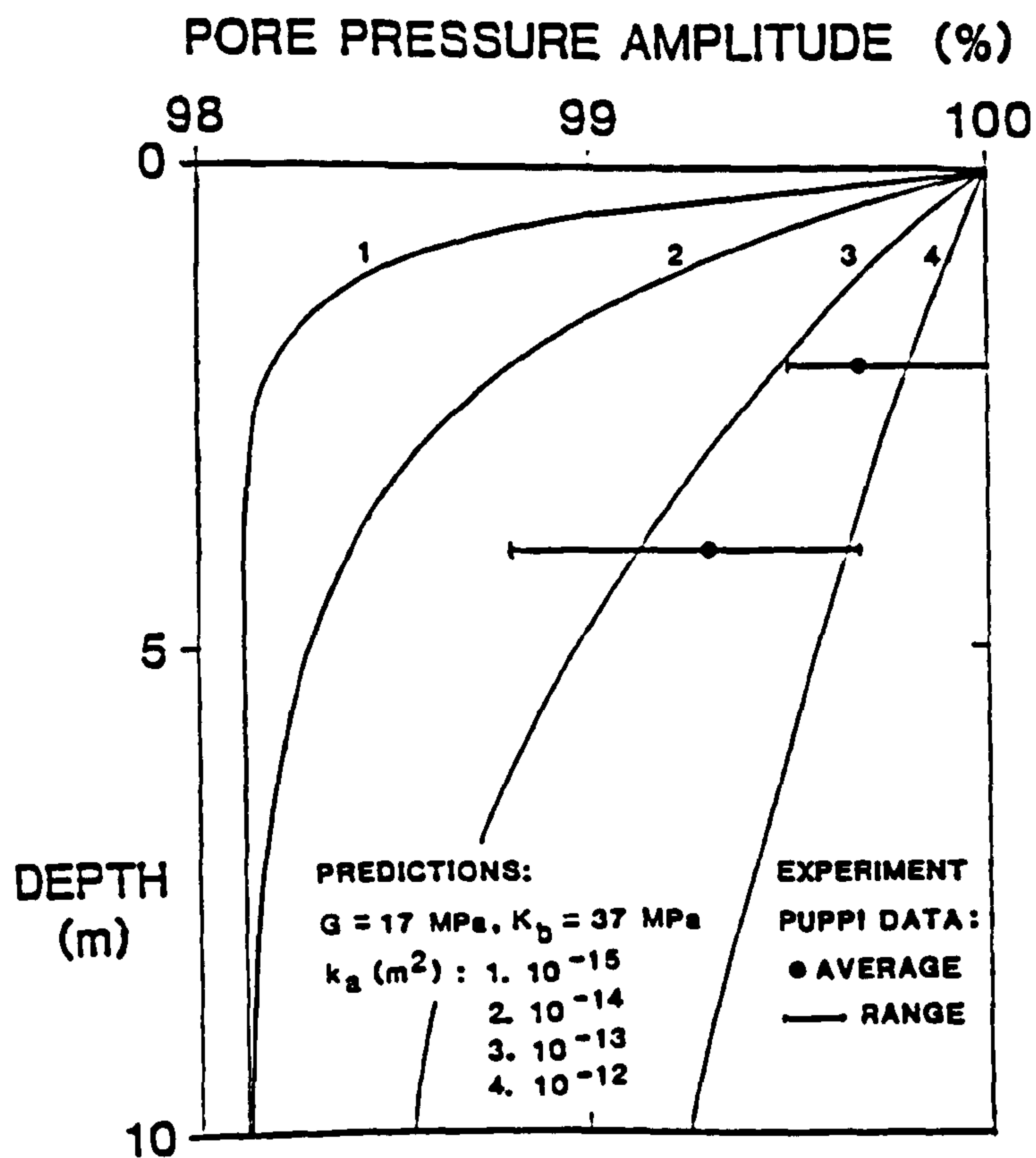
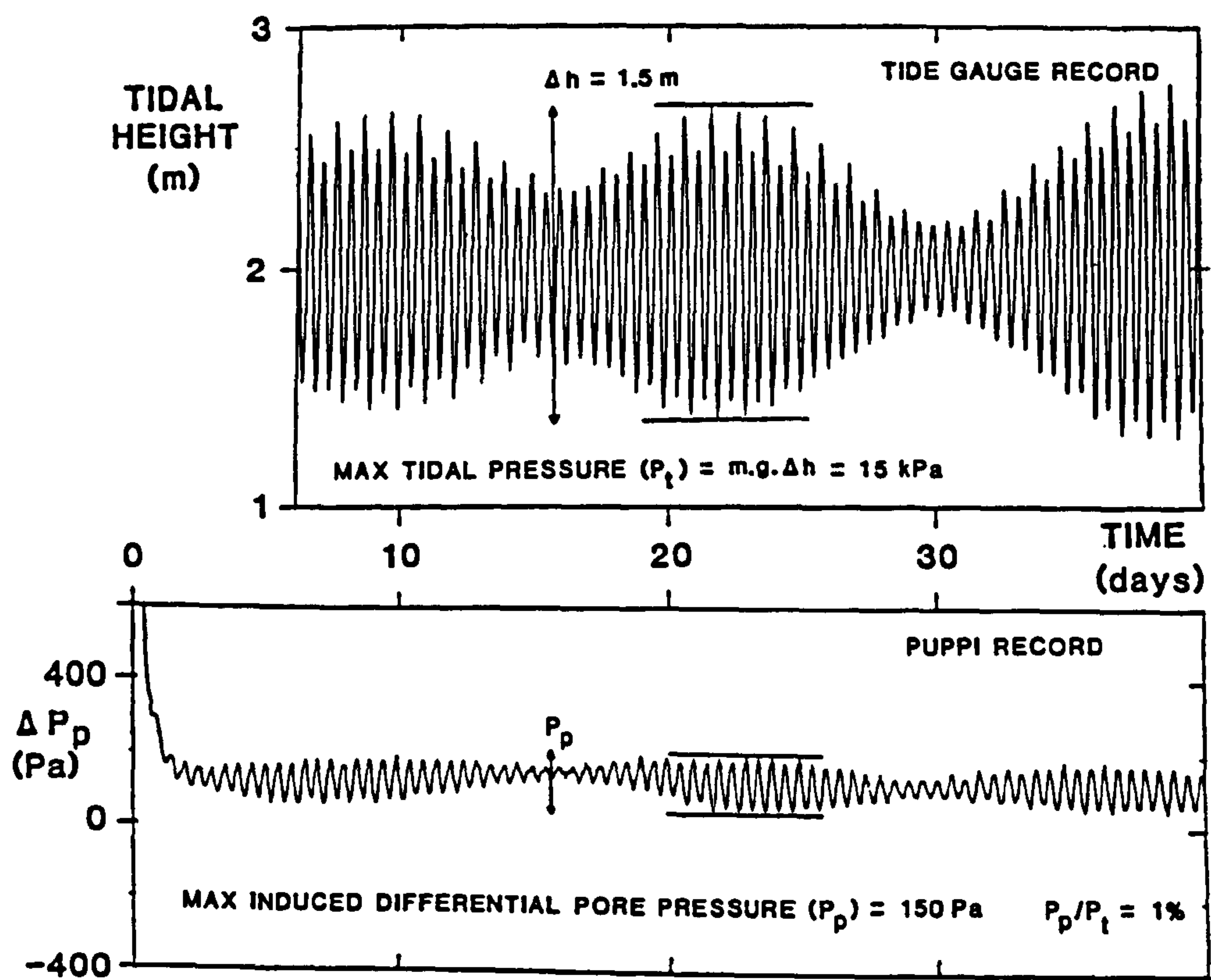


Figure 4.7 Predicted and measured tidally-induced pore-pressures at Site 1

As the PUPPI measurements shown in Figure 4.6 were obtained close to the bit resolution of the differential pressure transducer there is a fair spread in the results shown in Table 4.2. Therefore, it is this range of values which is used for comparison with the predicted percentage differential tidal pressure at any one depth. A further consideration is that there are two free variables in the prediction (k_a and G) so data from two ports at different depths must be used in the comparison. (Note that the predicted solution has phase information also and if the temporal resolution of the PUPPI system were improved this result could act as an independent check on the pore-pressure amplitude analysis). The comparison between experimental and predicted percentage differential pore-pressure results are shown in Figure 4.7. The best-fit values for k_a and G are $(2) \cdot 10^{-13} \text{ m}^2$ and 17 MPa respectively.

4.8 Method 5: Permeability from grain size (k_{a5})

4.8.1 The Kozeny-Carman equation

The model of a sediment as a bundle of capillary tubes of tortuosity T and radius a , as described in Chapter 2, was used by Kozeny in deriving a permeability (equation 4.5) using a hydraulic radius theory (as described in Bear, 1972). This hypothetical capillary tube radius (a) is taken to represent some kind of "average pore radius" of a sediment. Often a is unknown, but it may be approximated (equation 4.6) if an average grain-diameter (d_m) and the porosity (ϕ) are known:

$$k_a = \frac{\phi \cdot a^2}{8 \cdot T} \quad 4.5$$

$$a = \frac{d_m \cdot \phi}{3(1-\phi)} \quad 4.6$$

In Kozeny's permeability equation (4.5) a pore-shape factor of 0.5 is used. Through various experimental measurements Carman proposed that a pore-shape factor of 0.2 was better than Kozeny's value of 0.5: therefore multiplying equation 4.5 by 0.4 gives the Kozeny-Carman equation (Bear, 1972). Note, that this relationship should hold for sands and fine silts, but it may not hold for clays.

4.8.2 Permeability results for Site 1

A detailed grain-size study for the sediments at Site 1 was undertaken by Weaver and Rothwell (1987). Average values of the grain diameter (d_m) for the turbidites and the silty bases of the turbidites are given in Table 4.4, along with the calculated permeabilities using the Kozeny-Carman relationship using a porosity of 0.7 and a tortuosity of 1.5.

Table 4.4 Permeabilities of sediments from Site 1 calculated using the Kozeny-Carman equation

Sediment type	Average grain diameter (m)	Average pore ^{*1} radius (m)	Permeability ^{*2} (m ²)
Turbidite	$(1.9) \cdot 10^{-6}$	$(1.5) \cdot 10^{-6}$	$(8.4) \cdot 10^{-14}$
Fine silty turbidite	$(3.9) \cdot 10^{-6}$	$(3.0) \cdot 10^{-6}$	$(2.2) \cdot 10^{-13}$
Silty turbidite	$(3.1) \cdot 10^{-5}$	$(2.4) \cdot 10^{-5}$	$(1.4) \cdot 10^{-11}$

*1 calculated using equation 4.6

*2 calculated using equation 4.5 multiplied by 0.4, (both *1 and *2 use $\phi = 0.7$, $T = 1.5$, and d_m data from Weaver and Rothwell, 1987)

4.9 Method 6: Permeability from dispersion (k_{a6})

4.9.1 Use of Biot's (1956 a,b) theory to predict permeability

The permeability is a key parameter in determining the frequency range over which fast compressional wave dispersion occurs (Chapter 7). If experimental velocity measurements are less than the infinite frequency velocity, predicted by Biot's theory (see Chapter 2), then this discrepancy may be due to an incorrect value of the permeability used in the prediction. If it is assumed that this discrepancy is entirely due to a wayward permeability, the permeability input into the theory can be allowed to vary and it can be tuned to give the best agreement between the predicted and experimental velocities. Such an approach was adopted by Hamdi and Taylor-Smith (1982) and Taylor-Smith (1986).

4.9.2 Permeability results for Site 1

The results for permeability, obtained by forcing theoretical compressional wave velocities to agree with experimental data (as near as possible) for 47 samples from Site 1 using the method outlined in 4.9.1, are shown in Figure 4.8. The experimental measurements for V_p , ρ , and G for these samples, are shown in Table 10.1. These values were used along with the parameters shown in Table 10.2 to calculate the permeability from inverse Biot dispersion analysis (using Biot's 1956 a,b theory).

Looking at Figure 4.8, the turbidite samples with experimental velocities close to the compressional velocity in water (1530 m/s) show little dispersion, and the theoretical and experimental velocities can be made to coincide by using permeabilities of between $(3) \cdot 10^{-14}$ and $(3) \cdot 10^{-13} \text{ m}^2$. The silty bases of the turbidites at Site 1 show greater dispersion (Chapter 10) and these sediments require greater permeabilities of between $(1) \cdot 10^{-12}$ to $(2) \cdot 10^{-12} \text{ m}^2$ to make experimental and theoretical velocities to agree.

Figure 4.8 Predicted permeabilities from inverse dispersion analysis for turbidites and pelagic sediments from Site 1

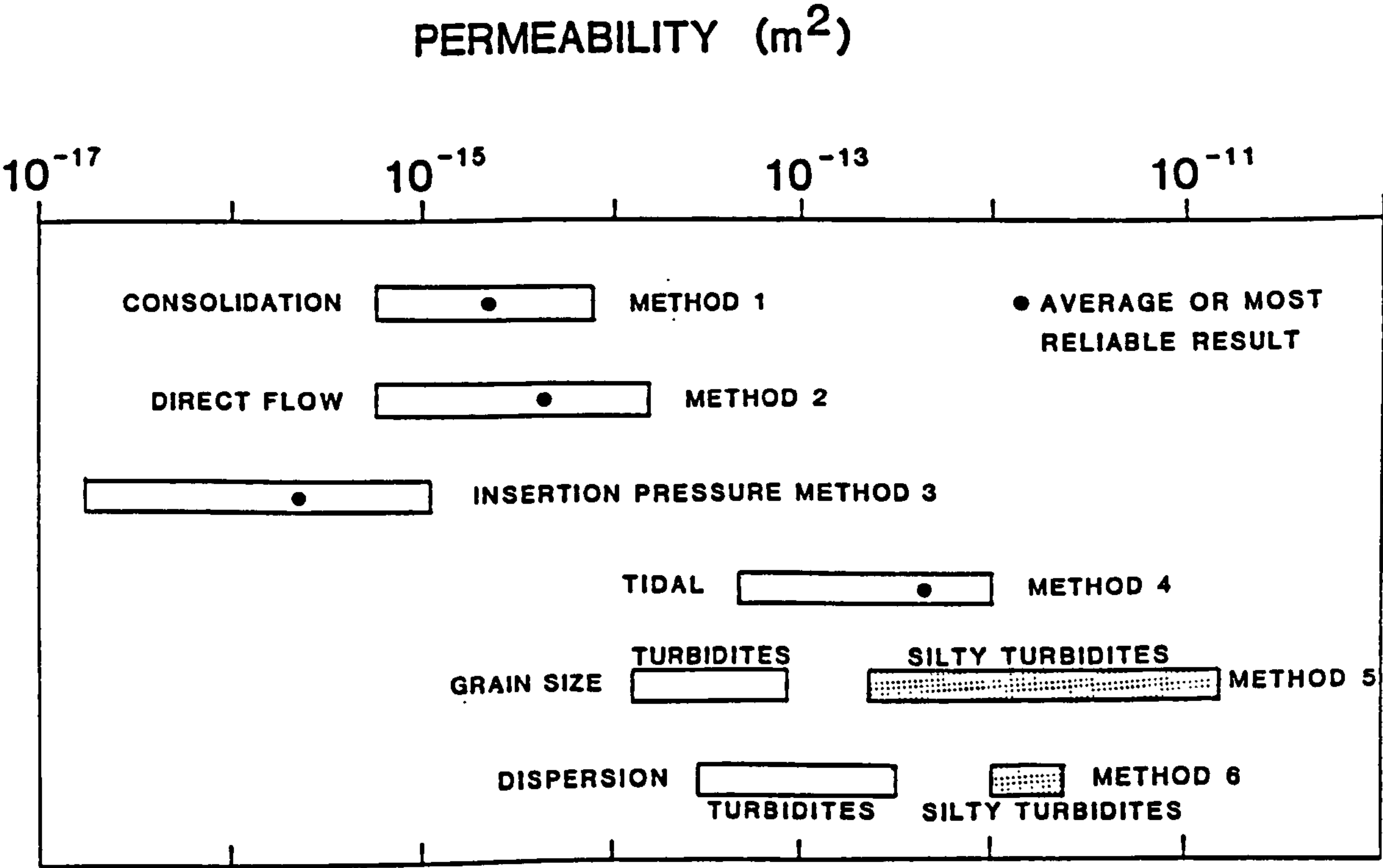
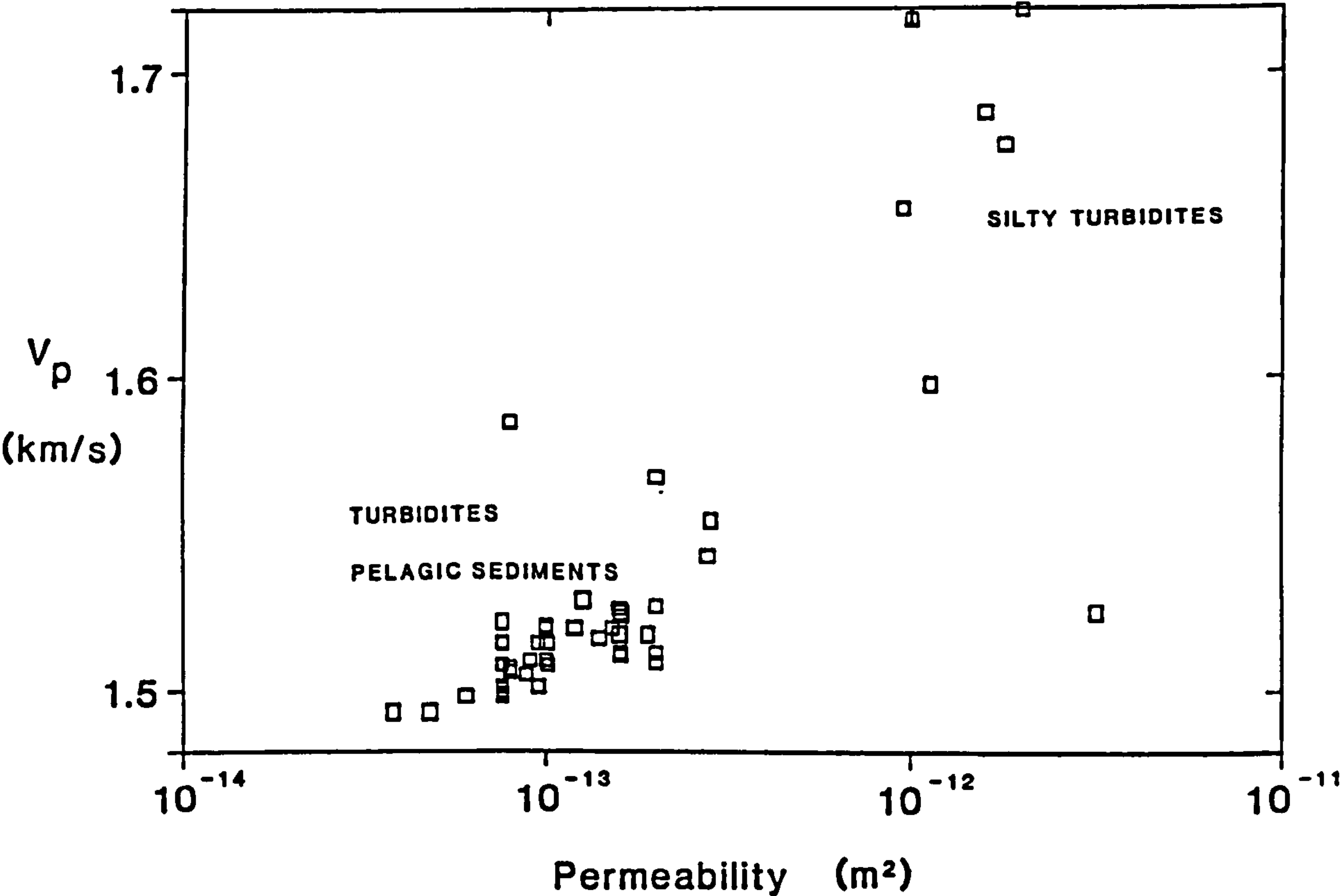


Figure 4.9 Predicted and measured permeabilities from techniques 1 to 6 for turbidite sediments from Site 1

4.10 Discussion

4.10.1 A comparison of the results from the six methods used to determine the permeability of the turbidite sediments of Site 1

Average values and ranges of the permeabilities of sediments from Site 1, determined by the six different methods, are shown in Figure 4.9. It is very interesting to note that these results span over 6 orders of magnitude - which requires some explanation!

4.10.2 Permeability from laboratory consolidation analysis (method 1)

The disturbance of the sample before and during the consolidation test pose the greatest problems for this method. As for all tests performed on sediments recovered from the sea-bed (methods 1,2,5,6), the samples will have undergone considerable disturbance prior to testing. Deformation of the sediment will occur during coring (Mayer, 1982). Such deformation may introduce small cracks or fissures in the sample. As the cores are rapidly brought to the sea-surface through the water column the sediment will expand due to the pressure release (Hamilton, 1976a) causing a small increase in the porosity and (presumably) the permeability. Careless storage of the sediment on land and the subsequent splitting and sub-sampling of cores can also cause an unknown degree of disturbance. Note, all these effects are qualitative and that it is virtually impossible to return any sediment sample to its original in-situ state.

The consolidation test itself introduces sample disturbance as the sediment undergoes elasto-plastic deformations during consolidation. This violates the assumption that the coefficient of consolidation (C_v) remains constant during the test (Znidarcic et al., 1984). Consequently, lower C_v , hence lower permeabilities (equation 4.3) are obtained from the test. Further problems causing unreliable values of C_v during these tests were caused by the erratic nature of the settlement and pore pressure versus

time plots from which the constant t_{50} was obtained (see 4.3). This latter problem can be attributed to "sticking" of the loading ram (Figure 4.1) and/or irregular drainage from the sample due to seepage down the sides. In fact Nickerson (1978) suggested that clogging of the porous discs often causes an impedance to the free drainage of samples in consolidation tests, hence giving an effectively lower recorded permeability than actually exists. This is plausible, but there was little evidence for this in these series of tests.

The constrained modulus (D_c) derived from a consolidation test is a high strain non-elastic value and is considerably smaller than its low strain elastic counterpart (Taylor-Smith, 1974). Therefore, the average value of $D_c = 370$ kPa used to calculate the permeabilities for the consolidation data from Site 1 (4.3.2), could be made an order of magnitude or so greater for a true elastic test. Paradoxically this would make the permeability even smaller (see equation 4.3).

4.10.3 Permeability from laboratory direct flow analysis (method 2)

Although the direct flow tests suffer from the same sample disturbance problems that all laboratory experiments experience (see 4.10.2), the tests themselves are very accurate. The tests are good because of the low amplitude stresses (hence linear elastic strains) which are applied to the sample by a small static head of water. It may be argued that a little amount of consolidation occurs on the instantaneous application of the head, but this can be assumed to be small. Therefore, data from such tests (4.4) represent a very good determination of the intrinsic permeability of the sediment samples tested. However, these data may not be that representative of the in-situ permeability of the sea-bed due to the sample disturbance problems and also because of the inadequacy of small-scale samples to capture large scale features that influence the in-situ permeability.

4.10.4 Permeability from piezometer insertion pressure (method 3)

Problems arise here from the sudden insertion of the piezometer probe in the sea-bed causing the sediments immediately surrounding the probe to be highly plastically deformed. As well as this plastic deformation, radial stress release fractures may occur which would have a major effect on pore pressures measured just after insertion (such fractures may well close up after equilibrium of the initial pore pressure has been attained). This latter fracture problem will depend upon the in-situ shear strength of the sea-bed - which is a controversial quantity (Lee, 1985).

Accepting that considerable plastic deformation occurs around the probe (and ignoring any possible fracturing), there remains the problem of modelling these elasto-plastic deformations accurately. Although the analysis presented in 4.6 does take into account the components due to plastic deformation of the sediment (Bennett et al., 1985, Soderberg, 1962) such theories still require considerable refinement (Hardin, 1978)

Questions may also be raised as to whether the probe has sealed itself well within the sea-bed, and whether there is vertical seepage along its length. However, the vertical entry, the in-situ lateral stress and the surface roughness of the probe make these unlikely (Schultheiss, personal communication). Also the data from successive deployments are remarkably similar; suggesting that if seepage does occur it happens in the same way for each deployment (which is unlikely). There is also a problem with the time response of the differential pressure transducer and logging rate of the piezometer, in that the system is often too slow to measure the entire magnitude of the initial insertion pressure (p_i). If p_i is incorrectly determined then so will be t_{50} , and ultimately the permeability will be affected (equations 4.3, 4.4).

4.10.5 Permeability from piezometer tidal cycle analysis (method 4)

For the tidal cycle analysis, in-situ values for the permeability are obtained using the elastic (linear) response of the sea-bed to a well defined dynamic forcing function, after the probe has reached static equilibrium. The attraction towards this determination of permeability is due to the stability of the sea-bed environment (no pressure-release or temperature drifting effects which affect laboratory measurements) and the fact that permeabilities are obtained from purely elastic deformations. Also, this technique does not just sample the sediment immediately around the lower pressure port on the probe (Figure 4.4), but measures the total (integral) effect of the deformation of the sea-bed between the bottom port and the sea-bed surface. This latter point is important as larger scale features, which are not detected by point measurements, will be exhibited (see Chapter 10). It is interesting to note that the permeabilities from this method (4) are up to two orders of magnitude greater than those obtained from the high quality laboratory point measurements (method 2).

This method (4) also has its limitations; in both the theory and the experimental measurements. The simple theory used does not account for permeability and shear modulus gradients - which undoubtedly exist over the upper few metres of the sea-bed. An extension along these lines is possible, but not really warranted as the quality and quantity of the PUPPI tidal pore pressure data is lacking. Also, seepage along the probe (4.10.4) would greatly affect the measured pore-pressure response. However, this method does give a determination of the permeability obtained under stable in-situ conditions. Further development of the theory and of the measuring system PUPPI (e.g. increasing the number of ports and the length of the probe) could greatly enhance the effectiveness of this simple method.

4.10.6 Permeability from grain size analysis (method 5)

The main problem with this method arises from the uncertainties introduced by use of the Kozeny-Carman relationship (4.8.1), which assumes a crude model of the pore-space of sediments. Further problems arise when this relationship (obtained from measurements on sands) is used for high porosity silty to clayey turbidite sediments. The equation relating pore size to grain diameter (equation 4.6) breaks down for porosities exceeding 0.75; as it gives pore radii greater than the grain diameter! Also, it is a poor assumption that clay-rich turbidite acts as a regular array of spheres of constant radius. However, Goldsberry (1985) has reported the application of the Kozeny-Carman relationship for some more sandy marine sediments with some success.

4.10.7 Permeability from compressional wave dispersion (method 6)

This method suffers from the assumption that the apparent dispersion observed in experimental compressional velocity can be entirely attributed to variations in the permeability of the samples in question. There are a number of parameters which affect the apparent dispersion; in fact the tortuosity of the sediment has the greatest influence and the shear and frame bulk moduli are also important (Chapter 7).

From the results presented in Figures 4.8, 10.3 and 10.4) some velocity dispersion can be inferred; but whether this can be entirely accounted for by variations in the permeability is questionable. Alternatively, it could be argued that the increase in compressional wave velocity in the silty bases of the turbidites is due entirely to increased shear moduli of these coarser grained sediments (Hamilton *et al.*, 1982) and has nothing to do with dispersion, real or apparent. This point is pursued further in Chapters 7 and 11.

4.11 Definitions and uses of "large-scale", "small scale" and "micro" permeabilities

From the discussions in 4.10.1 to 4.10.7, it is apparent that the effect of large-scale features (cracks or fissures) need to be accounted for if the in-situ permeability of the sea-bed is required. However, accurate direct-flow laboratory measurements will give a good indication of the intrinsic (small-scale) permeability of sediment samples, but will not capture the effect of large-scale features. Hence, such "large-scale" permeabilities over the scale of metres will be greater than the "small-scale" permeabilities which are appropriate to scales of millimetres.

The small-scale direct flow permeability is different to the permeability required for Biot's theory of stress wave propagation, which deals with fluid-flows of the order of the pore-size of sediments (i.e. micrometres). Berryman (1986) and Berryman and Thigpen (1987), show that the micro-permeability of sediments will always be significantly greater than the small scale permeability (they use the terms "local" and "global" respectively). This argument can be appreciated by considering a porous material which comprises n parallel layers of thickness l_j and permeability k_j , and with all other physical parameters remaining constant. The effective flow permeability (k_{eff}) across such a material can be found by applying Darcy's law across the series of layers:

$$\frac{1}{k_{eff}} = \frac{1}{l} \sum_j^n \frac{l_j}{k_j} \quad 4.7$$

$$l = \sum_j^n l_j \quad 4.8$$

Here, k_{eff} is equivalent to the small-scale or global permeability. Now, for Biot's theory of acoustical propagation, the permeability of each layer has to be considered individually, and the effective permeability for Biot-type dispersion and attenuation is given by the mean micro-permeability (\bar{k}_{eff}):

$$\bar{k}_{eff} = \frac{1}{l} \sum_j^n l_j k_j \quad 4.9$$

As, $k_{eff} \leq \bar{k}_{eff}$ the small-scale permeability will give the lowest possible limit of the micro-permeability. In practice, the micro-permeability will be somewhat larger than the small-scale permeability. In many of the dispersion and attenuation examples discussed later (in Chapters 7, 8, 9, 10 and 11), there are no available data for the micro-permeability. In these cases, the small-scale permeability is used, remembering that this will be lower than the true micro-permeability of the porous media.

From Figure 4.9, it appears that permeabilities obtained from different techniques (which operate over different length scales) vary considerably in magnitude. Whether this range in the data is due to each technique measuring a different intrinsic "type" of permeability, or whether the range is strictly a function of length-scale is uncertain. It can be appreciated that the consolidation permeability derived from elasto-plastic "squeezing" of sediments is arrived at by a different process than elastic Darcian flow permeabilities. Furthermore, the permeability obtained from the micro-oscillation of pore-fluids within the pore-space, induced by the passage of stress waves (permeability from Biot dispersion analysis), is again a different "type" of permeability. The problem is further complicated by the relative accuracy of each of the

various experimental techniques in measuring the different "types" of permeability.

As the term "type of permeability" is rather ambiguous, the spread in all the data shown in Figure 4.9 will be assumed to be due to differences in length-scale and experimental uncertainties. The "large-scale" permeability is greater in magnitude than the "small-scale" permeability due to gross features (cracks, etc). However, the "micro-permeability" is greater than small-scale permeability (equations 4.7 to 4.9).

4.12 Summary

Six different methods were used to determine the intrinsic permeability (k_a) of deep-sea sediments; k_{a1} from consolidation, k_{a2} from direct-flow tests, k_{a3} from pore-pressure decay, k_{a4} from inverse tidal cycle analysis, k_{a5} from grain size and k_{a6} from inverse dispersion analysis. The permeabilities determined by the six different methods range from 10^{-17} m^2 to 10^{-12} m^2 for the turbidite sediments from Site 1 (Great Meteor East in the North Atlantic Ocean). In order of decreasing magnitude these are; k_{a4} , k_{a6} , k_{a5} , k_{a2} , k_{a1} and k_{a3} .

The scale of the problem for which the permeability is required is important in choosing which method is most appropriate. "Large scale" in-situ problems over lengths of metres require that large scale inhomogeneities are considered, such as cracks or fissures. For this type of problem the permeabilities determined from in-situ experiments, such as those obtained from the tidal cycle analysis (k_{a4}), are most appropriate. For "small-scale" problems on the scale of millimetres, the appropriate permeabilities are those obtained from most laboratory studies (e.g. k_{a1} and k_{a2}). For problems involving Biot's theory of wave propagation, the "micro-permeability" on the scale of micro-metres is best.

It can be shown that the micro-permeability is greater or equal to the small-scale permeability; this means that permeabilities obtained from Biot dispersion or attenuation studies will be expected to be larger than the small-scale permeabilities. This is indeed the case, as $k_{a6} > k_{a1}$, k_{a2} .

For the fast wave dispersion and attenuation studies in Chapters 7, 8, 9, 10 and 11, no direct measurements of the micro-permeability of sediments exist. For these cases, direct flow permeability (k_{a2}) measurements are used wherever possible, remembering that these values will give the lower permeability bound of the micro-permeability. Where no direct-flow permeability data exist, the permeability is determined from the grain size of the sediments (k_{a5}). It is interesting to note that $k_{a5} \approx k_{a6}$, and therefore permeability from the grain size will be expected to be roughly of the same order of magnitude as the micro-permeability, which is required for Biot acoustic propagation studies.

The extensive studies investigating the permeability of deep-sea sediments were prompted by the importance of this parameter for the boundary problem of tidal loading of the sea-bed (Chapter 3). It transpires (Chapters 6, 7 and 8), that this parameter is also important for acoustic propagation in sea-bed sediments. It is shown in Chapters 6, 7 and 8, that the frame moduli of deep-sea sediments are also very important for acoustic propagation problems. In Chapter 5, the available methods for determining the frame moduli of deep-sea sediments are assessed.

5.1 Introduction

In order to apply elastic theory (Appendix 1), poroelastic theory (Chapter 2) or anelastic theory (Appendix 2), to deep-sea sediments, two "frame" elastic constants of the sediment are required. In principle it should be possible to measure these constants using a simple experimental set-up where a known stress is applied to a sediment sample and the elastic strain deformation which the sample undergoes is measured. In practice there are considerable experimental difficulties in attaining this goal, as there are eleven identified experimental variables which affect the magnitude of the elastic constants (Hardin and Black, 1968). Often, it is difficult to assess whether results showing variability in the elastic "constants" are due to experimental oversights (e.g. uncorrected temporal temperature drift), or to other intrinsic variations (e.g. temporal creep). All this makes comparison of data for different sediments, obtained using different experimental methods, very difficult.

The most straightforward frame elastic constant to experimentally determine is the shear modulus (G) through shear wave propagation tests. Unfortunately, propagating shear waves through small scale laboratory samples is not simple, although the development of new shear-wave bender element techniques do assist with this problem (Shirley and Hampton, 1978, Schultheiss, 1981). Bender element methods allow G to be obtained simply and quickly, although a large measure of uncertainty is introduced as the bender element technique has remained largely uncalibrated. Bennell *et al.* (1984) incorporated bender elements into a resonant column system, which is the ASTM recognised experimental method for obtaining G . Therefore, a series of experiments comparing results from the two techniques should act as a good test of the merits of the bender element method. A favourable

comparison would allow G to be obtained for a variety of sediments with relative ease and confidence, by using bender element techniques alone.

The second frame elastic constant is considerably more difficult to obtain than G . Of the various experimental methods available, the mechanical uniaxial (laterally constrained) consolidation test and the triaxial shear-strength test have been repeatedly used in geotechnics to obtain the constant D_c . However, it has been recognised for some time (e.g. Taylor-Smith, 1974) that sediments do not behave elastically under large amplitude ($>10^{-3}$) mechanically derived strains, whilst they do behave elastically (more or less) under small amplitude (10^{-6}) strains. Therefore, large-strain elasto-plastic D_c measurements do not give a true representation of the elastic properties of sediments. The elastic behaviour of sediments at small strain amplitudes can be investigated by using acoustical waves, or by using very sensitive mechanical devices (such as the resonant column).

The decrease in the magnitude of a modulus (e.g. G), with increasing strain amplitude from its value at low strain amplitude G_{max} , is called modulus degradation. The question remains as to whether elastic constants obtained at high strain amplitudes have any bearing on their low amplitude counterparts. This question can be addressed by using a variable strain amplitude device, such as described by Bennell et al. (1984), which applies longitudinal or rotational stresses on a sediment sample which is not laterally constrained, allowing G and the Young's modulus (E) to be determined at different strain amplitudes.

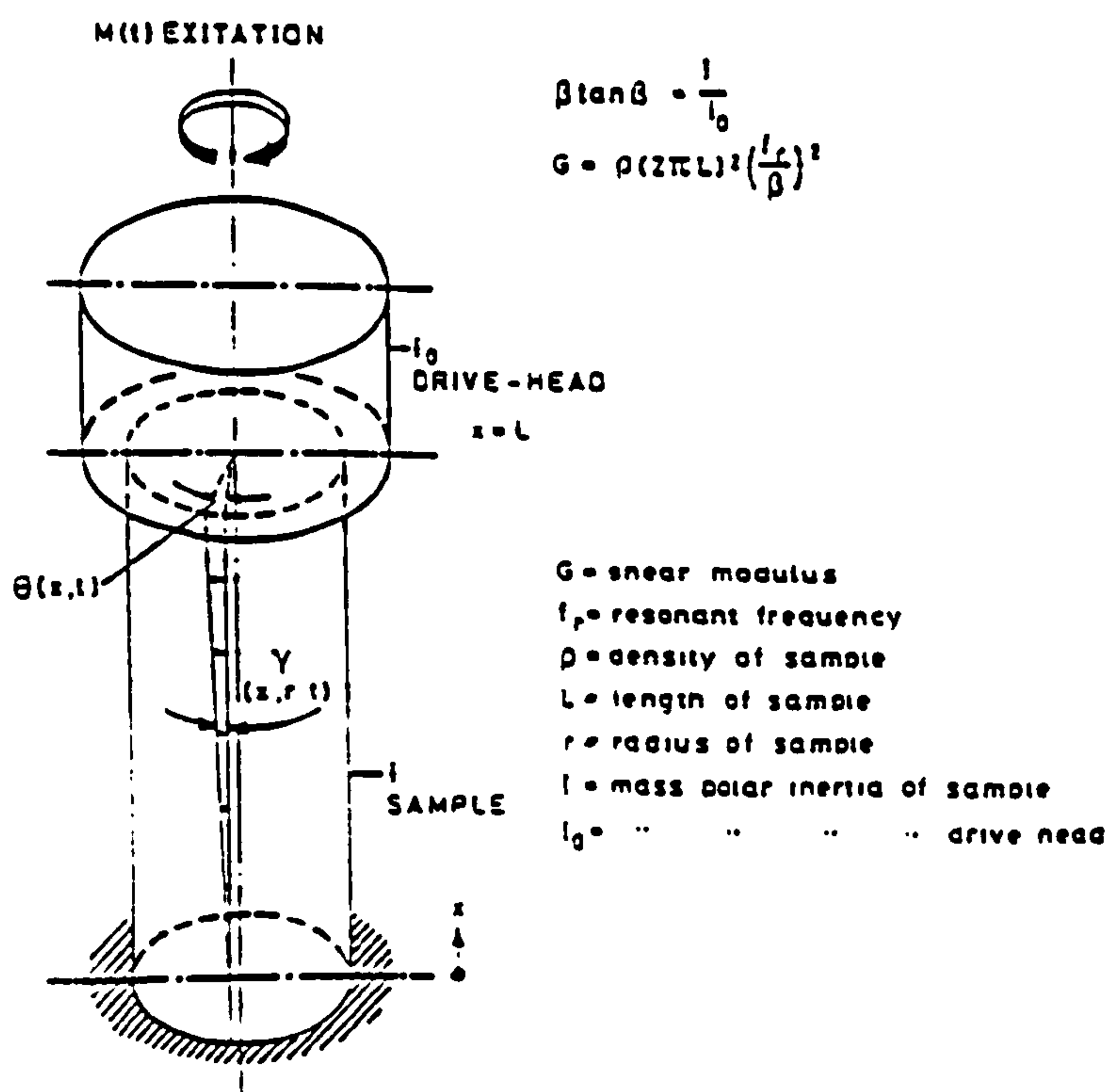
Lastly, the question as to whether the elastic constants are really "constant" requires some attention. Allowing for the experimental conditions which affect the magnitude of the elastic constants (Hardin and Black, 1968), only the variation of the "constants" with frequency or time will characterise their anelastic (non-constant) nature (Appendix 2).

5.2 Resonant column method for obtaining E and G

5.2.1 The principle of the resonant column

The resonant column is a device which allows a small sediment sample to be vibrated in extensional or torsional modes (Figure 5.1). If the wavelengths of vibrations are selected such that they are some integer multiple of the length (L) of the sample, the sample will resonate at one of these normal modes. These resonant angular frequencies (ω_r) are attained when the applied dynamic stress is exactly in phase with the resulting dynamic strain. At these normal modes, standing waves will be set up and the velocity of these waves will be related to the frequency of the applied vibrations, the dimensions of the sample and the elastic constants of the sample. Therefore, if the sample dimensions, the frequency of the applied stress and the phase angle between stress and strain are known, it is straightforward to calculate the elastic constants G and E for torsional and extensional resonant vibrations.

Figure 5.1 Principle of the resonant column device



In practice the situation is complicated slightly by the inertia of the system applying the stress and measuring the strain, which sits on top of the sample (Figure 5.1). It is straightforward to allow for this additional mass when calculating G or E by using a simple correction equation (Drnevich et al., 1967). Accounting for this correction and solving the wave equation for the fixed-free boundary conditions gives the following relationships (Bennell et al., 1984):

$$G = \rho \cdot V_s^2 = \frac{\rho \cdot L^2 \omega^2}{\theta} r^2 \quad 5.1$$

$$\frac{I}{I_0} = \theta \cdot \tan \theta \quad 5.2$$

$$E = \rho \cdot V_r^2 = \frac{\rho \cdot L^2 \omega^2}{\beta} r^2 \quad 5.3$$

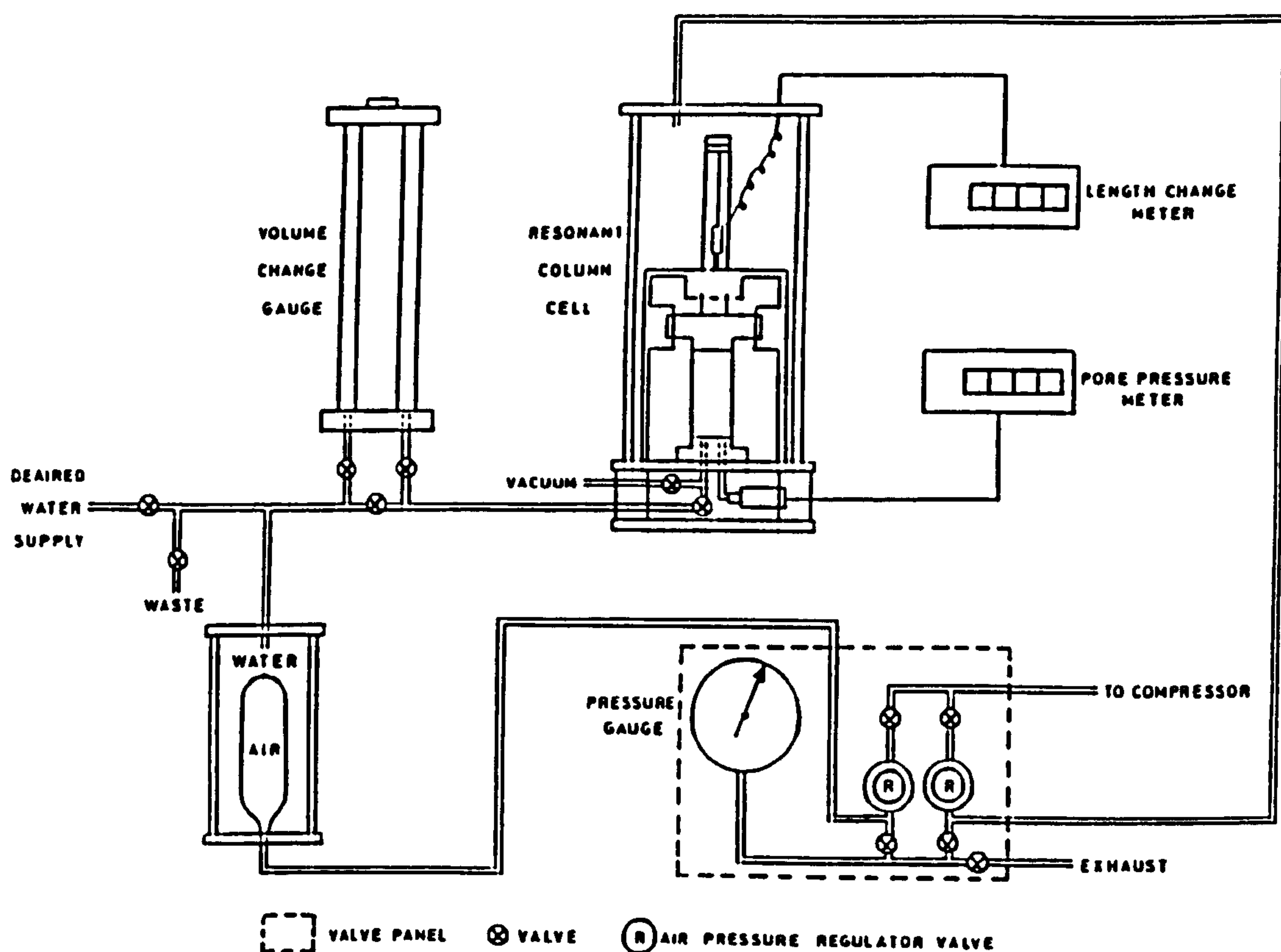
$$\frac{m_s}{m_a} = \beta \cdot \tan \beta \quad 5.4$$

Here, G is the shear modulus, ρ is the density of the sample, V_s is the shear velocity, I is the mass polar inertia of the sample, I_0 is the mass polar inertia of the additional mass, E is the Young's modulus, V_r is the rod wave velocity, m_s is the weight of the sample and m_a is the weight of the added mass.

5.2.2 The resonant column system

The resonant column system used to investigate the elastic properties of various sediments from Sites 1 and 4, is shown in Figure 5.2. The system consists of a resonant column cell which accommodates the sample, a back-pressured hydraulic confining apparatus and a mechanical electronic system which applies stress and measures strain in the sample.

Figure 5.2 Schematic diagram of the resonant column testing system



The cell houses a sample which is sealed in a rubber membrane and confined by water. The bottom of the sample rests on a permeable disc on the base of the cell. A top-cap containing drive-coils and an accelerometer is affixed to the top of the sample. Permanent magnets are arranged around the top-cap and torsional or longitudinal stresses are applied to the sample via the drive coils. The resulting sample motion is recorded by the accelerometer. A displacement transducer is attached to the top-cap to monitor changes in the sample's length during consolidation stages.

The back-pressured confining system (Figure 5.2) allows triaxial hydraulic pressures up to 1 MPa to be applied to the sample. Also, pore-pressures may be applied to the sample, allowing the sample to be placed under various effective stresses by the appropriate adjustment of

the confining and back pressures. On the application of a confining pressure the sample will undergo consolidation, with drainage occurring from the base of the sample. The confining pressure can be stepped up on a logarithmic incremental basis allowing a triaxial consolidation test to be performed (see 4.2 for details on uni-axial consolidation).

The input signals to the drive coils are generated by a variable frequency sine-wave oscillator, amplified, passed through a power resistor, then fed to the coils. The voltage drop across the resistor (which is directly proportional to the applied stress) is connected in parallel to the X axis of an oscilloscope. The output signal from the accelerometer is integrated twice then fed to the Y axis of the oscilloscope. The phase angle between the applied stress and measured strain is given by the area of the hysteresis curve produced on the oscilloscope (see Appendix 2).

Due to the versatility of this resonant column system, it is also possible to determine the damping characteristics of the sample and the variation of E and G with strain amplitude and frequency. The damping-ratios for extensional and torsional vibrations at resonance (D_E and D_S) can be obtained by measuring the decay of the strain amplitude with time as a sample relaxes after the driving stress is shut off at resonance (Appendix 2). Also, if the sample is driven at various non-resonant frequencies with a constant driving force (hence constant strain amplitude), then the variation of E or G with frequency can be determined by the magnitude of the applied stresses and measured strains. For this case, the driving stress is fed (in parallel) to the Y axis of a X-Y pen plotter, the measured strain is fed to the X axis, and the modulus and damping characteristics of the sample are obtained from the hysteresis curve. Lastly, using the X-Y plotter again, the variation of E , G , D_E and D_S at a fixed frequency and variable strain amplitude can be investigated.

5.2.3 Samples, sample preparation and resonant column test procedure

Resonant column tests were performed on 7 samples; 2 from Site 4 and 5 from Site 1 (Appendix 3 for sample descriptions) by J.D. Bennell. The sample description and some low-amplitude test results for one of the sand samples from Site 4 are given in Bennell et al. (1984). Also, some high strain amplitude results on a very similar sample are given by Davis and Bennell (1986). A selection of the test results for the two sand samples from Site 4 and the samples from Site 1 (Bennell, personal communication) are presented in this chapter.

The samples from Site 1 were taken from 65 mm diameter gravity core-sections recovered on RRS Discovery cruise 153. Samples of 70 mm in length and 35 mm in diameter were trimmed from sediment sections extruded from the core-liner. A rubber membrane was fitted tightly around each sample and each sample was placed, in turn, into the resonant column cell [a slightly different procedure was adopted for the two sand samples (see Bennell et al., 1984 and Davis and Bennell, 1986)]. Once a sample was in the cell the top-cap and associated driving/measuring assembly was affixed to it. The hydraulic confining system was connected to the cell and a confining pressure of 210 kPa along with a back-pressure of 200 kPa was applied to the sample. The sample was left to consolidate and equilibrate under this small effective stress of 10 kPa before testing began. A back pressure of 200 kPa was chosen as it would force any free air in the sample into solution.

The initial consolidation stage was taken as being complete when the pore-pressure across the sample had dissipated (4.2). The effective stress was noted and then low-strain amplitude resonant column tests were performed on the sample giving experimental values for G_{\max} , E_{\max} , D_S and D_E . Then a series of high strain amplitude tests were performed on the sample at various frequencies and strain amplitudes.

After any measurement at a high strain amplitude ($>10^{-3}$) a low-strain measurement was taken immediately after to allow quantification and correction for any sample disturbance caused by the high (elasto-plastic) strains. After the high amplitude sequence of tests had been completed, the sample was left to recover and equilibrate before a higher confining pressure was applied to it and the testing repeated at the new effective stress. Details of test procedures are given in Bennell et al. (1984).

5.3 Bender element method for obtaining G_{\max}

5.3.1 Mounting bender elements in soil testing devices

Ceramic bender transducers were first used to measure shear wave velocities in unconsolidated sediments by Shirley and Hampton (1978). Schultheiss (1981) mounted bender transducers in the end-caps of a consolidation cell, to allow determination of the shear velocity (hence G_{\max}) at various effective stresses. Since then, bender transducers have been incorporated in other soil testing devices (Figure 5.3) including triaxial cells (De Alba et al., 1984) and resonant column cells (Bennell et al., 1984 and Dyvik and Madshus, 1986).

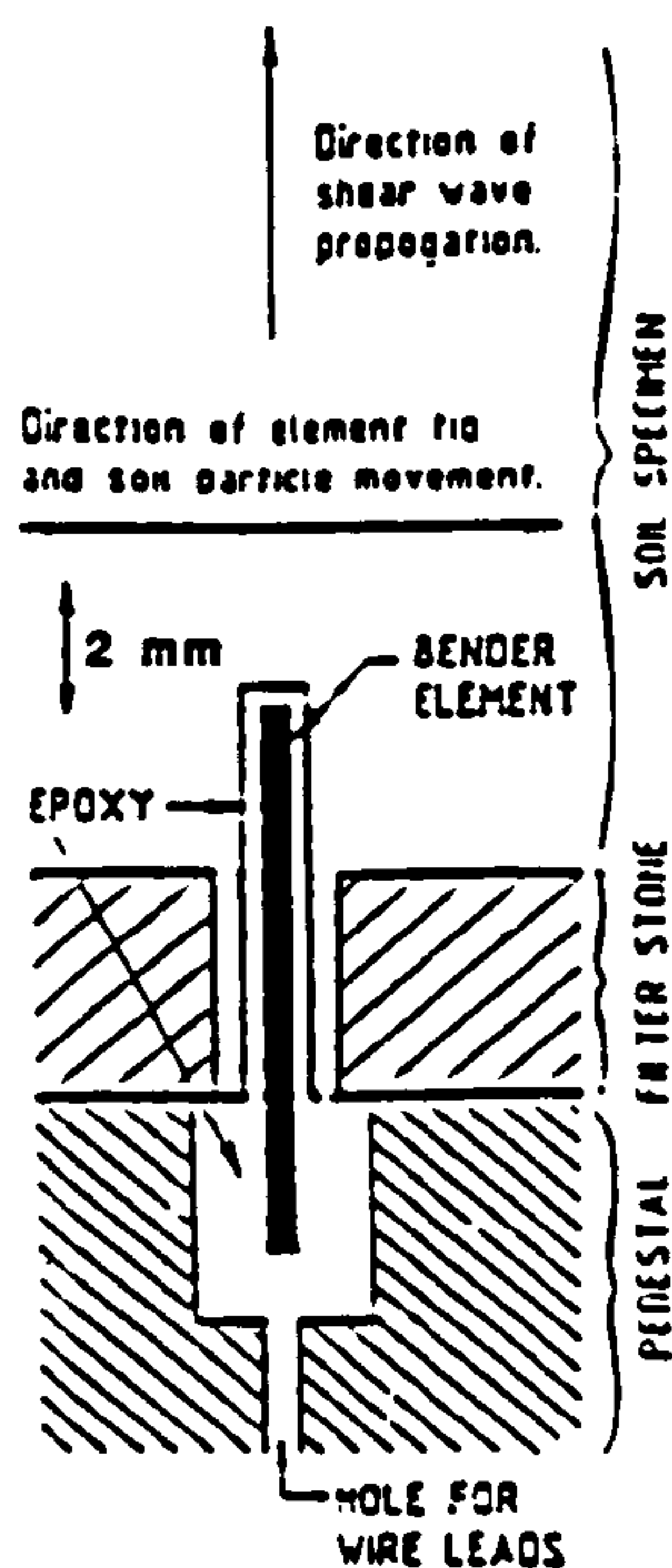


Figure 5.3 Shear wave mode bender element mounted in the end-cap of a soil test device

Three soil testing devices were adapted to incorporate bender (and other) transducers for various experiments. The first was the resonant column cell described by Bennell et al. (1984), the second was a 65 mm sample diameter triaxial cell (see Figure 6.1) and the third was a 50 mm sample diameter back-pressured consolidation cell (similar to that shown in Figure 4.1). In each of these cases the bender transducers were mounted into the top and bottom end-caps of the cells (Figure 5.3). The bender elements protrude through the porous drainage discs of the end-caps into the sediment sample.

5.3.2 Driving / measurement system

The wires from the outer faces of the piezoelectric crystals which make up the bender transducers (for details see Schultheiss, 1981) were connected to driving and measuring electric circuits. The electronic driving pulse was a 10 volt square wave, repeated at a frequency of about 1 kHz, which was also used to trigger the time base of an oscilloscope. The received signal was put through a variable gain amplifier then input into the oscilloscope. The oscilloscope was set up with a variable delay time for the triggering pulse, so the resultant display of the input signal could be presented on a high resolution time-base.

5.3.3 Factors affecting received bender signals

The character of the received signal from bender transducers embedded into a material is strongly affected by many experimental variables: coupling between sediment and transducers, type of material, stresses (effective or otherwise) acting on the material, separation of transducers, amplitude of driving voltage and any amplification / filtering of the received signal. The word "character" is taken to mean the amplitude and distribution of the various spectral components of the

signal which are present in the time-domain display (on an oscilloscope). Schultheiss (1981) shows the effect of an increase in the frequency of the received signal with an increase in the effective stress applied to a sand sample. This change in signal character with effective stress is due to the greater constraint applied to the transducer at higher stresses, which makes it resonate at higher frequencies. Any such subtle alteration in the sediment-transducer coupling can have a large effect upon the received signal character. This coupling effect poses the greatest problem as the "degree" of coupling is difficult to define or measure, let alone repeat.

5.3.4 Interpretation of received bender signals: problems

The art of determining shear wave velocities from the received signals of bender elements depends upon the correct interpretation of the signal. In theory (Shirley and Hampton, 1978 and Schultheiss, 1981) the shear wave velocity is obtained from the ratio of the separation of the bender transducers to the "onset time" of the shear wave component of the received signal. Interpreting this "onset" is made most difficult by the fact that it is unclear what one is meant to be looking for. In general, (Shirley and Hampton, 1978 and Schultheiss, 1981) the onset of the shear wave is taken as the place in the time-domain signal where the first zero-crossing of a large low-frequency positive or negative sinusoidal peak occurs. If the peak is not present it is taken that there is poor coupling between the sediment and the transducer so the shear wave (hence shear wave peak?) is not measured. Another possibility is that the shear wave peak may always be present but it may be obscured by other features in the received signal which have a larger amplitude but a similar frequency. Energy coupled into compressional waves, which arrive earlier than the shear wave, cause the greatest interference problem.

5.3.5 Benefits of signal conditioning

There is some evidence to show that the compressional waves produced by bender elements are generated at a distinctly different frequency to the shear wave component (e.g. Schultheiss, 1981). In principle, if the appropriate kind of filtering is applied to a received signal from a bender transducer, then the different spectral components could be isolated and identified. Various experiments have shown that digital filtering in the frequency domain and/or analogue filtering in the time domain of the received signals from bender transducers does not particularly enhance the (suppressed?) shear wave peak. It was concluded that it was best to use the more complex, but undistorted, unfiltered signals for interpretation.

5.3.6 Characterisation of received bender signals in different media

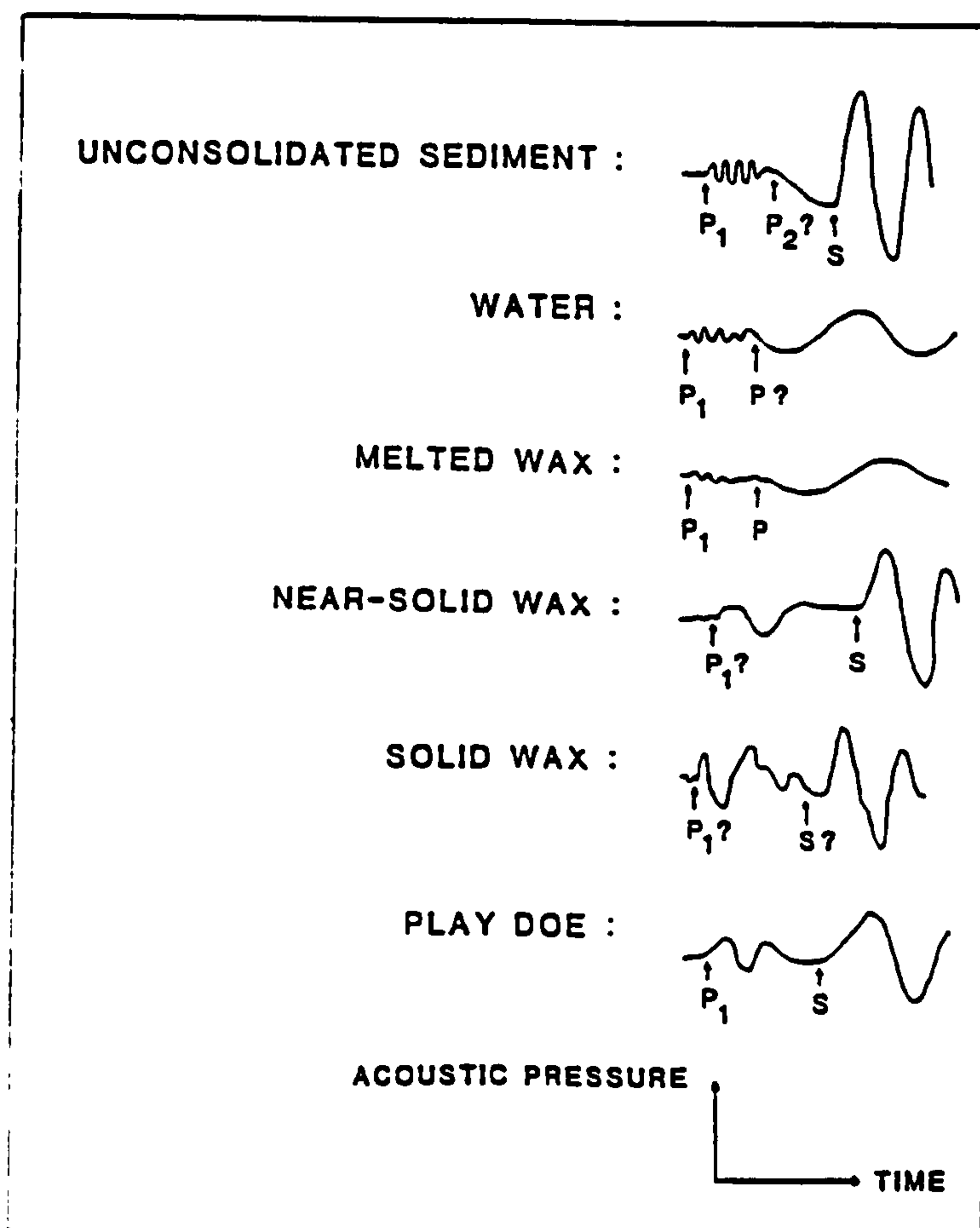
In an attempt to better understand the character of received signals, experiments were carried out using bender transducers in different media. Typical results for received signals in six different media are shown in Figure 5.4. These signals were sketched from the received voltage - time display of the oscilloscope to which the output of the bender transducers were fed. The time-base and voltage amplitude of these signals are immaterial as it is the relative character which is important.

The signal for an unconsolidated sediment was typical of many received signals obtained in various bender transducer experiments on sediments at low effective (<200 kPa) stresses. It consists of three distinct components: a (fast) high frequency small amplitude component associated with the fast compressional wave (P_1), a slower much lower frequency component (P_2 ?) which was tentatively linked with Biot's slow wave by Schultheiss (1981), and lastly a much slower intermediate

frequency high amplitude component (S) which is associated with a shear wave. Signals such as this degenerate with increasing effective stress and the isolation of the three components becomes unclear (Schultheiss, 1981).

The signal for water (with a very high amplification) has a fast compressional wave component (P_1), a slower lower frequency component (P_2) - which appears to be associated with a delayed lower frequency "ringing" or some resonance within the transducer. This observation of the slower lower frequency component in water, which is similar to that observed in unconsolidated sediments, suggests that these components should not be associated with Biot's slow wave as only the fast wave should exist in a fluid.

Figure 5.4 Shear-wave bender element signals for propagation through different media



There next follows a series of signals for a wax sample which was initially melted, but was left to solidify. The signal for the melted wax is similar to that in water. The signal for near-solid wax is much altered; with the P_1 component becoming lower in frequency and increasing in amplitude, and also the emergence of a similar frequency but distinctly larger amplitude component (S) associated with the shear wave. Lastly, for the solid wax the P_1 component and the S component have merged to produce a signal which is virtually uninterpretable. This latter signal is typical of many unconsolidated sediments placed under effective stresses of greater than 200 kPa. Note, that the lower frequency component observed in the melted wax is unidentifiable for the near-solid and solid cases.

The last signal is for "Play-doe", which is a plasticine type material. Here the P_1 component is identifiable, but the slower S component is more obscure. "Play-doe" was chosen for various experiments testing the repeatability of measurements (as it could be simply remoulded into its initial form). These experiments showed that there was still a great variation in the character of the signal depending on the way in which the transducers had coupled themselves upon insertion. In some cases the S component would become more distinct, but in other cases both P and S components would be combined.

5.3.7 Criteria for interpreting received bender signals to obtain V_s and G_{max}

Based upon the observations discussed in 5.3.3 - 5.3.6, the following criteria were established to interpret received bender signals to allow the calculation of the shear wave velocity (V_s) in a consistent manner:

1. Unfiltered signals are used for interpretation
2. Low-frequency, low amplitude negatively directed peaks are not

associated with S waves (or Biot's slow wave).

3. The "onset time" of the shear wave is determined by the first occurrence of a sharp higher frequency peak in a positive direction, which is superimposed upon the low-frequency peak described in 2.

4. Picking of the "onset time" of the shear wave at high effective stresses will be more subjective, if at all possible.

5. The separation distance between transducers is taken as the distance between the tips of the two transducers.

6. The shear wave velocity is determined from the ratio of the separation to the onset time.

5.3.8 Samples tested using bender elements

A number of different samples were tested using bender elements mounted in various cells. The 5 samples from Site 1 and one sample from Site 4 (SAND 1), used in the resonant column (5.2.3), were tested using bender elements mounted in the device (5.3.1). Six carbonate samples from Site 2 at sub-bottom depths ranging from 20 to 120 m (see Appendix 3) were tested in a consolidation cell modified to contain bender transducers. Consolidation and permeability results for these samples are given in 11.2.3. Other bender element experiments which were carried out on other samples included tests in a modified triaxial cell on a marine sand (discussed in Chapter 6) and experiments in split-core sections of carbonate sediments from Site 2 (results given in 11.2.2).

5.4 G_{max} and E_{max} results for sediments from Sites 1, 2 and 4

5.4.1 Failure of E_{max} experiments on samples from Site 1

Longitudinal resonant experiments conducted on the soft samples from Site 1 were not successful, but they were successful for a sand sample from Site 4. The soft samples could not be aligned perfectly

in the resonant column cell and these samples could not move freely (in a longitudinal direction) past the magnets surrounding the sample top-cap (5.2.2). This was not a problem for the sand sample. However, the soft Site 1 samples did appear to "free" themselves during high amplitude longitudinal tests (5.6). A selection of the low-amplitude resonant column results for sample SAND 1 are shown in Table 5.1.

5.4.2 Comparison of G_{\max} from resonant column and bender techniques

One of the draw-backs of using bender techniques for obtaining V_s , hence G_{\max} , is that calibration of the transducers in a medium with known V_s is difficult (unlike compressional wave transducers which are simply calibrated in water). However, mounting a set of bender transducers in a resonant column device (5.3.1) allows G_{\max} from bender techniques to be compared with G_{\max} from the resonant column. The closeness of G_{\max} results between the two techniques tests the effectiveness of the criteria established for interpreting the bender signals (5.3.7), allowing a calibration of bender techniques.

G_{\max} results from four different samples at various effective stresses, using bender and resonant column techniques from Sites 1 and 4, are given in Tables 5.1 and 5.2, and shown in Figure 5.5. The agreement between the two techniques is striking, particularly when there are many factors which can introduce errors in G_{\max} determined from bender techniques (5.3). It is encouraging to note that a similar independent comparison by Dyvik and Madshus (1986) was also favourable. The results in Figure 5.5 show that bender elements can be used to obtain G_{\max} successfully, (but a degree of caution should always be taken when using bender results alone) and also that there is little apparent shear wave velocity dispersion between the two sets of results, although this difference may be swallowed up by experimental uncertainties.

Table 5.1 Resonant column G_{max} and E_{max} results and bender element G_{max} for sample SAND 1, Site 4

Effective	G_{max}		D_S	E_{max}	D_E	ν_b	ρ
stress	res'col	bender					
(kPa)	(MPa)	(MPa)	%	(MPa)	%		(kg/m ³)
20	34.8	31.3	1.29	87.6	4.3	0.40	1590
30	46.7	43.1	0.98	115.3	4.5	0.34	1590
50	66.0	61.4	1.29	150.0	3.3	0.22	1590
75	83.0	78.1	0.76	183.0	3.4	0.17	1590
100	97.0	91.7	0.68	248.7	9.8	0.36	1590
125	--	104.2	0.71	272.0	7.7	--	1590
150	118.6	115.3	0.84	293.0	4.3	0.30	1590
200	136.0	134.6	0.91	326.3	3.3	0.27	1590
250	149.1	150.1	0.65	360.0	3.5	0.21	1590
300	160.7	164.3	0.55	388.0	4.0	0.20	1590
400	182.8	185.8	0.54	427.8	5.4	0.18	1590
500	201.0	205.1	0.52	454.1	9.0	0.15	1590
600	216.2	220.7	0.61	474.4	9.8	0.11	1590
700	230.7	232.7	0.63	--	--	0.08	1590

Table 5.2 Resonant column and bender element G_{max} results for Site 1

Sample	Effective		G_{max}	E_{max}	ρ
	Stress	res'col			
	(kPa)	(MPa)	bender (MPa)	(MPa)	(kg/m ³)
CLAY	35	8.0	6.0	61.9	1420
CLAY	100	14.7	10.9	84.1	1478
CLAY	300	27.2	23.6	143.0	1538
CARB	20	36.1	42.0	159.9	1818
CARB	50	59.2	65.5	240.4	1835
CARB	150	114.8	119.1	395.7	1860
CARB	450	189.5	198.2	633.6	1888
TURB 2	60	18.4	16.5	96.8	1620
TURB 2	125	30.7	27.3	134.2	1668
TURB 2	260	77.1	67.4	256.4	1772
TURB 3	20	5.2	6.5	44.4	1529
TURB 3	60	19.7	19.2	92.0	1568
TURB 3	165	45.7	45.8	202.7	1642
TURB 4	580	91.9	82.6	44.0	1532
TURB 4	50	8.4	6.5	64.0	1541
TURB 4	100	9.8	9.1	191.0	1678
TURB 4	295	46.8	45.7	278.0	1722

Figure 5.5 Comparison of G_{max} results from resonant column and bender element techniques for sediments from Site 1

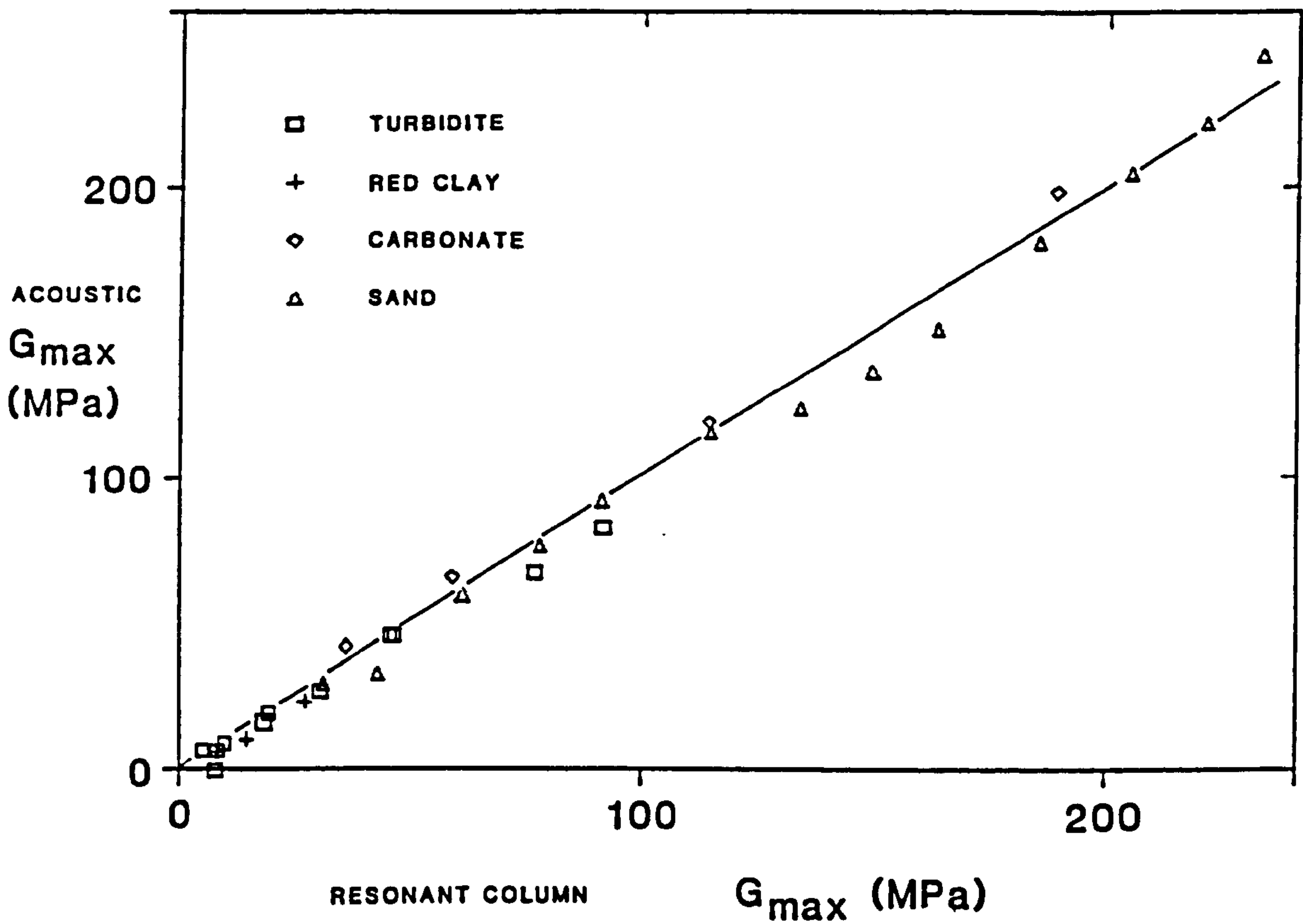
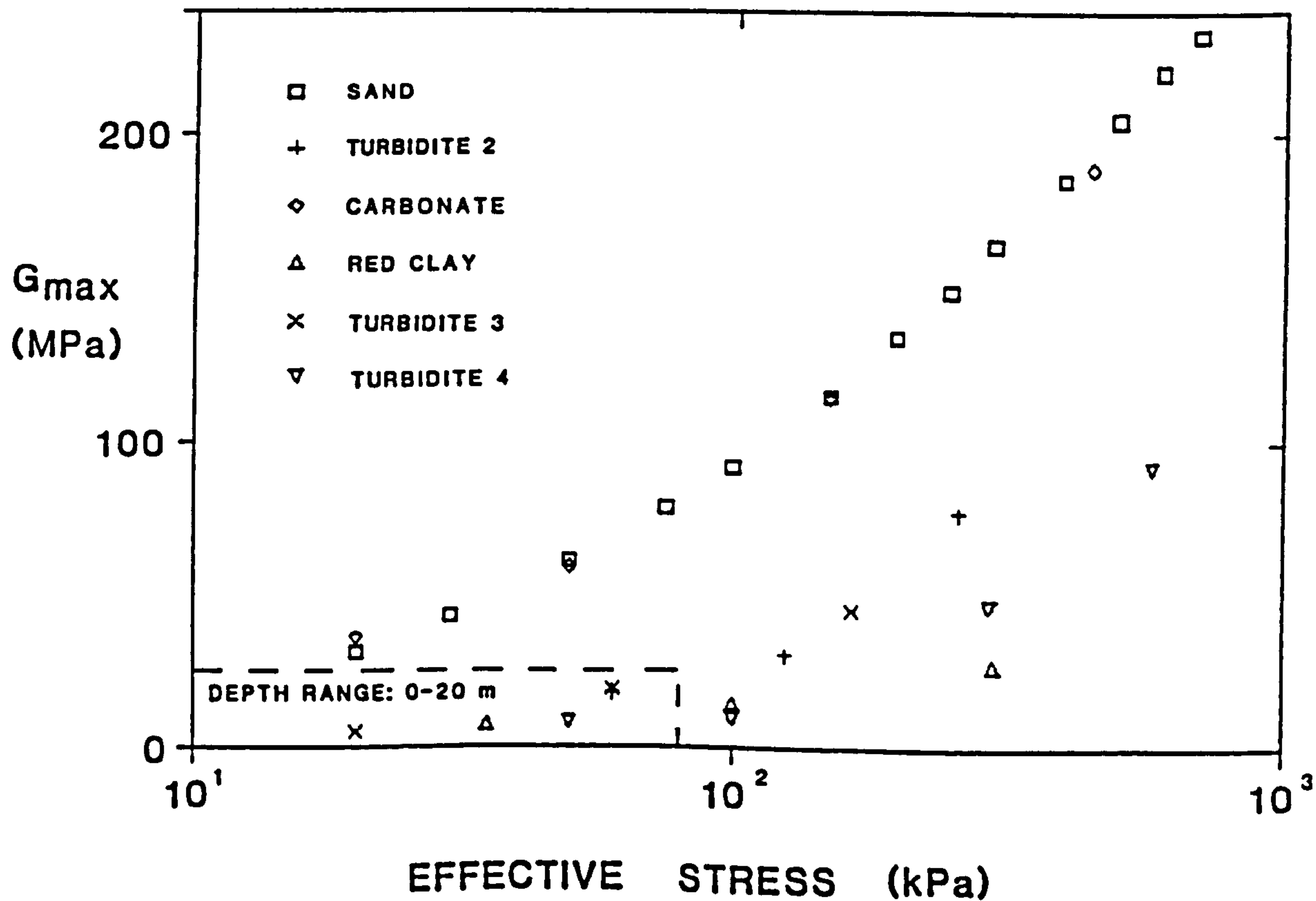


Figure 5.6 G_{max} versus effective stress resonant column results for sediments from Site 1

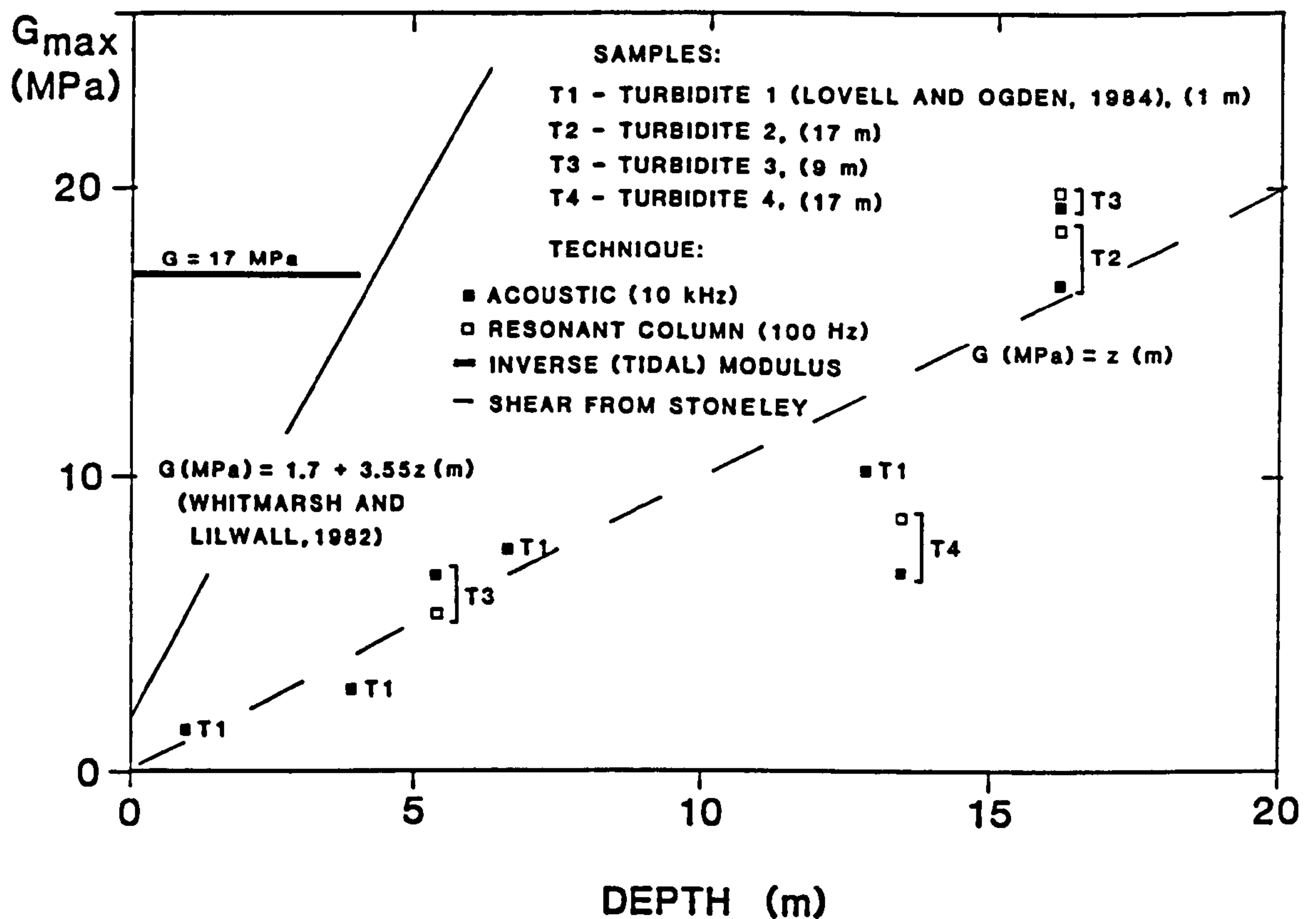


5.4.3 G_{\max} versus effective stress and sub-bottom depth at Sites 1, 4

The variation of G_{\max} (obtained from the resonant column) with effective stress, for 5 samples from Site 1 and a sand sample from Site 4 are shown in Figure 5.6. The three turbidite samples were taken from the same core at a vertical separation of less than eight metres (Appendix 3) and should all behave virtually the same under the application of the effective stresses used in the resonant column test. Figure 5.6 shows some experimental spread for the data for these turbidites; but they do behave in a similar fashion with a slow increase in G_{\max} with increasing effective stress. The clay sample from Site 1 also behaves like the turbidites. The sand sample from Site 4 and the near-surface carbonate sample from Site 1 show a remarkably similar dependence of G_{\max} with effective stress. This apparent similarity between the elastic properties of these two samples is useful; as longitudinal resonant column results were not successful on the carbonate sample (5.4.1) so they can be assumed to be similar to the longitudinal results for the sand.

The effective stress range within the dashed box shown on Figure 5.6 applies to sub-bottom depths up to 20 metres. Results for G_{\max} at given effective stresses can be converted to equivalent depth values by using the effective-stress / depth profile at Site 1 (see 10.2.2). The G_{\max} results within the box are converted in this way and are shown in Figure 5.7 with G_{\max} results obtained from three other techniques at Site 1. The data points labelled T1 are G_{\max} experimental results obtained by Lovell and Ogden (1984) who used a turbidite sample from Site 1 mounted in a consolidation cell with bender elements. Results T2 - T4 are taken from Table 5.1. The linear equation of G_{\max} versus depth is taken from results of Whitmarsh and Lilwall (1982), who obtain inverse in-situ G_{\max} determinations from Stoneley wave dispersion experiments at Site 1. Lastly, $G_{\max} = 17$ MPa is determined from the (inverse) analysis method.

Figure 5.7 G_{max} versus depth for surficial turbidite sediments, Site 1



The results of G_{max} versus depth at Site 1 (Figure 5.7) are interesting. The laboratory results for different turbidite samples using different techniques (bender and resonant column) and different observers, all provide G_{max} data from which the simple linear relationship $G_{max}(\text{MPa}) = 10^6 z(\text{m})$ would be deduced (from Figure 5.7). However, this is a far cry from the Whitmarsh and Lilwall (1982) relationship which predicts G_{max} linearly increasing more rapidly with depth. Sample disturbance during coring etc (see discussion in 4.10.2) degrading G_{max} for the laboratory measurements and/or uncertainties in the analysis of Whitmarsh and Lilwall (1982) are obvious reasons for this discrepancy. However, the rather crude average in-situ G_{max} result from the tidal cycle analysis (see 4.7.2) does appear to be of similar magnitude to the in-situ results of Whitmarsh and Lilwall (1982).

It is interesting to note that a linear increase of G_{\max} with depth is given by both the laboratory measurements and the in-situ results of Whitmarsh and Lilwall (1982) in Figure 5.7. This contrasts strongly with results from a recent review of G_{\max} data in near-surface sediments (Taylor-Smith, 1986), where G_{\max} is found to increase in a parabolic fashion with depth. It is most likely that the actual in-situ relationship between G_{\max} and depth at Site 1 is also parabolic (for the surficial sediments) and that the linear relationships seen in Figure 5.7 are over simplifications. From all these results, the general observation that laboratory measurements of G_{\max} are considerably less than in-situ determinations, seems fair.

5.4.4 G_{\max} versus effective stress results at Site 2

From an experimental view-point the quality of the bender signals obtained for the samples at Site 2, (which were tested in a modified consolidation cell), was far inferior to the quality of signals obtained on samples from Site 1 (in the modified resonant column cell). This may have been simply due to the difference in materials; however the much smaller separation between the bender elements in the consolidation cell, as compared that in the resonant column cell (15 mm : 65 mm), may have had some influence on the quality of the bender signals.

G_{\max} for 6 samples from Site 2, spanning over 100 m of core (see Appendix 3), were obtained from bender experiments in a modified consolidation cell. The results of G_{\max} versus effective stress for these samples are shown in Figure 5.8 and Table 5.3. Samples taken at shallow depths would be expected to have G_{\max} values less than deeper samples, at low effective stresses, and also the shape of the G_{\max} versus effective stress curve would be expected to be different for each sample.

Figure 5.8 G_{max} versus effective stress bender element results for carbonate sediments from Site 2

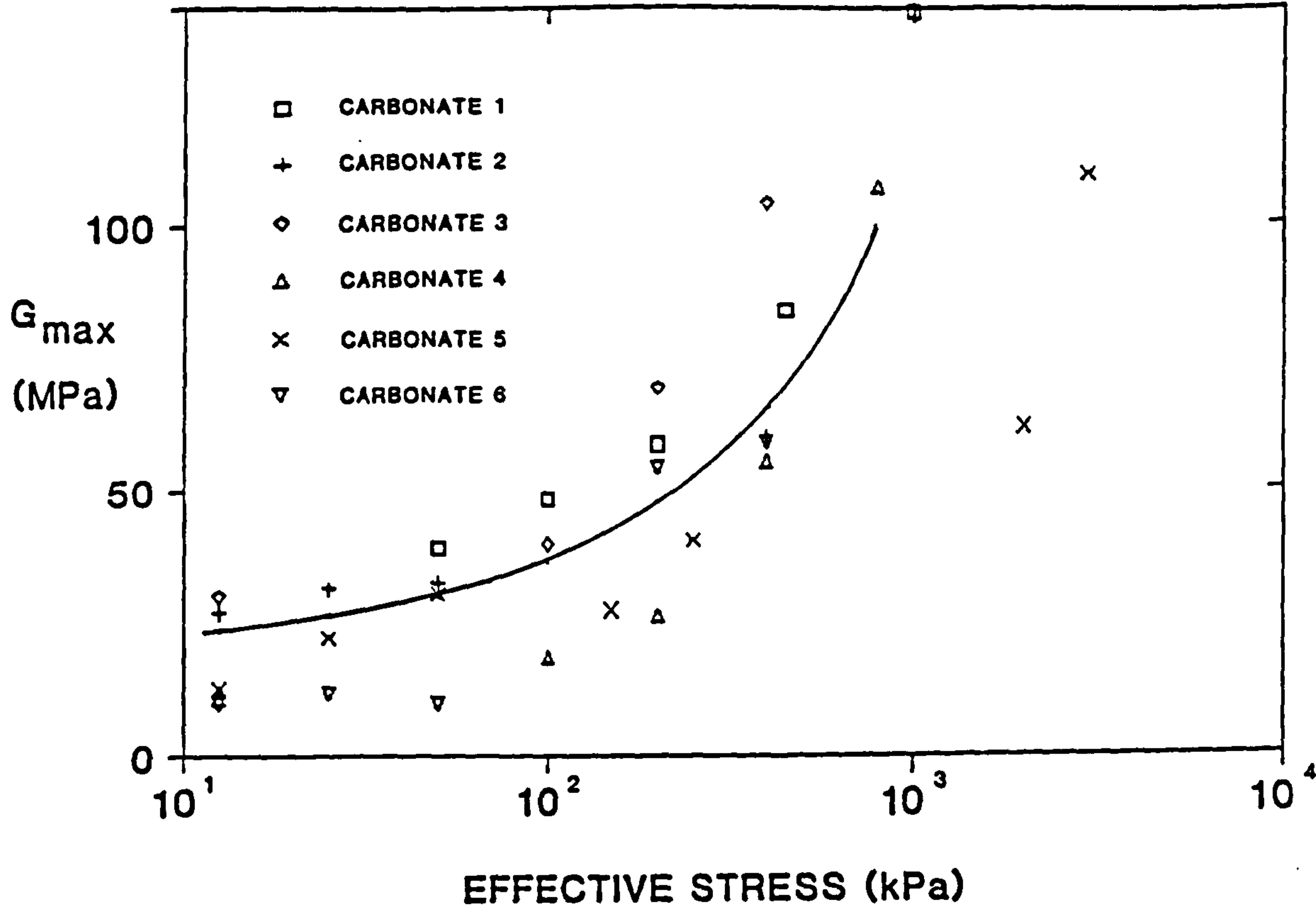


Table 5.3 Bender element G_{max} results for carbonates from Site 2

Sample	σ_{eff} (kPa)	V_s m/s	ρ kg/m ³	G_{max} (MPa)
CARB 1	50	151	1719	39.2
CARB 1	100	167	1740	48.5
CARB 1	200	183	1755	58.8
CARB 1	450	217	1780	83.8
CARB 1	1000	277	1819	140.0
CARB 2	12.5	130	1612	27.2
CARB 2	25	140	1617	31.7
CARB 2	50	142	1621	32.7
CARB 2	400	190	1664	60.1
CARB 3	12.5	135	1664	30.3
CARB 3	100	154	1689	40.1
CARB 3	200	202	1704	69.5
CARB 3	400	245	1724	103.0
CARB 4	12.5	82	1664	11.2
CARB 4	100	105	1689	18.6
CARB 4	200	125	1704	26.6
CARB 4	400	179	1724	55.2
CARB 4	800	246	1758	106.0
CARB 5	12.5	92	1515	12.8
CARB 5	25	121	1528	22.4
CARB 5	50	141	1539	30.6
CARB 5	150	134	1541	27.7
CARB 5	250	162	1554	40.8
CARB 5	2000	191	1699	62.0
CARB 5	3000	250	1748	109.0
CARB 6	12.5	81	1552	10.2
CARB 6	25	87	1556	11.8
CARB 6	50	80	1559	10.0
CARB 6	200	185	1585	54.3
CARB 6	400	191	1612	58.8

Neither of these traits are observable in the results shown in Figure 5.8, and any subtle variations between the behaviour of different samples is disguised by scatter in the data. As no differences can be resolved, all the G_{\max} data are lumped together and a single curve fitted through them.

5.5 Anelastic behaviour of sediments: Q and shear modulus dispersion

5.5.1 Band limited constant Q model of sediments

As all materials are never absolutely elastic, it should be possible to investigate the anelastic properties of sediments. Anelastic materials will exhibit dispersion of compressional and shear waves, creep and stress relaxation (Appendix 2). Note, these effects will be independent of dispersion and attenuation in poroelastic materials which is due to dissipation of energy due to Biot's (1941, 1956 a,b) viscous-flow mechanism (Chapter 2). Biot (1962 a,b) accounted for these additional anelastic effects in his poro-anelastic theory, by using results from anelastic theory, such as those offered by the band limited constant Q (BLCQ) model (Kjartansson, 1979).

The BLCQ model is semi-empirical. It relies on the experimental observation that the specific shear (say) attenuation ($1/Q_s$) (see Appendix 2) remains constant over a specified frequency band width. Constant Q_s implies a series of loss (stress relaxation) mechanisms, each of which is triggered at a successive discrete frequency. Each mechanism causes attenuation (and associated dispersion) of an equal amplitude Q_s . If the discrete series of mechanisms is blurred into a spectrum of equal amplitude mechanisms over the band width, then the BLCQ model results. The exact nature of the loss mechanisms, e.g. thermal losses, fluid flow between pores, frictional sliding, need not be specified (or modelled), as it is only the BLCQ result which is required.

Once the BLCQ model has been invoked it is possible to calculate the magnitude of the associated dispersion by standard anelastic theory (Norwick and Berry, 1972). [Alternatively, it is possible to calculate both Q and the dispersion from expressions obtained from experimental creep measurements (characterising attenuation in the time as opposed to frequency domain - see Appendix 2, Norwick and Berry, 1972 and Kjartansson, 1979)]. Neglecting the analysis and just quoting the results gives the following expression for the shear modulus (G) dispersion from the BLCQ model:

$$G = G_0 \cdot \left[\frac{f}{f_0} \right]^{2/(\pi Q_s)} \quad 5.5$$

Here, G_0 and f_0 are reference shear modulus and frequencies and $1/Q_s$ is the specific shear attenuation. Note, $1/Q_s$ is simply related to the damping ratio (Appendix 2).

Therefore, if constant Q_s can be experimentally determined, and measured shear wave dispersion characterised successfully by equation 5.5, the BLCQ model will hold for the sediment/material in question. This would allow determination of the complex anelastic modulus \hat{G} , and similar longitudinal analysis would allow the complex anelastic modulus \hat{E} to be determined. It would then be possible to follow Stoll's (1974) example and to substitute these complex anelastic moduli for the elastic moduli in Biot's (1956 a,b) theory. Biot (1962a) recognised that sediments would behave poro-anelastically, but he expressed the anelastic moduli as complex operators, which are more rigorous than Stoll's (1974) complex moduli, but less physically identifiable.

5.5.2 Shear modulus dispersion analysis at Site 1

In theory it should be possible to obtain $1/Q_s$ and G at various frequencies by using the stress-strain loop method (Appendix 2) offered by the resonant column device (5.2.2). Unfortunately, the stress - strain loop data for the samples tested (5.2.3) could not be amplified sufficiently to allow $1/Q_s$ to be resolved from the area of the stress - strain loop. G measurements (from the slope of the major axis of the stress - strain loop) were obtained at various frequencies. However, even these measurements must be analysed carefully as they were obtained at high strain amplitudes ($>10^{-3}$) and will therefore be somewhat degraded.

Although no continuous $1/Q_s$ versus frequency data were collected, $1/Q_s$ was measured at the resonant frequency (10 Hz) (by using the amplitude decay technique, see 5.2.2). Using this $1/Q_s$ value, and assuming a BLCQ down to the lowest stress - strain loop frequency (0.01 Hz), it is possible to predict shear modulus dispersion using equation 5.5.

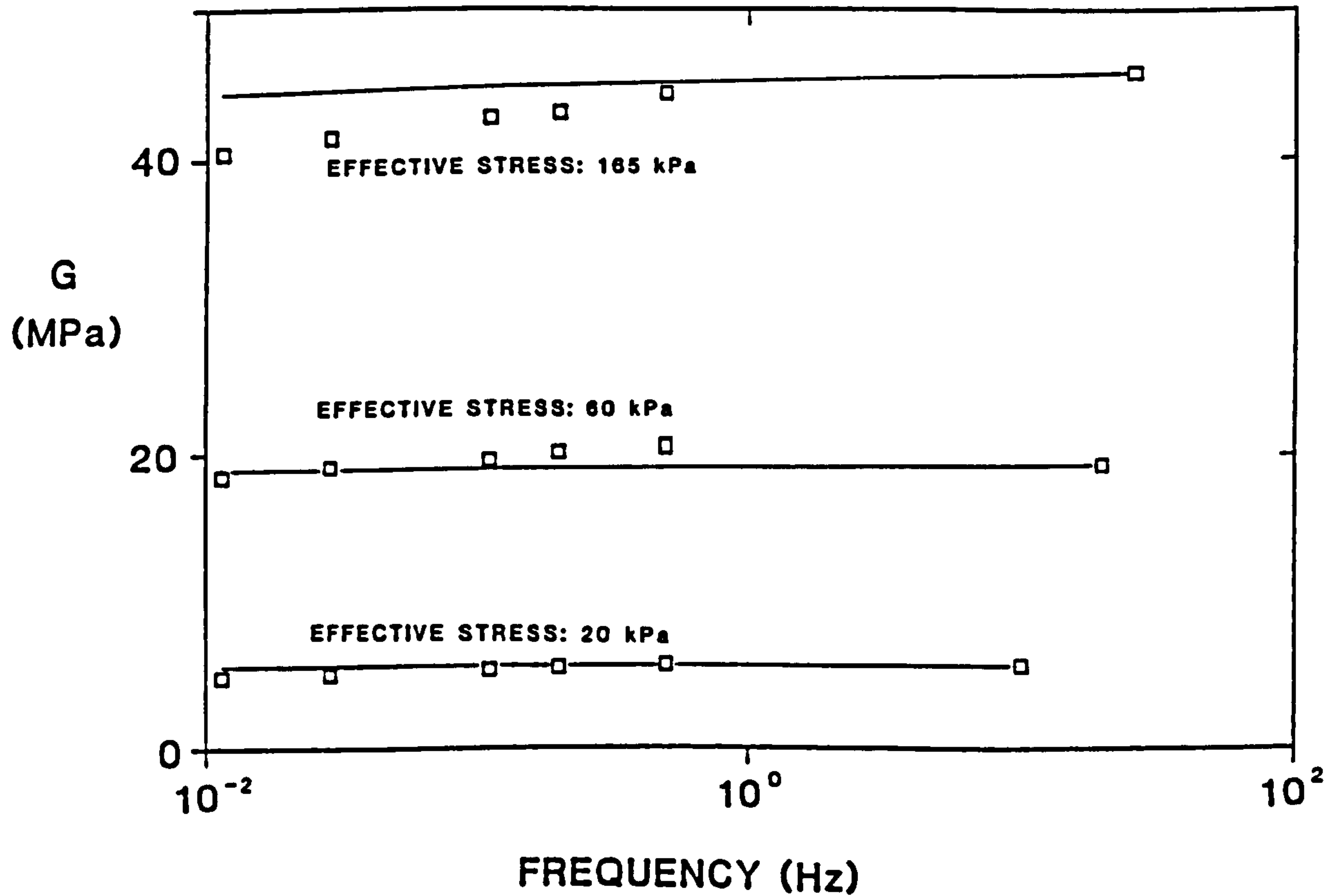
Experimental results for the variation in G with frequency, at three different effective stresses (σ_{eff}), for a selected sample from Site 1 are given in Figure 5.9 and Table 5.4. Shear modulus dispersion predictions from equation 5.5 are also shown. Predicted dispersions for different σ_{eff} are calculated using the G values at resonance (10 Hz) as the reference moduli, and with experimental values of $1/\pi Q_s$: $(3.183) \cdot 10^{-3}$, $(2.228) \cdot 10^{-3}$ and $(2.037) \cdot 10^{-3}$ used at σ_{eff} of 20, 60 and 165 kPa.

Initially it appears that there is a good agreement between the measured G values at low-frequencies and those predicted by the dispersion equation (especially at the effective stress of 20 kPa). However, a closer look at the predictions show they have a significantly different gradient to lines fitted through the experimental data at low-frequencies. Furthermore, the higher frequency measurements (at resonance) are not always greater than their lower frequency counterparts (e.g. for 60 kPa).

Table 5.4 G and D_s versus frequency: TURB 3, Site 1

Effective stress	f	G	D _s	strain amplitude	ρ
(kPa)	(Hz)	(MPa)	%		kg/m ³
20	0.011	4.86	5.7	0.0025	1529
20	0.029	5.08	5.7	0.0025	1529
20	0.111	5.34	5.7	0.0025	1529
20	0.200	5.49	5.7	0.0080	1529
20	0.500	5.67	5.7	0.0080	1529
20	10.000	5.70	5.7	0.0080	1529
60	0.011	18.40	3.6	0.0018	1568
60	0.029	19.10	3.6	0.0018	1568
60	0.111	19.60	3.6	0.0018	1568
60	0.200	20.10	3.6	0.0045	1568
60	0.500	20.50	3.6	0.0045	1568
60	20.000	19.20	3.6	0.0045	1568
165	0.011	40.30	2.1	0.0016	1642
165	0.029	41.30	2.1	0.0016	1642
165	0.111	42.60	2.1	0.0016	1642
165	0.200	43.00	2.1	0.0037	1642
165	0.500	44.30	2.1	0.0037	1642
165	25.974	45.70	2.1	0.0037	1642

Figure 5.9 G versus frequency for sample TURB 3, Site 1



There are a number of possible reasons for the differences between the low-frequency stress-strain loop G values and the higher frequency resonance G values. The low-frequency relatively high strain amplitude G values may suffer modulus degradation (lowering G - see 5.6.1), but also dispersive increases in G . For the G values obtained at resonance, degradation will be less and also the modulus dispersion will be greater; resulting in higher G values. Another possible cause is that the assumption of constant Q_s across this total band width is invalid. Another possible cause is that the accuracy of the measurements at lower and higher frequencies are widely different, not allowing a practical resolution of differences in G . There are many permutations of these arguments.

In practice, the limitations of this data set (and others not shown) mean that no clear conclusion can be drawn on the measured or predicted values for \hat{G} for the sediments from Site 1 tested on this system (5.2.2). Furthermore, extensional stress - strain measurements are not currently possible on this system and therefore attempting to conjure up \hat{E} or \hat{K}_b values for use in the Biot - Stoll theory is unwise (Chapter 2).

5.6 Determining a second elastic constant E or ν_b for Sites 1 and 4

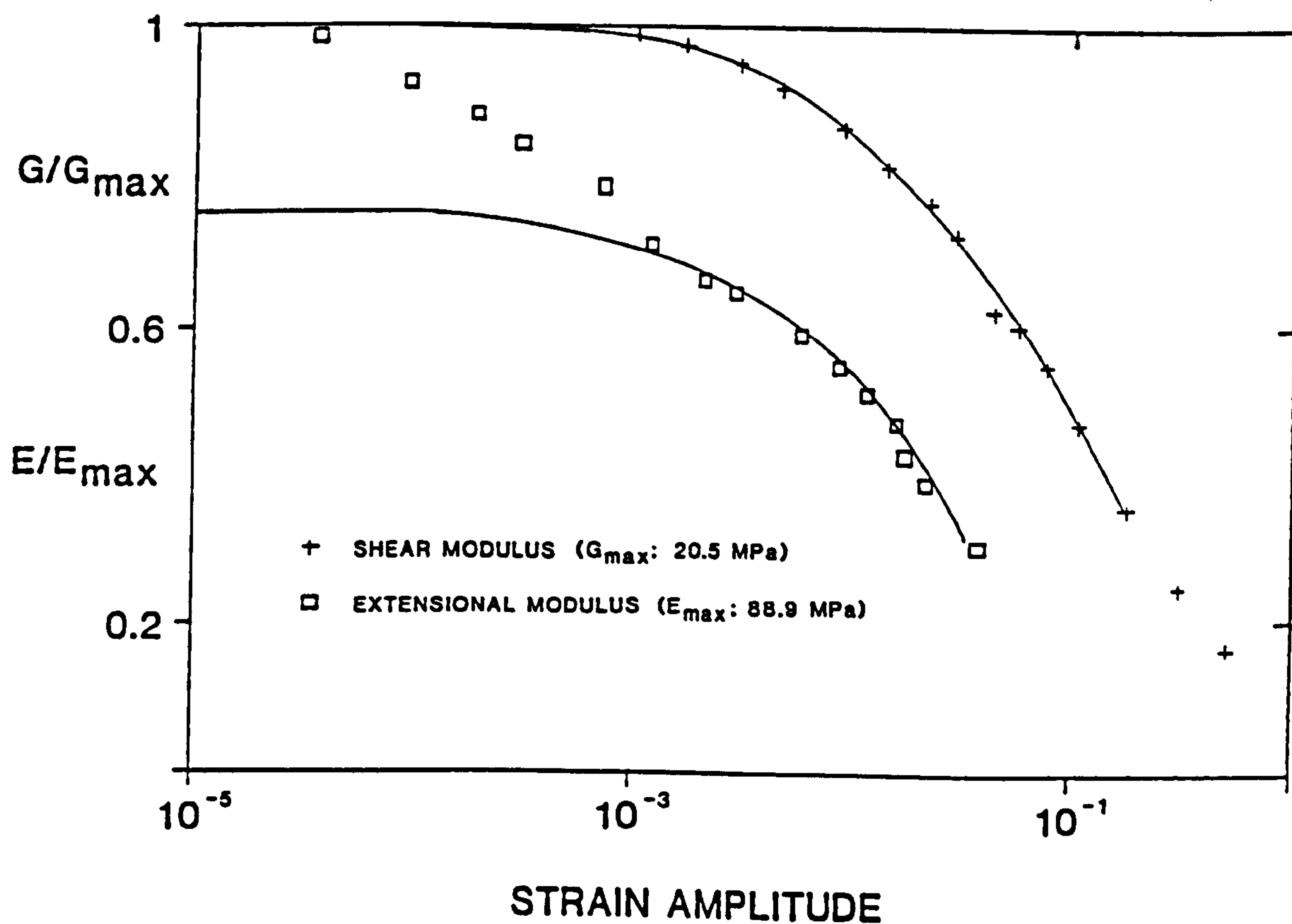
5.6.1 E results for Sites 1 and 4: degradation and experimental problems

As noted in 5.4.1, experimental problems meant that E_{\max} values could not be measured on the "soft" samples from Site 1 using the resonance technique. However, it was possible to carry out higher strain amplitude longitudinal tests (5.2.2) allowing E to be determined for these samples. Typical results for E and G , versus strain amplitude for one sample at Site 1, are shown in Figure 5.10 and Table 5.5. These results must be interpreted with care.

Table 5.5 High strain amplitude E and G results: TURB 3, Site 1
(at an effective stress of 55 kPa)

Strain amplitude	E (MPa)	G (MPa)	ν_b	ρ kg/m ³
(3).10 ⁻²	32.1	14.9	0.08	1560
(1).10 ⁻²	47.6	17.8	0.34	1560
(3).10 ⁻³	56.4	19.8	0.42	1560
(1).10 ⁻³	62.1	20.5	0.51	1560
(3).10 ⁻⁴	64.8	20.9	0.55	1560
(1).10 ⁻⁴	66.6	21.0	0.58	1560
(3).10 ⁻⁵	66.6	21.0	0.58	1560

Figure 5.10 High strain amplitude E and G results for sample
TURB 3, Site 1 at an effective stress of 55 kPa



The shear results of G and D_s versus strain amplitude show the well known effect of modulus degradation with accompanying increases in the damping ratio (not shown) (Hardin and Drnevich, 1972). The main feature of these results are that G remains constant at its low strain amplitude (elastic) value (G_{\max}) up to some critical strain amplitude, whereupon it decreases smoothly with increasing strain amplitude. The critical strain amplitude is around $(3) \cdot 10^{-3}$ for G (there is a corresponding increase in D_s at larger strain amplitudes). These two phenomena are connected: decreasing G being caused by slipping of grains as the sample undergoes elasto-plastic deformation at higher strain amplitudes, and increasing attenuation caused by the greater energy loss in the plastic (non-recoverable) deformations.

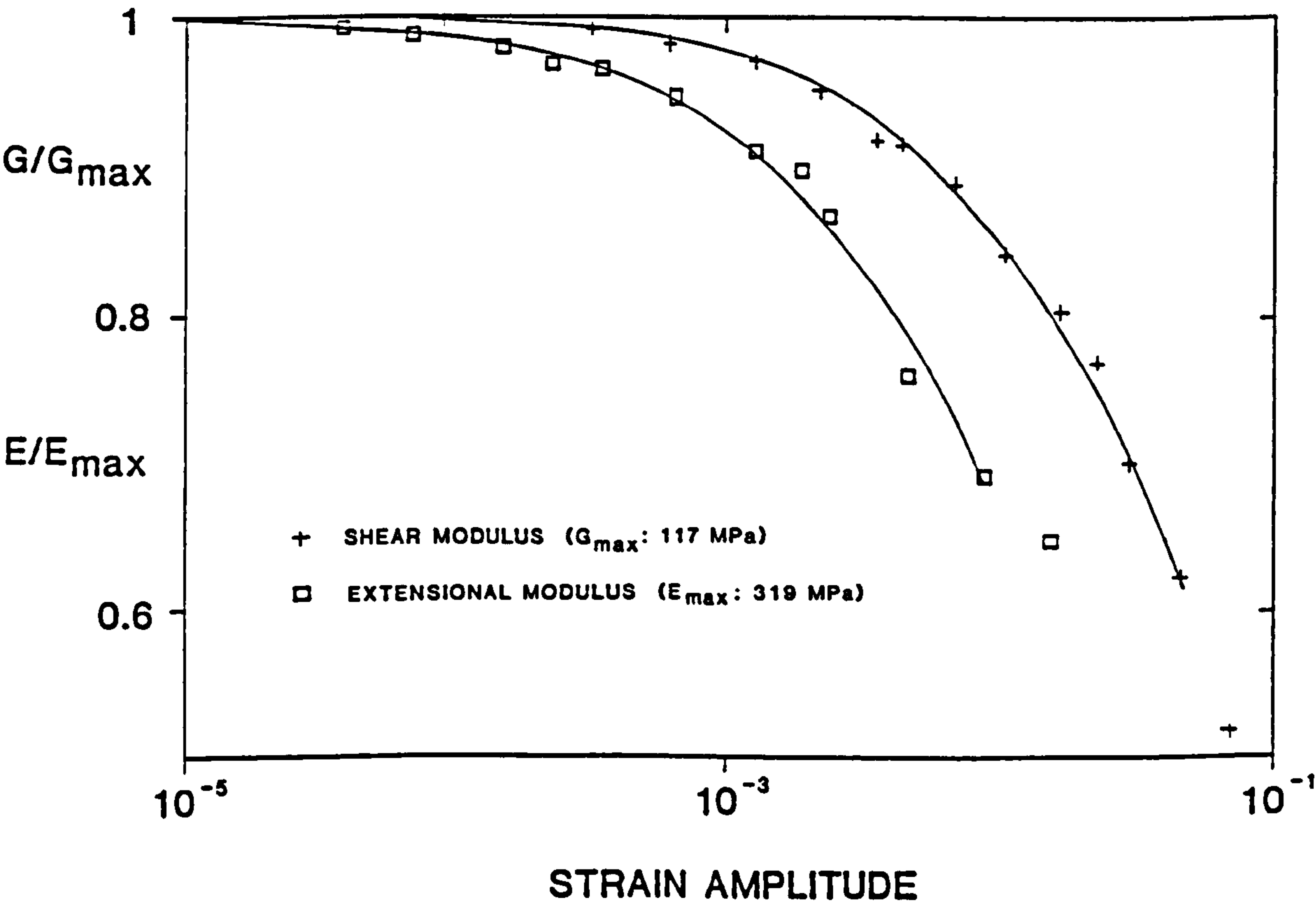
In principle the longitudinal results should be similar to the shear results. However, the sample "sticking" problem encountered in the resonance tests (5.4.1) was still present for the data collected at low-strain amplitudes in these tests; giving excessively high values for E and low values for D_E . This problem appeared to disappear at higher strain amplitudes as the sample became "shaken free" (Bennell, personal communication), whereupon it follows the expected behaviour of a smooth decrease in E and increase in D_E . Therefore, when extrapolating back to obtain a low-strain amplitude value of E , this "sticking" problem must be accounted for (Bennell, personal communication). Smooth lines are fitted through the E and G data, at high strain amplitudes, allowing for a corrected extrapolation of E_{\max} (see Figure 5.10). Some E and G points are taken off these lines, at equal strain amplitudes, are given in Table 5.5.

No such "sticky" problems were found for the sand sample (SAND 2) from Site 4. The experimental E and G values for this sample show the normal dependence on strain amplitude (Figure 5.11). Smooth lines are fitted through the data and equal strain amplitude E and G data are shown in Table 5.6.

Table 5.6 High strain amplitude E and G results: SAND 2, Site 4
(at an effective stress of 100 kPa)

Strain amplitude	E (MPa)	G (MPa)	ν_b	ρ kg/m ³
(1).10 ⁻²	229.3	101.0	0.14	1580
(3).10 ⁻³	270.4	108.8	0.24	1580
(1).10 ⁻³	294.1	113.3	0.30	1580
(3).10 ⁻⁴	309.0	116.0	0.33	1580
(1).10 ⁻⁴	315.3	116.5	0.35	1580
(3).10 ⁻⁵	317.8	117.0	0.36	1580

Figure 5.11 High strain amplitude E and G results for sample
SAND 2, Site 4 at an effective stress of 100 kPa



5.6.2 Calculating the elastic constant ν_b for samples from Sites 1, 2 and 4

As discussed in 5.1, two elastic constants are required to describe the elastic properties of the "frame" of a sediment or rock. So far, usable data for the elastic constant G_{\max} have been presented for sediments from Sites 1, 2 and 4 at different effective stresses (5.4.3 and 5.4.4). Some fair data have been presented for the elastic constant E_{\max} for a sample at Site 4 at different effective stresses (5.4.1), and some poor data for E_{\max} for samples at Site 1 have also been given (5.4.1). Additionally, some data for the variation of E and G with strain amplitude have been presented for one sample from Site 1 and one from Site 4 (5.6.1).

It would appear that G_{\max} has been fairly well characterised for the sediments from Sites 1, 2 and 4. Further, if the good quality E or E_{\max} data is selected from the remaining experimental results, then the elastic properties of the frame of these sediments could be defined. One good way to test if the E or E_{\max} results lie within the bounds of reason is to calculate the frame Poisson's ratio (ν_b) from E (or E_{\max}) and G (or G_{\max}). For a non-fluid, the frame Poisson's ratio has the limits $0 < \nu_b < 0.5$, and any calculated value outside this range is physically unacceptable. If reasonable values for the frame Poisson's ratio (ν_b) are calculated, then the frame bulk modulus (K_b) can be simply calculated from ν_b and G (see Appendix 2):

$$\nu_b = \frac{E}{2G} - 1 \quad 5.6$$

$$K_b = \frac{2G.(1 + \nu_b)}{3.(1 - 2\nu_b)} \quad 5.7$$

Note that the "frame" Poisson's ratio (ν_b) and the "frame" bulk modulus (K_b) of a sediment are different quantities to the Poisson's ratio (ν) and the bulk modulus (K). The latter quantities are properties characterised by "undrained" deformation of sediments. The bulk modulus of sediments (K), will always exceed the bulk modulus of the saturating pore-fluid: so for soft, water saturated sea-bed sediments (1) $K > K_f \gg G$. However, the "drained frame" bulk modulus (K_b) is considerably smaller than K_f for soft sea-bed sediments and will typically lie within the range (2) $2G/3 < K_b < 5G$. Therefore, using inequality (2) in equation 5.7 gives $0 < \nu_b < 0.4$, and using inequality (1) in equation 5.7 (substituting K for K_b and ν for ν_b) gives $\nu > 0.48$. It is useful to note that ν is close to 0.5 for most soft sediments (Davis and Schultheiss, 1980), while ν_b takes on a value less than 0.4 for the same type of sediments.

Tackling the suspect E_{\max} data for Site 4 (see Table 5.2), it can be seen that $(E_{\max}/2G_{\max}) > 1.5$ for all the samples, therefore ν_b will always be physically unacceptable. If the better E_{\max} data for Site 1 are considered, then the ν_b values are all reasonable (see Table 5.1). Also, the E and G data for Site 4 give sensible values for ν_b (see Table 5.6). However, the G and corrected E data from Site 1 do not all give physically acceptable values for ν_b (see Table 5.5), although using the corrected E values give calculated ν_b values nearer the bounds of reality. It is important to note ν_b (equation 5.6) is very sensitive to small uncertainties in the values of E and G . Therefore, calculated ν_b values which lie just outside the physical limits of acceptability may be due to subtle errors in E or G .

As there are no E (hence ν_b data) for Site 2, and that the ν_b values for Site 1 are mostly physically unacceptable, the (reasonable) ν_b values for Site 4 will be assumed to hold for Sites 1, 2 and 4 - with the assumption that the variation between the elastic properties of each site

is characterised by the differences in G_{\max} alone. There appears some justification in equating the elastic properties of some samples; the similarity of the G_{\max} behaviour of the carbonate sample from Site 1 and the sand sample of Site 4 (see Figure 5.6) is striking. The extension of the applicability of ν_b from Site 4 to Site 2 can be argued as the carbonates at Site 2 are similar to the carbonate sample from Site 1. The extension to the other samples at Site 1 can only be justified through the lack of any reasonable ν_b data for these samples.

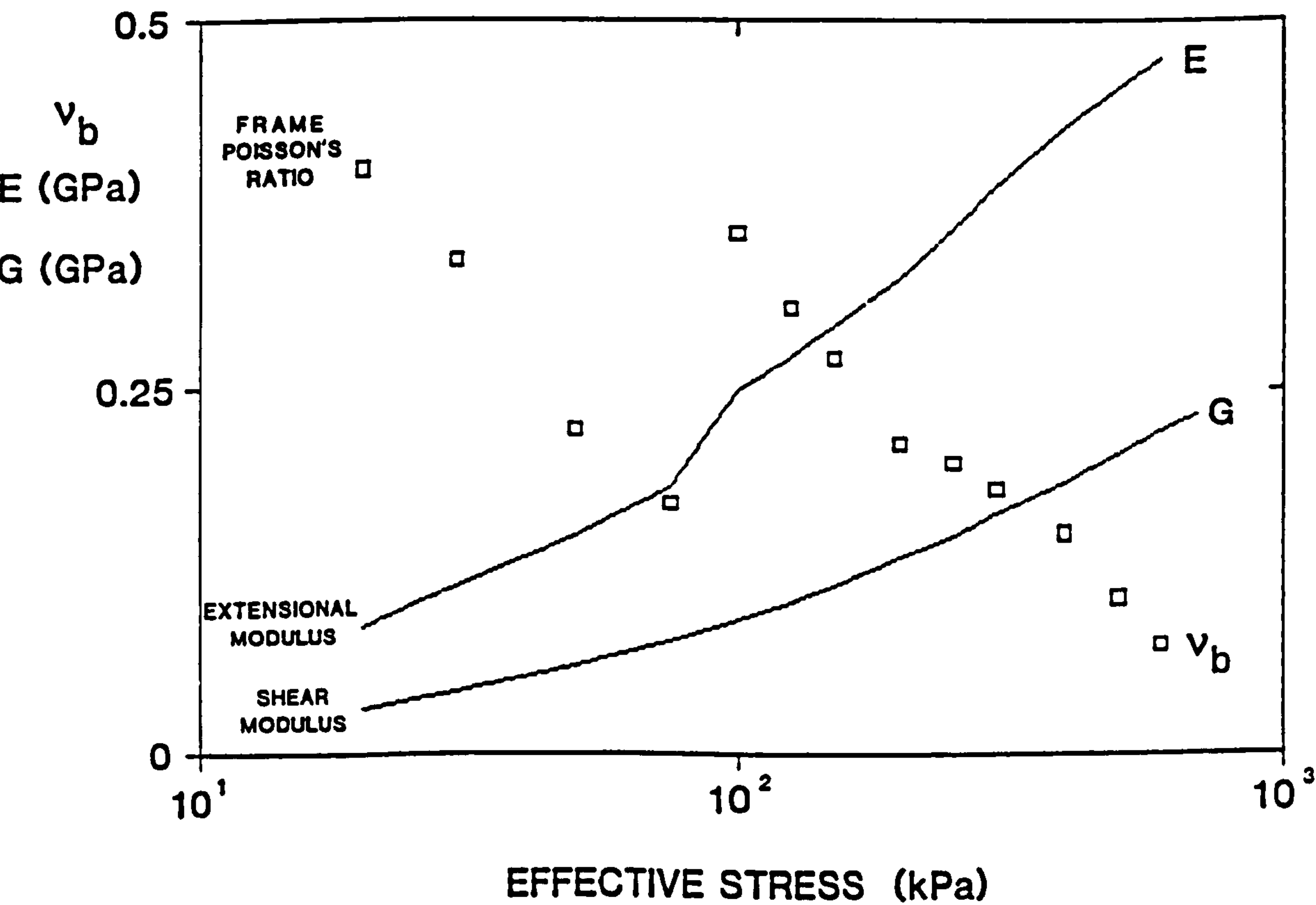
The task of finding a second elastic constant for Sites 1, 2 and 4 is therefore reduced to sensible interpretation of the ν_b data from Site 4. Values of ν_b calculated from the high strain amplitude E and G results given in Table 5.6 are shown in Figure 5.11. It would appear that ν_b tends to a low-amplitude value of around 0.36 at 100 kPa. Next, the ν_b values calculated from E_{\max} and G_{\max} (Table 5.1) are shown in Figure 5.12. These results appear to show a trend of decreasing ν_b with increasing effective stress, with a jump in the data at 100 kPa. The jump in ν_b is caused by the jump in E (incidentally, this shows the sensitivity of calculated ν_b on small changes in E), which was probably due to an accidental change in the sample's properties (due to some knock etc) during experimentation. Also shown on Figure 5.12 are the span of high amplitude data. It must be a coincidence that the E_{\max} result from Table 5.1 and the low amplitude E result from Table 5.6 both have $\nu_b = 0.36$: they were obtained on slightly different sand samples and the low amplitude E result may have been different if the experiment had run smoothly.

So, narrowing down the choice of E and ν_b data to those presented in Figure 5.12, still does not give a clear definition of ν_b versus effective stress for Sites 1, 2 and 4. For most purposes, ν_b will be required for effective stresses up to 100 kPa, which roughly translates to sub-bottom depths up to 20 metres (see 10.2.2). Therefore, an average

value of $\nu_b = 0.3$ is calculated from the E_{max} and G_{max} data from Site 4 over this effective stress range. A value of $\nu_b = 0.3$ gives $K_b = 2.17G$ (equation 5.7).

It is assumed that this value of $\nu_b = 0.3$ holds for the sediments from Sites 1 and 2. The influence of the exact value of ν_b in hydrodynamic and acoustic deformations of the sea-bed at Sites 1 and 2 is addressed in Chapters 9, 10 and 11 allowing the relative importance of this crude approximation of ν_b to be tested. The only case where a value of ν_b is required at effective stresses greater than 100 kPa is for the analysis of the carbonate sediments from Site 2 (see Chapter 11). For this case it is interesting to note that in a similar analysis of acoustic propagation in carbonate sediments Ogushwitz (1985) chose a constant value of $\nu_b = 0.3$ in his calculations.

Figure 5.12 Frame Poisson's ratio, Emax and Gmax results versus effective stress for sample SAND 1, Site 4



5.7 Summary

The shear modulus (G) of soft deep-sea sediments can be determined using bender transducer techniques, providing that the received signals are interpreted correctly. Criteria have been established to interpret received signals in a consistent fashion and G was obtained for different sediments from a number of sites. The bender transducers were mounted in a resonant column cell, which allowed G to be determined simultaneously and independently from resonance techniques. A favourable agreement was found for the G measurements between the techniques. This suggests that bender techniques can be used in a routine way to obtain G with some degree of confidence.

Measurements of the shear modulus obtained from laboratory resonant column and bender transducer methods were compared with in-situ determinations of G at Site 1 (Great Meteor East, N Atlantic Ocean). The in-situ determinations were obtained in an inverse way from Stoneley wave experiments (Whitmarsh and Lilwall, 1982) and from the tidally-induced pore-pressure boundary problem introduced in Chapter 3. The laboratory measurements of G for surficial sediments were up to a factor of 4 less than the in-situ determinations. This was attributed partially to disturbance during the coring and recovery process for the laboratory samples (reducing G), and to the inherent uncertainties in the inverse in-situ methods. With no simple reconciliation of the differences, both in-situ and laboratory G measurements are used in a specific case study at Site 1 (10.4), and the importance of these differences in G are assessed.

Results from low strain-amplitude torsional resonant column tests showed that the deep-sea sediments tested all behaved anelastically. However, the anelastic behaviour was only fairly well characterised by a band limited constant Q (BLCQ) model of the sediments. As only a reasonable fit between BLCQ predictions and experimental measurements was

obtained, it was not possible to define a frequency dependent anelastic shear modulus \hat{G} with confidence. Furthermore, experimental frictional problems during low-strain amplitude tests meant that neither E or \hat{E} could be determined for the soft deep-sea sediments tested.

High strain amplitude torsional experiments on deep-sea sediments showed degradation of the shear modulus occurring at strain amplitudes of around 10^{-3} . At these high strain levels, the frictional problems encountered in the low strain amplitude extensional tests were overcome. However, the high strain amplitude E and G measurements were of limited use when E and G were combined: they often yielded physically unacceptable values of the frame Poisson's ratio ν_b . Therefore, no useful E (hence ν_b and K_b) measurements were obtained on the deep-sea sediments tested.

It is essential to have a sensible determination of ν_b for any study involving poroelasticity (Chapter 2). Successful low amplitude resonance tests giving both E and G were performed on a marine sand sample. Combining E and G from these results gave an average value of $\nu_b = 0.3$ for effective stresses up to 150 kPa. In absence of reliable ν_b measurements for the deep-sea sediments, they were assigned a value of 0.3, leaving the intrinsic differences between samples to be characterised by variations in the shear modulus alone. A value of $\nu_b = 0.3$ gives $K_b = 2.17G$. Therefore, the task of characterising the frame moduli of deep-sea sediments has been simplified to determining G from bender transducer techniques and calculating K_b assuming $\nu_b = 0.3$. Some G results from Sites 1 and 2 presented in this chapter are used in later analysis (Chapters 10 and 11). The G and K_b results for the marine sand from Site 4 are used in Chapter 6.

The studies investigating the available methods for determining the frame moduli of sediments in this chapter have followed similar investigations for the permeability (k_a , Chapter 4). These experimental

studies were prompted by the analysis of Chapter 3, which showed that K_b , G and k_a were important in a quasi-static boundary value problem solved using Biot's theory. The next step in isolating the important aspects of Biot's theory is to examine dynamic deformations where other variables in addition to K_b , G and k_a come into play. In Chapter 6 the character of Biot's slow wave is investigated. In Chapters 7 and 8 the parameters influencing Biot fast wave velocity and attenuation predictions are studied. After these three chapters, the parameters important to dynamic deformations can be identified allowing the construction and use of practical geoacoustic and hydrodynamic models (Chapters 9, 10 and 11) at Sites 1 and 2.

6.1 Introduction

Biot's theory has been successful in predicting the quasi-static consolidation behaviour of soils (Biot, 1941, Rice and Cleary, 1976) and it has also been applied to various low frequency harmonic problems (see Chapter 3). It is of interest to investigate if the theory still holds at higher (acoustic - ultrasonic) frequencies. Three diagnostic phenomena will occur if Biot's theory holds: viscous-flow dispersion of the fast wave (see Chapter 7); viscous-flow attenuation of the fast wave (see Chapter 8), and the existence of a propagative slow compressional wave. Attenuation and dispersion may be due to many reasons (see Chapter 5), but the existence of the slow wave can only be explained by Biot's theory.

The fast wave is the compressional wave which is normally observed in fluid saturated poroelastic media. The slow wave remained an elusive phenomenon in water saturated porous media until Plona's (1980) observations in sintered porous materials. Soon after, Berryman (1980) heralded these results as confirmation of Biot's theory. However, in the field of absorption of sound by air-saturated porous media, experimental existence of the slow wave has been documented for many years (see review by Attenborough, 1982). Interestingly, for this latter case it is the fast wave which is difficult to measure.

Neither of the observations of the slow wave outlined by Plona (1980), or Attenborough (1982), pertain to water-saturated natural sediments. Although there have been some tentative observations of the propagating slow wave in natural sediments (Patterson, 1956, Schultheiss, 1981), there is no overwhelming evidence to prove its existence. There also remain some misconceptions in visualising what the slow wave is. Perhaps the slow wave has become elusive because the most appropriate type of measurements required to detect it are not being made?

It is of interest to attempt to follow up the experiments of Patterson (1956), Plona (1980) and Schultheiss (1981) to see if any experimental insight into the slow wave can be gained. Furthermore, it is worthwhile attempting to study Biot's theory to see if any light can be shed on the physical character of the slow wave. Should a straightforward method be obtained to measure the slow wave, then it would be a useful acoustical probe supplementing the information obtained from fast compressional and shear waves.

6.2 Previous studies involving Biot's slow wave in unconsolidated fluid saturated natural sediments

6.2.1 Features of Biot's slow wave

Through various numerical examples, Biot (1956 a,b) realised that the slow wave would suffer from very high attenuation. This attenuation increases as the frequency approaches the characteristic frequency (f_c) - where Biot's viscous flow mechanism is most apparent:

$$f_c = \frac{\phi \eta}{k_a 2\pi \rho_f} \quad 6.1$$

In addition, the slow wave is diffusive in nature until the characteristic frequency is reached, whereupon it becomes propagative. Cleary (1980) noted that the propagative slow wave would be best observed within a very narrow frequency band: large enough to be greater than the critical frequency, but not too large to give massive attenuation.

Another very important factor which controls the amplitude of the slow wave is the stiffness of the frame of the poroelastic material in which the wave is propagating. Johnson and Plona (1982) showed that for very stiff (almost rigid) poroelastic materials, the pore fluid becomes completely uncoupled from the frame. In this case, the fast wave

propagates through the frame of the poroelastic material, and the slow wave propagates through the fluid infiltrated channels within the material. In this way, they interpreted Plona's (1980) observation of the slow wave as a "fluid wave". Conversely, Johnson (1982) showed that for a poroelastic material with a very weak frame (nearing a suspension), such as a gel, that the slow wave travels through the frame of the gel.

For the case of an unconsolidated sediment of intermediate frame stiffness, the frame and pore fluid do not completely decouple. The slow (and fast) waves cannot therefore be viewed as simply frame and fluid waves, but they will propagate due to deformations of both frame and pore-fluid. However, it may be that the slow wave resides more within the frame than in the pore-fluid. At this stage of the argument this question remains unanswered.

6.2.2 Experimental observations of the slow wave in unconsolidated sediments?

There have been very few reported observations of the propagating Biot's slow wave in water saturated poroelastic materials. This is not entirely surprising as the slow wave suffers severe attenuation: it arrives after the fast (and sometimes the shear) wave and therefore is interfered with by the signal from these waves.

Plona (1980) observed the slow wave propagating through a fluid-saturated sintered glass bead block. He used a refraction method to isolate the fast, shear and slow waves passing through the block (see 6.3.5). The frequency used was 500 kHz, which puts it neatly within the required frequency band for this material. Also the sintered glass bead material is virtually rigid, so the slow compressional wave is a decoupled fluid wave.

Patterson (1956) reports two compressional waves propagating within a confined unconsolidated fluid saturated sand. His observations were made at 50 kHz, which lies within the desired frequency band, and his results show the arrival of two distinct events recorded on an oscilloscope. The first event Patterson calls a fluid wave and associates it with the normal fast wave. The later event, which is of equal amplitude and half the frequency of the first event, Patterson calls a frame wave (this is an unfortunate misnomer which has been propagated through the literature). Cleary (1980) links Patterson's (1956) frame wave to Biot's slow wave. However, attempts to repeat Patterson's experiments have not been successful (Taylor-Smith, personal communication), and verification of Patterson's results are still lacking.

Schultheiss (1981) carried out shear wave experiments in sands at 10 kHz using bender techniques. He observed three distinct events which could be separated in terms of arrival time and frequency. He associated the first and last events with the fast and shear waves, and, taking Patterson's (1956) lead, tentatively associated the other event with a frame wave.

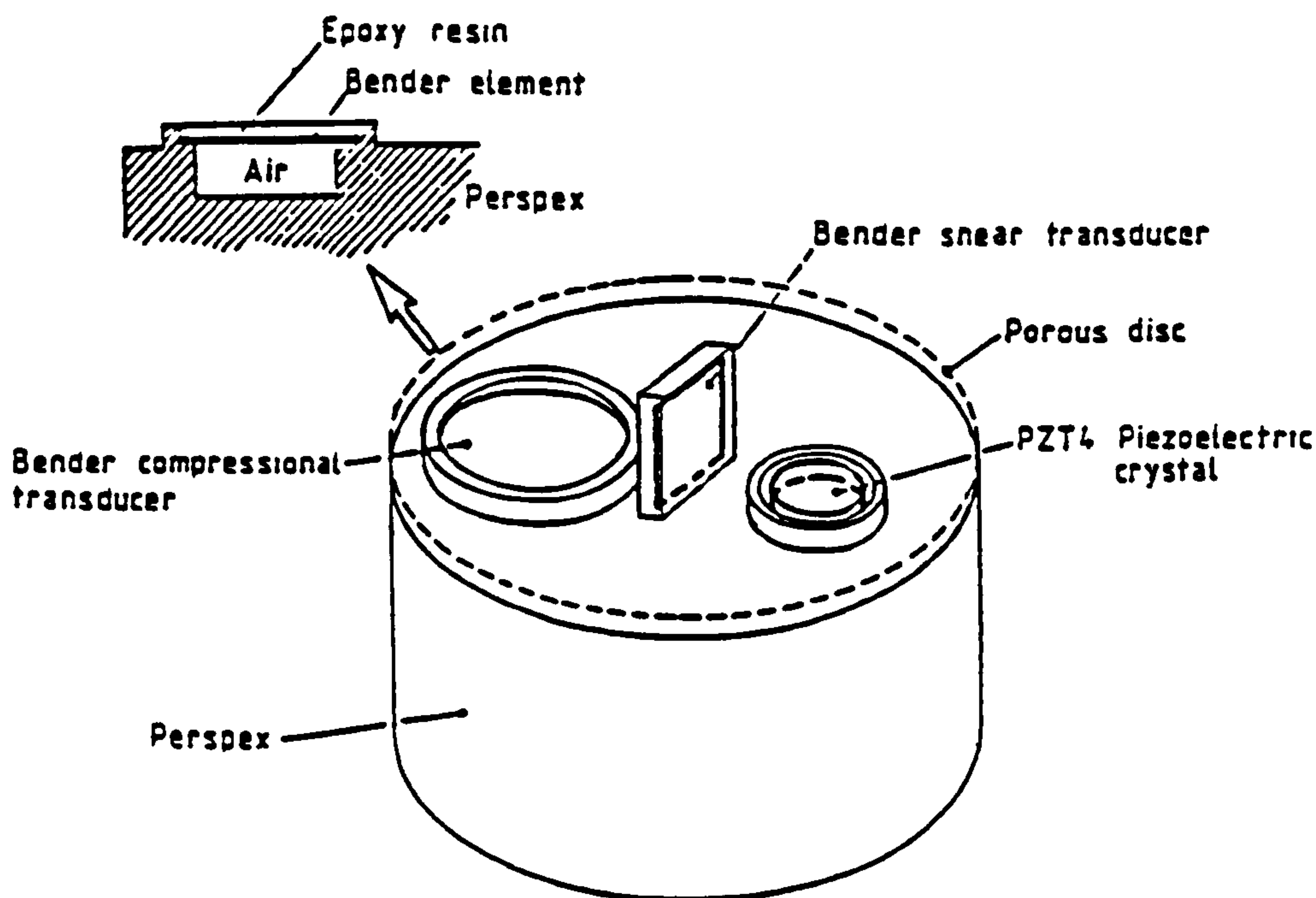
A closer examination of similar shear mode bender experimental data (Chapter 4) has shown that this other event can also be detected in fluids - therefore it has nothing to do with a frame wave. However, Schultheiss' work (1981) showed that the shear mode bender techniques were ideal for coupling much energy into the frame of an unconsolidated sediment. Therefore, bender element materials mounted in a compressional mode would be a suitable choice for coupling compressional energy into the frame of an unconsolidated sand. Using this idea, attempts were made to see if Biot's slow wave could be associated with a frame wave, with the frame wave being produced by compressional mode bender transducers (see 6.3).

6.3 Experimental attempts to detect Biot's slow wave

6.3.1 Design of a new compressional mode bender transducer

If Biot's slow wave can be thought of as a frame wave in unconsolidated fluid saturated sediments, then a transducer which is well coupled to the frame of the sediment would transfer most energy into this mode. If such a transducer were to be abbuted against a sediment sample then two design criteria require consideration. The major criterion is that the compliance of the transducer is closely matched to that of the sediment - a feature which is evident in shear wave bender element studies (Schultheiss, 1981). A second criterion is that free drainage should be allowed around the face of the transducer to maximize the relative motion of the frame to the fluid. With these points in mind, a new transducer was made up by mounting a bender element in a compressional mode within a triaxial end-cap (Figure 6.1). This transducer was mounted alongside a shear mode bender transducer and a conventional 500 kHz compressional wave transducer (Figure 6.1).

Figure 6.1 Triaxial cell end-cap modified to contain shear and compessional mode bender transducers



6.3.2 Experimental set-up for using the new compressional wave transducer in sand, at different effective stresses

Some initial experiments on a sand sample from Site 4 were undertaken using the new compressional transducer. A rubber membrane was fitted around the lower triaxial end cap and filled up with dry sand. The top cap was then placed on top of the sand column, the transducers were aligned, and the membrane fitted around the top cap. The sample was then placed within a triaxial cell, saturated with water, subjected to a back pressure of 200 kPa, then placed under a small effective stress. This part of the sample preparation is virtually identical to the preparation for the sand sample used in the resonant column cell (see 5.2.3). By varying the back pressure and confining pressure, the sample could be subjected to effective stresses of up to 600 kPa.

The transducer leads from top and bottom end caps were connected to a switch box allowing any one set to be used. The shear or compressional mode bender transducers were driven by the rising edge of a 10 V square wave. The conventional compressional transducer was driven by a 240 V spike. The received signal was passed through an amplifier and a filter, then displayed on the time base of a digital oscilloscope which was triggered by the rising edge of the square wave. Arrival times of events on the time domain were obtained from the calibrated digital display. Velocities of events were calculated, after electronic delay times had been corrected for, by using the transducer separation and the interpreted arrival times.

A typical time domain signal of the new compressional wave transducer in sand from some preliminary experiments is shown in Figure 6.2. The first portion of the signal is greatly distorted by electronic pick-up. This distortion initially could not be removed, and was ignored (this was a poor judgement, as it can lead to some misinterpretation of subsequent experimental results - as discussed in 6.3.3 and 6.3.4).

Figure 6.2 Typical received signal from the compressional mode bender transducer

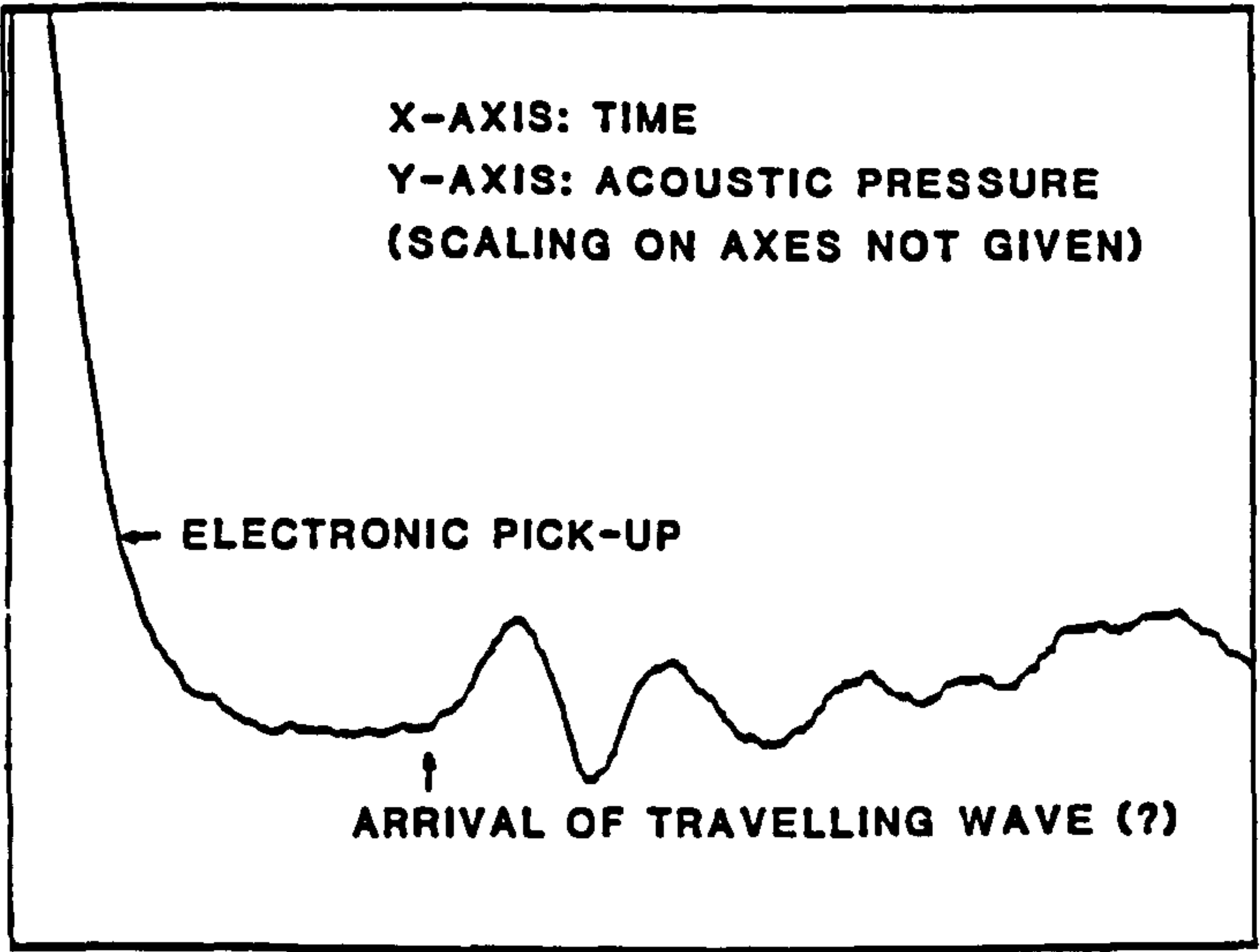
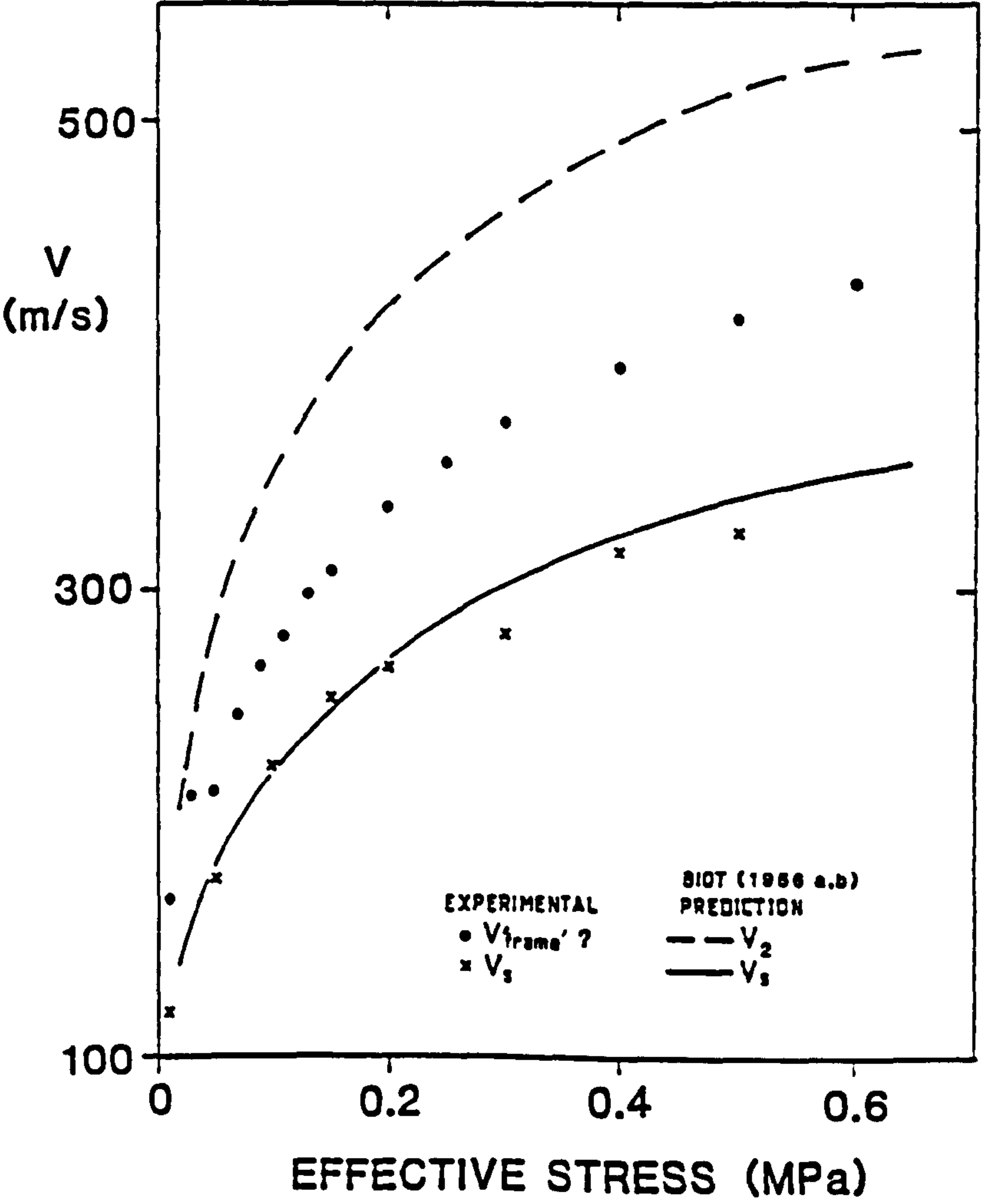


Figure 6.3 Experimental "frame" and shear wave velocities and predicted shear and slow wave velocities versus effective stress, sand sample Site 4



6.3.3 Some initial results using the new transducer in saturated sand at different effective stresses

Some initial experiments were carried out using the new compressional transducer in saturated sand at different effective stresses. Received signals were similar to those shown in Figure 6.2, and the onset of a sinusoidal wave-train arriving after the decay of the electronic pick-up was interpreted as the onset of a travelling wave. The travel time for this event was recorded and its velocity was calculated. Temporarily, this velocity will be denoted V_{frame} - implying an association with a compressional wave travelling through the frame.

Shear wave velocities and compressional wave velocities (using the conventional transducers) were also calculated. The measured results of V_{frame} and V_s in the sand, at different effective stresses, are shown in Figure 6.3. Also shown are predictions of the shear velocity (V_s) and the slow wave velocity (V_2) obtained from Biot's theory. The input parameters for the predictions are given in Table 6.1 and are based upon other experimental data collected on similar sand samples from Site 4.

Table 6.1 Physical parameters characterising data set SAND_M1

1. Porosity	0.42
2. Fluid density	1000 kg/m ³
3. Grain density	2670 kg/m ³
4. Fluid modulus	(2.0).10 ⁹ Pa
5. Grain modulus	(5.0).10 ¹⁰ Pa
6. Dynamic viscosity	0.001 Pa.s
7. Circular frequency	2 π .10 ⁴ Hz
8. Shear modulus	(3.8).10 ⁷ to (2.7).10 ⁸ Pa
9. Frame bulk modulus	2.17 G
10. Permeability	(4.2).10 ⁻¹¹ m ²
11. Pore radius	(4.3).10 ⁻⁵ m
12. Tortuosity	1.36
1-6,10,12	Lovell and Ogden (1984)
8,9	from from Table 5.1
11	Hovem and Ingram (1979)

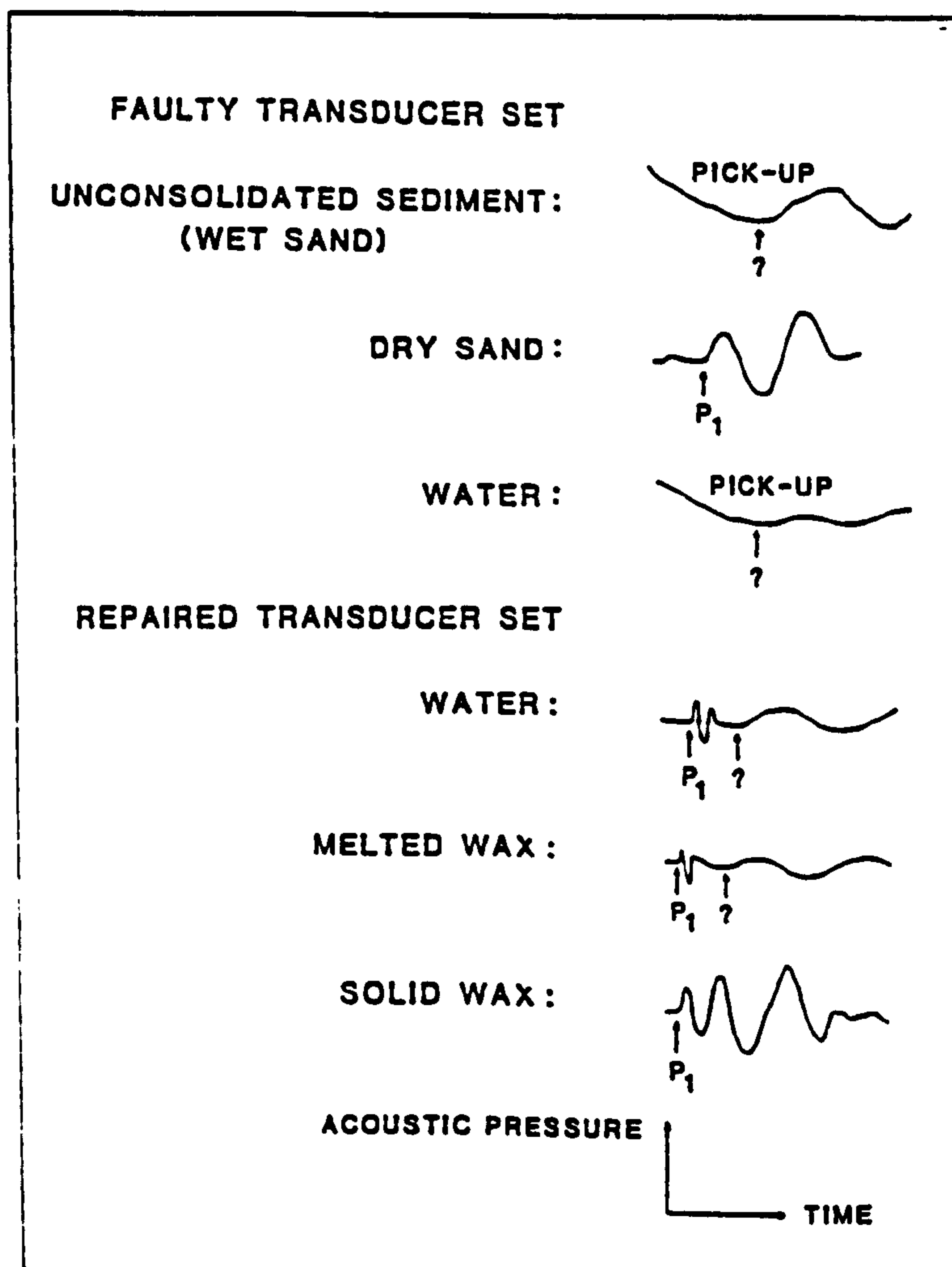
There appears to be a good fit between the experimental and predicted shear wave velocities. Further, the predicted slow wave velocity V_2 and the V_{frame} event do not appear too dissimilar. However, there are some flaws in drawing a direct comparison. Firstly, the compressional mode bender transducer should be expected to produce a very high amplitude fast compressional wave - in addition to a possible frame wave. This fast wave component would be expected to interfere destructively with any later event. Secondly, the predicted attenuation of the slow wave is over 40 dB/m, which means that the pressure of the slow wave will decay to less than 2% of its initial amplitude over the 100 mm path length within the sample. Also, the fact that the compressional mode bender transducer may be producing energy coupled as a shear wave must not be overlooked. Therefore, before concluding that the V_{frame} event is linked to Biot's slow wave, a more detailed study of the character of the received signal must be undertaken, along with a verification that Biot's slow wave does propagate predominantly through the frame of an unconsolidated sediment. These points are looked at in 6.3.4 and 6.4.

6.3.4 Experiments using the compressional mode bender transducer in different media

A major problem with the results from the compressional mode bender transducer presented in 6.3.3 is that significant information may be obscured by the electronic pick up at the start of the signal. The origin of this pick up was found (accidentally) to be due to an electronic short within the transducers caused by water seeping into the air-filled compartment behind the transducer face (Figure 6.1). This fault was repaired by re-sealing the bender element with a new layer of epoxy resin. This repair had a dramatic affect upon the types of signals received by the compressional mode bender transducers in different media.

Some results of the received signals from the faulty and repaired transducer sets are shown in Figure 6.4. In unconsolidated saturated sands and in water the faulty set give the familiar signals with a large amount of electronic pick up. However, when this is removed in the repaired set, the signal for water is very revealing. It shows that there is a high frequency early event which is superimposed upon a lower frequency reverberation. Therefore, this lower frequency event has nothing to do with any "frame" (as water is a pure fluid!), so any linking of this type of feature with a frame wave, or Biot's slow wave, as suggested in 6.3.3 is wrong.

Figure 6.4 Received signals from faulty and repaired compressional mode bender transducer sets in different media

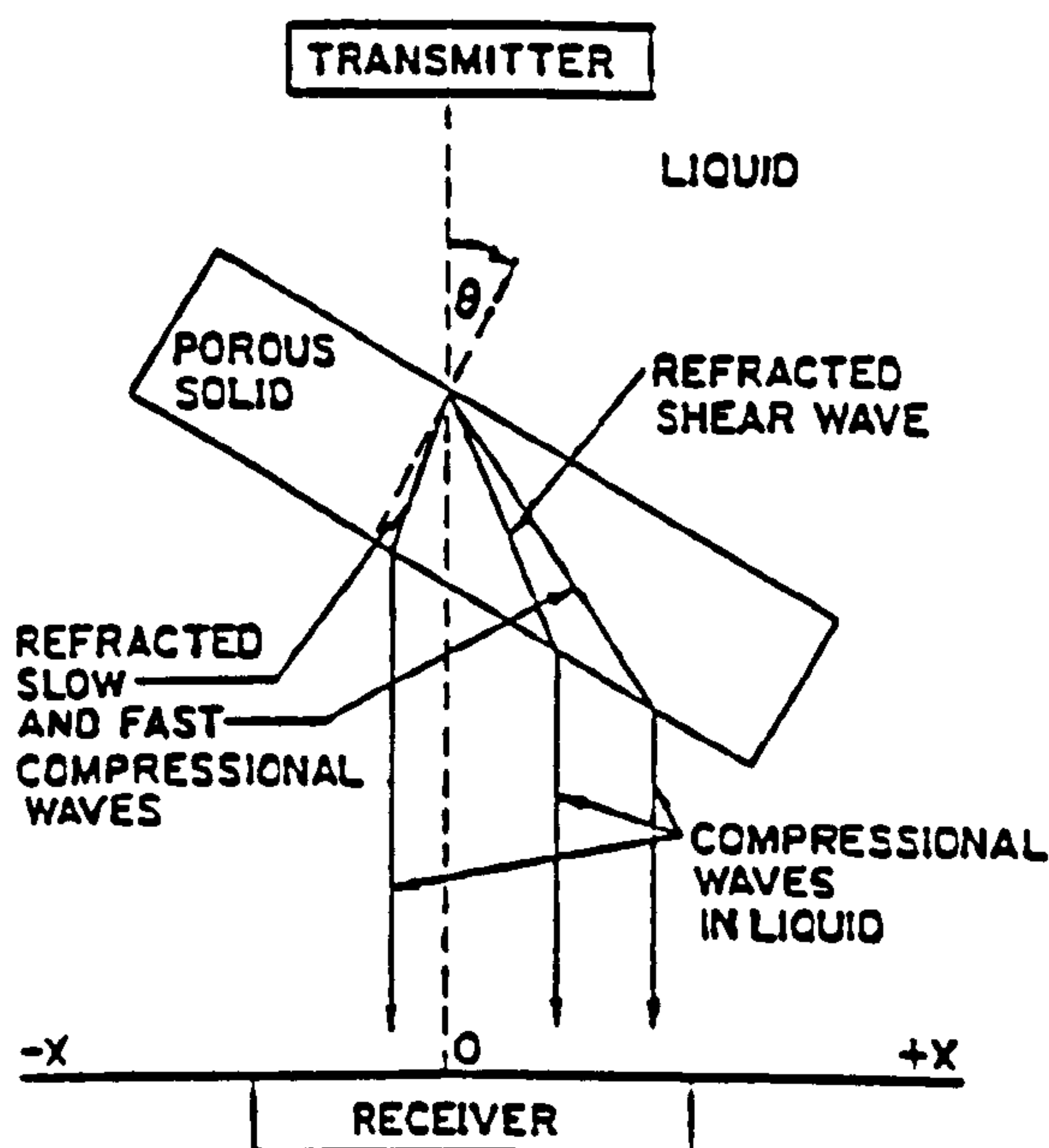


6.3.5 Problems with attempts to detect Biot's slow wave in unconsolidated sediments

The unsuccessful attempts to detect Biot's slow wave using a compressional mode bender transducer described above highlight some of the problems of detecting this wave. Although the compressional wave transducer operates within the correct frequency band (near the critical frequency), the problem of isolating the slow wave component from the fast compressional wave and shear components (present in any received signal) is evident. This is compounded by the small amplitude of the (highly attenuated) slow wave which requires resolution.

An ideal way of separating the fast, slow and shear wave components of a signal passing through a porous medium is described by Plona (1980). A schematic diagram of Plona's (1980) refraction experiment is shown in Figure 6.5. Attempts were made to first repeat Plona's observations of a slow wave in a sintered glass bead block, with thoughts of extending the principle to unconsolidated sediments. A similar experiment to Plona's (1980) was set-up using his sintered glass block.

Figure 6.5 Schematic diagram of Plona's (1980) slow wave refraction experiment



Unfortunately, the signals obtained from these experiments were far more noisy and unclear in comparison with Plona's. This was probably due to the poorer quality transducers used in the experiment which had poorer directivity and sensitivity than Plona's. Also, problems were encountered in fully saturating the glass bead block in a non-back pressured system. Some attempts were made to try the experiment upon unconsolidated sand samples (which were confined within a thin metal box), but with no success.

The experimental problems discussed so far were compounded by an ignorance of the physical character of the slow wave in unconsolidated sediments. The premise that the slow wave can be linked with some kind of frame wave, was not verified by the experimentation described in 6.3.1 to 6.3.4. A better idea of the physical character of the slow wave would be given by obtaining general solutions for the pore pressure and the total stress. If the magnitude of the slow wave contributions to the pore pressure and total stress can be assessed, then it would be possible to determine whether the slow wave resided mainly in the frame or in the fluid of the sediment. This would allow the design of more appropriate experiments to detect the slow wave.

6.4 General solutions and a boundary value problem for a propagating slow wave

6.4.1 Explicit form of a general solution for propagating slow waves

In principle it should be possible to obtain an explicit form of the general solutions for the primary variables (u , U , p and σ) at all frequencies. Such a solution was obtained in Chapter 3 for low frequencies, where the slow wave is diffusive and is uncoupled from the fast wave. However, great problems arise if attempts are made to extend this analysis to higher frequencies where the slow wave becomes propagative.

At low frequencies the assumption^{is} that the slow wave resides purely in the fluid. This is because all fluid-flow is left to the slow wave, as no fluid-flow occurs for the fast wave (see equation 3.10). However, at higher frequencies fluid-flow occurs for the fast wave also (which is verified if higher frequency solutions for \hat{z}_j are substituted in 3.9). Without this simplification (equation 3.10), explicit definition of the general solution for the primary variables at high frequencies is difficult, but at least possible in principle (Cleary, 1980). However, an alternative numerical approach of Mengi and McNiven (1976) can offer some insight into the physical nature of the slow wave.

6.4.2 Boundary problem of a fluid-filled porous medium subjected to a transient input

Mengi and McNiven (1976) used approximate numerical methods to predict the pore pressure and total stress induced in a fluid-filled porous medium which was subjected to a transient input. This problem is essentially similar to the tidal-cycle boundary problem addressed in Chapter 3, but is significantly more difficult as the fast and slow waves are not decoupled. Without any attempt to repeat Mengi and McNiven's analysis, it is of interest to study their results to observe the role of the fast and slow waves on the pore pressure and total stress induced in the porous medium.

The case in question considered by Mengi and McNiven (1976) is shown in Figure 6.6. A transient ramp-shaped pulse is subjected to the frame of a poroelastic medium along the length of a freely drained plane boundary. As the pulse travels through the frame of the medium it will reach stations A, B and C (see Figure 6.6) at different times, and will have changed shape slightly due to dispersion and attenuation effects.

However, the pulse does not travel through the frame of the medium alone, and induces a coupled response in the pore fluid - which is exhibited by variations in the pore pressure at each of the stations as the pulse passes them. If the shape of the total stress and pore pressure pulses at the different stations are examined, then it is possible to elucidate the relative character of the fast and slow waves.

Figure 6.6 Pore-pressure and total stress responses of a poroelastic medium subjected to a transient load (after Mengi and McNiven, 1976)

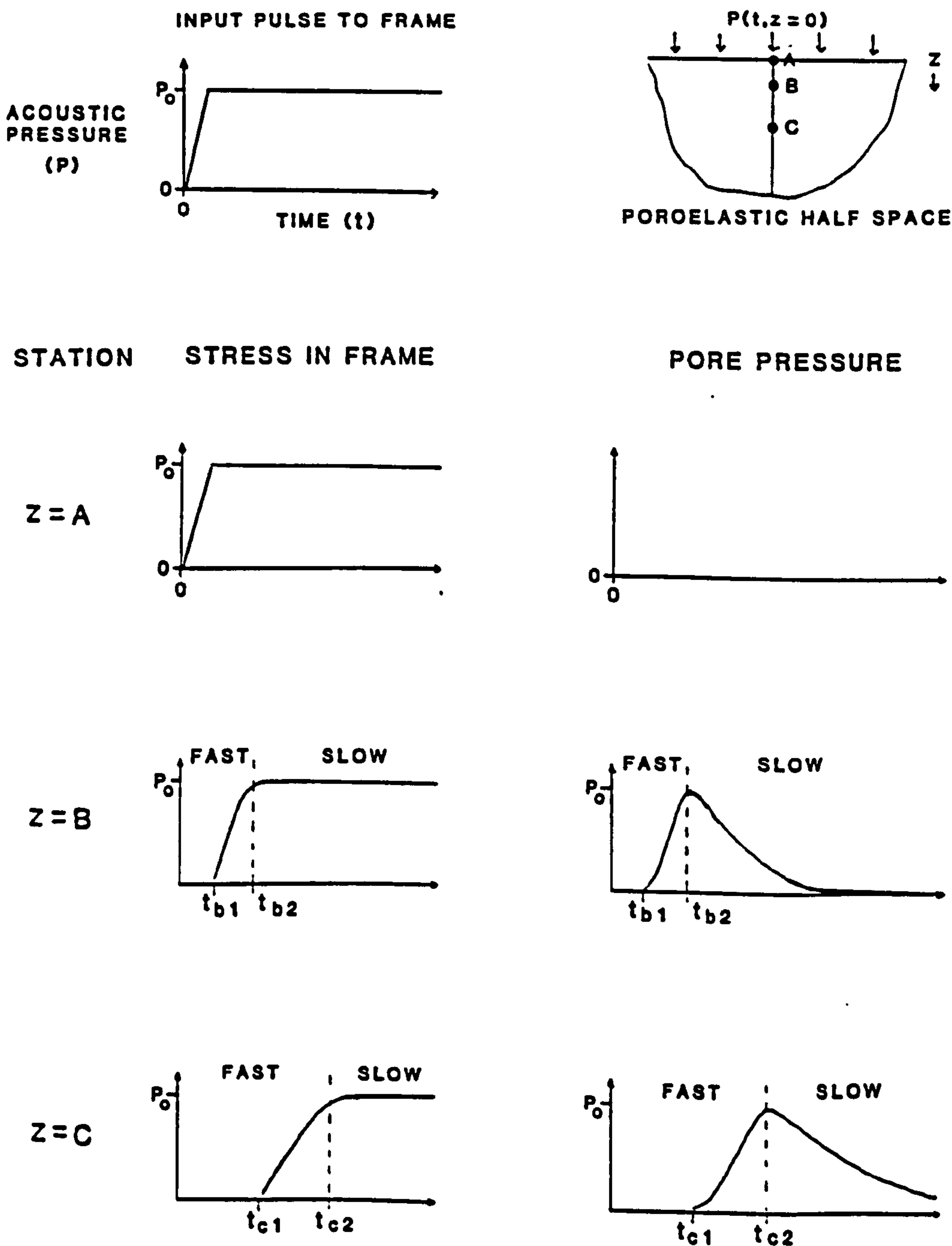


Figure 6.6 shows the results of Mengi and McNiven (1976) giving the shape of the total stress (σ) and pore pressure (p) pulses at each of the stations A, B and C. At station A, the stress in the frame is equivalent to the input signal and the pore pressure is zero - showing the free drainage at the interface. At station B, the shape of the σ pulse is slightly smoothed - due to attenuation of the higher frequency components and slight velocity dispersion along the time base. The p pulse at station B shows an increase in the pore pressure, followed by a very slow smooth decay. The p pulse at station B can be interpreted to consist of two components; a fast wave arriving at TB1, and an antiphase slow wave arriving at TB2. Similarly at station C, the σ and p pulses are smoothed and stretched out more along the time base. The p pulse at station C can be interpreted to consist of a fast wave arriving at TC1 and a slow wave at TC2.

If the interpretation of Mengi and McNiven's results given above is correct, then the following conclusions can be drawn: (1) the slow wave does not contribute significantly to the stress in the frame; (2) dispersion of the fast wave causes the time domain pore-pressure signal to be stretched; (3) the arrival of the slow wave is marked by a reduction in the pore pressure from a maximum peak; (4) the rate of this reduction depends upon the amplitude of the slow wave; (5) the slow wave amplitude decreases with increasing distance, (6) hence the pore pressure reduction is at a slower rate at greater distances from the boundary. Therefore, if the above interpretation is correct, the slow wave appears to reside mainly in the fluid and acts as a transient pore pressure release to the pressure developed by the passage of the fast wave. The fast wave causes stresses to be developed within the frame as well as the pore-fluid. The critical observation made above, that the slow wave does not contribute to the stress in the frame, was assumed by Cleary (1980) in similar studies.

6.4.3 On the question: is Biot's slow wave a fluid or frame wave?

There is little argument that Biot's slow wave is a propagative fluid wave in poroelastic materials with a stiff frame (Johnson and Plona, 1982). Further, at much lower frequencies in the stiff frame limit, the slow wave reduces to a diffusive pore pressure pulse (Chandler and Johnson, 1980). With sediments which are not at the stiff frame limit the slow wave is still a diffusive pore pressure pulse (Biot, 1941 and see Chapter 3). Therefore, the extension that the slow wave is a propagative fluid wave at higher frequencies within non-rigid sediments seems fair, by implication. This hypothesis is backed up by the failure of the experiments linking Biot's slow wave to a frame wave (6.3) and also by the interpretations of Mengi and McNiven's (1976) results (6.4.2). The exception to this hypothesis is offered by Johnson's (1980) claim that for very weak framed poroelastic materials (such as gels), the slow wave is a diffusive frame wave.

It appears that the propagative slow wave is dominated by the pore-pressures in the fluid and should not be linked with a frame wave in sediments and rocks. Therefore, the best way to detect a slow wave would be through a pore-pressure transducer and not a stress motion sensor coupled to the frame of the sediment. A similar conclusion was made by Cleary (1980).

6.5 Summary

The character of Biot's slow wave has been investigated. Initial assumptions that the slow wave was analagous to a wave travelling through the frame of a sediment were not substantiated by results from a new compressional mode transducer developed for this purpose. The results of Mengi and McNiven (1976), who obtained numerical solutions for a dynamic free-flow boundary value problem involving the slow wave, were examined.

Interpretation of these results led to the conclusion that the slow wave was dominated by pore-pressure induced flows of the fluid in a sediment, and should not be linked with a frame wave. The amplitude of the slow wave was shown to be greatest near the free-flow boundary of the sediment. The attenuation of the slow wave was shown to be large, rapidly diminishing the amplitude of the slow wave from its originally small value. It is unlikely that the slow wave would be propagated far through a sediment sample, and it would be very unlikely to be detected by a stress motion sensor abutted against the end of such a sample.

The small amplitude of slow waves, their rapid attenuation and their restriction to regions close to free-flow boundaries mean that they are of little interest to acoustical problems with long propagation distances and few interfaces. In the geoacoustical problems considered in Chapters 9, 10 and 11, the length scales of the problems mean that the slow wave is of little consequence and can be ignored. However, for other geoacoustical problems involving the reflection of acoustical energy from hard, high permeability sea-beds, the effect of slow waves will be similar those of "shear wave softening" of the sea-bed (see Akal, 1980 and Stoll and Kan, 1981).

Considering the difficulties involved in measuring Biot's slow wave, it is not considered in the practical geoacoustic problems outlined in Chapters 9, 10 and 11. The next step is to examine Biot's fast wave. Two important phenomena are predicted for the fast wave by Biot's theory; dispersion (the variation of velocity with frequency) and attenuation. The significance of these two phenomena is studied in Chapters 7 and 8.

7.1 Introduction

Dispersion is the term which describes the variation of the velocity of a stress wave with frequency. If a stress wave suffers attenuation it must also exhibit velocity dispersion. Although there are many experimental examples showing attenuation of compressional waves in rocks and sediments (see Chapter 8), there are few measurements of compressional (fast) wave velocity dispersion. This is mainly due to the difficulty in collecting velocity data over orders of magnitude of frequency on the same sediment sample. Some authors dismiss compressional wave velocity dispersion as being negligible within the acoustic to ultrasonic frequency range (e.g. Hamilton, 1972). However, other authors recognise that in order to account for attenuation of compressional waves, velocity dispersion must also be considered (Kjartansson, 1979, Wingham, 1985).

A number of authors have made indirect and direct measurements of velocity dispersion in sediments over the acoustic to ultrasonic frequency range (e.g. Spencer, 1981, Hamdi and Taylor-Smith, 1982, Bedford *et al.*, 1982, Wingham, 1985 and Winkler, 1985). Of these cases, Hamdi and Taylor-Smith (1982), Bedford *et al.*, (1982) and Winkler, (1985) compare their results with predictions from Biot's (1956 a,b) theory (in one guise or another), whilst White (1986) and Dunn (1986) compare Spencer's (1981) results with predictions from Biot's (1956 a,b) theory. It is of interest to use the experimental data from some of these (and other) studies to identify the key parameters in Biot's (1956 a,b) theory which control the fast wave dispersion, and to allow an assessment as to whether Biot's (1956 a,b) theory can satisfactorily predict fast compressional wave velocity dispersion in sediments and rocks.

The following data sets, each denoted by a different data set code, are used to study Biot fast wave dispersion in this chapter: CARB_M1 - a generic data set for deep-sea (5000 m) carbonate sediments; CARB_M2 - a data set for intermediate (1000 m) to deep-sea (3000 m) carbonate sediments from the Ontong-Java plateau after Johnson et al. (1977); SILT_M1 - a data set for fine marine silts after Hamdi and Taylor-Smith, (1982); SAND_M4 - a beach sand after McCann and McCann (1985); SAND_M2 - a beach sand after Wingham (1985) and SAND_M3 - a sand after Bedford et al. (1982). A full description of these data sets is given in Appendix 3.

7.2 Parameters affecting the magnitude of fast wave dispersion

7.2.1 The effect of tortuosity

In their studies of compressional wave dispersion modelling using Geertsma and Smit's (1961) approximate version of Biot's theory, Hamdi and Taylor-Smith (1982) recognised the need to account for the tortuosity of their sediments. Later, Taylor-Smith (1986) re-analysed this experimental data using additional measurements for the tortuosity (T) - concluding that T should not be ignored in predicting velocity dispersion using the approximate version of Biot's theory. It is useful to examine the full version of Biot's theory in order to elucidate the role of the tortuosity in fast wave velocity dispersion.

The tortuosity (T) may be calculated from electrical resistivity measurements as discussed by Brown (1980). Following Brown, Taylor-Smith (1986) uses electrical resistivity results from Jackson et al. (1978) to calculate tortuosities for marine clays, silts and sands. The resulting values range between 1.4 and 1.6, which are not inconsistent with Stoll's (1974) values of 1.25 for sands. In the absence of any T measurements for surficial carbonate sediments, a range of values between 1.25 and 2 are used to study how the tortuosity affects predicted fast wave velocities in

these types of sediments. Note, that the tortuosity (by definition) must have a value greater than unity. Using a value of $T = 1$ in Biot's theory is incorrect for natural sediments (see 7.4.2).

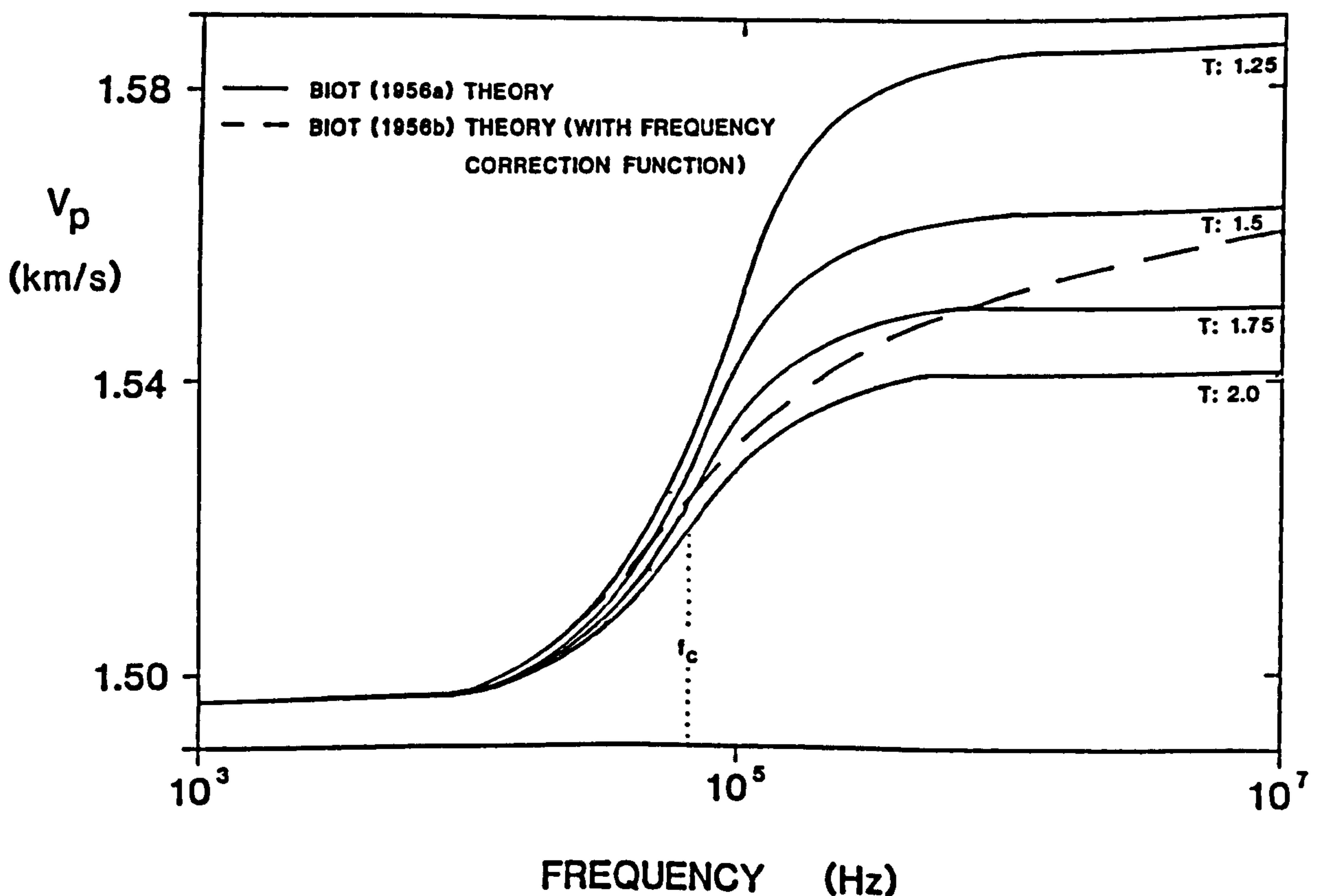
The data set CARB_M1, shown in Table 7.1, characterises the physical properties of near surface carbonate sediments. It was assembled from a number of sources; Hamilton (1976a), Ogushwitz (1985), Johnson et al. (1977), Bear (1972), Hamilton (1976b) and results from Chapter 5. The parameters from CARB_M1 were input into a computer program (Appendix 4), based upon Biot's (1956 a,b) theory of poroelasticity (Chapter 2). The program gives the velocity and attenuation coefficients of the fast and slow waves as a function of frequency.

Table 7.1 Physical parameters characterising near surface carbonate sediments - data set CARB_M1 / CARB_M2

1. Porosity	$0.72 - (9.87z).10^{-4} + (8.3z^2).10^{-7}$
2. Fluid density	1024 kg/m^3
3. Grain density	2720 kg/m^3
4. Fluid modulus	$(2.39).10^9 \text{ Pa}$
5. Grain modulus	$(6.3).10^{10} \text{ Pa}$
6. Dynamic viscosity	0.001 Pa.s
7. Circular frequency	$4\pi.10^5 \text{ Hz}$
8. Shear modulus	$\rho.16400z^{0.65} \text{ Pa}$
9. Frame bulk modulus	2.17 G
10. Permeability	$(1.59).10^{-12} \text{ m}^2$
11. Pore radius	$(5.14).10^{-6} \text{ m}$
12. Tortuosity	$1.25 \text{ to } 2$
13. Grain size	$(6).10^{-6} \text{ m}$
1	Hamilton (1976a)
2-6	Ogushwitz (1985)
7,13	Johnson <u>et al.</u> (1977)
8	Hamilton (1976b)
9	from Table 5.1
10	equation 4.5
11	arbitrary values
12	equation 4.6

The fast wave velocity predictions from Biot's theory for the data set CARB_M1, at a depth of 1 m ($z = 1$ in Table 7.1), are shown in Figure 7.1, for values of T between 1.25 and 2. The shape of the dispersion curves for the different tortuosity values are the same - rising steeply from the zero frequency velocity limit (V_Z) at about 1/10th the critical frequency (see equation 6.1), and then rapidly flattening off to tend to the infinite frequency limit (V_I). The increase in predicted fast wave velocity from V_Z to V_I happens over only two orders of magnitude. The dashed curve in Figure 7.1 was calculated including Biot's (1956b) frequency correction function term (equations 2.12 to 2.14). The effect of this is to smear out the dispersion over a wider frequency band-width. The importance of the frequency correction factor will be addressed in 7.4.2. Note, the infinite frequency limit velocity (V_I) is strongly dependent upon the tortuosity; this can be verified by examining equation 2.25.

Figure 7.1 V_p predictions versus frequency for the data set CARB_M1



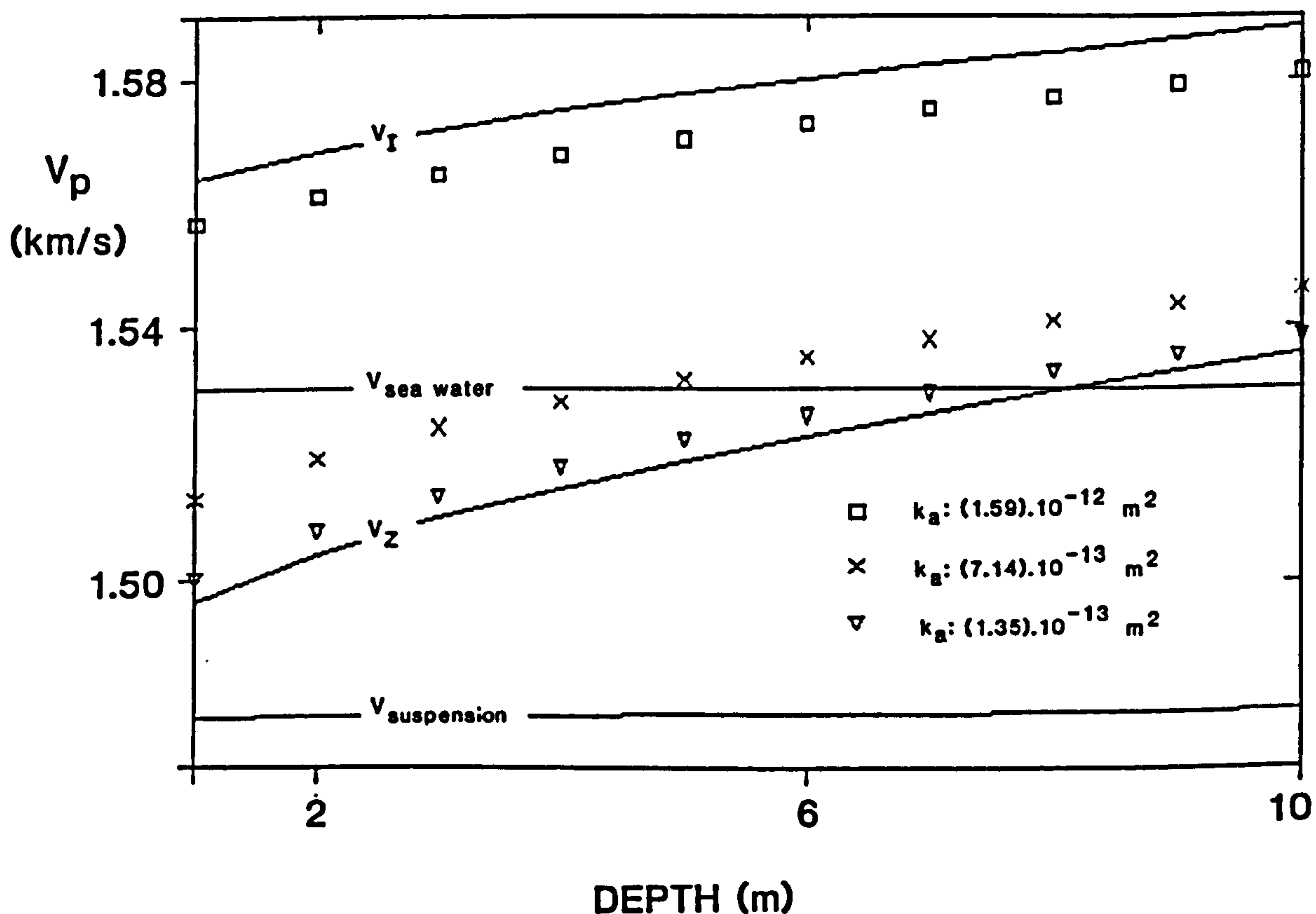
7.2.2 Effect of shear modulus on dispersion in surficial sediments

It is well known that the shear modulus increases rapidly with increasing depth in surficial sediments of the sea-bed (see Hamilton, 1976b and Taylor-Smith, 1986). Conversely, the porosity usually decreases only by a few percent with increasing depth in surficial sea-bed sediments. The relative importance of the changes in porosity and shear modulus upon the magnitudes of the predicted fast wave velocity and fast wave velocity dispersion, in the upper ten metres of a typical carbonate-type sea-bed, is assessed by using the data set CARB_M1. The importance of the shear modulus on predicted fast wave velocities and dispersion for deeper sediments is looked at in Chapter 9.

Various predictions for the magnitude of the fast wave velocity in the upper ten metres of a carbonate sea-bed are shown in Figure 7.2. The predictions are made at a frequency of 200 kHz and use a tortuosity of 1.5, with the other parameters given in Table 7.1 ($1 < z < 10$). Biot's (1956b) frequency correction factor is not used.

In Figure 7.2, predictions from the Biot theory are given by the solid lines marked V_Z and V_I and also the three different sets of symbols; corresponding to predictions using different permeabilities (7.3.3). The two other solid lines in Figure 7.2 refer to the velocity of the sea-water (1530 m/s at an arbitrary temperature of 3° C and pressure of 400 kg/cm³, Wilson, 1960) and the velocity of a cohesionless (fluid-suspension) sea-bed (1477-1480 m/s). The line for the suspension is given by setting the shear and frame bulk moduli to zero in the data set CARB_M1. This velocity prediction is the same as is given by Wood's (1941) equation which isolates the effect of the changes in porosity upon predicted velocities. As can be seen, the velocities predicted from Wood's equation vary little over the upper 10 metres of the sea-bed.

Figure 7.2 V_p predictions versus depths up to 10 metres, for the data set CARB_M1



The increase in the shear modulus with depth affects both the V_Z and V_I limits. At any one depth the maximum possible (predicted) dispersion is given by $V_I - V_Z$. At a depth of 1 m, $V_I - V_Z = 68 \text{ m/s}$, while at 10 m, $V_I - V_Z = 52 \text{ m/s}$. As the sediment becomes stiffer with increasing depth $V_I - V_Z$ tends to a constant value; however the relative importance of the dispersion becomes less as $(V_I - V_Z) / V_Z$ becomes small (see 9.4.2). Therefore, Biot fast wave dispersion will be most apparent and important in low rigidity, high porosity/permeability, surficial sea-bed sediments.

7.3 Parameters affecting the location of fast wave dispersion in the frequency band

7.3.1 Inferences from the characteristic equation

Looking at the characteristic equation (2.18), the angular frequency (ω), the permeability (k_a) and the viscosity (η) are all included in the imaginary viscous damping term. It is this term which controls the frequency at which the viscous dispersion occurs. In this term, the roles of ω , k_a and $1/\eta$ are all interchangeable - so increasing ω by an order of magnitude is equivalent to increasing k_a or $1/\eta$ by an order of magnitude. Therefore, sweeping k_a or $1/\eta$ through orders of magnitude will result in similar curves as for a frequency sweep (e.g. Figure 7.1). Biot (1956a) recognised the importance of the parameters ω , k_a and $1/\eta$ upon the viscous damping mechanism, and he combined them in the definition of the critical frequency (f_c , see equation 6.1). For frequencies approaching, or greater than f_c , the damping mechanism will operate causing dispersion and attenuation of the fast compressional wave. The critical frequency is equal to 70 kHz for the example shown in Figure 7.1 (f_c being calculated from equation 6.1 using the parameters given in Table 7.1).

The second component which makes up the viscous damping term in the characteristic equation is the frequency correction function $\hat{F}(\kappa)$. This correction function is strongly dependent upon the pore-radius (a) of the sediment, and to a lesser degree the viscosity of the pore fluid (see equations 2.12 - 2.15). Therefore, a will be expected to affect the fast wave dispersion. Further, the pore radius, the permeability and the grain size are all intrinsically linked in some fashion (see Chapter 4). So varying the grain size will almost certainly change the permeability and the pore radius.

7.3.2 Effect of permeability

As discussed at length in Chapter 4, there is a large range in the magnitude of the permeability of deep-sea sediments arising from differences in methodology as well as intrinsic differences within sediments. A conclusion from Chapter 4 was that the micro-permeability - which would appear to be the appropriate parameter for dispersion - cannot be easily measured. However, laboratory direct flow methods for obtaining the small-scale permeability can give the lower bounds to the micro-permeability (4.11). Unfortunately, these types of measurements are not always available, and one is forced to use permeabilities determined empirically from the grain-size. However, the accuracy of such empirical methods is usually poor, but in some cases the permeability obtained from grain-size analysis is comparable to the micro-permeabilities obtained from inverse Biot dispersion analysis (see Figure 4.9).

7.3.3 Effect of grain size

The mean grain diameter d_m affects Biot fast wave dispersion indirectly, by influencing the permeability (k_a) and pore-radius (a) of sediments. Semi-empirical equations such as 4.5 and 4.6 can be used to roughly estimate k_a and a . Permeability estimates using these equations for fine-silt grade sediments compare well with direct-flow measurements, but for silt-sand grade sediments the estimates are about five times greater than measured values (Goldsberry, 1985). Another observation made by Goldsberry (1985) is that for a bimodal sand-silt sediment a grain diameter of $2/3 d_m$ gives the best fit between measured and experimental permeabilities. Lastly, Stoll (1974) uses a permeability calculated using a pore radius given by $a = d_m/6$. In the following examples calculating fast wave dispersion in bimodal silt-sand grade materials, three semi-empirical methods for obtaining permeability are used:

- A. k_a calculated from equations 4.5 and 4.6 and the result divided by 5.
- B. d_m set to $2/3d_m$ and then k_a calculated from 4.5 and 4.6
- C. a set to $d_m/6$ and k_a calculated from 4.6.

For the surficial carbonate data set CARB_M1 (Table 7.1) the following permeabilities are calculated using the empirical methods outlined above: A. $(7.14) \cdot 10^{-13} \text{ m}^2$, B. $(1.59) \cdot 10^{-12} \text{ m}^2$, C. $(1.35) \cdot 10^{-13} \text{ m}^2$, which span over an order of magnitude. The critical frequencies for these permeabilities (equation 6.1) are: A. 150 kHz, B. 70 kHz, C. 830 kHz.

Predicted velocities for the data set CARB_M1, calculated using the three permeability estimates given above are shown in Figure 7.2. These different permeabilities give a wide range in the predicted velocities - due to the fact that the f_c values are close to the compressional wave frequency of 200 kHz used in the data set. Therefore, if attempting to calculate compressional wave velocities in surficial carbonate sediments similar to the data set CARB_M1, around frequencies of 200 kHz, the grain-size / permeability may be critical in determining the amount of Biot velocity dispersion present. This point is well illustrated by the next data set CARB_M2.

The data set CARB_M2 uses data from Johnson et al. (1977), who obtained measurements of wet bulk density (ρ), mean grain size (d_m) and compressional wave velocity (V_p) on 54 surficial carbonate sediment samples, given in Table 7.2. Data set CARB_M2 comprises the values shown in Table 7.1 except: ρ and d_m values from Table 7.2; permeabilities calculated using method A (above), and a constant shear modulus of $G \text{ (Pa)} = 5625 \cdot \rho$, (based upon an extrapolation of the results given in Table 5.1 at an equivalent depth of $z = 1 \text{ m}$).

Figure 7.3 V_p experimental measurements (Johnson, et al., 1977) and predictions versus grain diameter for the data set CARB_M2

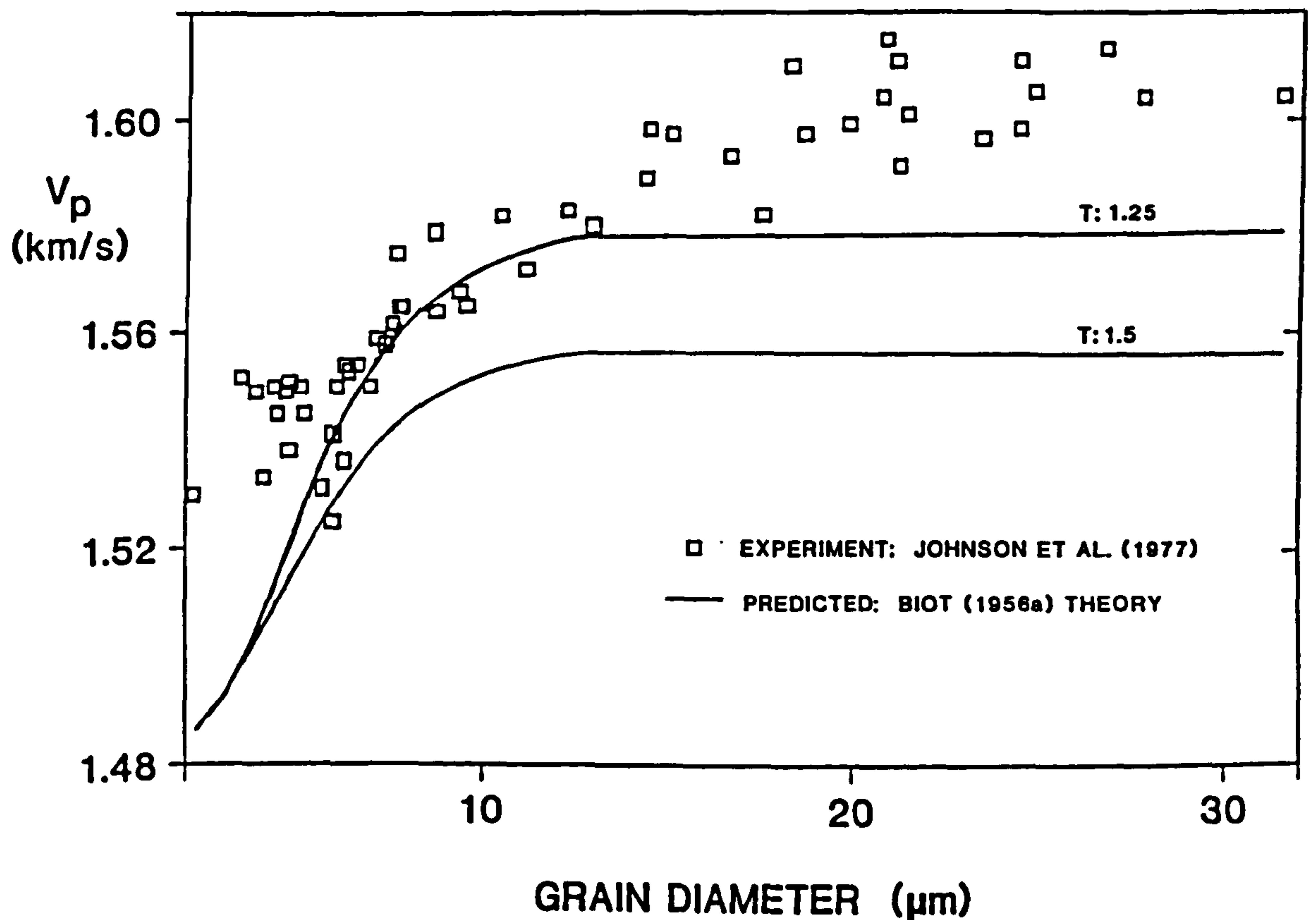


Figure 7.3 shows the predicted compressional wave velocities from the Biot theory using the data set CARB_M2, along with the experimental V_p results from Johnson et al. (1977). Smooth lines were fitted through the V_p predictions. Predicted velocities are made at two different tortuosities of 1.25 and 1.5, and the predicted curves show a similar trend of an increase in velocity with an increase in grain size as exhibited by the experimental data. The role of the permeability in these predictions is critical. At small grain sizes ($d_g < 4\mu\text{m}$) the predicted velocities are close to V_z , and as the grain size increases to $10\mu\text{m}$, the predicted velocities increase sharply to V_I . The increase in velocity over this grain size interval is due to the corresponding increase in the permeability (equations 4.5 and 4.6), which takes the predicted velocities from V_z , through to V_I , at frequencies near f_c . Although no attempt was made to "fit" the predicted and experimental velocities, an appropriate selection of the tortuosity could make the match better.

Table 7.2 Velocity, grain size and density data after Johnson et al., 1977

Sample	V_p	ρ	d_m
ID	(m/s)	(kg/m ³)	(m)
77.00	1553	1481	0.0000064
77.17	1550	1508	0.0000044
77.41	1550	1510	0.0000070
79.00	1579	1482	0.0000087
79.19	1615	1496	0.0000209
79.40	1575	1519	0.0000077
83.00	1582	1447	0.0000176
83.20	1605	1503	0.0000249
83.40	1583	1486	0.0000123
88.00	1604	1479	0.0000278
88.16	1610	1525	0.0000183
88.20	1611	1513	0.0000245
92.00	1604	1510	0.0000315
92.15	1613	1528	0.0000268
92.26	1611	1515	0.0000212
102.00	1596	1496	0.0000235
102.14	1599	1519	0.0000199
102.25	1597	1532	0.0000187
108.00	1564	1488	0.0000088
108.20	1565	1474	0.0000096
108.33	1550	1501	0.0000061
112.00	1598	1493	0.0000245
112.20	1604	1523	0.0000208
112.31	1598	1511	0.0000145
120.00	1591	1482	0.0000213
120.18	1601	1483	0.0000215
120.31	1597	1495	0.0000151
123.00	1580	1469	0.0000130
123.21	1593	1478	0.0000167
123.34	1589	1490	0.0000144
125.00	1565	1461	0.0000078
125.18	1582	1479	0.0000105
125.34	1549	1467	0.0000039
128.00	1554	1470	0.0000067
128.24	1568	1471	0.0000094
128.41	1541	1491	0.0000060
129.00	1554	1488	0.0000063
129.20	1545	1467	0.0000045
129.35	1549	1509	0.0000047
131.00	1533	1423	0.0000041
131.21	1530	1477	0.0000022
131.31	1552	1484	0.0000035
135.00	1562	1474	0.0000076
135.22	1572	1475	0.0000112
135.38	1565	1516	0.0000079
136.00	1558	1495	0.0000074
136.23	1559	1484	0.0000072
136.34	1538	1492	0.0000048
139.00	1550	1485	0.0000051
139.22	1551	1524	0.0000048
139.36	1545	1524	0.0000052
141.00	1531	1513	0.0000057
141.20	1536	1516	0.0000063
141.38	1525	1456	0.0000060

7.3.4 Effect of pore radius

As seen in 7.3.3, the pore radius can influence the predicted compressional wave velocity indirectly through the permeability, but as discussed in 7.3.1 it has a direct affect upon the frequency correction function - which also influences the predicted velocity. The importance of the pore radius term in the high frequency range $f > f_t$, where f_t is the transitional frequency (equation 2.15), is shown by the following analysis on the data set SAND_M2, based on the measurements of Wingham (1985).

Wingham (1985) measured fast wave attenuation and dispersion in sands over the frequency range 50 - 350 kHz. The attenuation measurements will be examined later (see 8.3.3), the compressional wave dispersion results are compared with predictions from Biot's theory in Figure 7.4, which is based on the data set SAND_M2. This data set is shown in Table 7.3, and is based on measurements of properties on sands of grain diameter 240 - 250 μm (Wingham, 1985, Bedford et al, 1982 and data from Table 5.1).

Table 7.3 Physical parameters characterising data set SAND_M2

1. Porosity	0.432
2. Fluid density	1000 kg/m ³
3. Grain density	2650 kg/m ³
4. Fluid modulus	(2.22).10 ⁹ Pa
5. Grain modulus	(3.6).10 ¹⁰ Pa
6. Dynamic viscosity	0.001 Pa.s
7. Circular frequency	4 π .10 ⁵ Hz
8. Shear modulus	(4.85).10 ⁶ Pa
9. Frame bulk modulus	2.17 G
10. Permeability	(2.17) to (4.68).10 ⁻¹¹ m ²
11. Pore radius	(4.17) to (6.34).10 ⁻⁵ m
12. Tortuosity	2
13. Grain size	(250).10 ⁻⁶ m

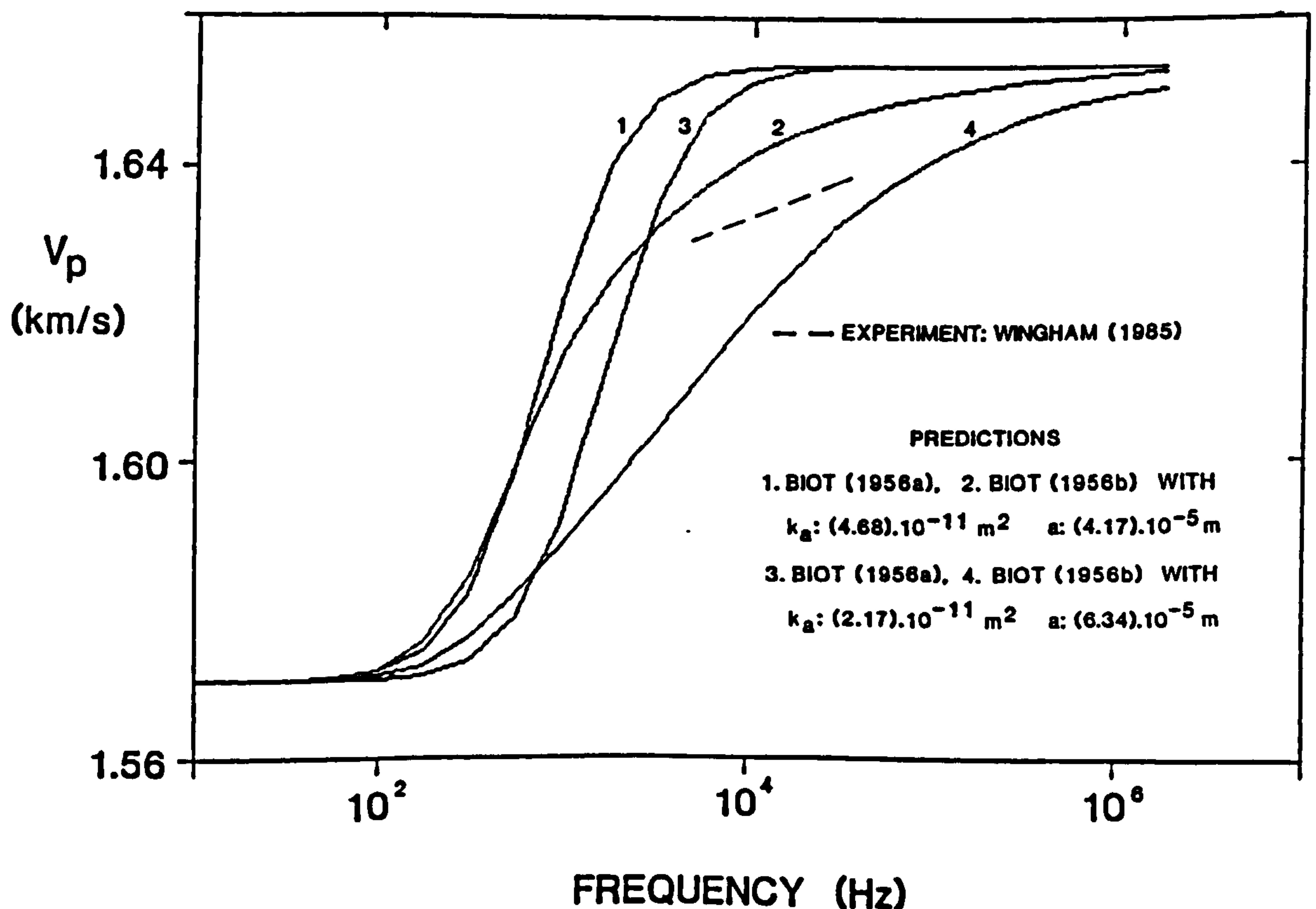
1,3,7,13 Wingham (1985)
 2,4,5,6,12 McCann and McCann (1985)
 8,9 from Table 5.1
 10,11 methods A and C (7.3.3)

In Figure 7.4, fast wave velocity predictions are given for the data set SAND_M2 using the following k_a and a combinations:

1. $k_a = (2.169) \cdot 10^{-11} \text{ m}^2$ - calculated from method A (7.3.3) and
 $a = (6.34) \cdot 10^{-5} \text{ m}$ - calculated from equation 4.5
2. $k_a = (4.68) \cdot 10^{-11} \text{ m}^2$ - calculated from method C (7.3.3) and
 $a = (4.17) \cdot 10^{-5} \text{ m}$ - calculated from equation 4.6.

Curves 1 and 3 are calculated without Biot's (1956b) frequency correction function, while curves 2 and 4 make use of this correction. It is apparent that the curves 1 and 3 do not match the experimental data very well; however the experimental data falls between curves 2 and 4. The influence of the small change in pore radius on the predicted curves which include the frequency correction function (curves 2 and 4), is great. Therefore, the magnitude of the pore-size is critical to the shape of the fast wave dispersion curve in the high frequency range.

Figure 7.4 V_p experimental measurements (Wingham, 1985) and predictions versus frequency for the data set SAND_M2



7.3.5 Effect of fluid viscosity

Apart from varying k_a , (d_m) , or ω , another way to investigate Biot fast wave dispersion can be achieved by varying the fluid viscosity (η). Experimental data on fast wave attenuation and dispersion in sands have been collected by Bedford et al. (1982). They also collected other measurements characterising the physical properties of these sands, and made fast wave attenuation and velocity predictions using a modified form of Biot's (1956 a,b) theory, proposed by Hovem and Ingram (1979). Unfortunately, this modification of Biot's theory is incorrect (see 7.4.2) and it is worthwhile repeating the analysis of the data collected by Bedford et al. (1982) using Biot's original theory.

The data set SAND_M3 shown in Table 7.4 is based upon the measurements of Bedford et al. (1982). In their experiments, they changed the viscosity of the pore fluid by adding small amounts of glycerine to it. The changes in η , ρ_f , and K_f , for various percentage concentrates of glycerine are shown in Table 7.5. Using the values given in Tables 7.4 and 7.5 predicted fast wave velocities can be compared with the experimental values as shown in Figure 7.5. Also shown in Figure 7.5 are the (incorrect see 7.4.2) velocity predictions made by Bedford et al. (1982) and the (correct) zero frequency velocity limit (V_z). It can be seen that the (correct) predicted fast wave velocities (V_1) lie about 50 m/s below the experimental values over the entire range of glycerine concentrations. More significantly, the difference $V_1 - V_z$ is virtually constant over this range too. This means that increasing the glycerine concentration from 0 to 28% has little effect upon the Biot dispersion predictions. The increases of predicted and experimental velocities are mainly due to the effect of the increase in the fluid bulk modulus with increasing concentration (Table 7.5) rather than dispersion effects: the viscosity is only decreased by a factor of two over the concentration range and f_c only changes from 2.2 kHz to 4.7 kHz.

Table 7.4 Physical parameters characterising a sand - data set SAND_M3

1. Porosity	0.365
2. Fluid density	1000 kg/m ³
3. Grain density	2500 kg/m ³
4. Fluid modulus	(2.17).10 ⁹ Pa
5. Grain modulus	(3.5).10 ¹⁰ Pa
6. Dynamic viscosity	0.001 Pa.s
7. Circular frequency	228 π .10 ³ Hz
8. Shear modulus	(8.0).10 ⁷ Pa
9. Frame bulk modulus	(8.0).10 ⁷ Pa
10. Permeability	(2.64).10 ⁻¹¹ m ²
11. Pore radius	(3.39).10 ⁻⁵ m
12. Tortuosity	2
13. Grain size	(117).10 ⁻⁶ m
1-10,12,13	Bedford <u>et al.</u> (1982)
11	equation 4.5

Table 7.5 Physical parameters characterising glycerine diluted water (after Bedford et al., 1982)

Saturation	ρ_f	η	K_f
%	(kg/m ³)	(Pa.s)	(G Pa)
0	993	0.00100	2.175
2	997	0.00105	2.217
4	1002	0.00110	2.259
6	1007	0.00116	2.303
8	1012	0.00122	2.348
10	1016	0.00129	2.394
12	1021	0.00136	2.441
14	1026	0.00144	2.489
16	1030	0.00153	2.538
18	1035	0.00163	2.589
20	1039	0.00174	2.640
22	1044	0.00185	2.692
24	1049	0.00198	2.746
26	1054	0.00212	2.800
28	1059	0.00228	2.856

Figure 7.5 V_p experimental measurements (Bedford et al., 1982) and predictions versus percentage glycerine saturation of the pore-fluid for the data set SAND_M3

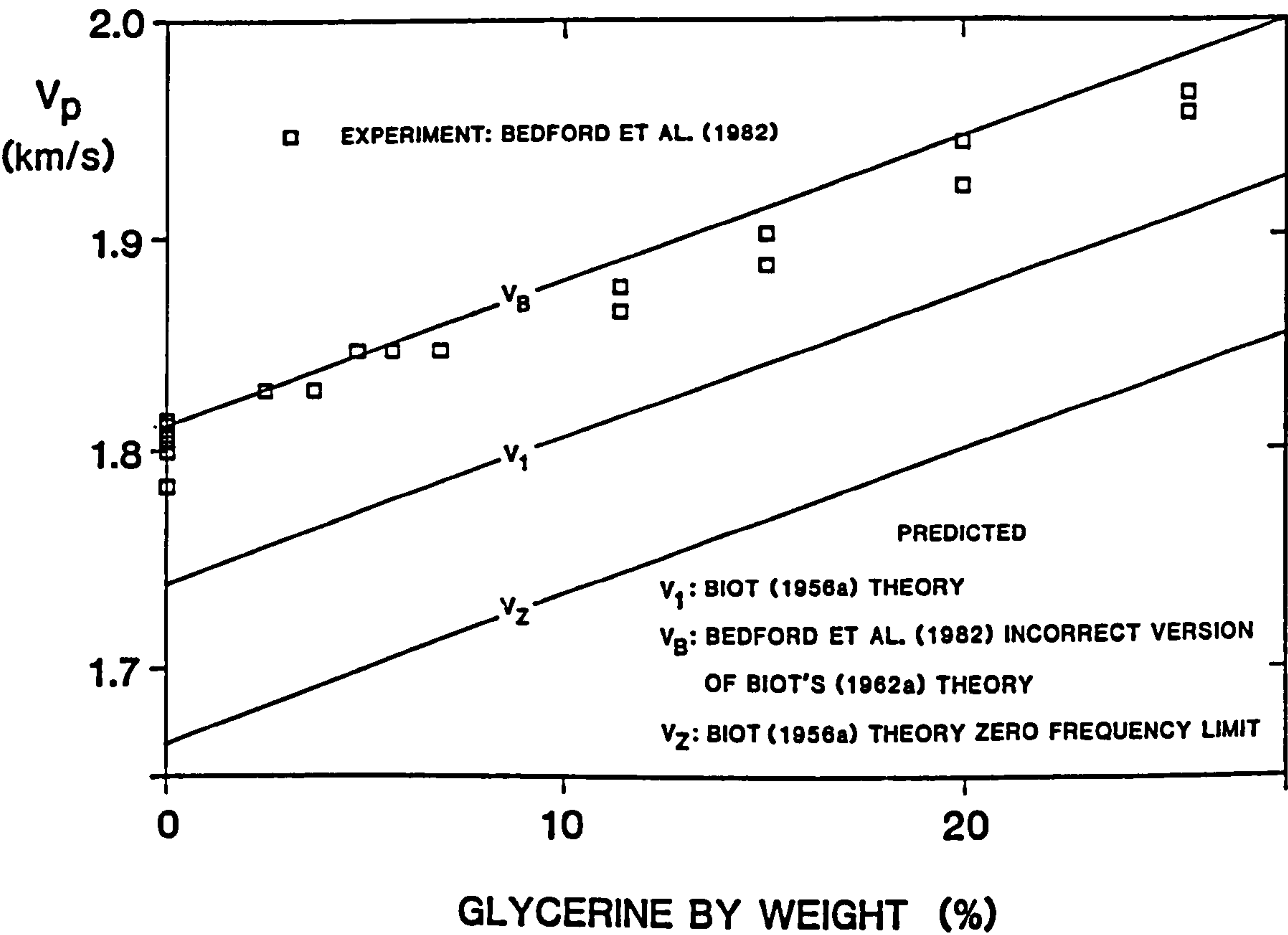
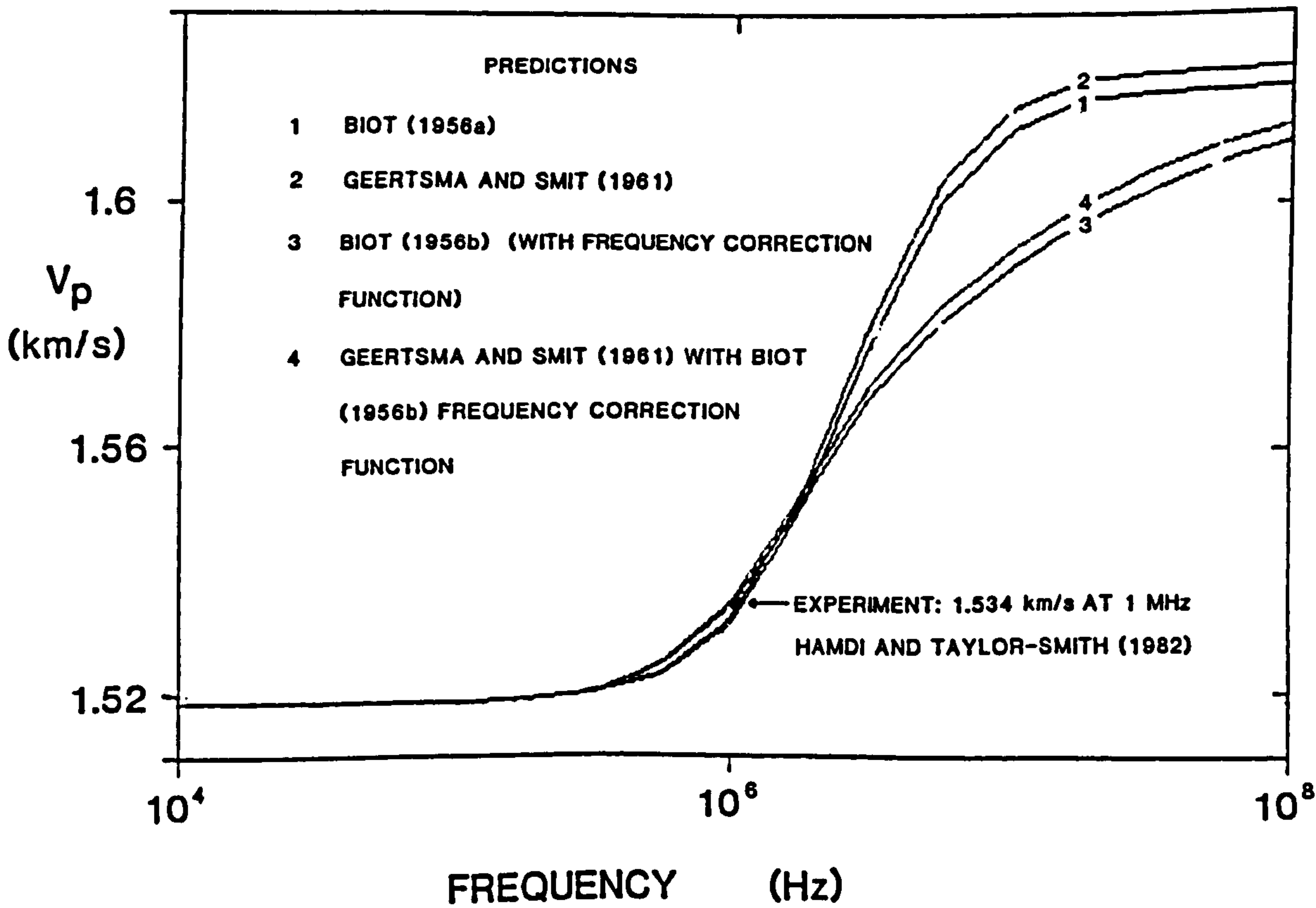


Figure 7.6 V_p experimental measurement (Hamdi and Taylor-Smith, 1982) and predictions versus frequency for the data set SILT_M1



The limited range in f_c , along with the problems of the increases in velocity due to the increased fluid bulk modulus, rather restricts the usefulness of experiments of this type.

7.4 Dispersion predictions using variations of Biot's theory

7.4.1 The approximate theory of Geertsma and Smit (1961)

Hamdi and Taylor-Smith (1982) and Taylor-Smith (1986) use Geerstma and Smit's (1961) approximation to Biot's theory (see 2.4.3) to examine the relationship between fast wave dispersion and permeability. The approximate theory is far simpler to use than the exact theory and is not complicated by Biot's (1956b) frequency correction function. It is of interest to re-analyse Hamdi and Taylor-Smith's (1982) data using full (Biot, 1956 a,b), approximate (Geertsma and Smit, 1961) and modified approximate (Geertsma and Smit with frequency correction) theories. Predictions for velocity dispersion using these theories are shown in Figure 7.6 for the data set SILT_M1 (which is based upon data from Hamdi and Taylor-Smith, 1982 and Taylor-Smith, 1986) shown in Table 7.6.

Table 7.6 Physical parameters characterising data set SILT_M1

1. Porosity	0.6
2. Fluid density	1024 kg/m ³
3. Grain density	2650 kg/m ³
4. Fluid modulus	(2.38).10 ⁹ Pa
5. Grain modulus	(3.6).10 ¹⁰ Pa
6. Dynamic viscosity	0.001 Pa.s
7. Circular frequency	2 π .10 ⁶ Hz
8. Shear modulus	(1.2).10 ⁷ Pa
9. Frame bulk modulus	(6.7).10 ⁶ Pa
10. Permeability	(3.0).10 ⁻¹⁴ m ²
11. Pore radius	(7.75).10 ⁻⁶ m
12. Tortuosity	1.5
13. Grain size	(4.4).10 ⁻⁶ m
1-10,13	Hamdi and Taylor-Smith (1982)
11	equation 4.5
12	Lovell and Ogden (1984)

The critical and transitional frequencies for these predictions shown in Figure 7.6 are $f_c = 3.1$ MHz, $f_t = 1.3$ MHz, while the experimental velocity data point was collected at 1 MHz. From Figure 7.6 it can be seen that all four velocity prediction curves give similar results up to f_c (all agreeing well with the single experimental data point), after which they diverge.

For frequencies greater than f_c , the Geertsma and Smit and Biot velocity predictions are of very similar shape, for both frequency corrected (3 and 4) and not frequency corrected (1 and 2) curves. However, velocities obtained from the Geertsma and Smit theory are slightly higher than the Biot predictions for $f > f_c$. For this set of data, the difference between the two is not that significant, but in some cases this difference may exceed 100 m/s and be highly significant. The reason for this difference is due to a breakdown of the high-frequency approximate asymptote for critical values of the elastic constants and density terms in equation 2.25. The approximate theory holds providing the elastic constants and density terms satisfy equation 2.27. Therefore, this inequality must be checked before using the approximate theory.

7.4.2 The non-tortuous viscous flow theory of Hovem and Ingram (1979)

Hovem and Ingram (1979) modified Biot's theory incorrectly; and their analysis is criticised in passing by Cleary (1980) and by Johnson and Plona (1982). With reference to Table 7.7, the Hovem and Ingram (1979) analysis differs in two ways from that derived by Biot (1956 a,b). Hovem and Ingram (1979) assume a tortuosity equal to one; which is physically unacceptable for a natural porous sediment or rock (see Figure 2.1). To compensate for the zero inertial coupling [$\rho_{12} = 0$, in Biot (1956a) notation] that this gives, Hovem and Ingram use Biot's (1956b) frequency correction over both high and low frequency ranges; in particular, they

assume that $F_i \neq 0$ for $f < f_t$. This latter assumption contradicts the definition of $\hat{F}(\kappa)$ given by Biot (1956b); for $f < f_t$, $F_r = 1$ and $F_i = 0$; for $f > f_t$, F_r and F_i are given by equations 2.12 to 2.14. Note, that Hovem and Ingram (1979) do re-introduce the tortuosity into their analysis, through their semi-empirical definition of the permeability (similar to equation 4.5). However, this does not make up for the consequences of their initial incorrect assumption that $T = 1$, hence there is no inertial mass coupling.

Table 7.7 Comparison of Biot's (1956 a,b) theory and the modifications of Hovem and Ingram (1979)

	Hovem and Ingram	Biot
Definition of mass coupling	$\rho_{12} = 0$ (assuming $T = 1$)	$\rho_{12} = (1 - T)\rho_f \phi$
Complex mass coupling	$\hat{\rho}_{12} = -\frac{b}{\omega} F_i + i\frac{b}{\omega} F_r$	$\hat{\rho}_{12} = \rho_{12} - \frac{b}{\omega} F_i + i\frac{b}{\omega} F_r$
Limit at low frequencies	$\hat{\rho}_{12} \rightarrow -\phi \frac{\rho}{3} f + i\frac{b}{\omega}$ (assuming $F_i \neq 0$)	$\hat{\rho}_{12} \rightarrow \rho_{12} + i\frac{b}{\omega}$

In Table 7.7 the notation of Biot (1956 a,b) has been adopted, along with Gardner's (1962) definition of the complex mass coupling coefficient. To convert to the notation used elsewhere in this thesis, use the following definitions:

$$\rho_{12} = \rho_f \phi - \rho_f^2 / m, \quad \text{and} \quad b = \phi^2 \frac{\eta}{k}$$

7.4.3 The variable pore-size theory of McCann and McCann (1985)

Another variation of Biot's theory was offered by McCann and McCann (1985) who calculated fast wave velocity and attenuations using a distribution of pore-sizes and hence permeabilities. They assumed that a unit element of sediment of thickness l , could be divided up into a series of thin sections of constant area each characterised by a different pore-size. The total intrinsic permeability across l is then equal to the combined permeability effect from each of the thin sections. They calculated the volume of pore space which each pore-size occupied (V_x), and assumed that the volume of each of the sections was proportional to V_x/V_t , where V_t is the total volume of the pore-space. In this way the thickness and permeability effect of each section is weighted by the relative volume of pore-space occupied by each pore-size in the selected pore-size distribution.

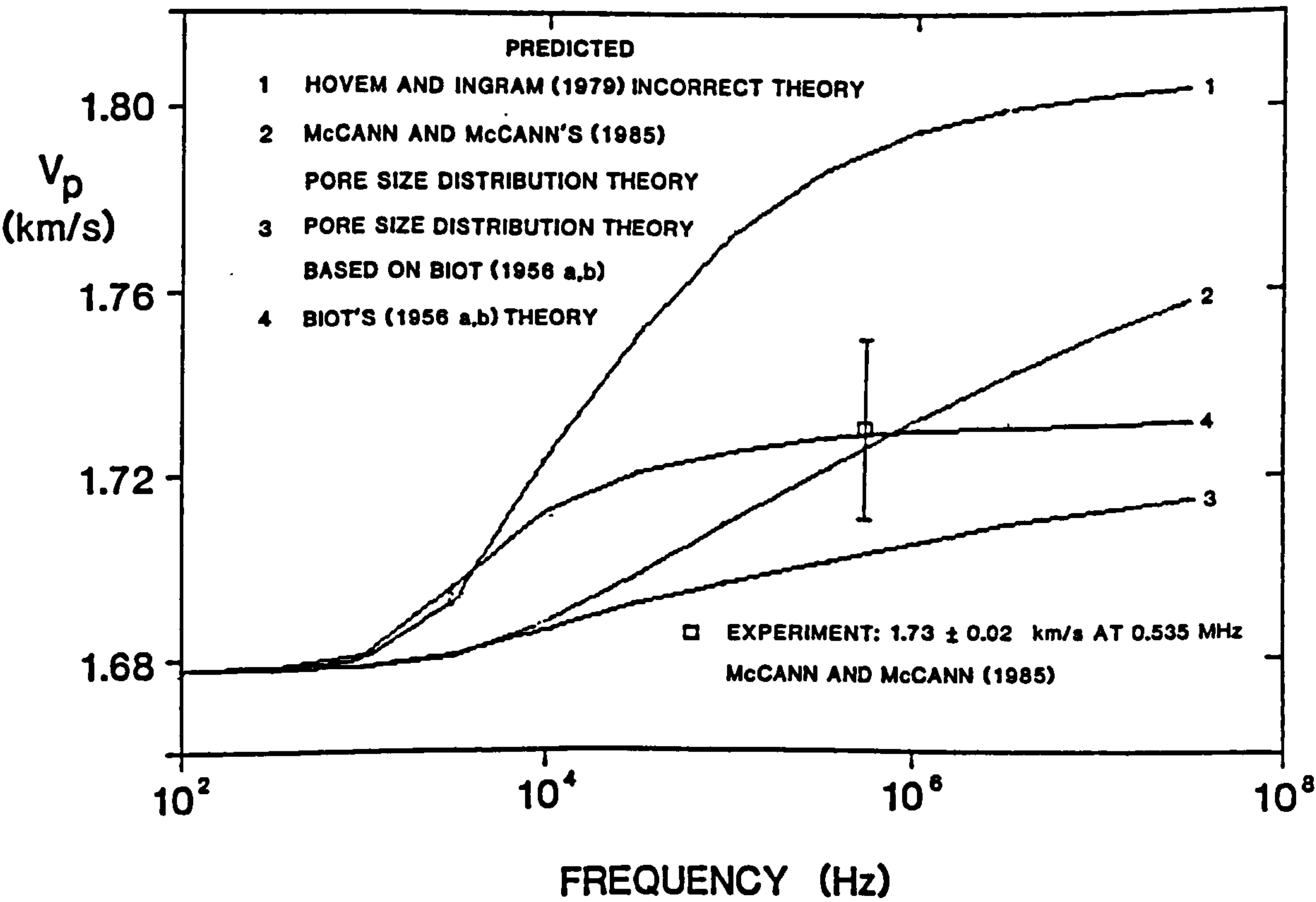
Undoubtedly the micro-permeability and pore-size of a sediment will not be characterised by single values, but rather spectra of different permeabilities and pore-sizes. The Lees (1970) pore-size distribution model is weighted according to pore-volume considerations. Pore-size models which rely on the volume or the surface area of the pore-space are a problem when considering Biot-type dispersion; as it is the radii of the inter-pore connections which affect the micro-permeability of sediments and not the size of the pores themselves (7.5).

McCann and McCann (1985) use the Lees (1970) pore-size distribution model in their modification of Biot's theory. Unfortunately, they use Hovem and Ingram's (1979) incorrect version of Biot's theory to make their velocity and attenuation predictions. The permeability distribution method described by McCann and McCann (1985) with the correct version of Biot's theory was tested using the data set SAND_M4 (Table 7.8), which is based on the measurements of McCann and McCann (1985).

Table 7.8 Physical parameters characterising a glass bead pack
 - data set SAND_M4, after McCann and McCann (1985)

1. Porosity	0.4
2. Fluid density	1000 kg/m ³
3. Grain density	2860 kg/m ³
4. Fluid modulus	(2.23).10 ⁹ Pa
5. Grain modulus	(3.6).10 ¹⁰ Pa
6. Dynamic viscosity	0.001 Pa.s
7. Circular frequency	π .10 ⁶ Hz
8. Shear modulus	(7.0).10 ⁶ Pa
9. Frame bulk modulus	(1.2).10 ⁹ Pa !
10. Permeability	(7.9).10 ⁻¹² m ²
11. Pore radius	(1.77).10 ⁻⁵ m
12. Tortuosity	2
13. Grain size	(250).10 ⁻⁶ m
1-9,12,13	McCann and McCann (1985)
10	equation 4.5
11	equation 4.6

Figure 7.7 V_p experimental measurements (McCann and McCann, 1985) and predictions versus frequency for the data set SAND_M4



The predictions of compressional wave dispersion using the data set SAND_M4 with the correct version of Biot's theory and (Hoven and Ingram's) incorrect version are shown in Figure 7.7. The curves are calculated for both a single permeability and a spectrum of permeabilities (based on McCann and McCann's 1985 technique). It can be seen that the (incorrect) theory of Hoven and Ingram (1979) using a single pore size (curve 1) gives a predicted velocity far in excess of the measurement at 0.5 MHz; whereas with McCann and McCann's spectrum of permeabilities, the prediction (curve 2) does indeed agree with the velocity data point at 0.5 M Hz - but for the wrong reasons. Using the (correct) Biot theory, along with McCann and McCann's (1985) permeability distribution gives a predicted velocity some 20 m/s lower than the experimental data point (curve 3), whereas the single pore size prediction (curve 4) agrees with the measurement!

A normal distribution of pore-sizes, hence permeabilities, was tested in addition to the Lees (1970) distribution on which McCann and McCann based their work. For both distributions the dispersion is smeared out over a larger band-width which tends to agree more with experimental observations. Therefore, a distribution of pore sizes and permeabilities does appear to advance Biot's dispersion theory somewhat, although the difficulties in determining the appropriate experimental measurements may make such advances of little practical use.

7.5 A discussion on the applicability of Biot's theory for accounting for fast wave dispersion in sediments

There is no doubt that dispersion of the fast wave must exist in sediments which exhibit attenuation, as dictated by causality considerations (e.g. Kjartansson, 1979, Wingham, 1985). However, there are few experimental data characterising the magnitude and the shape of

dispersion curves. The data from Wingham (1985), and the results for shear modulus dispersion shown in Figure 5.9, tend to suggest that dispersion is dependent on $\log(\text{frequency})$, over limited frequency bands. However, there is still the lack of a complete data set over many orders of magnitude which experimentally characterises dispersion for different types of sediment. These data sets do not really give enough scope in the frequency domain to satisfactorily test Biot's theory.

An alternative method for testing Biot's theory in an indirect fashion is through varying the permeability or the viscosity parameters over orders of magnitude. Unfortunately, as was seen for the analysis of data from Bedford et al. (1982), dispersive effects due to changing the viscosity of the pore fluid may be overwhelmed by velocity contrasts due to corresponding changes in the bulk modulus of the fluid. The last option, of varying the permeability of sediment samples whilst keeping the frequency fixed, is possible but problematic. Ideally, it would be best to vary the permeability of the same sample by orders of magnitude, while keeping the other parameters required for Biot's theory constant. Experimentally, this is not possible as the best method for changing the permeability is through consolidation experiments; but such experiments also change the porosity (ϕ), the shear modulus (G) and the frame bulk modulus (K_b). Therefore, it is best to attempt to use data from different samples where ϕ , G and K_b are roughly equivalent, but where k_a varies over orders of magnitude. Such a data set is offered by Johnson et al. (1977).

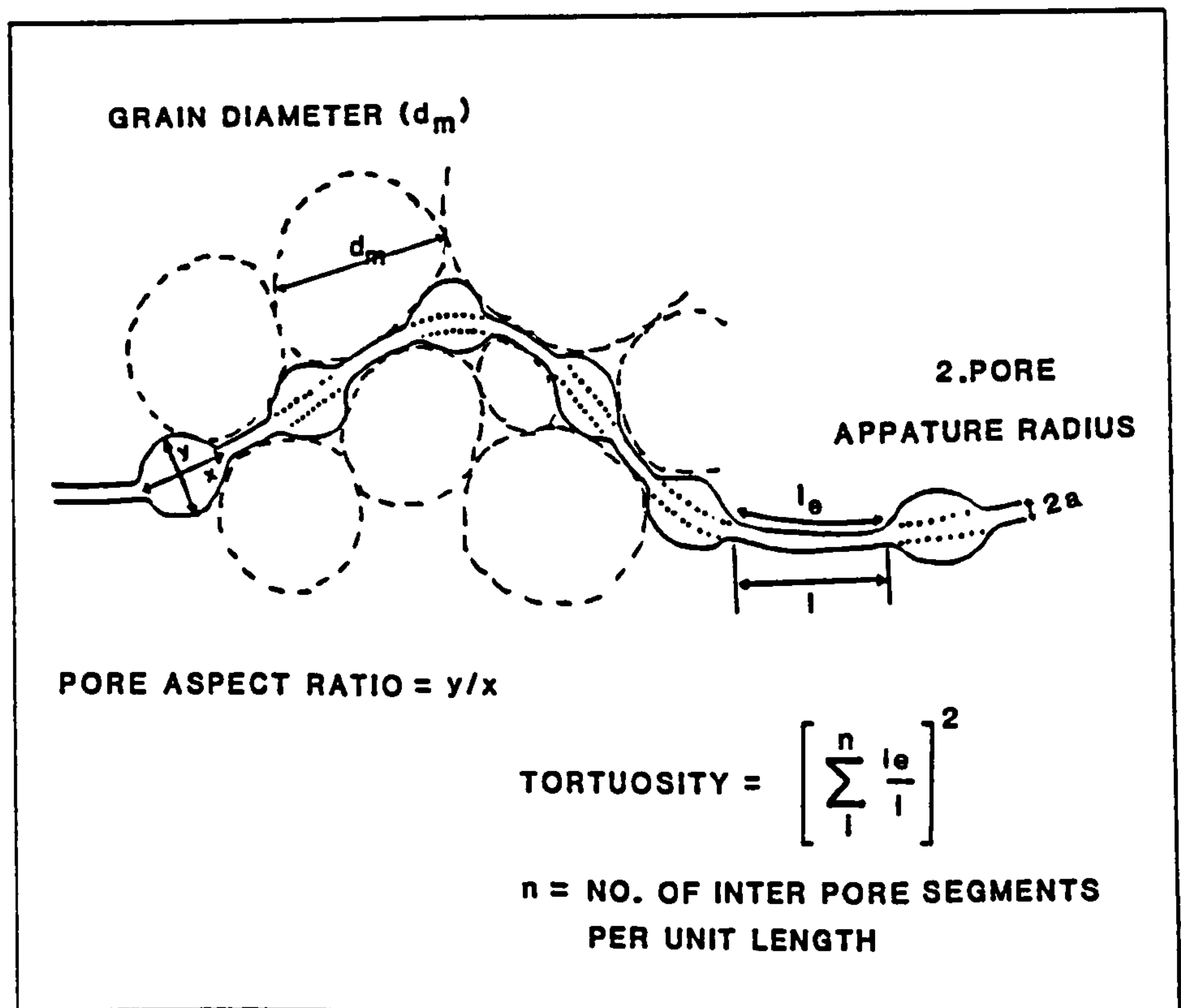
The problem with using data sets, such as given by Johnson et al. (1977) in Biot fast wave dispersion analysis is that the permeabilities of the sediment samples have to be calculated from the sample's grain size. The Kozeny - Carman relationship and variations thereof used for this purpose are by no means fool-proof methods for determining k_a . Therefore, one would expect Biot dispersion analysis based on such methods to reveal

general trends, but not to give accurate velocity predictions. Looking at the analysis of the data of Johnson *et al.* (1977), presented in Figure 7.3, a fair agreement of trends can be inferred between predictions and experimental velocities. No attempt was made to give a "best fit" between the experimental and predicted velocities, although a better agreement could be attained by suitable adjustment of various input parameters. The relative importance of the different input parameters are illustrated by Figures 7.1 to 7.7.

From Figures 7.1 and 7.3 (and 7.7) the tortuosity can be seen to play an important part in fixing the high frequency limit velocity (V_I). From Figure 7.2, the shear modulus affects not only V_I , but also the zero frequency limit velocity V_Z . For near-surface sediments the variations in the shear modulus do not have an overwhelming effect upon the total amount of dispersion possible ($V_I - V_Z$), and for deeper (more rigid) sediments $(V_I - V_Z) / V_Z$ becomes small (see 9.4.2). From Figure 7.4, the magnitude of the pore-radius can be seen to affect the band-width over which the dispersion is smeared at frequencies $f > f_c$. Similarly, a distribution of pore-sizes (Figure 7.7) smears the dispersion over an even greater band-width.

In all these discussions it has been glibly assumed that the permeability, tortuosity and pore-radius are all real parameters which can be feasibly determined experimentally. However, it is worth while considering what is meant by these terms in the context of Biot's theory, and further, to consider whether the experimental determinations for k_a , T and a are appropriate for use in Biot's theory. It is useful to make the idealised model of a poroelastic medium, as shown in Figure 2.1, slightly more complex (Figure 7.8); to better simulate the microgeometry of the pore-space for Biot's (1956 a,b) theory.

Figure 7.8 Micro-geometry of pore-space for Biot's (1956 a,b) theory



The permeability terms in Biot's theory refer to the permeability of capillary-like tubes which interconnect the pores (see Figure 7.8). This "local" micro-permeability may indeed be far different from "global" permeability as obtained from laboratory measurements on samples. Berryman (1986) and Berryman and Thigpen (1987) suggest that "global" permeability measurements should not be used in Biot's theory, rather a "local" value which is determined from digital image analysis of SEM photographs of the sediment (see 4.10).

The pore-radius in Biot's theory actually refers to the radii of the apertures of the capillary-like tubes which interconnect the pores (Figure 7.8). The determination of a pore-radius from the Kozeny's relationship (equation 4.5) is rather inappropriate - as this is based on "specific wetted surface" theories of the pore-space (Bear, 1972).

Therefore, pore-radii determined from such methods relate to the surface area of the pores themselves, which will not necessarily have any bearing upon the radii of the pore apertures. Also, experimental determinations of pore radius distributions using mercury injection techniques are based upon the the specific volume of the pore-space (Wardlaw and McKeller, 1981), which will not necessarily represent the radii of the apertures. It could be argued that SEM image processing methods could give a more appropriate determination of the radii of the apertures; however the extension from 2-D to 3-D models is not obvious (Chatzis and Dullen, 1977), especially for the case of interpreting 2-D images for 3-D parameters. Further, the additional problem of characterising a properly weighted pore aperture radius distribution complicates matters more.

In conclusion, Biot's fast wave dispersion mechanism may indeed mimic some trends shown in experimental observations. However, the experimental and theoretical difficulties in obtaining an accurate description of the pore-space of sediments mean that Biot-type dispersion predictions will be limited in their accuracy. More sophisticated versions of Biot's (1956a) theory are theoretically more attractive, but practically more difficult to use. It is thought best to sacrifice in theoretical elegance and opt for the cruder Biot (1956a) version of poroelasticity, where only k_a and T are required above the usual elastic and density parameters required for Gassmann's (elastic) equation. To make use of more theoretically attractive versions of Biot's original work (e.g. Berryman and Thigpen, 1987), better experimental techniques to characterise the pore-space of sediments are required. Some progress is being made through image analysis techniques (e.g. Berryman and Blair 1986). The problem here is that such techniques are complex, costly and not practical for common-place use.

7.6 Summary

The parameters controlling the magnitude, shape and location (in the frequency band) of fast wave dispersion predicted by Biot's theory have been studied. The role of Biot's (1956b) frequency correction function has also been assessed. The relative successes of extended and approximate forms of Biot's theory have been examined. Lastly, the ability of Biot's theory to account for measured (or inferred) fast wave dispersion has been looked at.

The tortuosity and shear modulus were found to be the most important parameters controlling the magnitude of fast wave dispersion in high porosity deep-sea sediments. It is clear that the micro-permeability of the sediments controls the frequency at which Biot dispersion occurs. At a fixed frequency, sediments with a significantly high enough micro-permeability will show greater predicted dispersion than similar sediments with a low micro-permeability. The increases in compressional wave velocity with increasing grain size shown by the experimental results of Johnson et al. (1977) can be explained by a Biot type dispersion effect. Sediments with a small grain size have a smaller intrinsic permeability than that for larger grain size sediments, when calculated by the empirical Kozeny method (Chapter 4). The dispersion for the larger grain-size (larger permeability) samples causes an increase in the compressional wave velocity above the predicted value for the smaller grain-size samples. The Biot predictions are in fairly good agreement with the experimental results.

The roles of the viscosity (η) of the pore fluid and the pore-size (a) parameter upon predicted dispersion depend on whether or not the Biot (1956b) frequency correction function ($\hat{F}(\kappa)$) is used. If $\hat{F}(\kappa)$ is not used then η has an inverse effect to the intrinsic permeability, and a does not enter the prediction. If $\hat{F}(\kappa)$ is used, then the effect of changing a or η

is to smear the predicted dispersion out by differing amounts over the frequency band. This smearing effect introduced by $\hat{F}(\kappa)$ brings the shape of the predicted velocity versus frequency curve more into line with the experimental dispersion measurements of Wingham (1985). However, the exact shape of the smeared predicted curve is very sensitive to the value of the pore-size parameter.

The approximate dispersion theory of Geertsma and Smit (1961) was shown to give similar predictions to Biot's (1956a) theory (providing the inequality given in equation 2.27 holds). Furthermore, if $\hat{F}(\kappa)$ is included then Geertsma and Smit's approximate prediction is very similar to that from the full Biot (1956 a,b) theory. Hovem and Ingram's (1979) modification of Biot's theory was shown to be incorrect. Using McCann and McCann's (1985) variable pore-size distribution idea with Biot's (1956 a,b) theory, predicted velocities were much lower than experimental velocity measurements.

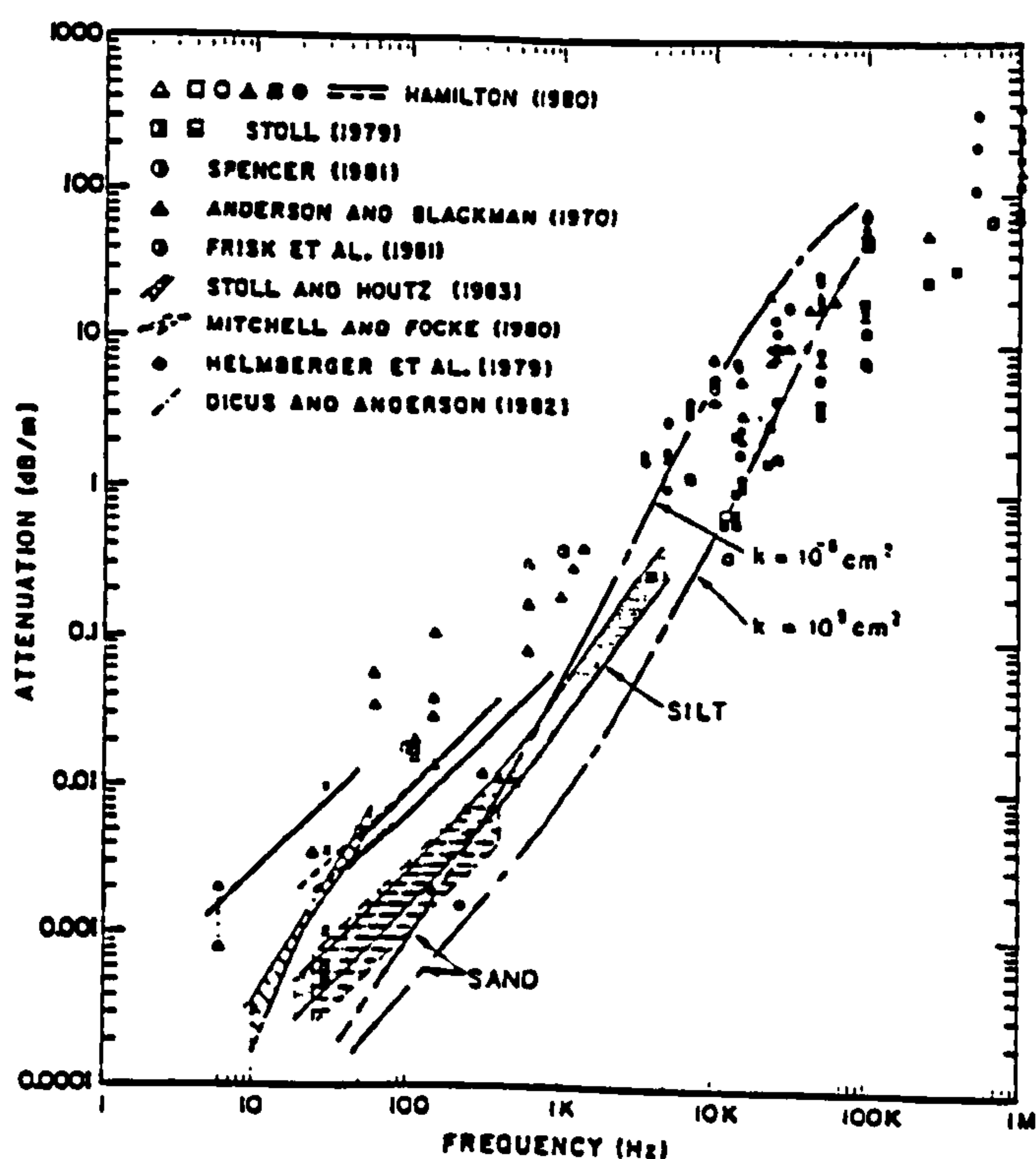
It was concluded that Biot's fast wave dispersion mechanism can explain some experimental trends, but prediction of the magnitude of fast wave dispersion may be difficult. The simplest method to calculate dispersion uses Biot's (1956a) theory, where only k_a and T are required in addition to the usual elastic - density parameters. Other modifications of this theory require that the pore-space be described in more detail, and are of limited practical benefit.

Having looked at Biot fast wave dispersion predictions and eliminated the less practical aspects in this chapter, the next step is to look at Biot attenuation (Chapter 8). Once the ability of Biot's theory to predict fast wave attenuation has been assessed, practical geoacoustic and hydrodynamic models of the sea-bed can be defined in Chapter 9, based on the studies of Chapters 2 to 8.

8.1 Introduction

A recent review by Stoll (1985) summarises experimental fast compressional wave attenuation data collected over the last two decades (see Figure 8.1). From these data, the empirical observation that the attenuation coefficient is linearly dependent upon frequency (Hamilton, 1972), appears to be roughly confirmed. Stoll (1985, 1974) prefers to use Biot's (1962a) theory to explain these data, and his attenuation predictions (shown in Figure 8.1) appear to give a fair fit. Stoll's (1985) analysis uses complex viscoelastic moduli (\hat{K}_b and \hat{G} - see Chapter 5). He uses resonant column measurements to give \hat{G} and assumes values for \hat{K}_b . As discussed in Chapter 5, it was concluded that the use of the more sophisticated Biot (1962a) theory was generally unwise in the absence of actual measurements for both \hat{K}_b and \hat{G} . This chapter is concerned with testing Biot's (1956 a,b) theory with minimal assumptions.

Figure 8.1 Experimental and predicted fast wave attenuation versus frequency for an assemblage of sediments, after Stoll (1985)



In earlier work Stoll (1974) and Stoll and Bryan (1970) noted that, without additional viscoelastic contributions, Biot's (1956 a,b) theory predicted attenuations substantially less than measured values. In more recent studies using modified versions of Biot's theory (e.g. McCann and McCann, 1985, Berryman, 1986 and Berryman and Thigpen, 1987), the authors argue that, providing the pore-space is appropriately defined, Biot's (1956 a,b) viscous flow attenuation mechanism can satisfactorily explain experimental attenuation results without the need of viscoelastic moduli. Further, White (1986) and Dunn (1986) showed that the experimental attenuation measurements of Spencer (1981) could be (partly) explained by using unmodified versions of Biot's (1956 a,b) theory. In order to rationalise such conflicting opinions, it was thought worthwhile to attempt to make some new attenuation measurements and analyse these (and other) experimental data using Biot's (1956 a,b) theory in various forms.

The following data sets, each denoted by a different code, are used to study Biot fast wave attenuation in this chapter; SAND_M5 - new experimental results for attenuation measured on a Berea sandstone sample; SAND_M2, SAND_M3 and SAND_M4 (see Chapter 7).

8.2 Extensional wave attenuation in porous rods

8.2.1 Low-frequency attenuation / modulus experimental set-up

In theory, longitudinal resonant column experiments can give information on the anelastic extensional properties of sediments and rocks. However, such experiments rarely give good experimental data for the complex Young's modulus \hat{E} (see discussion in Chapter 5 and also Stoll, 1985). An alternative approach for measuring the anelastic properties of (lithified) sandstone samples was described by Spencer (1981). Spencer's technique uses a set-up in which a sinusoidal stress is applied to the free end of a fixed-free rod of sandstone. Very accurate measurements are

made of the amplitude and phase of the applied stress and resultant strain. The phase difference between the stress and the strain gives a measurement of the attenuative properties of the sandstone (E_i), while the ratio of stress to strain gives E_r (see appendix 2). Therefore, \hat{E} can be determined over a fairly wide frequency band with the upper limit constrained by the fundamental resonance of the bar. This "forced vibration" method is more attractive than resonance methods, which are restricted to discrete frequencies. However, the strain amplitude of the vibrations must be kept below 10^{-4} otherwise plastic deformations will occur (see Chapter 5). Spencer (1981) claims an operational frequency range of 4-400 Hz (fundamental resonance occurs at >10 kHz for his sample's dimensions), with strain amplitudes near 10^{-7} .

A duplicate of Spencer's (1981) apparatus was set up with the aim of investigating the low frequency anelastic properties of various sandstones. The apparatus is described in 8.2.4 and schematic diagrams are shown in Figures 8.3 and 8.4 (full details are given by Spencer, 1981 and Manghnani et al., 1987). However, numerous problems were encountered in using the apparatus due to the extreme accuracy and sensitivity required of the measurements (see 8.2.4 and 8.2.5). In fact, some doubt is raised on the validity of Spencer's initial measurements. These points are discussed after a brief resume of Spencer's (1981) results and the analysis which White (1986) applied to them using Biot's (1956 a,b) theory.

8.2.2 The Biot-Gardner theory of extensional waves in porous rods

Gardner (1962) extended Biot's (1956 a,b) plane wave theory to the case of extensional waves in fluid saturated rods. Both fast and slow (extensional) waves propagate along the rod. The main feature of Gardner's (1962) analysis is that the attenuation of the fast and slow extensional

waves are strongly affected by the boundary conditions along the sides of the rod. If drainage is allowed across this boundary ("open pore" condition) then strong viscous-flow dissipation (Biot 1956 a,b) will occur across it. Conversely, if no drainage is allowed across the boundary ("closed pore" condition), then the normal viscous flow dissipation will occur resulting in normally attenuated fast and slow waves propagating extensionally along the rod. Therefore, Gardner (1962) calculates the velocity and attenuation of extensional waves for the closed boundary condition in the normal fashion (see Chapter 2 for compressional fast and slow waves), and applies a boundary correction for the open pore condition.

White (1986) and Dunn (1986) used Gardner's (1962) results to analyse Spencer's (1981) experimental data in the light of Biot's theory. Following White's simplification of Gardner's (1962) equations, it is possible to define the complex (fast wave) extensional modulus \hat{E} for the open pore boundary condition (see equations 8.1 to 8.4). Instead of re-calculating Gardner's (1962) complex boundary correction function ($\hat{\theta}$), White read off numerical values from Gardner's (1962) Figure 1. These values are shown in Table 8.1.

$$\hat{E} = 4G \cdot \frac{X - \theta_r + i\theta_i}{Y - \theta_r + i\theta_i} \quad 8.1$$

$$X = \left[\frac{3\bar{K}}{4} \right] \cdot \left[\frac{K_b}{G} + \frac{4}{3} \right] \cdot [\bar{K} - K_b]^{-1} \quad 8.2$$

$$Y = \left[\bar{K} + \frac{G}{3} \right] \cdot \left[\frac{K_b}{G} + \frac{4}{3} \right] \cdot [\bar{K} - K_b]^{-1} \quad 8.3$$

$$\bar{K} = K_b + \frac{\alpha^2}{Q} \quad 8.4$$

Table 8.1 Complex boundary correction function for a porous rod with an "open pore" boundary condition (after White, 1986)

$\frac{\omega r}{V_{2Z}}$	θ_r	θ_i
0.0	1.00	0.00
0.4	0.99	0.03
0.8	0.97	0.08
1.2	0.94	0.17
1.6	0.89	0.27
2.0	0.83	0.35
2.8	0.61	0.37
3.2	0.53	0.35
3.6	0.48	0.32
4.0	0.43	0.30
4.4	0.39	0.28
4.8	0.36	0.26
5.2	0.33	0.24
5.6	0.31	0.22
6.0	0.29	0.21

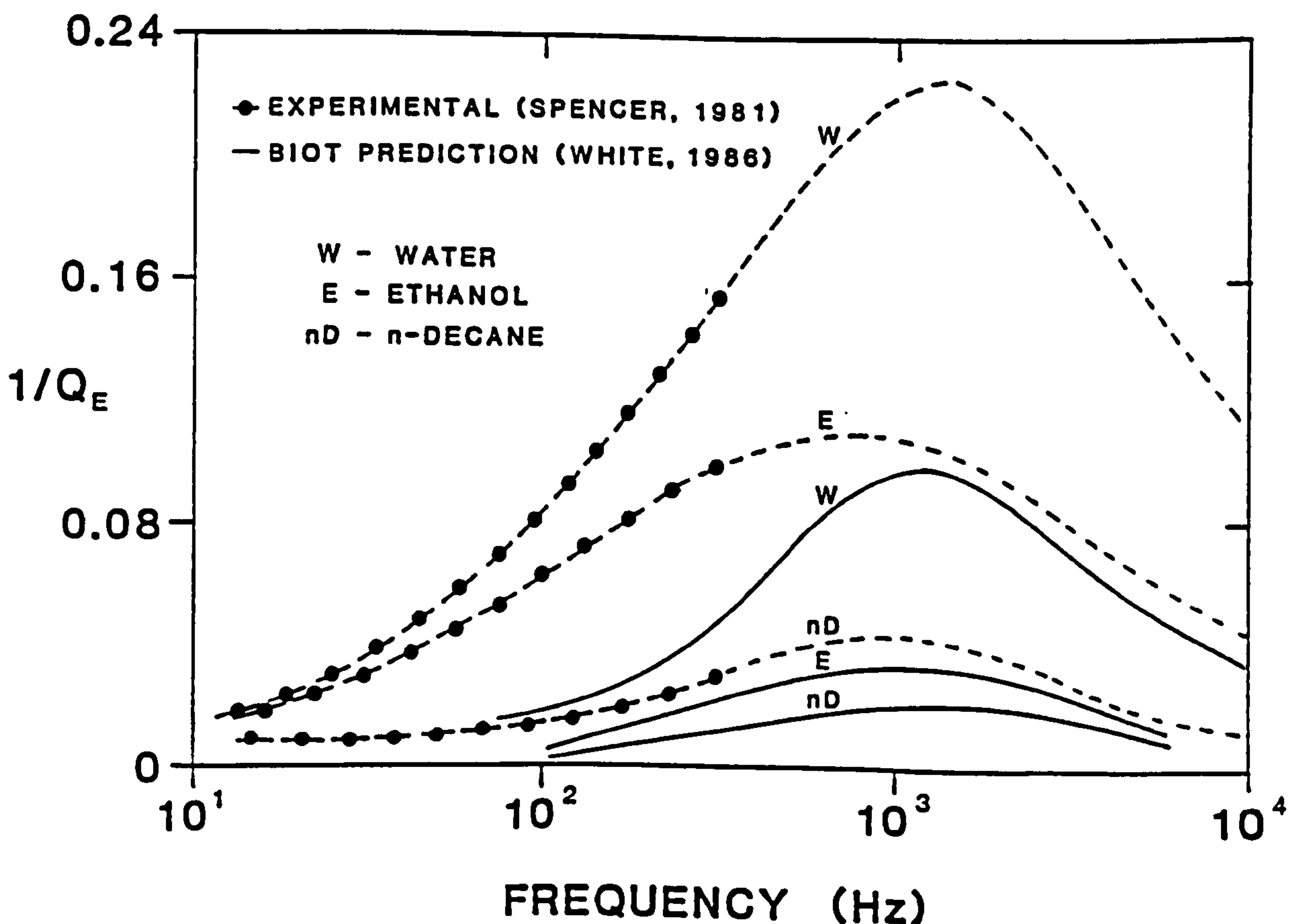
Here, $\frac{\omega r}{V_{2Z}}$ is a dimensionless parameter, ω is the circular frequency, r is the radius of the porous rod and V_{2Z} is the (low frequency) asymptote of the slow wave velocity, see Chapter 2

8.2.3 White's (1986) analysis of Spencer's (1981) results

White (1986) used equations similar to 8.1 to 8.4 and the results of Table 8.1 to analyse Spencer's (1981) experimental results for the extensional anelastic properties of Navajo sandstone saturated with different pore-fluids. White's predictions for E and $1/Q_E$ show similar trends to the experimental data of Spencer (see Figure 8.2). The main features of the predictions are that they show attenuation peaks centred near 1 kHz; these vary in magnitude and shift along the frequency axis depending on the viscosity of the saturating pore fluid. The experimental data can be interpreted as rising limbs of attenuation peaks. The data do not span any of these assumed peaks, but the centre frequency location and magnitude of these peaks depend upon the properties of the saturating fluid (Spencer, 1981).

White (1986) selects appropriate values of the physical properties of Navajo sandstone to allow good agreement between the predicted and experimental modulus dispersion curves (not shown). The attenuation predictions (Figure 8.2) are not so close, being under half the magnitude of the experimental data. However, the general trends of the experimental and predicted data sets are similar. In both White's (1986) and Spencer's (1981) analyses, the attenuation data are assumed to reach peaks around 1 kHz and then fall off. White attributes these attenuation peaks to the "open-boundary" dissipation from the Biot-Gardner theory, while Spencer (1981) attributes them to other (intrinsic) attenuation mechanisms. Neither arguments are completely convincing as the experimental data do not span any of the (assumed) peaks.

Figure 8.2 Experimental measurements (Spencer, 1981) and predicted $1/Q_E$ for a rod of Navajo sandstone with different saturating fluids, after White (1986)



8.2.4 Calibration of the low frequency attenuation apparatus

The low frequency modulus / attenuation apparatus shown in Figures 8.3 and 8.4 is an absolute measuring device. Providing that a sample is held rigidly within the sample jig, the only calibrations which are required are for the force and displacement transducers (E and F in Figure 8.3). Initial calibration constants for both these transducers were found to be within 5% of the manufacturers figures. The next step taken was to check that the apparatus could accurately determine the elastic properties of a standard aluminium rod. A sample of 6061-T440 aluminium with manufacturers values of $E = 69 \text{ GPa}$ and $1/Q \approx 0$ was used. If any phase lag between the applied stress and measured strain were detected and if the magnitude of stress to strain did not give a value close to 69 GPa, the apparatus would not be performing in the desired way.

An exhaustive series of experiments over a period of 14 months was carried out using the aluminium bar in the low frequency attenuation apparatus. Over this period, the apparatus only briefly gave consistent, almost correct, results for the aluminium bar. Some other results for a sandstone bar, which were made when the apparatus was well-behaved, are described in 8.2.5. However, the reasons for the apparatus suddenly becoming well behaved were not entirely understood. Overall, the system did not behave satisfactorily and it was not possible to determine the properties of the aluminium, or other calibration rods with accuracy and reliability. Some of the problems which were encountered are briefly described below, and a detailed account can be found in Manghnani et al. (1987).

The main problem with the device was inconsistency of results from consecutive runs which made identification and diagnosis of faults difficult. Some errors were traced to the processing of the data (aliasing and filtering problems), but apart from these, consistent results could

not be obtained from (what would appear to be) identical experimental conditions. Local environmental conditions were found to contribute somewhat to the erratic nature of results (temporal thermal drift, power surges and mechanical vibrations within the building), but the main cause was thought to lie within the device itself. As the device (Figure 8.3) worked at displacements of a few Angstroms and at stresses of a few kPa, very subtle differences within the experimental arrangement could cause variability of results from consecutive tests.

Without going into the detail of the cause and effect of altering the experimental set-up slightly, the following factors were found to strongly affect the consistency and accuracy of results: electrical leakage from the force transducer due to moisture - remedied by baking in an oven; the nature of the mechanical connections between force transducer, shaker and sample - altered by the amount of torque used to tighten connections and dust/dirt on the contact faces; the bonding between sample end caps and sample - compliance/repeatability of epoxy bond; and the static - dynamic compliance of the "fixed end" condition - altered by the torque used to secure the sample and dirt/grease within the threads of the locking rings. Most of these problems are mechanical in origin and are in series with the longitudinal measuring system. Perhaps the greatest problem is that of compliance within the "rigid fixed end". A static compliance correction can be introduced; however the magnitude of this correction was found to vary for no apparent reason. Furthermore, there was no way of testing whether or not the static correction was appropriate for the dynamic measurements. A strong criticism of Spencer's (1981) results is that he chose to ignore the effect of the measured compliance of his "rigid end" condition. Indeed, Spencer (personal communication) and Dunn (personal communication) noted that this problem appeared to be an experimental paradox!

Figure 8.3 Low frequency attenuation sample shaker

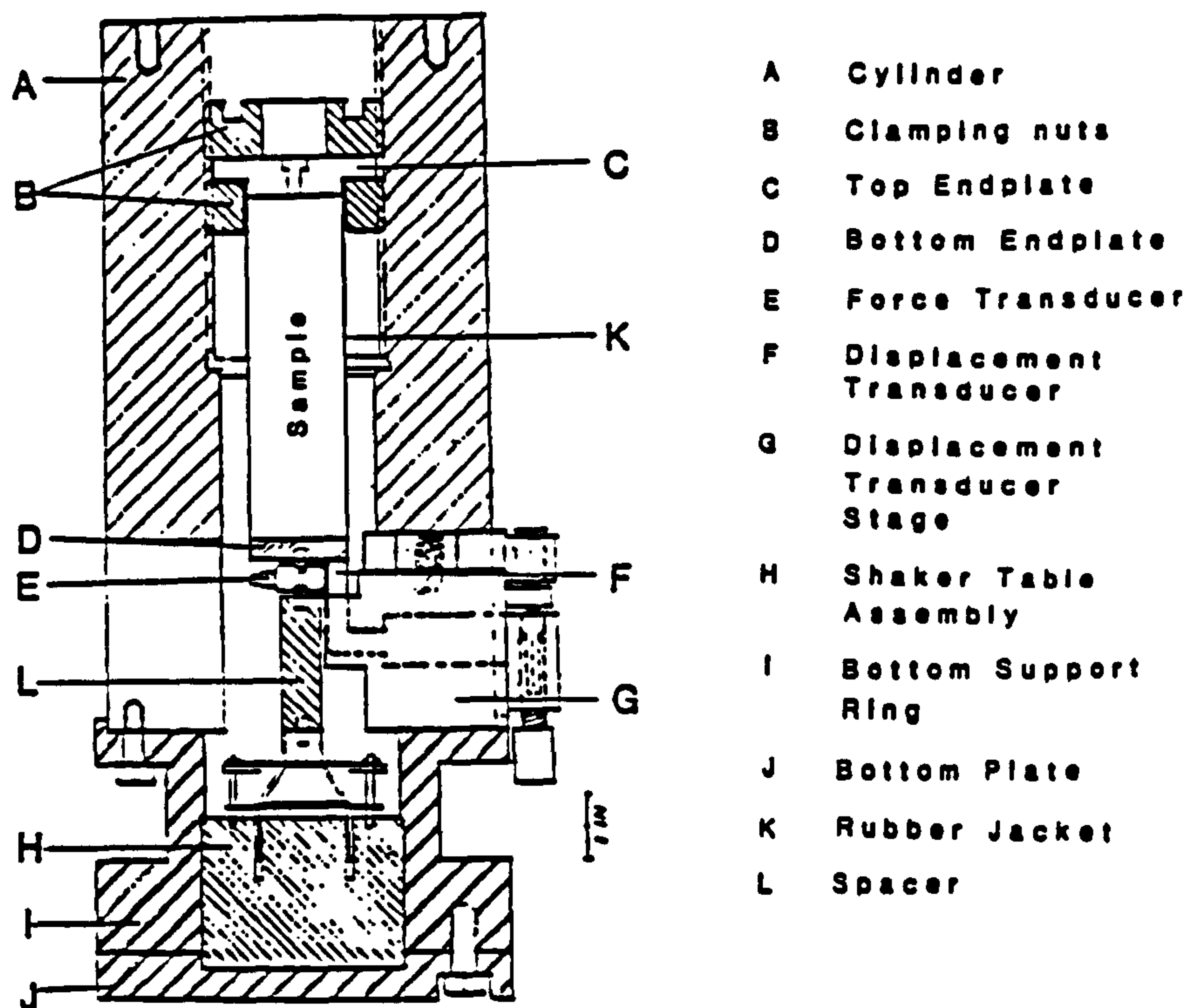
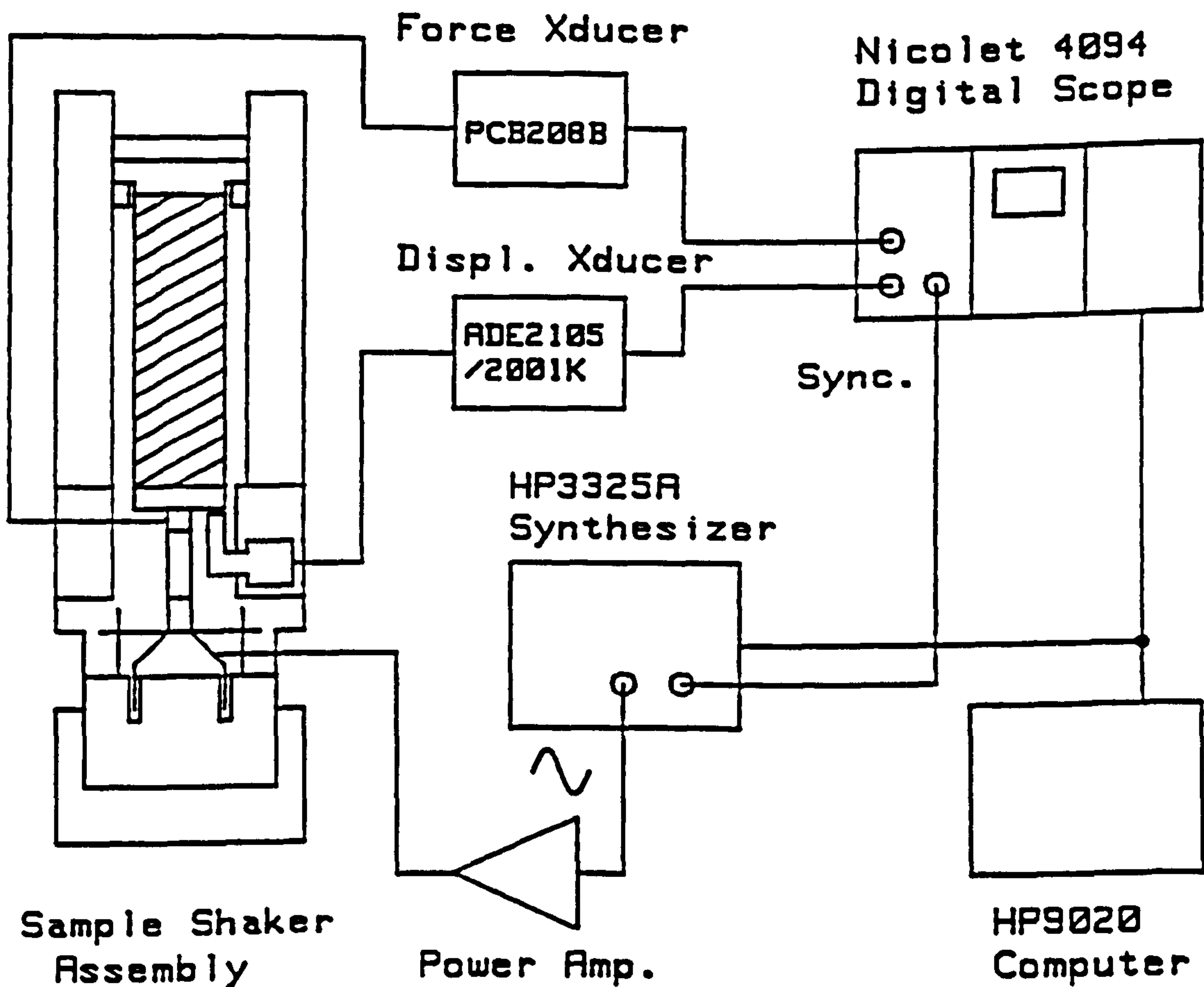


Figure 8.4 Schematic diagram of the low-frequency attenuation measuring system



8.2.5 Preliminary results for attenuation in wet and dry Berea sandstone samples

Some preliminary results for attenuation measurements made on a bar of Berea sandstone using the low frequency attenuation system (see 8.2.4) are shown in Figure 8.5. The measurements were made under both vacuum-dried and water-saturated conditions. For the dry sample the $1/Q_E$ appears to be fairly constant over the frequency range of 0.1 to 200 kHz. However, the data for the wet sample, although rather scattered, increase with increasing frequency, possibly rising to a peak at near 200 Hz. These attenuation results for wet and dry Berea sandstone are qualitatively similar to Spencer's (1981) results for wet and dry Navajo sandstone.

Also shown in Figure 8.5 are $1/Q_E$ predictions for the wet Berea sandstone sample made using the Biot-Gardner theory for the "open pore" condition (see 8.2.2). The parameters used for the predictions are taken from the data set SAND_M5, given in Table 8.2. The magnitude of the predicted attenuation is disappointingly low in comparison with the measured values. Also, the location of the predicted $1/Q_E$ peak is greater than 1 kHz; the measured values tend to a peak located well below 1 kHz.

Figure 8.5 $1/Q_E$ experimental measurements and predictions for a wet and dry Berea sandstone rod

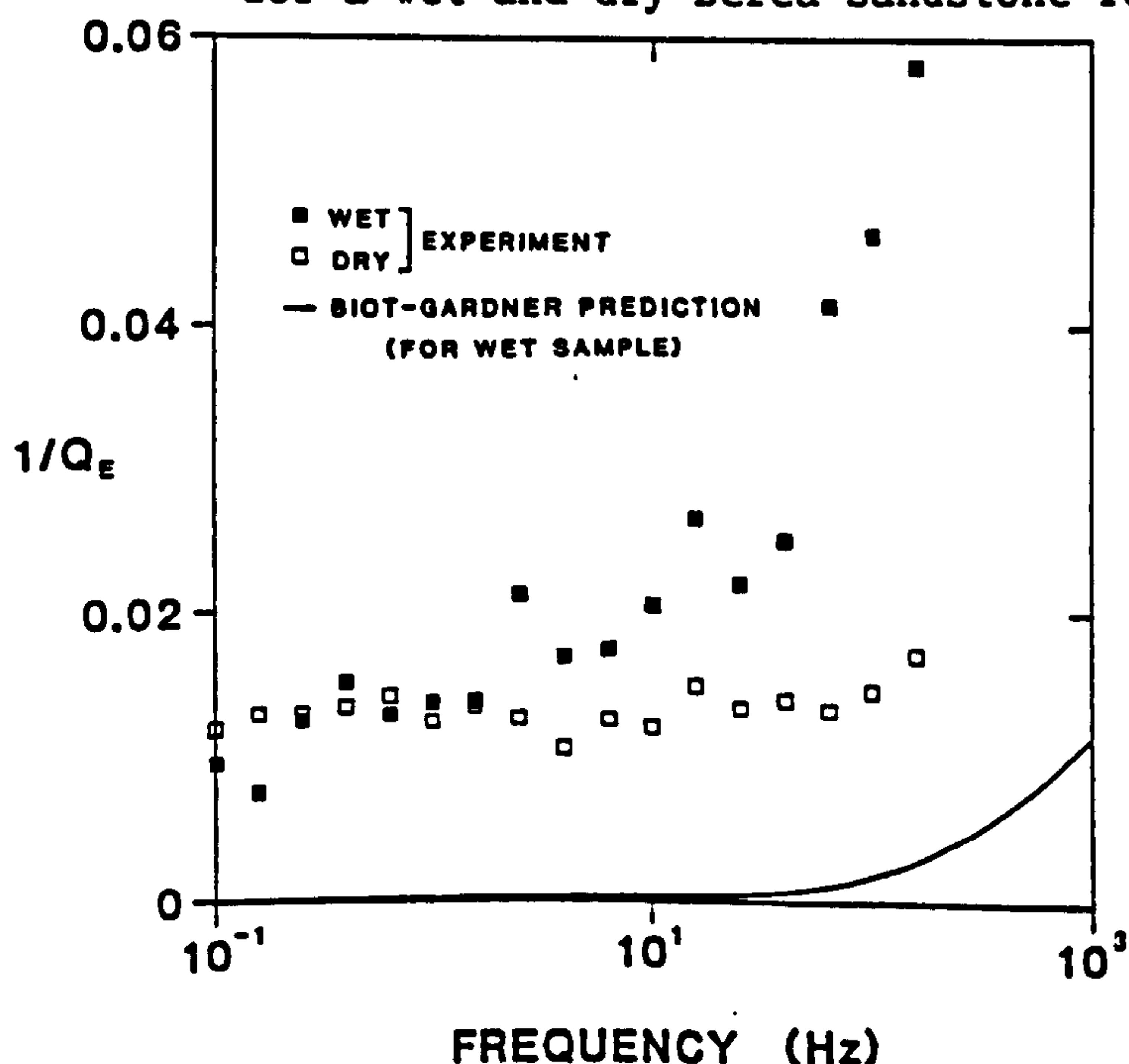


Table 8.2 Physical parameters characterising Berea sandstone
 - data set SAND_M5

1. Porosity	0.20
2. Fluid density	1000 kg/m ³
3. Grain density	2650 kg/m ³
4. Fluid modulus	(2.2).10 ⁹ Pa
5. Grain modulus	(3.5).10 ¹⁰ Pa
6. Dynamic viscosity	0.001 Pa.s
7. Circular frequency	0.1 to 1000 Hz
8. Shear modulus	(4.2).10 ⁹ Pa
9. Frame bulk modulus	(3.23).10 ⁹ Pa
10. Permeability	(1.0).10 ⁻¹³ m ²
11. Pore radius	(3.16).10 ⁻⁶ m
12. Tortuosity	2.5
13. Grain size	(150).10 ⁻⁶ m
1,8,9,10	Winkler (1983)
2-6	White (1986)
7	experimental range
11,12	equations 4.5, 4.6
13	Mesured

The discrepancy between the magnitudes of the predicted and measured attenuations seen in Figure 8.5 could be partially explained by the short-comings of the Biot-Gardner theory (see Figure 8.2). Alternatively, it could be argued that the other attenuation mechanisms are controlling the attenuation (Spencer, 1981, Murphy et al., 1986). Another possibility is that the measurements are not correct and the attenuation peak is simply a feature of the measuring system created by frequency variations in the compliance of the "fixed end"; there could be many reasons (see 8.2.4). Unfortunately, no clear-cut conclusions can be made from the measurements/analysis presented in 8.2.1 to 8.2.5. Therefore, it is desirable to use more reliable experimental attenuation data from the literature, to further investigate the ability of Biot's theory to predict compressional wave attenuation in sediments and rocks.

8.3 Factors affecting the magnitude and location of fast wave attenuation in the frequency band

8.3.1 Inferences from the characteristic equation

Unlike fast wave dispersion, the role of the various parameters controlling fast wave attenuation are not so easily deduced from the characteristic equation. If the frequency correction function $\hat{F}(\kappa)$ is ignored, the attenuation given by Biot's theory rises proportionally to the square of the frequency at low frequencies, trending to a constant value at very high frequencies (Stoll and Bryan, 1970). In this case of $\hat{F} = 1$, the magnitude of the high frequency attenuation coefficient asymptote (a_I) can be deduced from Geertsma and Smit's (1961) approximate analysis (note the following equation only holds if the inequality given by equation 2.27 is satisfied):

$$a_I = \left[\frac{\eta\pi}{k_a \cdot \rho\rho} \right] \cdot \frac{v_I^2 - v_z^2}{v_I^3 \cdot \left[\frac{T\rho_f}{\phi} - \frac{\rho_f^2}{\rho} \right]} \quad 8.5$$

From equation 8.5, it can be seen that both the permeability (k_a) and the fluid viscosity (η) affect the magnitude of the high frequency attenuation limit. Therefore, the simple inter-dependence of the frequency / permeability / viscosity terms, as noted for fast wave dispersion (in section 7.3.1), does not apply for fast wave attenuation. However, the situation is complicated further when $\hat{F}(\kappa)$ is introduced. In this case, the pore-size parameter and the frequency become important, and the attenuation no longer tends to a constant value at high frequencies, but increases as the square root of frequency (Stoll and Bryan, 1970).

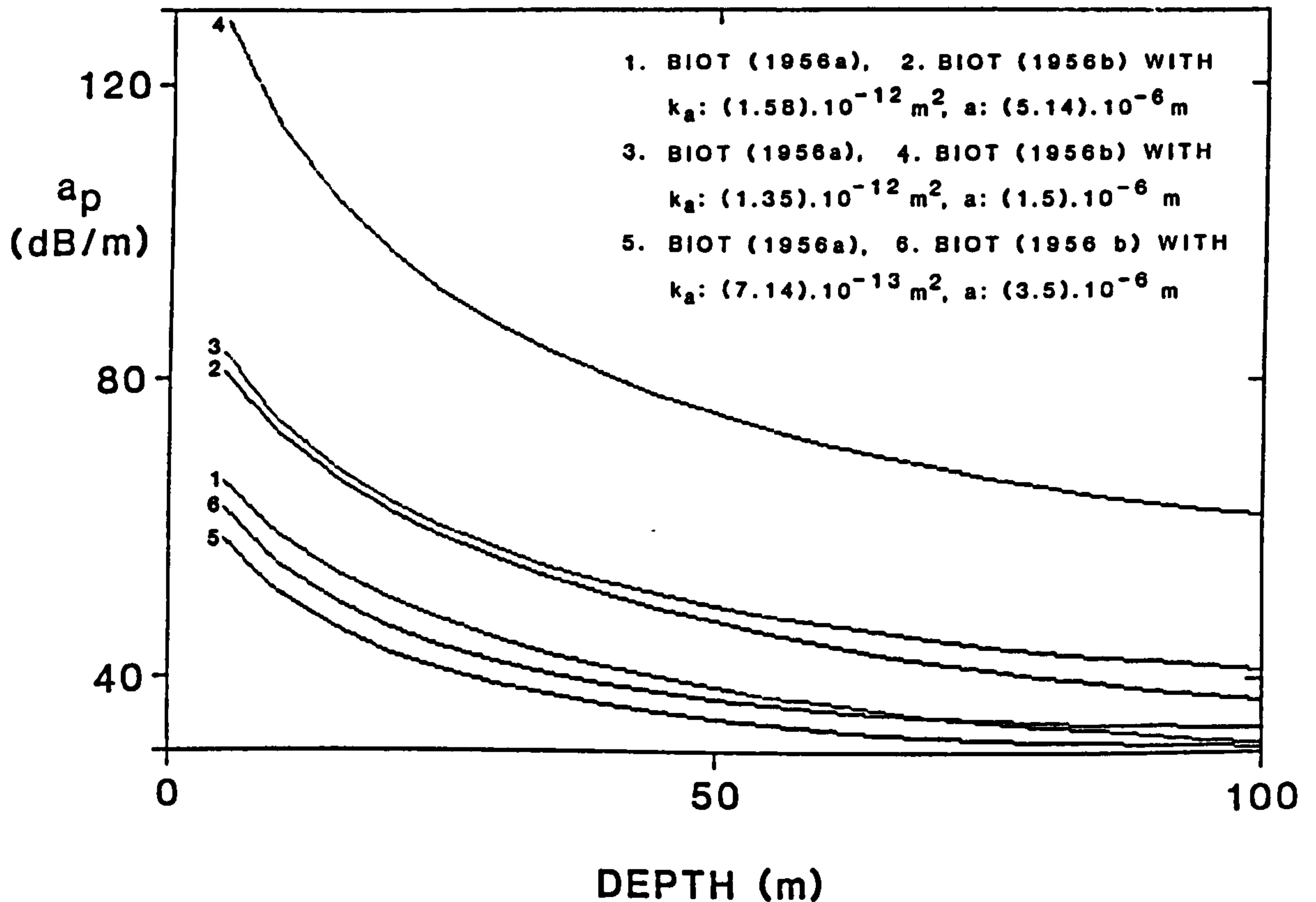
8.3.2 Effect of shear modulus, tortuosity and porosity

Due to the complex relationship that each parameter has with the fast wave attenuation (8.3.1), it is difficult to isolate the role which any one parameter has upon the shape of predicted attenuation versus frequency curves. Stoll and Bryan (1970) attempted to determine the relative importance of the porosity, tortuosity, permeability and pore-size parameters on attenuation - frequency predictions given by Biot's (1956 a,b) theory. They concluded that the tortuosity and porosity had a minor affect upon the shape and magnitude of predicted attenuation - frequency curves, but the pore-size and permeability parameters were significant. The role of these latter two parameters for attenuation predictions using some of the data sets introduced in Chapter 7 will be discussed in 8.3.3.

It is interesting to note the role which the shear modulus plays upon the magnitude of the fast wave attenuation. Using the data set CARB_M1 (Table 7.1), attenuation predictions are made to a depth of 100 metres, for a typical carbonate sediment sea-bed. The shear modulus and porosity are the only parameters which are allowed to vary with depth (see Table 7.1 for exact dependence).

Predicted attenuation - depth curves are shown in Figure 8.6 for three different permeability/pore size values (see 8.3.3). The decreases of predicted attenuations with depth are predominantly due to the increases of shear modulus with depth. This can be indirectly inferred from equation 8.5: as the shear modulus increases $(V_I^2 - V_Z^2)$ will decrease (see 7.2.2), and therefore the predicted attenuation will decrease. However, over the complete depth range, the predicted attenuation does not appear to be particularly sensitive to variations in the shear modulus.

Figure 8.6 a_p predictions versus depth for the data set CARB_M1



8.3.3 Effect of permeability and pore radius

Stoll and Bryan (1970) show some of the effects of varying the permeability and pore-radius on predicted fast wave attenuations. It is of interest to go one step further and compare attenuation predictions with experimental measurements for data sets which have already been analysed for fast wave dispersion. This is done for the data sets studied in Chapter 7, using similar ranges of permeability and pore size parameters which were used for the dispersion analysis. In Figure 8.6, predicted attenuations for the data set CARB_M1 are shown for the three permeability / pore size combinations:

$$A. k_a = (1.58) \cdot 10^{-12} \text{ m}^2, a = (5.1) \cdot 10^{-6} \text{ m}$$

$$B. k_a = (1.35) \cdot 10^{-13} \text{ m}^2, a = (1.5) \cdot 10^{-6} \text{ m}$$

$$C. k_a = (7.14) \cdot 10^{-13} \text{ m}^2, a = (3.5) \cdot 10^{-6} \text{ m}$$

For each of the three k_a a combinations, predictions are made using the frequency correction function (curves 2, 4, and 6 in Figure 8.6) and without the correction function (curves 1, 3 and 5 in Figure 8.6). Two interesting observations from Figure 8.6 can be made: firstly, that the predicted attenuations calculated using the frequency correction factor are greater than those calculated without; and secondly, that the largest k_a a combination (A, curves 1 and 2) does not yield the greatest attenuation. Therefore, it is apparent that the predicted attenuation will vary considerably with only minor changes in k_a and a .

In 7.3.4 the experimental dispersion measurements of Wingham (1985) were seen to fall between predictions using Biot's theory at permeabilities of $(2.17) \cdot 10^{-11} \text{ m}^2$ and $(4.68) \cdot 10^{-11} \text{ m}^2$ with respective pore sizes of $(6.34) \cdot 10^{-5}$ and $(4.17) \cdot 10^{-5} \text{ m}$ (see Figure 7.4). The predicted fast wave attenuations (with and without frequency correction function) using these permeability and pore-size values (along with values of the other parameters shown in Table 7.3) are shown in Figure 8.7. Also shown in Figure 8.7 are the attenuation measurements of Wingham (1985). The very important role of the frequency correction function can be seen: the attenuation predictions fall far below the measured values for the cases where the correction function is not used (curves 1 and 3). Further, when the frequency correction function is introduced, the pore-size can be seen to play an important part in controlling the magnitude of the predicted attenuation. The attenuation predictions when the frequency correction function is used, along with $k_a = (4.68) \cdot 10^{-11}$ and $a = (4.17) \cdot 10^{-5}$ (curve 2), are sufficiently close to the experimental measurements to claim a fair agreement; indeed, a better agreement could be obtained by suitable adjustment of k_a and a . The main point is that Biot's theory can offer an adequate explanation of the experimental dispersion and attenuation measurements of Wingham (1985), given appropriate values for k_a and a .

Figure 8.7 a_p experimental measurements (Wingham, 1985) and predictions versus frequency for the data set SAND_M2

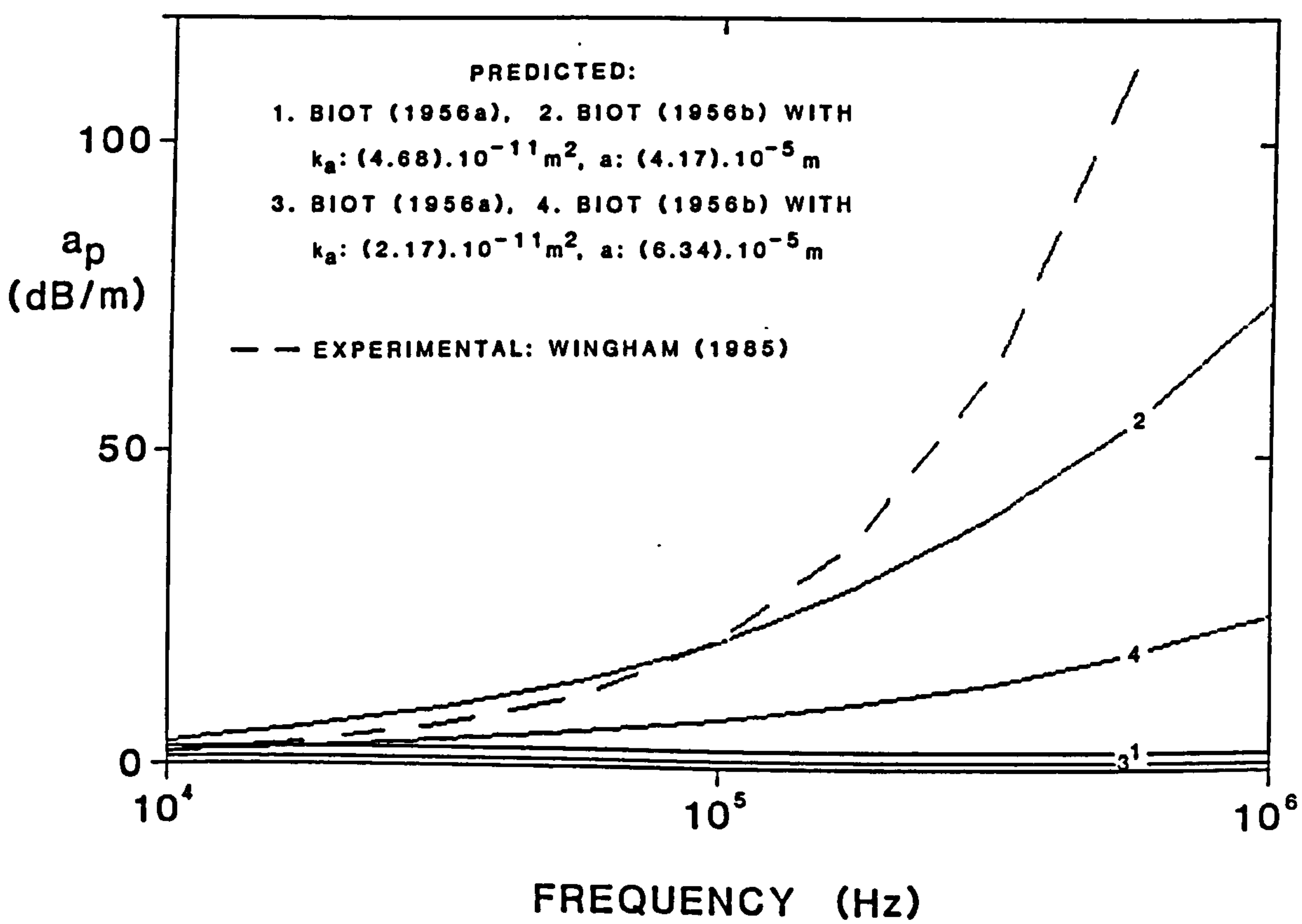
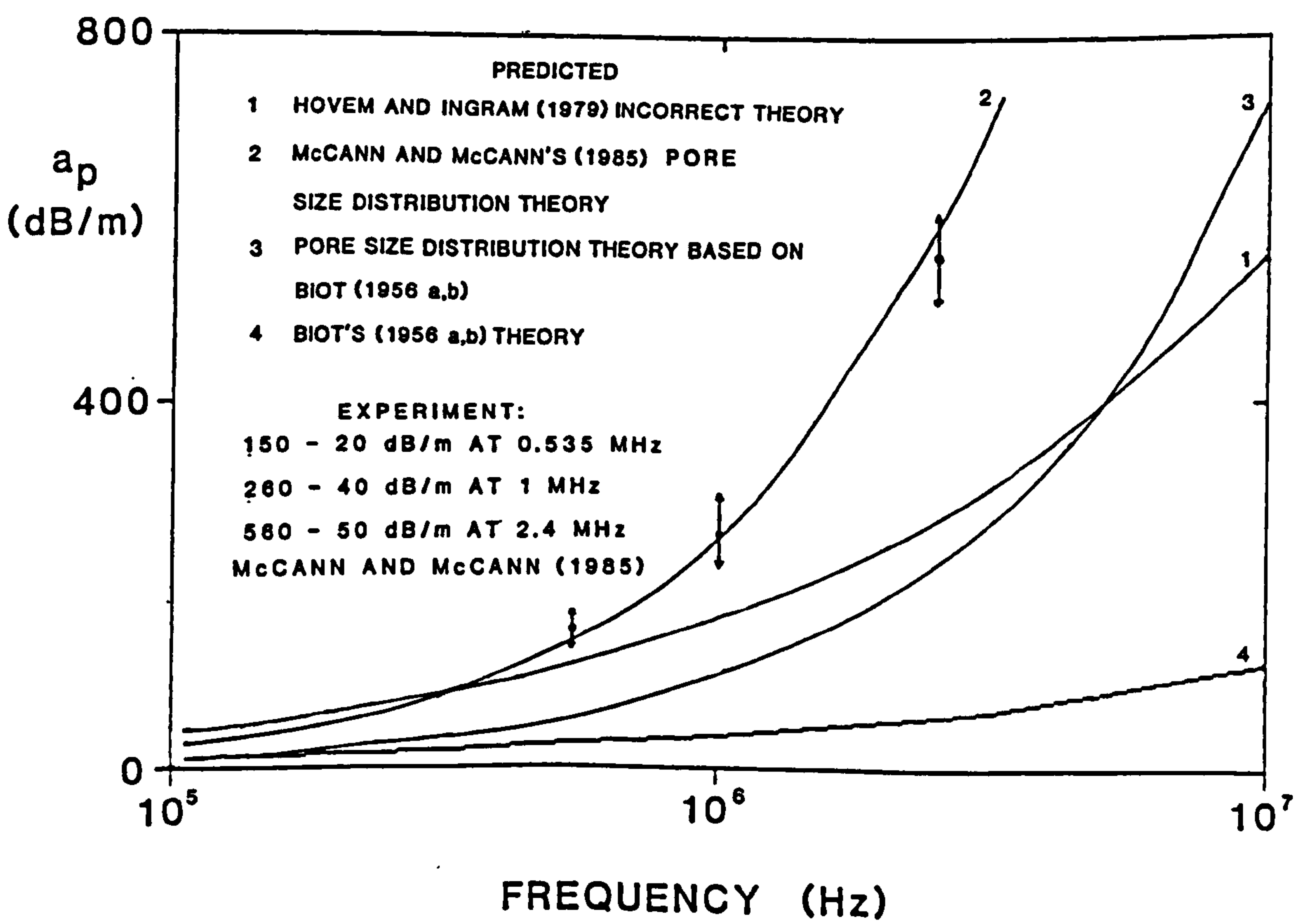


Figure 8.8 a_p experimental measurements (McCann and McCann, 1985) and predictions versus frequency for the data set SAND_M4

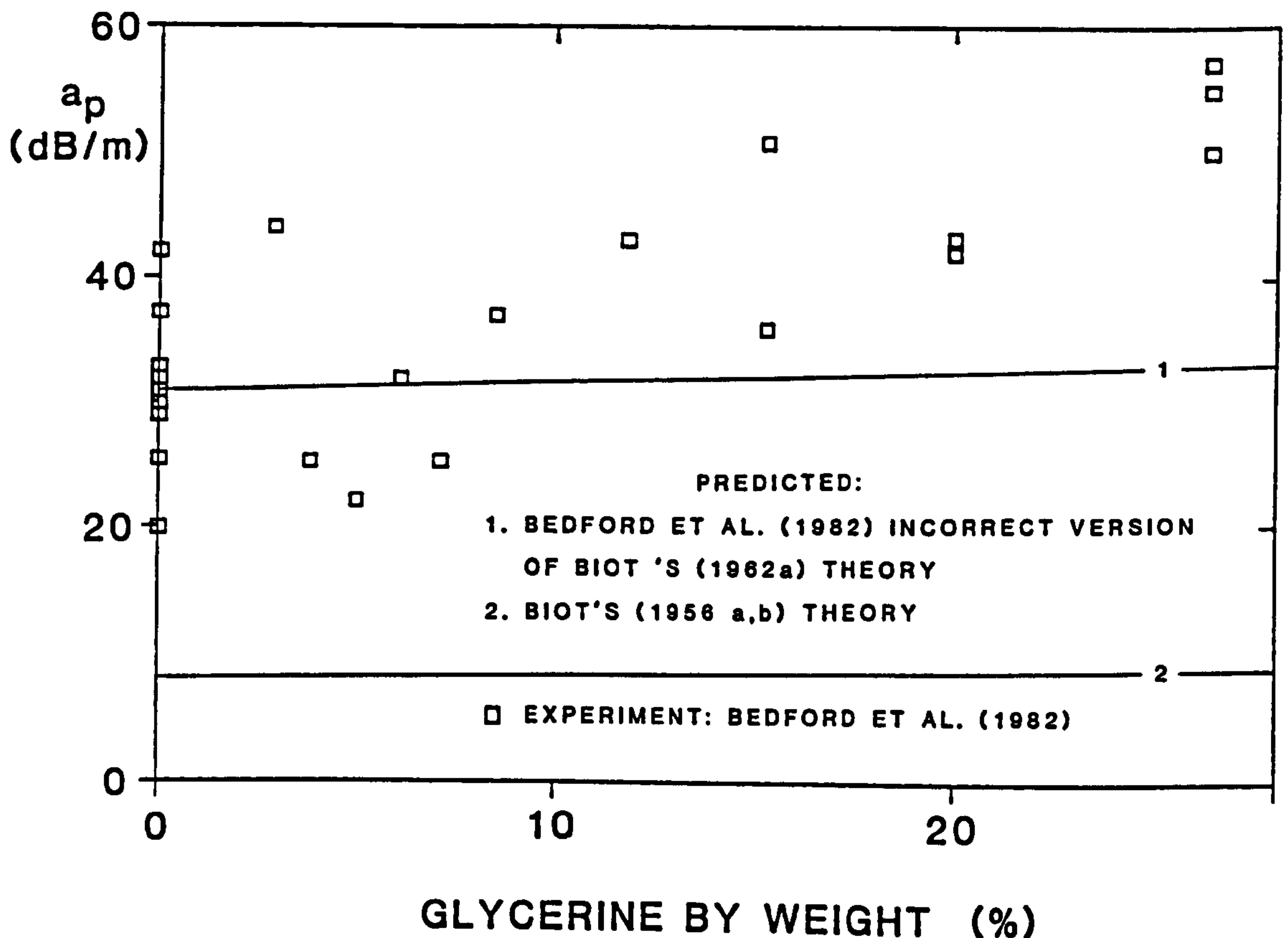


In 7.4.3 the experimental velocity measurements of McCann and McCann (1985) were compared with predictions from Biot's theory, and a modification of Biot's theory using a spectrum of pore-sizes and permeabilities. Fast compressional wave attenuation predictions using these two theories are shown in Figure 8.8, along with the experimental measurements of McCann and McCann (1985). Also shown are the attenuation predictions made by McCann and McCann (1985) (curve 2), which - due to the reasons outlined in 7.4.2 - are unfortunately incorrect. It can be seen that the attenuation prediction using the pore-size / permeability spectrum (curve 3) is closer to the experimental results than the prediction which uses a single pore size and single permeability (curve 4) without. However, the opposite is true for the dispersion analysis (Figure 7.6); with the single pore size prediction being closer than the value predicted using spectra of k_a and a .

8.3.4 Effect of fluid viscosity

Bedford et al. (1982) obtained compressional wave velocity and attenuation measurements in a fluid-saturated sand for different fluid viscosities. The velocity measurements were compared with predictions from Biot's theory in 7.3.5; predicted velocities were about 50 m/s lower than experimental values. The experimental attenuation measurements are shown along with predictions from Biot's (1956 a,b) theory (with the frequency correction fuction) in Figure 8.9 (curve 2). Also shown (curve 1) are the attenuation predictions given by Bedford et al. (1982), which are incorrect for the reasons outlined in 7.4.2. Again the fast compresional wave attenuation predictions from the correct version of Biot's (1956 a,b) theory are significantly less than the measured values.

Figure 8.9 a_p experimental measurements (Bedford et al., 1982) and predictions versus percentage glycerine saturation of the pore-fluid for the data set SAND_M4



8.4 A discussion on the applicability of Biot's theory to account for fast wave attenuation in sediments

Figure 8.1, from Stoll (1985) shows a fair agreement between Biot (1962a) attenuation predictions and experimental results. However, Stoll supplements the Biot (1956 a,b) viscous-flow attenuation by unspecified "internal friction" mechanisms, which require the use of complex anelastic moduli. In Chapter 5 it was shown that experimental determination of such anelastic frame moduli was very difficult and it was thought unwise to use estimated values for them for any predictive theory. Without the use of anelastic moduli, Stoll and Bryan (1970) showed that Biot (1956 a,b) attenuation predictions were significantly lower than experimental values. This observation is supported by the analysis of the data from Bedford et al. (1982) and McCann and McCann (1985) presented in 8.3.3 and 8.3.4.

White's (1985) analysis of Spencer's (1981) data shows that attenuation predictions using the Biot (1956 a,b) theory are lower than measured values for a sandstone bar infiltrated with different fluids (Figure 8.4). However, Biot's (1956a) viscous-flow mechanism does appear to explain some of Spencer's experimental observations especially the existence, frequency location and amplitude of an attenuation peak which changes character depending upon the viscosity of the infiltrating fluid. However, additional experiments along the same lines as those of Spencer's (see 8.2) did not satisfactorily confirm his observations of a viscosity/frequency dependent attenuation peak, and some doubt has to be raised as to the accuracy of Spencer's results.

Of the numerical examples studied, Biot's (1956 a,b) theory was only successful in accounting for both dispersion and attenuation in one case: the analysis of the data of Wingham (1985) (8.3.3). In this case, the values of the pore-size parameter and permeability were crucial in determining the character of the dispersion and attenuation versus frequency curves. As has been discussed in 7.5, these two parameters are by no means straightforward to experimentally determine, especially for the case of the pore-size parameter. Berryman and Thigpen (1987) argue that the difficulty associated with measuring these parameters does not detract from the validity of Biot's theory, and that discrepancies between measured and predicted fast wave attenuation are due to experimental shortcomings, rather than any inherent inadequacies within the theory. This may be so, but there is no way to support these claims.

It was argued (7.5) that dispersive effects could be somewhat accounted for because the critical controlling parameters (permeability and tortuosity) could be fairly well assessed by Darcian direct-flow (Chapter 4) and by electrical conductivity (Brown, 1980) experiments. The same cannot be said for Biot type attenuation, as it appears virtually

impossible (at current levels of technology) to experimentally measure the all important pore-size parameter. This does not mean that nothing has been gained from the analysis presented in this chapter: an understanding of the roles which each parameter plays in seismic wave propagation is an important step towards focussing attention on the critical parameters. This allows realistic guide-lines to be set for future studies and technical development. Clearly, significant experimental progress is required into numerically characterising the pore-space of sediments in terms of the tortuosity, micro-permeability, pore-size parameter etc. before firm attenuation predictions can be made with Biot's (1956 a,b) theory. However, there is a case to argue that present levels of experimental sophistication can provide fair predictions of dispersion using Biot's (1956 a,b) theory (see 7.5).

8.5 Summary

Experimental attempts have been made to measure low frequency attenuation in wet and dry sandstone rods. Verification of Biot-type attenuation was not possible due to additional attenuation contributions from the measuring system. The parameters controlling the magnitude, shape and location (in the frequency band) of fast wave attenuation predictions from Biot's theory have been studied, and the ability of the theory to account for measurements of attenuation was assessed.

Calibration of a low frequency attenuation experiment was attempted using a (virtually elastic) aluminium bar. Significant attenuation was introduced through the static and dynamic anelastic compliance of the "fixed end" condition. The intrinsic attenuation of samples of sandstone could not be reliably separated from the additional contributions from the system. Therefore, experimental attenuation results on wet and dry sandstone samples were well above predictions from Biot's

theory. Even the qualitative agreement between Biot predictions and experimental results that White (1986) demonstrated for a similar set of experiments could not be achieved. These attenuation measurements appear to be of little practical use.

An investigation into the importance of each of the parameters on predicted fast wave attenuation showed that the tortuosity and porosity had a minor effect. Increases in shear modulus reduce the amplitude of predicted attenuation slightly. However, the micro-permeability, pore-size parameter and viscosity all affect both the magnitude and shape of the attenuation versus frequency predictions from Biot's theory. If the frequency correction function is not employed, then the pore-size parameter is not important, and the predicted attenuation tends to an asymptotic value (which is controlled by the permeability) at high frequencies. However, empirical equations show that a near-linear increase of attenuation with frequency is expected and so a constant asymptotic attenuation limit is unrealistic. If the frequency correction function is used, the attenuation increases proportionally to the square root of the frequency. The exact dependence is controlled by the magnitudes of the pore-size parameter (a) and micro-permeability (k_a). The shape and amplitude of predicted attenuation versus frequency curves are very sensitive to slight variations in k_a and a .

In general, predicted attenuations, without the frequency correction function, are significantly lower than experimental measurements. Using the frequency correction function, predicted attenuations can be forced to match experimental measurements by using appropriate and reasonable values of k_a and a . However, the problem of accurately defining and experimentally measuring a still exists. In the studies of Biot dispersion in Chapter 7, it was concluded that it was best to ignore the frequency correction function, hence avoiding the need for

measurements of α . Excluding α means that the attenuation predictions of Biot's theory will be poor. Biot's viscous loss mechanism can qualitatively explain some attenuation phenomena, but the difficulties in measuring k_a and α make reliable attenuation predictions impracticable in most cases.

In this chapter it has been shown that experimental constraints make reliable measurements and predictions fast wave attenuation difficult. Furthermore, the studies of Chapter 7 have shown that dispersion predictions should be restricted to Biot's (1956a) theory. Using such observations from the studies on dynamic poroelasticity in Chapters 6 to 8, along with the results of experimental studies of the frame moduli and permeability of sediments in Chapters 4 and 5, and the studies of quasi-static poroelasticity from Chapters 2 and 3, practical geoacoustic and hydrodynamic models of the sea-bed can be defined in Chapter 9.

9.1 Introduction

Hamilton (1980) defines a geoacoustic model as "a model of the real sea-floor with emphasis on measured, extrapolated, and predicted values of those properties important in underwater acoustics and those aspects of geophysics involving sound transmission". For the purposes of this thesis, a qualifier is added to this definition: the appropriate properties must be characterised in the model to allow predictions of the fast compressional wave velocity from Biot's theory. A hydrodynamic model of the sea-bed can be defined similarly, except that it is pore-pressures which need to be predicted from Biot's theory. These definitions are thought more useful as they allow not only for a description of the sea-bed, but also give the necessary information for the stress response of the sea bed, and the inter-relationships between the measured physical properties, to be explored in a non-empirical way.

The predicted responses of such geoacoustic and hydrodynamic models of the sea-bed to the application of stresses will depend upon the frequency, magnitude and direction of the stresses and also any specified boundary conditions. For simplicity, the geoacoustic models will be used to study the propagation velocity of the fast compressional wave. Complex boundary value problems involving reflection and transmission of stress waves are not considered. Hydrodynamic models will be used to study the induced pore pressures for the boundary value problem of tidal loading of the sea-bed.

Using some of the results obtained from previous chapters, it is now possible to design geoacoustic and hydrodynamic models on which Biot's theory can be used. First, a brief review of the salient points from Chapters 2 to 8 will allow practical constraints on the sophistication of

the models to be made. Next, the experimental parameters for the models, required for the particular selected form of Biot's theory, are defined. Lastly, some simple studies are undertaken to examine the sensitivity of each of the experimental parameters on predictions from the theory. Once the experimental parameters required for well constrained models of the sea-bed have been isolated, appropriate measurements can be made on sea-bed samples. With the measurements made, Biot's theory can then be used to predict the response of the sea-bed to applied stresses. This is done for Sites 1 and 2 in Chapters 10 and 11.

9.2 Practical constraints on possible components of geoacoustic and hydrodynamic models

9.2.1 Permeability

The permeability was identified as an important parameter for controlling the magnitude of fast wave velocity dispersion in Chapter 7, and for controlling the magnitude of tidally-induced pore-pressures in Chapter 3. The experimental investigations of the permeability in Chapter 4 showed that it was possible to obtain a large range in measured permeability values for sediments from one location, depending upon the experimental methods used. It was suggested that one reason for this range in measurements was that each method determined the permeability over a different length scale (orders of magnitude in difference), and it was argued that the permeability would not necessarily remain the same over such lengths. Three different length-scale permeabilities were introduced: the large-scale permeability - referring to length scales of metres; the small-scale permeability - referring to length scales of millimetres, and the (dispersive) micro-permeability - referring to length scales of micrometres. Therefore, when using the permeability in a geoacoustic or hydrodynamic model the appropriate length scale must also be considered.

9.2.2 Elastic constants

The elastic constants G and K_b were shown to be important in determining the magnitude of tidally-induced pore-pressures in Chapter 3; important for controlling the magnitude of the fast and slow compressional wave velocities (Chapters 6 and 7), but of limited importance to the magnitude of fast wave attenuation (Chapter 8). The experimental studies in Chapter 5 showed that G could be determined fairly well by simple shear-wave bender techniques. However, the experiments of Chapters 5 and 8 showed it was very difficult to obtain reliable measurements of K_b , and only one set of data collected on a sand were of any use. These data give the approximate relationship $K_b = 2.17 G$, which is assumed to hold for most sea-bed sediment types (5.6.2). This assumption may well introduce significant uncertainties in geoacoustic or hydrodynamic models in which it is used.

The anelastic frequency dependence of \hat{G} and \hat{K}_b was also studied in Chapters 5 and 8. It was observed experimentally that possibly some low-frequency \hat{G} dispersion existed, with associated attenuation, but no clear-cut conclusions could be made. Also, no successful \hat{K}_b dispersion measurements were obtained making it impossible to define complex anelastic moduli \hat{G} and \hat{K}_b with confidence. This, therefore, rules out use of Biot's (1962 a,b) or the Biot-Stoll (Stoll, 1974) theories (which require \hat{G} and \hat{K}_b), leaving Biot's (1956 a,b) theory as the only viable option.

9.2.3 The slow wave

The studies of Chapter 6 showed that, in the acoustic - ultrasonic frequency range, the propagative slow wave is highly attenuative and can best be observed under a very limited set of circumstances. However, the results of Chapters 3 and 6 show that, at very low frequencies, the slow

wave is a simple pore-pressure diffusion process which is induced at boundaries of porous media where flow is allowed. In both high and low frequency cases the slow wave is predominantly a boundary effect which disappears a short distance from the boundary. Therefore, the length scale of the geoacoustic / hydrodynamic model must be considered, along with the boundary conditions, to determine if the slow wave is of any consequence.

For the case of a geacoustic model in which boundary conditions are not considered (see Chapters 10 and 11), the slow wave has no significance. Therefore, no attempt need be made to detect it, and the parameters which influence the magnitude of the slow wave (T , G and k_a) will not necessarily have to be included in the model (but T , G and k_a are in fact needed for fast wave considerations - see 9.2.4). Studies involving reflection from sea-bed lithological boundaries may need to take account of the generation of slow waves. For instance, the fast compressional wave reflection loss of the sea-bed will be increased if slow waves are considered: the generation of the slow wave causes an additional loss of energy which reduces the intensity of the reflected fast compressional wave. This process is somewhat similar to "shear wave softening" of the sea-bed (see Akal, 1980 and Stoll and Kan 1981).

The slow wave does play a part in the magnitude of pore-pressures predicted by Biot's theory for the case of tidal loading of the sea-bed. It's effect on the total induced pore pressure is controlled by the diffusive pore pressure boundary correction which depends upon the permeability of the sea-bed. The numerical examples given in Chapter 3 show that the diffusion effect occurs over a length-scale of metres. Therefore, in a hydrodynamic model where slow wave (diffusive) effects are to be studied, it is the global permeability term (see 9.2.1) which is required. Also, in-situ pore-pressure measurements are required if comparisons with the predictions from Biot's theory are to be made.

9.2.4 Fast wave and fast wave dispersion

Experimental measurements of the fast wave velocity are an essential component of geoacoustic models, but are not necessary for hydrodynamic models of the sea-bed. The importance of fast wave dispersion is somewhat debatable. From the results of Chapter 7 it was found that the magnitude of fast wave dispersion is controlled primarily by the tortuosity, the permeability and the shear modulus of sediments. For high permeability sediments with relatively low values of the shear modulus, significant dispersion of the order of 100 m/s is predicted by Biot's theory for fast waves in the acoustic - ultrasonic frequency range. Although none of the experimental data presented in Chapter 7 were taken over a wide enough frequency band to directly verify the magnitude of predicted dispersion, there was some indirect evidence to support Biot-type dispersion predictions. The indirect evidence consisted of variations in measured fast wave velocities for sediment samples of differing grain sizes and, hence, permeabilities: the finer sediments had low permeabilities and exhibited negligible velocity dispersion, whilst the converse occurred for the larger grain size sediments.

The roles of the frequency correction function $\hat{F}(\kappa)$ and the pore-size parameter a were investigated in 7.3.4. It was shown that when $\hat{F}(\kappa)$ was employed, the dispersion / frequency curve was smoothed out over a larger band-width, and that using $\hat{F}(\kappa)$ with varying a had a considerable affect upon the shape of this curve (Figure 7.4). However, it was concluded (7.5) that $\hat{F}(\kappa)$ and a could not be theoretically and experimentally tied down well enough to warrant their use.

As discussed in Chapters 4 and 7, the micro-permeability is most appropriate for the fast wave dispersion predictions. However, it was concluded that the best way to attempt to measure this micro-permeability was through 2-D imaging processing methods - which would be too complex

for routine use. In the absence of such measurements, the small-scale permeability can be used as an approximate substitute. Using this value, along with G and T, allows the magnitude of the predicted dispersion to be assessed at any one frequency. This dispersion could be important to geacoustic models, as laboratory-based fast wave measurements at ultrasonic frequencies may exhibit dispersion; whilst in-situ measurements at acoustic frequencies may be non-dispersive. Therefore, to check the applicability of (ultrasonic) laboratory fast wave data to geacoustic models, which are used for (acoustic) in-situ problems, dispersion should be considered. This is especially true for high permeability low shear modulus surficial sediments which exhibit maximum (Biot predicted) dispersion, and whose velocity structure happens to be of great importance to in-situ bottom interacting acoustic problems (Kuperman and Jensen, 1980).

9.2.5 Fast wave attenuation

Fast wave attenuation is a necessary component of any geacoustic model which is used to study problems involving the intensity of fast waves. However, the results of Chapter 8 show that Biot fast wave attenuation depends primarily upon the micro-permeability and pore-size parameters. Both micro-permeability and an average value for the pore-size parameter could be determined by complex image analysis of the sediment. In the absence of such measurements, it was shown in Chapter 8 that Biot type fast wave attenuation predictions (based on the small-scale permeability and a semi-empirically derived pore size) were not in that good agreement with experimental attenuation measurements. The limitations of the experimental measurements for the pore-size and micro-permeability mean that it is unwise to attempt to include these parameters in practical geacoustic models for making Biot attenuation predictions.

The practical problems in Chapters 10 and 11 which use geoaoustic models, do not require fast wave intensity information. Therefore, the complexities and uncertainties introduced by fast wave attenuation are avoided by not including this parameter in geoaoustic (or hydrodynamic) models.

9.3 The components of geoaoustic and hydrodynamic models

9.3.1 A geoaoustic model for use with Biot's theory

In section 9.1, the following parameters were isolated as being important for geoaoustic models:

V_p - compressional wave velocity (measured at frequency f)

G - shear modulus

K_b - frame bulk modulus

T - tortuosity

k_a - micro-permeability

ϕ - porosity

Parameters which are of secondary importance are:

ρ_f - fluid density

ρ_s - solids density

K_f - fluid bulk modulus

K_s - solid bulk modulus

η - fluid viscosity

It is possible to construct a geoaoustic model of the sea-bed, if all these parameters are known. Using such a model it is possible to use Biot's theory to predict the ~~the~~ fast compressional wave velocity at a given frequency. In addition, the geoaoustic model may act as a data base which can be applied to various practical problems. Such problems involving acoustical interactions with the sea bed may be very widespread and complex in character (see Kuperman and Jensen, 1980 and Akal and Berkson, 1986).

As the sea-bed commonly comprises a series of sedimentary layers, a realistic geoacoustic model of the sea-bed will have to account for this layering. Each layer (of known thickness) will be defined by a change in the lithology of the sea-bed. For each layer, the variation of the 11 parameters (given above) with depth, should be known. In practice, K_f , ρ_f and η can be found from tables (if the appropriate water depth is known), and if the composition of the sediments is known (and remains simple and constant), then ρ_s and K_s can also be looked up. These five parameters are assumed to remain constant with depth, as will K_b , which will commonly have to be assumed itself.

Measurements of the other six parameters should be made at different depths within each layer. This is most simply achieved by conducting laboratory experiments on samples taken from cores of the sea-bed. The experimental measurements taken in each layer should be taken at appropriate intervals such that any sharp changes of a parameter, or any gradual gradient of a parameter within the layer, are recognised. As well as showing significant variations of a parameter within a layer, average values should be given also. Whether the averaged values or the individual measurements are used will depend upon the problem for which the model is intended. Note, it is sometimes problematic to use the individual measurements as they are often collected at different depths within layers. This introduces interpolation / smoothing / filtering problems especially if a large amount of experimental data exists for each parameter.

An additional useful component for geoacoustic models is an effective stress versus depth profile. This profile allows any experimental data of a parameter (for example the shear modulus) collected as a function of effective stress, to be translated to an equivalent in-situ depth.

If the porosity is known as a function of depth $\phi(z)$, and the grain and fluid densities (ρ_s and ρ_f) are also known, then the effective stress (σ_{eff}) at a depth z , is given by:

$$\sigma_{eff}(z) = \int_0^z [1-\phi(z)] \cdot [\rho_s - \rho_f] \cdot [9.81] dz \quad 9.1$$

Other information, in addition to the effective stress profile, such as the water depth, geographical location and the lithology of the sea-bed / basement are important. Also, some corrections of the laboratory-determined experimental data may be required to give a more accurate representation of in-situ conditions. Pressure and temperature corrections have to be applied to V_p , pressure corrections to V_s measurements, and porosity rebound corrections to laboratory ϕ values. A very important quantity to know is the ratio $V_{lab} : V_{in-situ}$, where V_{lab} is the velocity of sound in sea-water measured in the laboratory and $V_{in-situ}$ is the velocity of sound in the sea-water at the bottom of the sea. Using this ratio, V_p measurements collected in the laboratory can be temperature corrected to in-situ conditions (Hamilton, 1971).

If the geacoustic model is to be used not just as a descriptive data base, but is to be applied to a specific practical problem at the geographical location, then additional measurements which relate to the problem are required. For example, Haumeder (1985) uses bottom reflection loss measurements collected from the Mediterranean sea-bed. He constructs a geoacoustical model of the sea-bed at this location, predicts frequency dependent bottom reflection losses (based on Biot's 1956 a,b theory), and compares predicted with experimental results.

When constructing a geoacoustic model for a specific practical problem, careful consideration of the type of problem and the length scales involved must be made. For example, in Chapter 11 a geoacoustic model is used to create a synthetic seismogram for a pulse with frequency near 50 Hz. The wavelength of such a pulse is of the order of 30 metres; so, for normal incidence, the absolute minimum depth separation required of experimental data points is 15 metres; for such an example it is pointless constructing a very detailed geoacoustic model with data points every 10 cm (say). Furthermore, for this same example, the computer program which calculates the synthetic seismogram does not handle attenuation losses of energy in the sea-bed. Therefore information on the attenuative properties of the sea-bed are not required.

9.3.2 A hydrodynamic model for use with Biot's theory

In Chapter 3, an expression (equation 3.12) was developed which gave the pore-pressure induced in the sea-bed due to hydrodynamic tidal pressures. This expression must be used with a rather straightforward hydrodynamic model of the sea-bed; one in which the component parameters are constant with depth. The physical constants required are: G , K_b , k_a , ϕ , K_f , K_s , η and ω . However, for near-surface sediments the following inequality applies: $G, K_b \ll K_f < K_s$. In practice this makes the K_s terms negligible in equations 2.7 and 2.8 and it is possible to make the simplifications $\alpha = 1$ and $1/Q = \phi/K_f$. Therefore, only seven constants are required, and this can be further reduced to four; with ω being simply calculated and K_f and η taken from tables. A simple hydrodynamic model of the sea-bed can be constructed if average values of the four constants G , K_b , ϕ and k_a are known. Such a simple model can be constructed by using a table of values (e.g. Table 4.3).

The permeability term required for the hydrodynamic model is the large-scale kind (see Chapter 4), which will include the effect of any fissures or cracks or channels which exist in the sea-bed. As for geoacoustic models, it is important to consider the length-scale of deformations, in order to give guide lines for the amount and separation of measurements. The numerical examples in Chapter 3 showed that, for a typical deep-sea sea-bed, the slow wave / diffusion component of the total induced pore-pressure was restricted to the near surface sediments (less than 10 metres). Further, the maximum depth of experimental pore pressures measured by the instrument PUPPI is 6 metres (see Table 4.2). Therefore, it is appropriate to restrict measurements to the upper ten metres (this also allows the simplifications $\alpha = 1$ and $1/Q = \phi/K_f$), and to construct a hydrodynamic model from average values of these physical constants.

One further important consideration in constructing a hydrodynamic model is to account for the presence of any free-gas which may exist in the sea-bed. As was shown in Chapter 2, free-gas in the pore fluid significantly decreases the effective fluid modulus giving dramatic reductions in the predicted pore-pressures in the sea-bed (Figure 2.3). However, as the water depth increases free gas present in the pore fluid is forced into solution. For the deep-sea environment, the great hydrostatic pressure will ensure that the volume (and effect) of any free gas will be negligible. Of course, free gas will play havoc with any geoacoustic model of the sea-bed as well. Some experimental and theoretical attempts have been made to study the behaviour of acoustic waves in partially saturated sediments and rocks (e.g. Murphy, 1982). Such studies have shown that, for compressional waves, the attenuation will increase dramatically if any gas is present, and the velocity will decrease significantly. To avoid such complications, both geoacoustic and hydrodynamic models of the sea-bed will be restricted to deep-sea environments where the free-gas problem is not important.

9.4 Sensitivity of predictions from Biot's theory to the uncertainties in the parameters in geacoustic and hydrodynamic models

9.4.1 Sensitivity analysis for geacoustic model

In Chapters 10 and 11, Biot's theory will be used in conjunction with geacoustic models (for two different locations) to predict compressional wave velocity at different depths in the sea-bed. Having isolated the significant parameters for this task in 9.1, it is useful to attempt to rank them in order of importance. The numerical examples of Chapter 7 have already shown that the tortuosity, permeability and shear modulus are important in influencing the magnitude of compressional wave dispersion; i.e. controlling the quantity $V_1 - V_z$, where V_z is the (non-dispersive) zero-frequency limit predicted velocity and V_1 is the predicted velocity at some finite frequency (f). However, there may well be the possibility that the uncertainty in the prediction of V_z (ΔV_z), is in fact greater than $V_1 - V_z$. In such a case, the uncertainty involved in predicting V_z will be such that any dispersive effects (if present) could lie within the uncertainty band of V_z , and hence need not be considered.

The most appropriate method for determining the sensitivity of each of the parameters upon the uncertainty in the zero frequency velocity limit (equation 2.24) is to apply a standard error analysis (e.g. Squires, 1968) to equations 2.6 - 2.8 and equation 2.24. Such an analysis requires that expressions giving the partial differentials of the equation for V_z , with respect to each parameter, be established. Also, an estimate for the uncertainty associated with each parameter is required. For example, equations 2.6 - 2.8 are differentiated with respect to the porosity (say) to give $\partial Q / \partial \phi$, $\partial a_b / \partial \phi$, etc. Then, equation 2.24 is differentiated with respect to Q , a_b , etc. to give $\partial V_z / \partial Q$, $\partial V_z / \partial a_b$, etc. These results can be combined (using the chain-rule) to give $\partial V_z / \partial \phi$. The error or uncertainty of V_z calculated with a porosity of ϕ_1 , with an uncertainty of $\Delta \phi_1$, is simply given by $\sqrt{(\Delta \phi_1)^2 \cdot (\partial V_z / \partial \phi)^2}$.

A similar analysis can be applied for the other parameters G , K_b , K_s , K_f , ρ_f and ρ_s . The total uncertainty in V_z then is given by:

$$\Delta V_z = \left[\left[\frac{\partial V}{\partial G} \right]^2 \cdot \Delta G_1^2 + \left[\frac{\partial V}{\partial \phi} \right]^2 \cdot \Delta \phi_1^2 + \dots \right]^{1/2} \quad 9.2$$

The normalised uncertainty which each parameter contributes to the total uncertainty in V_z (ΔV_z) is defined (for the porosity, for example) by:

$$U_\phi = \left[\frac{\partial V}{\partial \phi} \right]^2 \cdot \left[\Delta \phi_1 \right]^2 \cdot \left[1/\Delta V_z \right]^2 \quad 9.3$$

The other normalised uncertainties U_G , etc. can be defined likewise, and the sum of all these normalised uncertainties will be equal to one.

The equations required to perform such sensitivity / uncertainty analysis are lengthy and are not suitable for explicit expression. These equations are summarised in a computer code which is given in Appendix 5. It should be possible to extend this analysis to the roots of the characteristic equation (equations 2.18 - 2.20) at frequencies other than the zero frequency limit. However, this would require very lengthy algebraic manipulations to obtain the required partial differential equations. A simpler way to look at the sensitivity of each parameter individually at non-limiting frequencies is to include the uncertainties in calculations of the velocity. For example, to find ΔV_{ϕ_1} , two calculations are performed using $\phi_1 - \Delta \phi_1$ and $\phi_1 + \Delta \phi_1$ giving $V_{\phi_1 - \Delta \phi_1}$ and $V_{\phi_1 + \Delta \phi_1}$. Therefore it is possible to write:

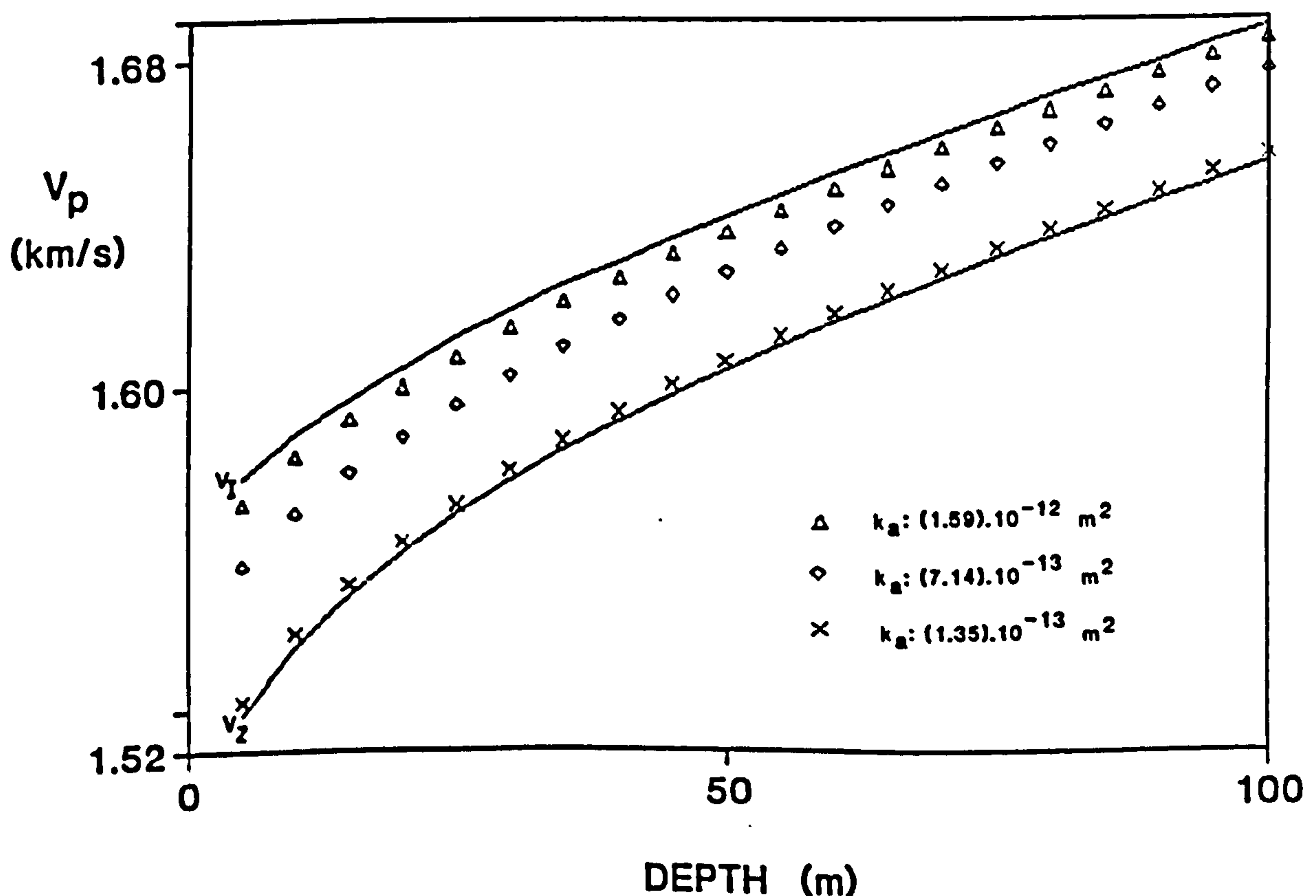
$$\Delta V_z \approx \frac{1}{2} \cdot \left[V_{\phi_1 + \Delta \phi_1} - V_{\phi_1 - \Delta \phi_1} \right] \quad 9.4$$

This procedure is recommended for simple expressions. However, it would prove to be rather tedious to do this for all the permutations and combinations of the 12 parameters and their uncertainties, required for solution of the characteristic equation at non-limiting frequencies.

9.4.2 A numerical example of a geoaoustic model for a carbonate sea-bed

In Chapters 7 and 8 the data set CARB_M1 was used to study dispersion and attenuation in near-surface sediments for a carbonate sea-bed. In Chapter 7, fast wave dispersion was predicted to a depth of 10 metres and the effect of shear modulus and porosity gradients upon predicted velocities for three different permeability values was shown (Figure 7.2). In Figure 9.1, the same analysis is extended to a depth of 100 metres: the increases in shear modulus again strongly influence the predicted velocities.

Figure 9.1 V_p predictions for versus depths up to 100 metres for the data set CARB_M1



It is of interest to find the uncertainty in the predicted zero frequency velocity limit for the predictions shown in Figure 9.1. The sensitivity analysis described in 9.4.1 was applied to the data set CARB_M1. The parameters required to calculate the zero frequency velocity are given in Table 7.1. Each parameter has some uncertainty associated with it and the following values were assigned to the relevant parameters; $\Delta\phi = 0.05\phi$, $\Delta K_f = 0.01K_f$, $\Delta K_s = 0.2K_s$, $\Delta G = 0.25G$, $\Delta K_b = 0.25K_b$, $\Delta\rho_f = 0.01\rho_f$ and $\Delta\rho_s = 0.01\rho_s$. The uncertainty in V_z (ΔV_z) and the normalised uncertainties U_ϕ , U_G , etc. were calculated using equations 9.2 and 9.3. The predicted values for V_z , $V_z + \Delta V_z$ and $V_z - \Delta V_z$ are shown in Figure 9.2 to a depth of 100 metres and the normalised uncertainties are likewise shown in Figure 9.3.

Looking at Figure 9.2, it can be seen that the uncertainty in V_z is less than 13 m/s for surficial sediments, increasing to 29 m/s at a depth of 100 metres. This uncertainty completely swamps the dispersive effects for the permeability of $(1.35) \cdot 10^{-13} \text{ m}^2$ shown by the crosses in Figure 9.1. The uncertainty in V_z also covers the dispersive effects for the permeability of $(7.1) \cdot 10^{-13} \text{ m}^2$ (diamonds), at depths greater than 50 metres, and it also threatens the dispersive effects of the permeability of $(1.59) \cdot 10^{-12} \text{ m}^2$ (triangles) at depths near 100 metres. Therefore, for this particular set of uncertainties in the parameters for the geoacoustic model (listed above), dispersive effects will only be discerned if the permeability is high enough to put the calculated dispersive velocity (V_1) close to the infinite frequency limit. Further, any residual dispersive effect ($V_1 - V_z - \Delta V_z$), will be most apparent in near surface sediments.

Figure 9.3 shows how the various normalised uncertainties contribute to the total uncertainty in V_z for depths up to 100 metres. The normalised uncertainties have been added accumulatively in Figure 9.3, so the magnitude of any one normalised uncertainty is given by the thickness

Figure 9.2 Uncertainty in the V_z prediction versus depth for the data set CARB_M1

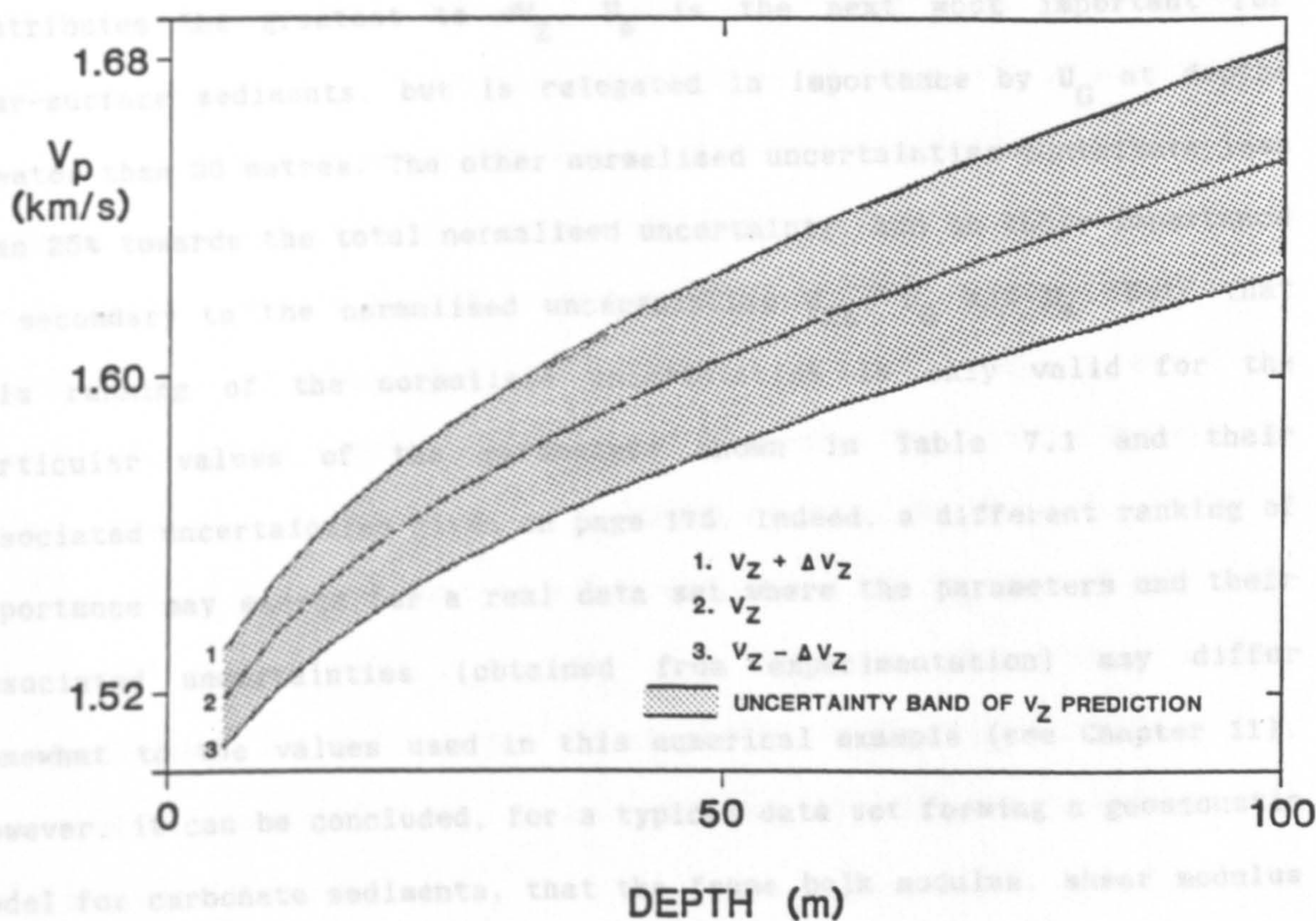
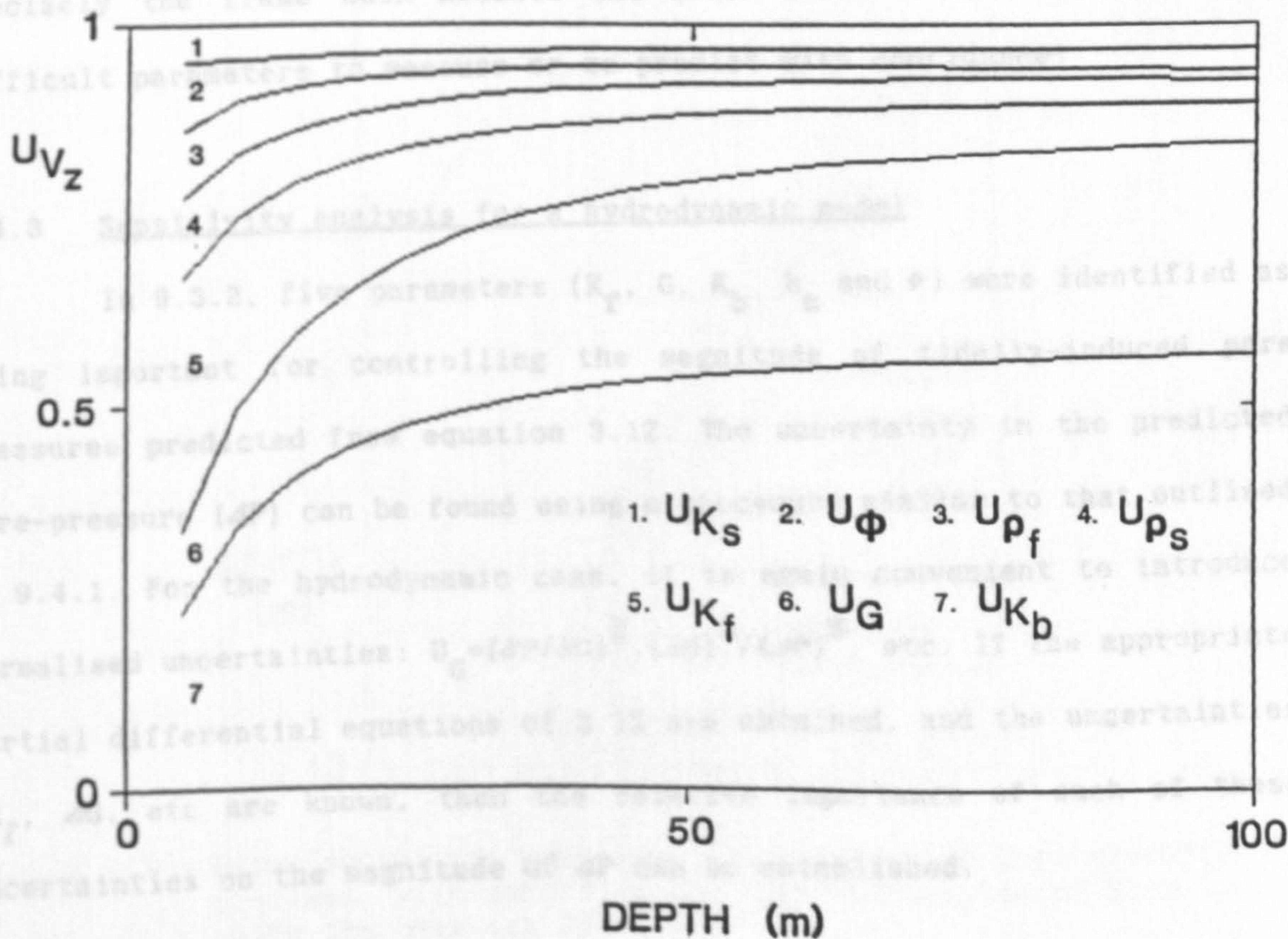


Figure 9.3 Normalised V_z uncertainty components versus depth for the data set CARB_M1



of the band which it occupies on the y-axis. It can be seen that U_{Kb} contributes the greatest to ΔV_z , U_ϕ is the next most important for near-surface sediments, but is relegated in importance by U_G at depths greater than 30 metres. The other normalised uncertainties contribute less than 25% towards the total normalised uncertainty, and so their importance is secondary to the normalised uncertainties U_{Kb} , U_G and U_ϕ . Note that this ranking of the normalised uncertainties is only valid for the particular values of the parameters shown in Table 7.1 and their associated uncertainties given on page 175. Indeed, a different ranking of importance may emerge for a real data set where the parameters and their associated uncertainties (obtained from experimentation) may differ somewhat to the values used in this numerical example (see Chapter 11). However, it can be concluded, for a typical data set forming a geoacoustic model for carbonate sediments, that the frame bulk modulus, shear modulus and porosity should be determined as accurately as possible to restrict the magnitude of ΔV_z . The studies of Chapter 5 revealed that it is precisely the frame bulk modulus and shear modulus which are the most difficult parameters to measure or to predict with confidence!

9.4.3 Sensitivity analysis for a hydrodynamic model

In 9.3.2, five parameters (K_f , G , K_b , k_a and ϕ) were identified as being important for controlling the magnitude of tidally-induced pore pressures predicted from equation 3.12. The uncertainty in the predicted pore-pressure (ΔP) can be found using a procedure similar to that outlined in 9.4.1. For the hydrodynamic case, it is again convenient to introduce normalised uncertainties: $U_G = (\partial P / \partial G)^2 \cdot (\Delta G)^2 / (\Delta P)^2$, etc. If the appropriate partial differential equations of 3.12 are obtained, and the uncertainties ΔK_f , ΔG , etc are known, then the relative importance of each of these uncertainties on the magnitude of ΔP can be established.

The following uncertainties can be assigned to the relevant parameters given in Table 4.3; $\Delta\phi = 0.05\phi$, $\Delta K_f = 0.01K_f$, $\Delta G = 0.25G$, $\Delta K_b = 0.25K_b$ and $\Delta k_a = 0.5k_a$. Using the values given in Table 4.3 in association with these uncertainties in the appropriate equations gives the following values for the uncertainty in predicted pore pressure and the normalised uncertainties; $\Delta P = 0.18\%$, $U_{Kb} = 0.7243$, $U_G = 0.2734$, $U_{ka} = 0.0012$, $U_{Kf} = 0.0010$, $U_\phi < 0.0001$. The predicted pore-pressure along with the uncertainty in the prediction are shown in Figure 9.4. It is interesting to note that the uncertainties in K_b and G dominate ΔP : i.e. the predicted pore pressure is most sensitive to variations in K_b and G (for the particular values of K_b , G , ΔK_b and ΔG used). Therefore, inverse determinations of K_b or G (obtained by comparing predicted and experimental pore-pressures - see Chapter 5) will be obtained with relative precision.

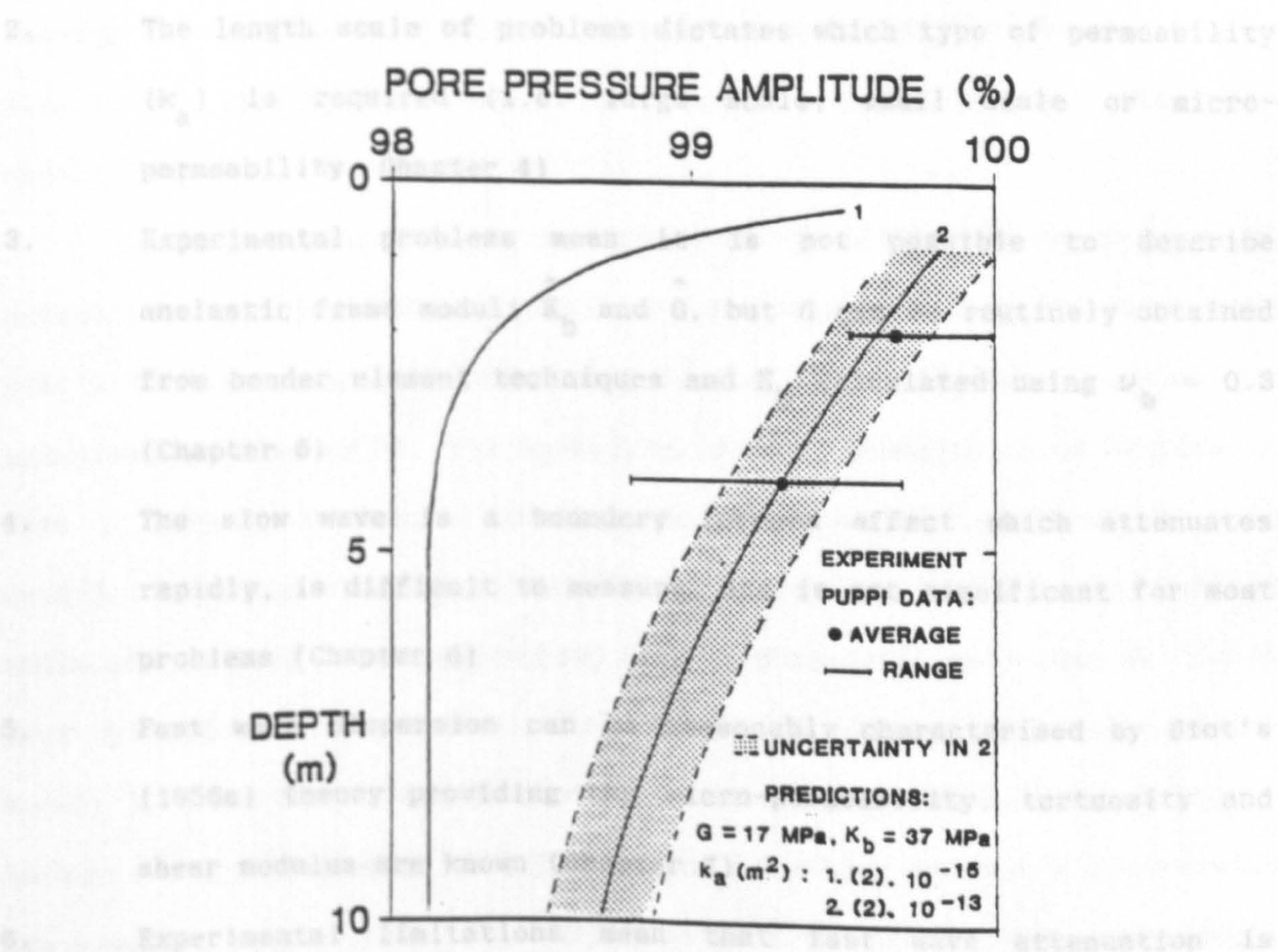


Figure 9.4 Experimental and predicted tidally-induced pore-pressure profiles, with uncertainties, for the sea-bed of Site 1, using the data set TURB_M2

9.5 Summary

A review of the salient results of Chapters 3 to 8 has allowed identification of the important components for geoacoustic and hydrodynamic models of the sea-bed, which can be used as input for a simplified version of Biot's theory. The uncertainties of the predictions, obtained by using the uncertainties of the components, have been studied. Two numerical examples were given: the first showed the uncertainty of V_1 predictions for a carbonate-type sea-bed. The second showed the uncertainty in the pore-pressure prediction for the hydrodynamic tidal boundary value problem introduced in Chapter 3. The following points from earlier chapters were used:

1. The solution for the tidally-induced hydrodynamic pore pressure problem obtained from Biot's theory is sensitive to the values of K_b , G and k_a (Chapter 3).
2. The length scale of problems dictates which type of permeability (k_a) is required (i.e. large scale, small scale or micro-permeability, Chapter 4)
3. Experimental problems mean it is not possible to describe anelastic frame moduli \hat{K}_b and \hat{G} , but G can be routinely obtained from bender element techniques and K_b calculated using $\nu_b = 0.3$ (Chapter 5)
4. The slow wave is a boundary induced effect which attenuates rapidly, is difficult to measure, and is not significant for most problems (Chapter 6)
5. Fast wave dispersion can be reasonably characterised by Biot's (1956a) theory providing the micro-permeability, tortuosity and shear modulus are known (Chapter 7)
6. Experimental limitations mean that fast wave attenuation is difficult to measure and reliable predict using Biot's theory (Chapter 8)

The important components for a geoacoustical model were shown to be V_p , G , K_b , T , k_a and ϕ , with ρ_f , ρ_s , K_f , K_s , η obtained from tables. Using such a model, Biot fast wave velocity dispersion predictions can be made. The important components for a hydrodynamic model were shown to be G , K_b , k_a and ϕ , with K_f obtained from tables. Using such a hydrodynamic model, the magnitude of tidally-induced pore-pressures can be predicted.

A sensitivity analysis was performed on the equation for Biot's low frequency velocity limit (V_z) and coded for a computer (Appendix 5). A numerical example studying the uncertainty in predicted V_z values (ΔV_z) for near-surface sediments for a carbonate sea-bed was given. For this example $\Delta V_z/V_z \approx 0.1\%$, with the uncertainties in the frame moduli and the fluid bulk modulus having the maximum contributions towards ΔV_z . In a similar way, a sensitivity analysis was performed on the equation for the solution to the tidal pore-pressure problem. A numerical example was given showing the uncertainty in predicted pore pressures Δp for the sea bed at Site 1. For this example $\Delta p/p \approx 0.2\%$, with the uncertainties in the frame moduli completely dominating Δp .

Having looked at the importance of the different components of geoacoustic and hydrodynamic models of the sea-bed on predictions using Biot's (1956a) theory, the next step is use these findings in practical examples. In Chapter 10, the hydrodynamic tidal boundary value problem at Site 1 (already introduced in Chapters 3 and 9) is looked at in more detail. Also in Chapter 10, a geoacoustical model of near surface sediments of Site 1 is constructed from experimental measurements, and a Biot dispersion related problem addressed. In Chapter 11, geoacoustical models of Site 2 are constructed from new experimental data collected on-board a drilling ship, and from a few carefully conducted post-cruise experimental measurements. The variation of predicted velocity with depth and the importance of Biot dispersion is studied for both models.

10 A CASE STUDY: BIOT'S THEORY APPLIED TO HYDRODYNAMIC AND
GEOACOUSTIC MODELS OF THE SEA-BED OF THE NORTH EAST ATLANTIC OCEAN

10.1 Introduction

Great Meteor East (GME) is an area of the Madeira Abyssal Plain situated in the North East Atlantic Ocean. Extensive geological and geophysical studies have been carried out on this area to assess its suitability for heat-emitting radioactive waste disposal (Searle et al., 1985). Many surficial sediment cores have been retrieved and the sedimentological (Weaver and Rothwell, 1987), geotechnical (Schultheiss and Gunn, 1985 and Shepard et al., 1987) and acoustical (Searle et al., 1985) properties of the sea-bed have been extremely well characterised. This wealth of background information, along with the availability of core-samples for laboratory experiments, makes this an area for which tightly constrained geoacoustical and hydrodynamic models can be made.

The area of GME between 30.5° N and 32.5° N, and 23° W and 26° W, is referred to as Site 1 in this study. Supplementing the background information for GME with laboratory experimental results (see results of Chapter 5 and also results presented in this chapter), hydrodynamic and geoacoustic models on which Biot's theory can be used (Chapter 9), can be constructed. Using these models, two particular problems can be addressed. The first allows comparison between measured tidally-induced pore-pressure obtained at Site 1 (Schultheiss, personal communication) and predictions from Biot's theory using the hydrodynamic model. The second allows assessment of the frequency dependence of reflection profile records: specifically, does Biot type dispersion significantly affect the reflection coefficients of beds of widely differing permeabilities? If so, can reflection coefficients based on laboratory (ultrasonic) measurements be satisfactorily applied to analysis of in-situ (acoustic) experiments?

10.2 Background information for Site 1

10.2.1 The geology of Site 1

Site 1 can be classified as a deep-water, soft sea-bed environment, where thick (100 metres) turbidite and pelagic sediments overlie a hard basaltic basement. For the hydrodynamic and geoacoustic models presented in 10.3 and 10.4, it is only the geology of the upper 20 metres of sediment which is important. Within this upper 20 metres of sediment, Weaver and Rothwell (1987) have identified nine different turbidite units (lettered a to k), up to 5 metres in thickness, which are often separated by thin (20 cm) pelagic units. The turbidites vary laterally in thickness, and it is rare for the thinner units to be present at any one location. The upper (a to i) turbidites have a carbonate composition between 40 - 60%, the lower two units have a carbonate composition of around 70%. The non-carbonate fraction is mostly clay.

Most turbidite units are remarkably homogeneous, but some exhibit strong graded bedding towards the base: coarsening from clay-size particles ^{to} silt size particles. The distinctive silty bases of the turbidites are normally less than 15 cm in thickness, but are not always present for each unit. The silty bases, which are easily identified from a compressional wave velocity profile at any one location, have been used by Weaver and Rothwell (1987) to map the distribution of the turbidites across GME; turbidites b and d/e dominate the upper ten metres of sediments in this area. A more detailed sedimentological and distributional description of these sediments can be found in Weaver and Rothwell (1987).

The geology of the upper part of the sea-bed at GME would appear to be very simple; comprising many thin graded turbidite deposits which have spilled from the N.W. African continental margin. Within the area shallow faults exist (Williams, 1987). Also, long vertical open burrows

within the upper few metres of the sea-bed (Weaver and Schultheiss, 1983b) have been detected. Both these features may have a significant effect upon the hydrology of the upper part of the sea-bed. The effect of the burrows is discussed in 10.3.

10.2.2 Results from laboratory geotechnical / acoustical experiments on sediments recovered from Site 1

Numerous geotechnical experiments have been carried out on sediments recovered from Site 1 (Lovell and Ogden, 1984, Searle et al., 1985, Schultheiss and Gunn, 1985, Lovell, 1985, Davis and Bennell, 1986, Shepard et al., 1987). Appropriate experimental data can be taken from these studies, supplemented by further experimental measurements (see below), to construct hydrodynamic and geoacoustic models for Site 1 (10.3 and 10.4).

Results from the permeability and consolidation experiments of Schultheiss and Gunn (1985), for pelagic and turbidite sediments from Site 1, have been introduced in Chapter 4. The turbidites have an average porosity of 80%, and have (direct-flow) permeabilities lying between $(6) \cdot 10^{-16}$ and $(1) \cdot 10^{-14} \text{ m}^2$, with an average value of $(7) \cdot 10^{-15} \text{ m}^2$ (see Table 4.1). The pelagic sediments have an average porosity of 72%, with an average permeability of $(1) \cdot 10^{-15} \text{ m}^2$.

Considering the much greater thicknesses of the turbidites with respect to the pelagic sediments at Site 1, and the not too dissimilar porosity and permeability of the pelagic sediments, it is to be expected that the pelagic sediments will play a minor role in geoacoustic and hydrodynamic models. The same cannot be assumed for the silty bases of the turbidites, which typically have porosities of 60% and permeabilities ranging between 10^{-14} and 10^{-12} m^2 (Searle et al., 1985).

Laboratory compressional wave experiments were carried out on a number of cores from GME using a prototype manual version of the whole core automated logger described by Schultheiss and McPhail (in press). The velocity profiles obtained on the following two cores are significant; core D01695 - from which some of the permeability / consolidation samples described in Chapter 4 were taken (Schultheiss and Gunn, 1985) and core D11174 - from which some of the resonant column samples described in Chapter 5 were taken. Figure 10.1 gives the velocity profiles for cores D11174 and D10695 and the dominance of tubidite units b and d/e can be seen. The measured compressional wave velocities for core D10695 are given in Table 10.1 and are used as the basis of a geoacoustical model for this Site (see 10.4). One important point to note, illustrated by comparing the logs for the two cores in Figure 10.1, is that the thickness of tubidite b in core D10695 is some two metres less than in core D11174. On the basis of coring records for D10695 and D11174, it is possible that the upper two metres of core D01695 were not retrieved. In fact, the whole subject of the ability of coring techniques to retrieve an accurate section of the sea-bed is one open to argument (see Weaver and Schultheiss, 1983a and Lee, 1985).

A number of 20 cm^3 samples were taken from split sections of core D10695 and wet-bulk densities were evaluated using gravimetric methods as outlined by Boyce (1976). These results are shown in Table 10.1. An average grain density of 2670 kg/m^3 was also computed. Using this grain density value and a sea-water density of 1024 kg/m^3 , gives porosities ranging between 84 and 58% with an average value of 76%, for the densities given in Table 10.1. This average porosity value, which is lowered by the silty bases of the turbidites and the pelagic material, is not far from the 80% value for the turbidite samples given in Table 10.1.

Figure 10.1 V_p experimental results for cores D10695 and D11174, Site 1

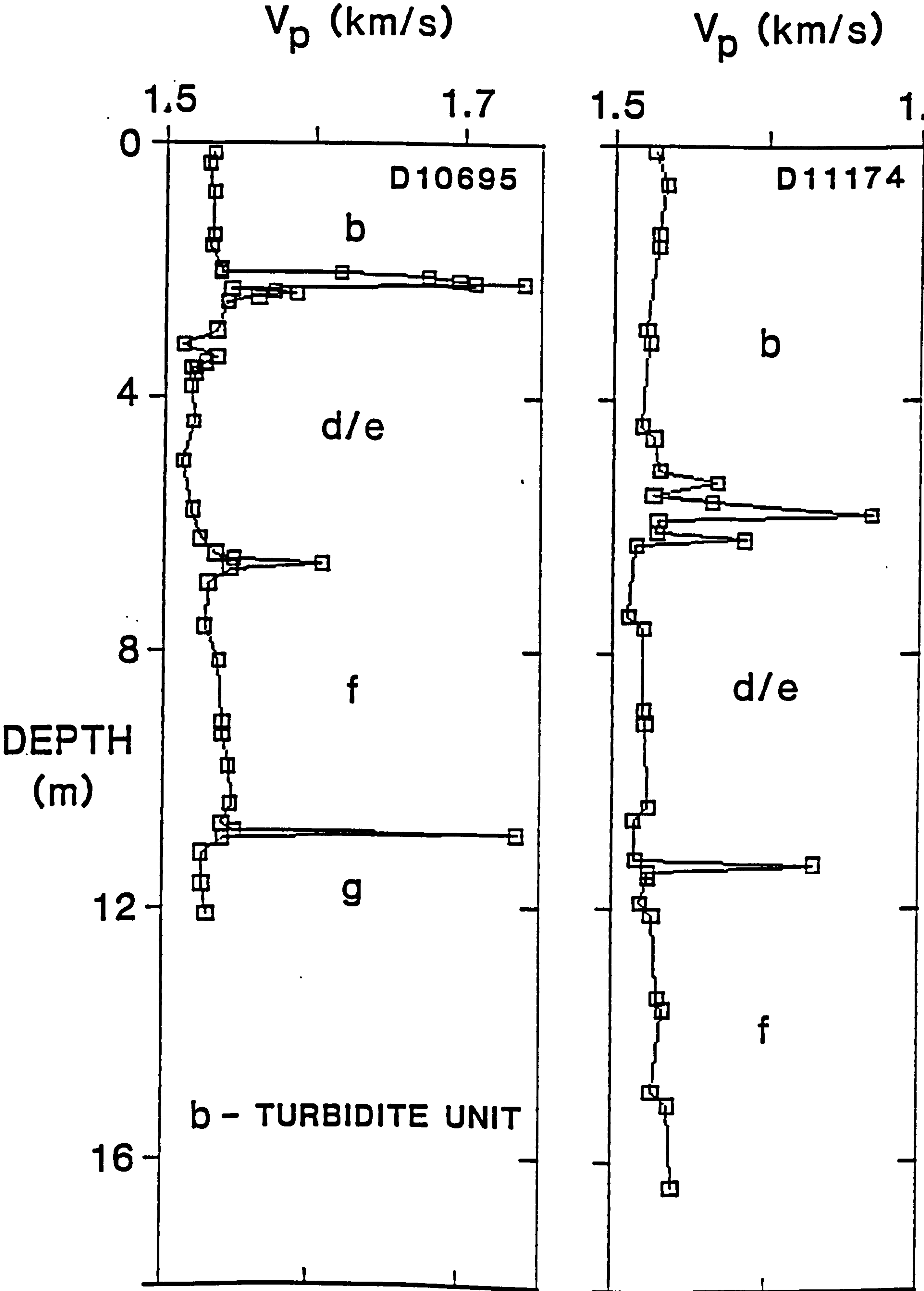


Table 10.1 Experimental physical and acoustical measurements
for turbidites and pelagic sediments from Site 1

Depth	V_p	ρ	G	k_a
m	m/s	kg/m ³	MPa	m ² ·10 ⁻¹⁵
0.15	1542	1322	0.15	2.0
0.31	1539	1236	0.31	2.0
0.77	1542	1283	0.77	2.0
1.46	1542	1337	1.46	2.0
1.62	1541	1343	1.62	2.0
2.00	1548	1377	2.00	3.0
2.05	1548	1380	2.05	5.0
2.06	1628	1495	2.06	9.0
2.11	1686	1685	2.11	30.0
2.19	1707	1460	2.19	30.0
2.22	1717	1460	2.22	100.0
2.23	1750	1592	2.23	200.0
2.31	1555	1327	2.31	80.0
2.36	1584	1502	2.36	0.9
2.39	1598	1575	2.39	0.8
2.43	1573	1462	2.43	0.7
2.51	1552	1537	2.51	0.6
2.96	1545	1465	2.96	0.6
3.17	1523	1460	3.17	0.6
3.37	1545	1502	3.37	0.6
3.45	1538	1472	3.45	0.6
3.53	1531	1318	3.53	0.6
3.54	1528	1323	3.54	0.6
3.62	1531	1422	3.62	0.6
3.82	1528	1438	3.82	0.6
4.39	1530	1386	4.39	0.6
5.01	1523	1386	5.01	0.6
5.78	1529	1396	5.78	0.6
6.24	1535	1402	6.24	0.7
6.47	1545	1437	6.47	4.0
6.55	1557	1515	6.55	20.0
6.62	1616	1740	6.62	50.0
6.70	1555	1410	6.70	8.0
6.93	1540	1392	6.93	1.0
7.62	1538	1407	7.62	0.8
8.16	1547	1404	8.16	0.7
9.13	1550	1407	9.13	0.6
9.32	1550	1425	9.32	0.6
9.81	1554	1417	9.81	0.8
10.4	1556	1413	10.4	5.0
10.7	1550	1456	10.7	10.0
10.83	1559	1465	10.83	200.0
10.86	1747	1770	10.86	500.0
10.93	1551	1455	10.93	80.0
11.17	1536	1393	11.17	5.0
11.66	1537	1392	11.66	1.0
12.12	1540	1386	12.12	0.9

An effective stress - depth profile can be simply calculated from the density values given in Table 10.1 and by using Equation 9.1. This profile is not plotted as it can be simply represented by the linear empirical equation σ_{eff} (kPa) = 3.7z (m). This equation can be used to convert experimental data collected at different effective stresses, to equivalent in-situ depths at Site 1.

The experimental compressional wave velocities given in Table 10.1 have been corrected to in-situ conditions. First an effective stress correction of ΔV (m/s) = 0.5z (m) (for $0 < z < 20$), obtained from measurements by Lovell and Ogden (1985), was added to the laboratory velocities. Then, in-situ temperature and hydrostatic pressure corrections were made by multiplying the experimental velocities by $V_{\text{in-situ}}/V_{\text{lab}}$ (Hamilton, 1971). Here the bottom sea water velocity ($V_{\text{in-situ}}$) of 1537 m/s and a laboratory sea-water velocity (V_{lab}) of 1530 m/s were used.

Ideally the density values shown in Table 10.1 should be corrected to their in-situ conditions to allow for porosity rebound effects (Hamilton, 1976a). Using the consolidation data collected on samples from Site 1 by Schultheiss and Gunn (1985), porosity rebound corrections were calculated using Hamilton's (1976a) method. These results are shown in Table 4.1 and give average porosity rebound corrections of $(3.7) \cdot 10^{-5}$ / kPa for the pelagic sediments and $(1.5) \cdot 10^{-5}$ / kPa for the turbidite sediments. Therefore, for a turbidite sample from a depth of 12 metres, with an equivalent effective stress of 45 kPa, has a porosity rebound correction less than 0.1%, which is negligible in comparison to the 2% error in determining the porosity (Boyce, 1976). Hamilton (1976a) does not give porosity rebound corrections for turbidite sediments, but his correction for a pelagic sediment for an equivalent effective stress of 45 kPa is 0.3%, which agrees favorably with the value of 0.2% calculated using the correction value obtained from Table 4.1. This fair agreement

shows that the calculated porosity rebound corrections from Table 4.1 are indeed of the correct magnitude, but their importance is still negligible. Note, a bigger correction in porosity may be needed due to the 1.5 - 2% expansion of pore-water, as samples are recovered from water depths of around 5 km.

Lovell (1985) performed electrical resistivity experiments on turbidites and pelagic sediments from Site 1. His results gave formation factors (FF) ranging from around 1.7 for porosities of 80%, to $FF = 2.7$ for porosities of 60%. These values are simply converted into tortuosities (T) of 1.36 and 1.62 using Brown's (1980) relationship; $T = FF/\phi$. As there is no straightforward empirical relationship between FF and ϕ for turbidite sediments from Lovell (1985), all the sediments from Site 1 are assigned a tortuosity of 1.5.

In Chapter 5, resonant column results on turbidite and pelagic samples from core D11174 were presented. Figure 5.7 shows measurements of G versus depth at Site 1 for various turbidite samples. Based on resonant column and shear-bender results, the simple empirical equation $G \text{ (MPa)} = z \text{ (m)}$ appears to hold (where z is the depth in the sediment column). As was discussed in detail 5.6.2, no useful measurements of the second elastic constant K_b were obtained for the turbidites. A compromise value of $K_b = 2.17G$ was decided on, based on experimental K_b measurements on a sand.

10.2.3 In-situ geotechnical / geophysical experiments at Site 1

Hydrodynamic (10.3) and geoacoustic (10.4) models of Site 1 can be constructed from the laboratory measurements described in 10.2.2. Predictions of in-situ tidally-induced pore pressures and compressional wave velocities can be made by using these models in conjunction with Biot's theory. The validity of these predictions can be examined if appropriate in-situ and remote sensing measurements exist.

In-situ tidally-induced pore pressures can be measured by the piezometer PUPPI (Schultheiss and McPhail, 1985, McPhail and Schultheiss, 1986). The instrument is described briefly in 4.5.1, and the data which it collects is described in 4.5.2. A summary of the PUPPI deployments at Site 1, along with the measurements of maximum tidally-induced differential pore pressure, are given in Table 4.2.

Many remote acoustical experiments have been carried out at Site 1. Of particular interest are the 3.5 kHz sub-bottom profile records which map the topography of the sea-bed as well as returning information on acoustical "reflectors" within the upper 20 metres of sediments. The profiles consist of uncalibrated acoustical intensity returns from the sea-bed, provided by a 1 second repeated 28 millisecond burst of sound swept from 3 to 4 kHz (centred at 3.5 kHz). The signals reflected from the sea-bed from any one tone burst are fed through a dispersive delay-line (DDL). The DDL analyses the frequency spectrum of reflected signals and isolates overlapping reflections (in the time domain) by recognising the 3 kHz leading component of the tone burst. After recognising and filtering out (on the basis of frequency) a reflected event, the 28ms burst from that event is compressed to a 2ms peak. The intensity of the 2ms peaks arising from different sea-bed reflections, from one source tone burst, are automatically plotted on a chart recorder. This gives a time domain profile of the reflected intensity returns from the sea-bed below the location of the source.

As the source moves horizontally along the sea to a new location, the reflected intensity profile from the next (1 second repeated) tone burst is plotted at the new location. In this way, successive profiles are plotted adjacent to each other for every new source location and a continuous record of the intensity of the 3.5 kHz energy reflected from the sea-bed is built up. Such a record can give the vertical temporal

distribution of sea-bed reflectors which are caused by vertical variations in the impedance of the sea-bed. The impedance is the product of the density and compressional wave velocity at any point.

The uncalibrated 3.5 kHz records do not give a direct measurement of the velocity of sediments in the upper sea-bed. However, the vertical temporal distribution of reflectors can be converted to a vertical spatial distribution if the compressional velocity of the sea-bed sediments is known. Physical vertical impedance contrasts, calculated from laboratory measurements of density and compressional wave velocity, can then be compared to the vertical spatially-corrected acoustic intensity from the 3.5 kHz records. Searle et al. (1985) do this for various locations in Site 1 and show that there appears to be some spatial agreement with strong intensity reflectors from 3.5 kHz profiles and impedance contrasts caused by the silty bases of the turbidites. This and other points are addressed in 10.4 with reference to a 3.5 kHz record taken over core D10695 (Searle et al., 1985) and the laboratory and density measurements shown in Table 10.1. The spatial distribution of the measurements given in Table 10.1 can be simply converted to two-way times (TWT) by using the velocity structure of the sea-bed, which is also given in Table 10.1.

The last set of in-situ experiments of note are those of Whitmarsh and Lilwall (1982). Their experiments give the shear velocity, hence shear modulus (G_{max}) for surficial sediments at Site 1. These results are shown in Figure 5.7, and it should be noted that their G_{max} values are up to 4 times greater than the laboratory measurements of G_{max} . Whitmarsh and Lilwall (1982) give the following relationship between the shear modulus (G) and the depth in the sediment column (z): $G \text{ (MPa)} = 1.7 + 3.6z \text{ (m)}$. Some reasons for the differences between the laboratory and in-situ measurements of G are discussed in 5.4.3.

10.3 A hydrodynamic model of Site 1 and comparisons between measured and predicted tidal pore-pressure responses

A possible hydrodynamic model for Site 1 can be defined by Table 4.3. The major features of this model are that G , K_b and k_a are constant and G and k_a are significantly higher than their laboratory-determined values. This model is used, with Biot's theory, to give the predicted tidally-induced pore-pressure profile shown in Figure 9.4. These predictions are in fair agreement with measured tidal pore-pressures obtained from the piezometer PUPPI. Before claiming that Biot's theory accurately predicts the pore-pressure response of the sea-bed, the in-situ values for G , and k_a used in the hydrodynamic model for Site 1 have to be justified.

As discussed in 9.4.3, the frame bulk modulus (K_b) and shear modulus (G) are the most important components of a hydrodynamic model of the sea-bed in deep water environments such as found at Site 1. The "best fit" values of K_b and G used for Figure 9.4 are 37 and 17 MPa respectively (assuming a frame Poisson's ratio of 0.3). However, the results shown in Figure 9.4 can be reproduced by using $K_b = 48$ MPa and $G = 9$ MPa, and using $K_b = 58$ MPa and $G = 2$ MPa. The figure of $G = 9$ MPa is an average value for the top four metres of sediment after the results of Whitmarsh and Lilwall (1982) (see Figure 5.7), while $G = 2$ MPa is an average over this interval from laboratory resonant column experiments (see Figure 5.7). The important point to note is that with K_b being (unavoidably) assumed, there are many reasonable combinations of K_b and G which give a similar predicted pore-pressure profile.

The permeability of $(2) \cdot 10^{-13} \text{ m}^2$ used in the hydrodynamic model is a "large scale" in-situ permeability which takes account of the effects of any cracks, fissures, etc within the sea-bed. This value is about two orders of magnitude greater than the average intrinsic (small-scale)

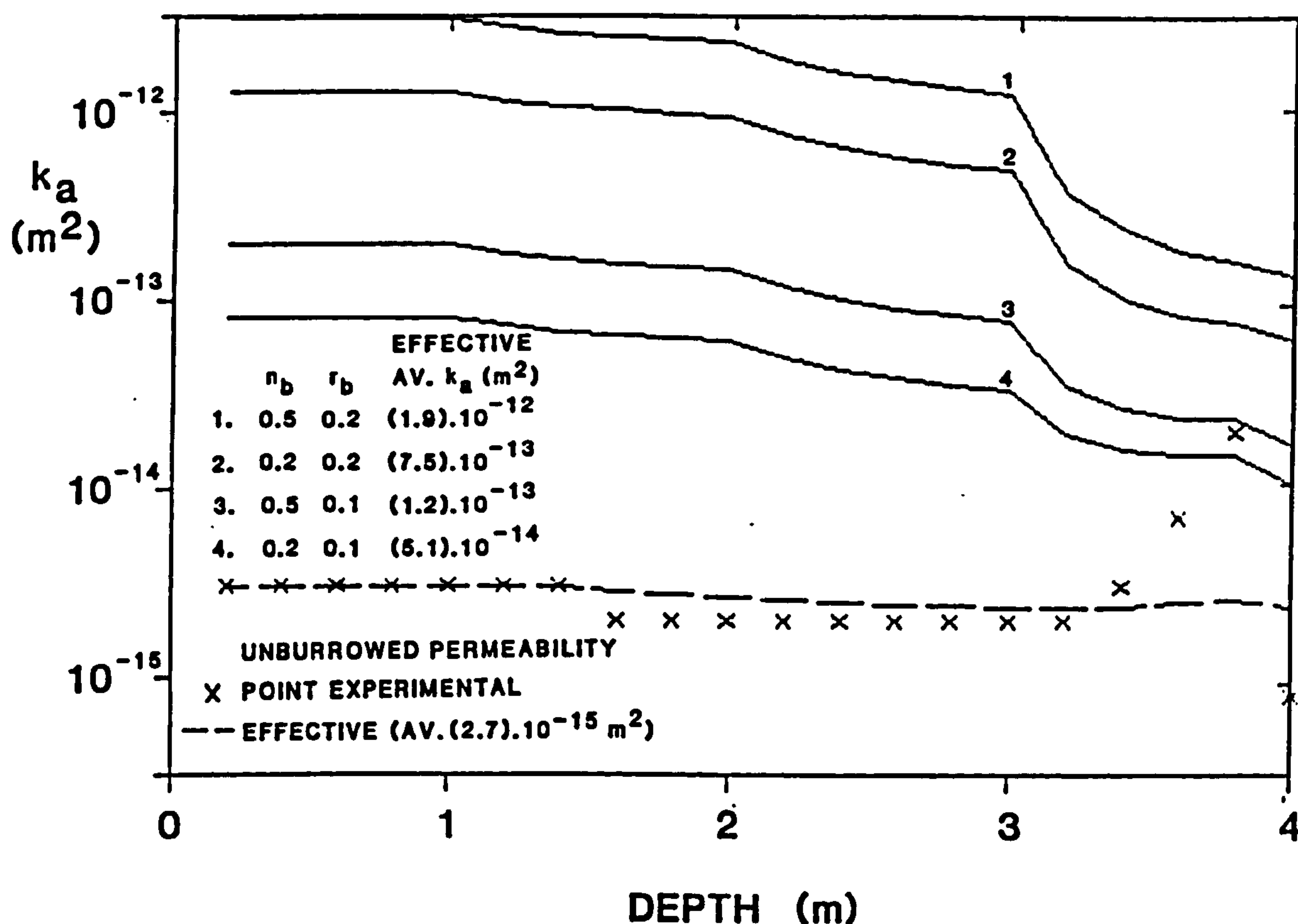
laboratory determined permeability of surficial sediments from Site 1 (see Figure 4.9). However, Weaver and Schultheiss (1983b) observed the widespread existence of long vertical open worm burrows in surficial sediments from Site 1, and noted that these would have a profound effect upon the in-situ permeability of the sea-bed. This effect is examined numerically below for Site 1.

Weaver and Schultheiss (1983b) characterised the vertical open burrows observed in Site 1 sediments as follows; burrow length was up to 2 metres, burrow radii (r_b) ranged from 0.1 to 0.2 cm, number of burrows per square centimetre (n_b) ranged from 0.2 to 0.5 in the upper two metres of sediment, falling to zero by a depth of four metres. If k_a is the small scale permeability of the unburrowed sediment, the large scale permeability k_s in the direction of the burrows is given by (Weaver and Schultheiss, 1983b):

$$k_s = k_a (1 - n_b r_b^2 \pi) + n_b r_b^4 \pi / 8 \quad 10.1$$

Using a simple small-scale permeability structure of the top four metres of sediment at Site 1 (see Figure 10.2), and letting the relative abundance of burrows vary as n_b for 0 to 1 m, $0.6n_b$ for 1 to 2 m, $0.2n_b$ for 2 to 3 m and $0.01n_b$ for 3 to 4 m, and using the r_b and n_b limits given above in Equation 10.1, gives the large-scale permeabilities shown in Figure 10.2. These large scale permeabilities are effective permeabilities calculated using equations 4.7 and 4.8. The average effective permeability gives an indication of the average permeability over the top four metres of the sea-bed. As can be seen from Figure 10.2, the average effective permeabilities for the four r_b , n_b combinations range from $(5.1) \cdot 10^{-14} \text{ m}^2$ to $(1.9) \cdot 10^{-12} \text{ m}^2$, as compared with a small-scale permeability (without the effect of burrows) of $(2.7) \cdot 10^{-15} \text{ m}^2$.

Figure 10.2 The effect of worm burrows on the large scale effective permeability of the upper four metres of Site 1



Looking at Figure 10.2, it can be imagined that an appropriate distribution of burrows of radii somewhere between 0.1 and 0.2 cm could account for the two orders of magnitude difference between the small-scale laboratory permeability and the large scale permeabilities at Site 1 $(2.0) \cdot 10^{-13} m^2$, which is required to give a good agreement between the theoretical and experimental pore-pressures at Site 1 (see Figure 9.4).

10.4 A geoacoustic model of Site 1 and comparisons between predicted and measured compressional wave velocities

A geoacoustic model for Site 1 is defined by the data given in Tables 10.1 and 10.2. Biot's theory is used in conjunction with this model to see if an impedance profile calculated at ultrasonic frequencies is applicable at acoustic frequencies. The calculated impedance profile then is compared to a 3.5 kHz record and the observation that the silty bases of turbidites correspond to "reflectors" on the 3.5 kHz record (Searl et al., 1985) is commented on.

Table 10.2 Physical and acoustical parameters characterising a geoacoustical model for Site 1, data set TURB_M3

1. Wet-bulk density	Table 10.1
2. Fluid density	1024 kg/m ³
3. Grain density	2650 kg/m ³
4. Fluid modulus	(2.39).10 ⁹ Pa
5. Grain modulus	(3.6).10 ¹⁰ Pa
6. Dynamic viscosity	0.001 Pa.s
7. Circular frequency	2 π .10 ⁶ Hz
8. Shear modulus	0.15 to 12.12 GPa
9. Frame bulk modulus	2.17 G
10. Permeability	(6).10 ⁻¹⁶ to (5).10 ⁻¹³ m ²
11. Tortuosity	1.5
1,8,10	Table 10.1
2-6	Ogushwitz (1985)
9	From table 5.1
11	From Lovell (1985)

Additional information: $V_{in-situ}/V_{lab} = 1537/1530$

Shear modulus - depth relationship: $G \text{ (MPa)} = z \text{ (m)}$

Alternative shear modulus - depth relationship: $G \text{ (MPa)} = 1.7+3.6z \text{ (m)}$

Effective stress - depth relationship: $\sigma_{eff} \text{ (kPa)} = 3.7z \text{ (m)}$

Fast wave velocity predictions are made by using the parameters given in Tables 10.1 and 10.2. Zero (V_Z) and infinite (V_I) frequency limit velocity predictions and experimental fast wave velocities for surficial sediments from Site 1 are shown in Figure 10.3. For the silty bases of the turbidites (denoted by the subscript "silt") both $V_{Z,silt}$ and $V_{I,silt}$ predictions increase sharply at depths of 2, 6, 8 and 11 metres and remain fairly constant at the remaining depths. The increases in $V_{Z,silt}$ for the silty bases are directly correlated to the increased density at these depths. Before assessing the importance of any dispersive effects, the uncertainties in the experimental and zero frequency limit predicted velocities have to be considered.

Figure 10.3 V_p experimental results and predictions of V_z and V_I , core D10695

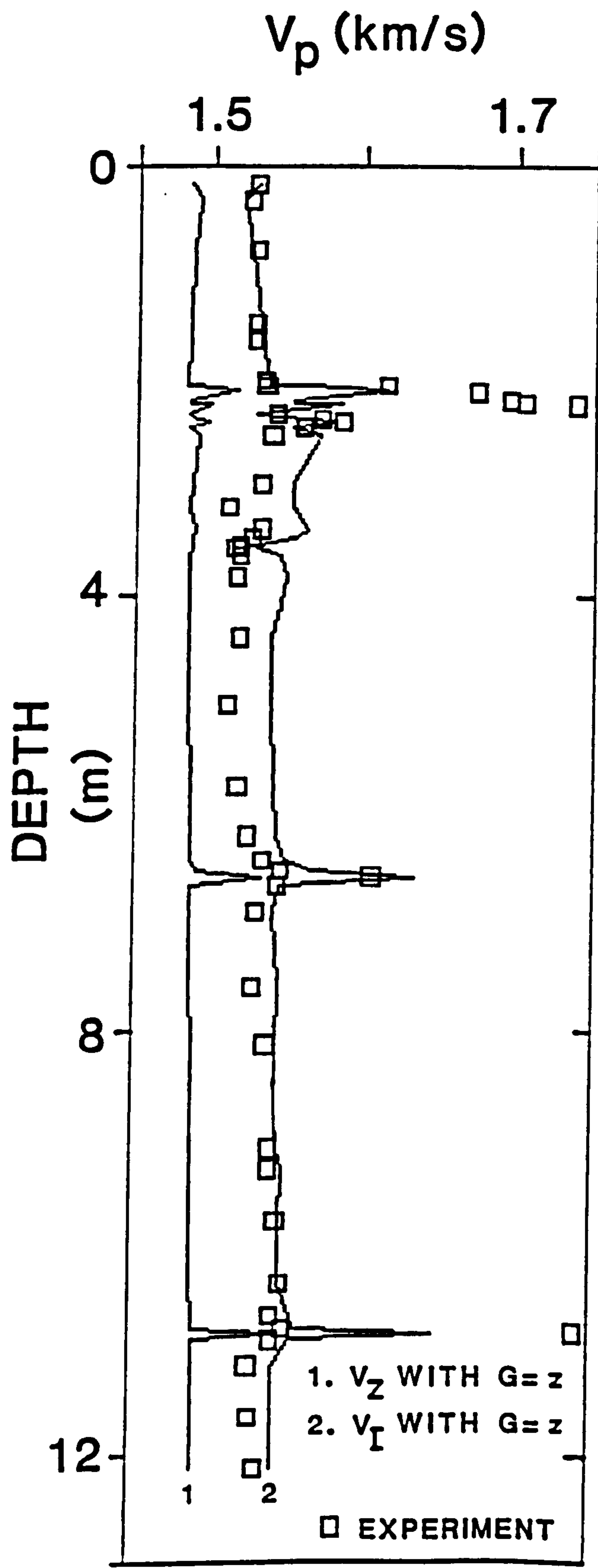
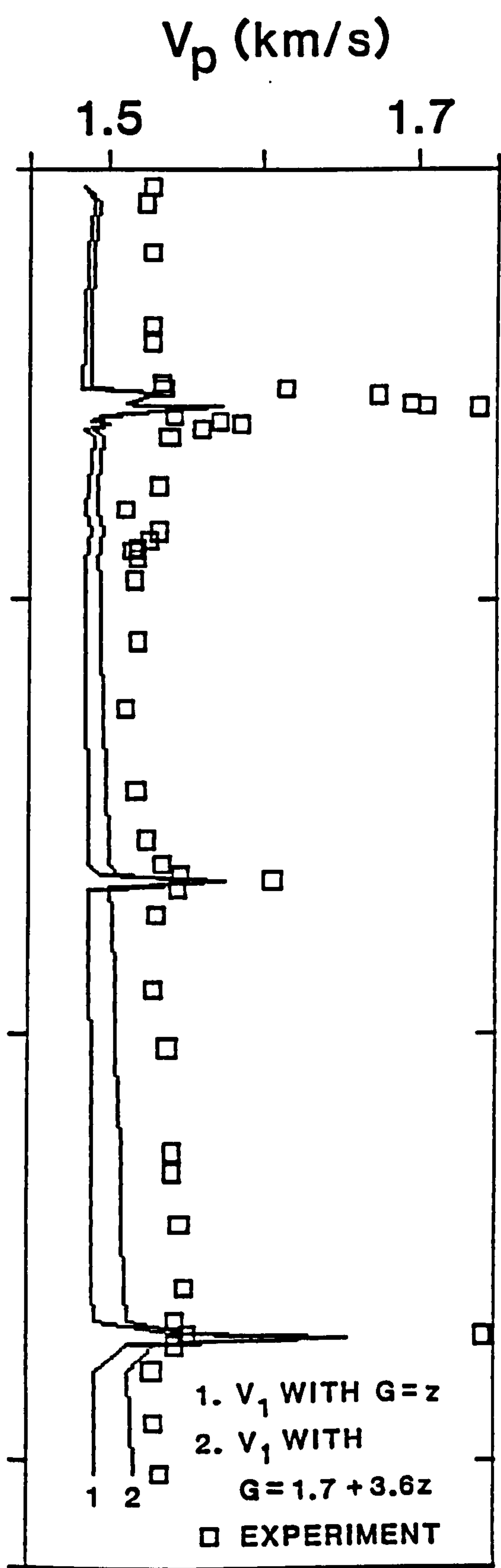


Figure 10.4 V_p experimental results and predictions of V_1 core D10695, Site 1



Experimental velocities (V_e) obtained using P-wave logging techniques can be of a precision of less than 0.1%, but may be accurate to only 0.2% (Schultheiss and McPhail, in press). To avoid cluttering, the uncertainties in V_e and in V_z predictions are not shown in Figure 10.3 (uncertainties in V_z are around 0.1% - see 9.4.2).

For the fine grained non-silty parts of the turbidites (denoted by the subscript "turb") an average predicted $V_{z,turb}$ value of 1490 m/s with an uncertainty of ± 15 m/s can be taken. For the experimental measurements for these sediments an average $V_{e,turb}$ value of 1520 m/s with a (maximum) error of ± 30 m/s can be taken. With these values, the uncertainties in measured and predicted values overlap and there ^{are} ~~is~~ no grounds for considering dispersive effects. However, for the silty bases with an average $V_{z,silt}$ value of 1530 m/s ± 15 m/s and an average experimental velocity ($V_{e,silt}$) value of 1700 m/s ± 34 m/s, there is a real discrepancy between $V_{e,silt}$ and $V_{z,silt}$, which may be due to dispersion.

In Figure 10.4, the experimental velocity data are shown alongside two sets of predicted (V_1) data, which are calculated for the ultrasonic frequency at which the experimental data were collected. (see Table 10.1). The lowest velocity predictions (curve 1) are calculated with the (laboratory derived) relationship G (MPa) = z (m), and the higher set (curve 2) are calculated with the (in-situ derived) relationship G (MPa) = $1.7+3.6z$ (m). Note that the predicted velocities calculated using the latter relationship are closer to the experimental values. For the non-silty turbidites, there is no way of knowing which is the best G versus z relationship to use - as the uncertainties in $V_{e,turb}$ overlap $V_{1,turb}$ predictions using both relationships. However, for the silty turbidites, the discrepancy between $V_{z,turb}$ and $V_{e,silt}$ still exists if G (MPa) = $1.7+3.6z$ (m) is used (not shown in Figure 10.4). Therefore, dispersion effects still cannot be discounted for the silty turbidites.

Comparison of Figures 10.3 and 10.4 show that for the $G \text{ (MPa)} = z \text{ (m)}$ predictions for the non-silty turbidites, $V_{1,\text{turb}} \approx V_{Z,\text{turb}}$. This means that the non-silty turbidites are of a low permeability, such that $f < f_c$, and so Biot's dispersive mechanism is not operating. However, the silty turbidite bases are of high enough permeability to make $f > f_c$, hence Biot dispersion takes place and $V_{1,\text{silt}}$ tends to $V_{I,\text{silt}}$. Now the magnitude of V_I is predominantly set by the tortuosity (T) (see Chapter 7), which was assigned a value of 1.5 for the silty turbidites. A slight reduction in T would result in V_I increasing substantially (for example see Figure 7.1). Therefore, a simple interpretation of these results could be that Biot dispersion does not take place for the non-silty turbidites, but it does take place for the silty bases. Furthermore, by taking values of $T < 1.5$ for the silty turbidite bases, predicted velocities would better approach experimental values. Experimental verification that $T < 1.5$ for the silty bases (using electrical conductivity tests) is needed.

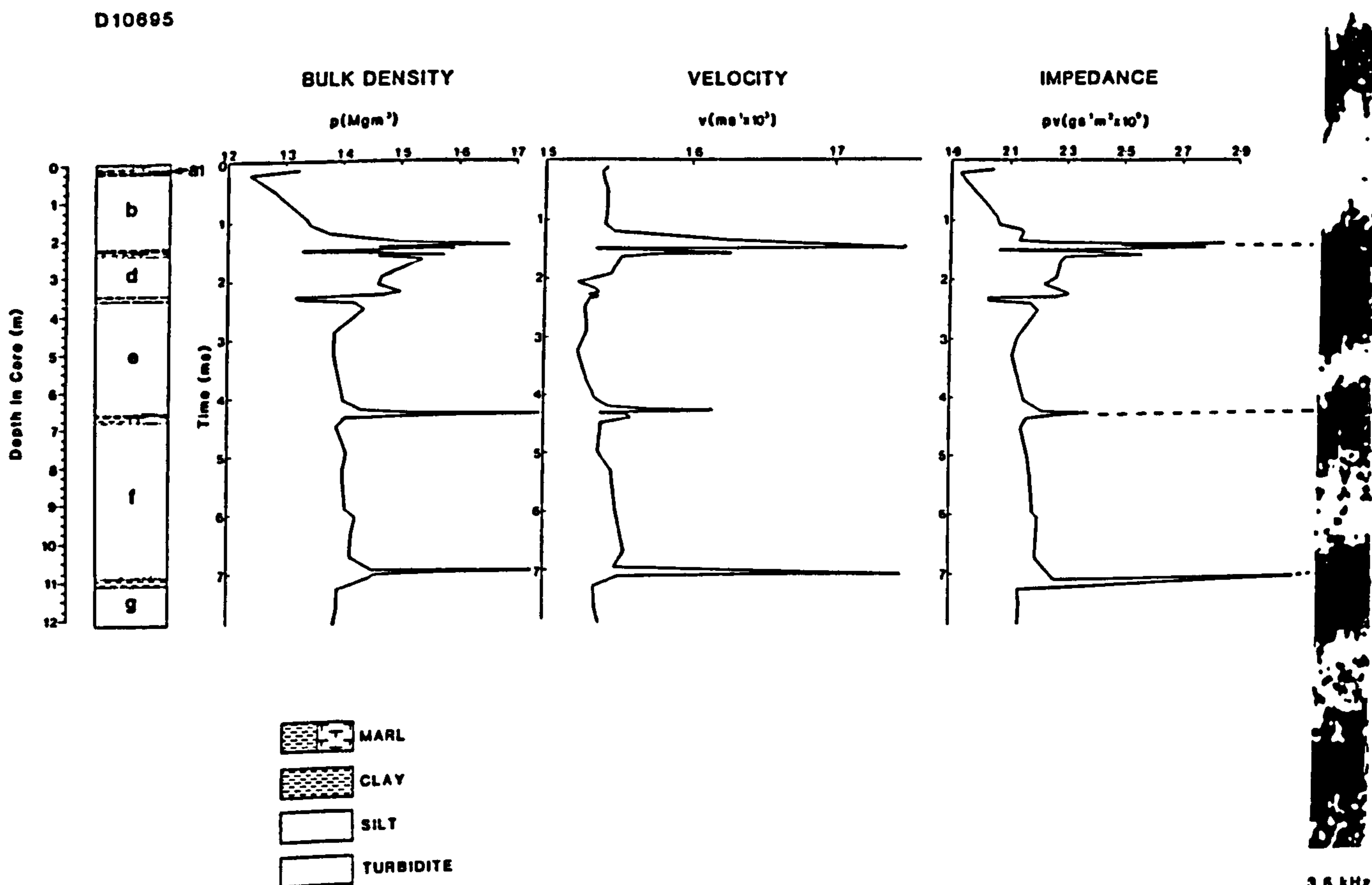
At ultrasonic frequencies the average velocity prediction for the silty turbidite $V_{1,\text{silt}}$ is 1600 m/s; giving a predicted velocity dispersion of 70 m/s over $V_{Z,\text{silt}}$. However, at acoustic (e.g 3.5 kHz) frequencies, $V_{1,\text{silt}}$ tends to $V_{Z,\text{silt}}$. Although the experimental values for $V_{e,\text{silt}}$ and $V_{e,\text{turb}}$ are not coincident with predictions $V_{1,\text{silt}}$ and $V_{1,\text{turb}}$ (see Figure 10.4), it is of interest to use the predictions $V_{1,\text{silt}}$ and $V_{1,\text{turb}}$ at ultrasonic and acoustic frequencies to examine if dispersion is important to calculated reflection coefficients.

Consider the case of a non-silty turbidite with $V_{1,\text{turb}} = 1490$ m/s, $\rho = 1350 \text{ kg/m}^3$ and predicted impedance $Z_{1,\text{turb}} = (2.01) \cdot 10^6 \text{ kg/s/m}^2$, which overlies a silty turbidite with $V_{1,\text{silt}} = 1600$ m/s, $\rho = 1620 \text{ kg/m}^3$, $Z_{1,\text{silt}} = (2.59) \cdot 10^6 \text{ kg/s/m}^2$ calculated at ultrasonic frequencies and, $V_{1,\text{silt}} = 1530$ m/s, $Z_{1,\text{silt}} = (2.48) \cdot 10^6 \text{ kg/s/m}^2$ calculated at acoustic frequencies.

Defining the normal incidence reflection coefficient R for the interface between the layers as the magnitude of the difference of the impedances divided by the sum of the impedances, gives $R = 0.126$ at ultrasonic frequencies and $R = 0.105$ at acoustic frequencies. Therefore, the frequency dependence of the reflection coefficient due to fast wave dispersion is low.

Discounting dispersion effects as being negligible, the impedance profile (in the time domain) calculated from the experimental measurements for sediments from Site 1 core D10695 is shown in Figure 10.5 alongside the 3.5 kHz record taken over the core-site. There appears to be a loose correlation between the time domain location of the large impedance (silty turbidite bases) spikes and the strong reflectors from the 3.5 kHz record (Searle *et al.*, 1985).

Figure 10.5 Calculated experimental impedance profile for core D10695 and 3.5 kHz record at Site 1, after Searle *et al.* (1985)



In principle, it should be possible to convolve the wavelet from the 3.5 kHz source with the impedance profile to give a synthetic 3.5 kHz record; this could be compared to the measured record at this core-site, confirming whether or not the strong reflectors are due to the silty bases of the turbidites. However, this task is made very difficult by the signal processing of reflected events by the DDL (see 10.2.2).

It is worth considering briefly some interference effects which may be present in the 3.5 kHz records at Site 1. With reference to Figure 10.5, the silty turbidite-base layers 2, 4, and 6 can be taken as being of negligible thickness in comparison to the non-silty turbidite layers 1, 3 and 5. Assume that the 3.5 kHz source is not swept between 3 to 4 kHz (see 10.2.2) but is located just at 3.5 kHz. Now, with a time domain pulse length of 28 ms, which is equivalent to a pulse 45 metres in length, and with the wavelength of the 3.5 kHz sound being approximately 0.5 metres, the possibility of interference effects in layers 1, 3 and 5 arises.

If layers 1, 3 or 5 are an odd number of half wavelengths, then reflections from interface 2-3, and interface 4-5 (say) will interfere destructively. The resultant combined received signal will start off with the reflection for a few cycles, which will then disappear as the out of phase reflections from 4-5 will cancel it out in the latter portion of the 28ms pulse. If layers 1, 3 or 5 are an even number of wavelengths, then constructive interference will occur in a similar way. Such interference effects will introduce artefacts in the 3.5 kHz profile and will obscure the true reflectors.

This interference mechanism may be important in explaining why the "reflectors" on the 3.5 kHz records from GME often appear to "disappear" then "re-appear" again: a phenomena which cannot be explained by simple sedimentological reasoning.

10.5 Summary

A case study has been conducted for Site 1, a sequence of turbidites, located in the N.E. Atlantic Ocean. Biot's theory was applied to geoacoustical and hydrodynamical models of the sea-bed at Site 1 and predicted compressional wave velocities and pore-pressures compared to experimental measurements. The effect of Biot-type dispersion on reflection coefficients calculated from the layered sea-bed at Site 1 was studied.

Samples from cores from Site 1 were used for permeability studies in Chapter 4 and frame moduli studies in Chapter 5. A simple hydrodynamic model for Site 1 has already been introduced in Chapters 3 and 9 in connection with the tidal boundary value pore-pressure problem. Laboratory experimental measurements of the compressional wave velocity and wet-bulk density allowed a geoacoustical model of Site 1 to be constructed. Additional information on in-situ tidally-induced pore-pressures and 3.5 kHz profiles were used to supplement these models.

Comparisons between predicted tidally-induced pore-pressures and those measured at Site 1 have already been shown in Chapter 9. In this chapter, it was shown that various combinations of the frame bulk moduli K_b and G gave equivalent pore-pressure predictions. Therefore, the inverse in-situ determination of G presented in Chapter 5, is only one of a number of possible values. The large scale permeability required to match predicted and measured pore pressures (hence is an inverse permeability determination) was shown to be over 2 orders of magnitude greater than small scale permeability. However, independent studies revealed the existence of long worm burrows in the upper few metres of the sea-bed at Site 1. Calculations showed that the large scale permeability increased by 2-3 orders of magnitude due to the presence of the burrows, which may explain the differences between large and small scale permeabilities here.

Compressional wave velocities were predicted by Biot's theory using data from the geoacoustical model for Site 1. In general, predictions were lower than experimental values if dispersive effects were ignored. However, including such effects brought predictions significantly closer to the experimental values for the silty bases of the turbidite units of this site. The apparent dispersion had little effect upon reflection coefficients calculated at ultrasonic and acoustic frequencies.

11 A CASE STUDY: BIOT'S THEORY APPLIED TO GEOACOUSTIC MODELS OF THE SEA-BED OF THE WESTERN INDIAN OCEAN

11.1 Introduction

The Ocean Drilling Project (ODP) and its predecessor the Deep Sea Drilling Project (DSDP) have contributed to much of our knowledge of the geological and geophysical processes occurring within the sea-bed. A recent leg (115) of the ODP, focussed on an area near the Seychelles Bank in the Western Indian Ocean, in order to study a paleoceanographic problem related to production and dissolution of carbonate sediments. A number of new bore-holes were drilled in this area, and the first (high quality) "Advanced Piston Coring System" cores were recovered from the Indian Ocean sea-bed. Extensive ship-board experiments were conducted on the sediments from these cores, ranging from lithostratigraphical, biostratigraphical, palaeomagnetic, geochemical, physical, acoustical and geophysical studies (Backman, Duncan, et al., in press). Of particular significance to this study are the physical and acoustical properties of these sediments obtained from ship-board measurements (Hurley and Hempel, in press). Also of interest are the results from various post-cruise laboratory geotechnical experiments some of which are presented in Chapter 5 and in this chapter.

Using the extensive set of ship-board and post-cruise laboratory data characterising the sediments obtained from Leg 115, a number of geological / geotechnical and geophysical problems can be studied. In this chapter, two problems will be addressed. In the first, a geoacoustic model of the sea-bed is constructed using selected ship-board data, and the ability of Biot's theory to predict compressional wave velocities at ambient laboratory temperatures and pressures is assessed. In the second, a geoacoustic model of the sea-bed is constructed from post-cruise

laboratory measurements, and the ability of Biot's theory to predict the dependence of compressional wave velocity with depth in the sea-bed is studied. Attention is focussed on data from two near-by bore hole-sites (707 and 709). These ODP Sites are located at 7.5° S, 59.0° E and 3.9° S, 60.5° E respectively, and this area is referred to as Site 2 here.

11.2 Background information for Site 2

11.2.1 The geology of Site 2

ODP Sites 707 and 709 are located at water-depths of 1552 and 3048 m respectively. The sediments from ODP Site 707 consist of a typical ooze - chalk - limestone sequence of carbonate sediments. The 376 metres of sediments are divided up into 5 lithological units:

Unit 1 (0.0-151.0 metres below sea floor, mbsf) is a
nannofossil-bearing foraminiferal ooze

Unit 2 (151.0-213.3 mbsf) is a nanno-fossil ooze

Unit 3 (213.3-251.4 mbsf) is a nanno-fossil ooze/chalk

Unit 4 (251.4-280.3 mbsf) is a radiolarian (silica) bearing chalk

Unit 5 (280.3-375.6 mbsf) is a complex chalk / limestone sequence

The 354 metres of sediments recovered from ODP Site 709 consist of a single major lithostratigraphic unit comprising alternating clay-bearing nannofossil ooze and nannofossil ooze. This single unit corresponds (roughly) to units 1 and 2 at ODP Site 707.

From the lithological description, Site 2 consists of a simple sequence of carbonate oozes which have undergone gradual lithification and diagenesis into chalks and limestones at depth. The carbonate composition for Site 2 is high, with an average of 92% at ODP Site 707 and 90% at ODP Site 709. The non-carbonate fraction consists mainly of opaline silica. The mean grain-size is dominated by the carbonate microfossils; varying from 50-200 μ m for the upper foraminiferal oozes to 1-5 μ m for the lower nannofossil oozes.

11.2.2 Results from ship-board laboratory physical properties measurements on sediments recovered from Site 2

An extensive suite of ship-board laboratory experiments were carried out to determine various physical properties of the sediments recovered from Site 2 (Hurley and Hempel, in press). The measurements significant to this study are; the wet-bulk density (ρ) the compressional (fast) wave velocity (V_p) and the shear wave velocity (V_s). The experimental procedures used to determine these parameters are outlined by Hurley and Hempel (in press) and are based on the methods outlined in Boyce (1976) and Schultheiss (1985). Selected experimental measurements for V_p , V_s and ρ for ODP Holes, 707A, 707B, 709A, 709B and 709C are shown in Tables 11.1 - 11.3. The experimental errors in ρ , V_p and V_s were approximately 5%, 1% and 20% respectively (Hurley and Hempel, in press).

Other important ship-board measurements taken were the porosity. using a gamma ray attenuation porosity evaluator (GRAPE porosity), the grain density, and the carbonate content. The average carbonate content was above 90% and average grain densities for ODP Sites 707 and 709 were 2670 and 2730 kg/m³ with standard errors of 210 and 70 kg/m³. With such high carbonate contents, the average grain density for Site 2 would be expected to be close to that for calcite (2720 kg/m³), obtained from tables.

The major reason for the discrepancy between the value for calcite from tables and the measured values of the grain density of these high carbonate sediments, is due to the fairly large uncertainties introduced by the experimental technique employed (see Hurley and Hempel, in press). These experimental grain density values are used in the geoacoustic models constructed for Site 2 in preference to the value from tables, not because they are more accurate, but they help illustrate the importance of sensitive accurate experimentation.

The ship-board wet-bulk density and average grain density measurements allow vertical effective stress (σ_{eff}) versus depth (z) profiles to be calculated for ODP Sites 707 and 709 using equation 9.1. These profiles are fairly similar for depths up to 150 metres and are simply characterised by a linear gradient of σ_{eff} (kPa) = 6.16z (m).

As well as ship-board measurements of the physical properties at Site 2, seismic air-gun lines were shot and 3.5 kHz profiles were taken. In addition, Hole 707C was geophysically logged. Unfortunately, some of the geophysical logging instruments malfunctioned, but in-situ values of the compressional wave velocity and the electrical resistivity of the sediments were obtained between depths of 140 and 350 mbsf.

The bore-hole electrical resistivity measurements (ρ_{bh}) were used to give the tortuosity (T) using the following procedure: with bore-hole measurements of the temperature, salinity and pressure of the pore-fluid, the electrical resistivity of the pore-fluid (ρ_{pf}) was determined using tables from Riley and Skirrow (1965); the formation factor (FF) was then evaluated by the ratio of the $\rho_{\text{bh}}/\rho_{\text{pf}}$ and these calculated FF values were used with GRAPE porosity values (corrected for porosity rebound) in Brown's (1980) formula: $T = FF.\phi$.

Plotting FF versus ϕ for these experimental data and obtaining an empirical equation according to Archie's (1942) law gives $FF = \phi^{-1.543}$, which gives $T = \phi^{-0.543}$. Therefore, for a porosity of 70% $T = 1.21$, and for a porosity of 80% $T = 1.12$. As the average porosity for Site 2 sediments is just above 70%, an average value of $T = 1.2$ is taken for all the sediments at this site. Note, the results of Jackson et al. (1978) for a marine sands and clays gave a porosity exponent of -2 for $\phi > 0.6$ and -1.5 for $\phi < 0.6$. Therefore, the exponent of -1.543 appears to be slightly low in comparison.

Table 11.1 Physical properties for ODP Holes 707A and 707B at Site 707

Hole 707A				Hole 707B			
Depth	V _p	ρ	V _s	Depth	V _p	ρ	V _s
(m)	(m/s)	(kg/m ³)	(m/s)	(m)	(m/s)	(kg/m ³)	(m/s)
85.93	1502	1600	150	40.53	1531	1510	54
88.96	1540	1680	-	43.75	1560	1610	97
91.55	1539	1560	-	49.75	1555	1530	-
104.83	1583	1540	-	53.14	1545	1550	-
105.15	1509	1540	-	60.44	1802	1520	-
110.80	1555	1630	-	63.23	1473	1570	-
113.70	1487	1540	-	66.23	1561	1570	-
124.04	1561	1590	-	72.83	1560	1580	-
126.97	1665	1530	-	75.34	1510	1680	-
133.68	1513	1460	-	79.44	1482	1530	-
136.64	1522	1460	188	82.05	1470	1570	-
143.32	1511	1680	56	93.61	1571	1620	-
148.33	1571	1640	78	103.16	1531	1540	-
152.25	1594	1610	106	103.42	1537	1580	-
178.13	1557	1690	167	198.23	1547	1750	62
189.31	1540	1740	72	202.37	1528	1730	88
191.74	1556	1740	177	226.20	1567	1760	225
197.50	1565	1740	116	226.51	1553	1790	162
200.49	1556	1690	153	236.52	1557	1700	117
208.05	1548	1770	110	238.16	1481	1820	132
				252.68	1604	1720	-
				266.67	1539	1720	178
				198.23	1547	1750	62
				202.37	1528	1730	88
				226.20	1567	1760	225
				226.51	1553	1790	162
				236.52	1557	1700	117
				238.16	1481	1820	132
				252.68	1604	1720	-
				266.67	1539	1720	178

Table 11.2 Physical properties for ODP Holes 709A and 709B at Site 709

Hole 709A				Hole 709B			
Depth	V _p	ρ	V _s	Depth	V _p	ρ	V _s
(m)	(m/s)	(kg/m ³)	(m/s)	(m)	(m/s)	(kg/m ³)	(m/s)
2.07	1531	1560	-	2.10	1509	1510	116
5.07	1541	1550	-	5.80	1505	1530	54
8.07	1558	1580	-	10.30	1522	1530	65
12.16	1549	1590	-	16.97	1511	1560	44
15.16	1519	1550	-	26.67	1501	1620	103
18.14	1513	1660	-	31.17	1514	1570	94
24.66	1517	1520	57	36.50	1500	1590	91
27.66	1530	1610	79	40.22	1524	1570	113
31.37	1526	1610	79	40.70	1507	1610	-
34.37	1500	1610	-	45.96	1533	1600	63
50.45	1551	1660	77	50.46	1509	1610	70
53.45	1526	1640	106	55.40	1503	1610	81
56.45	1514	1610	-	59.90	1495	1640	67
60.36	1530	1590	88	60.86	1500	1610	67
63.36	1473	1540	115	65.25	1525	1610	68
66.36	1516	1650	-	69.80	1517	1600	92
70.07	1515	1650	74	74.90	1515	1630	129
73.07	1518	1680	71	79.40	1511	1650	35
76.07	1510	1680	87	80.22	1512	1640	85
79.67	1524	1680	126	94.45	1536	1650	86
82.80	1506	1670	-	98.88	1512	1710	82
85.67	1519	1700	-	104.13	1527	1650	87
90.98	1553	1680	263	113.80	1543	1710	130
95.32	1540	1680	347	123.34	1542	1710	88
99.26	1544	1650	188	127.69	1551	1750	78
101.93	1533	1700	121	133.08	1555	1730	121
106.01	1539	1690	113	137.40	1529	1680	157
117.90	1521	1720	145	141.24	1531	1700	78
123.90	1531	1710	104	152.45	1544	1750	99
127.37	1522	1680	86	156.68	1554	1730	87
133.38	1537	1720	78	162.11	1548	1680	90
139.03	1530	1720	76	166.43	1537	1730	82
144.78	1539	1760	72	171.77	1559	1760	99
149.06	1548	1730	54	176.20	1575	1790	134
153.21	1523	1720	51	210.06	1517	1680	-
156.90	1519	1660	65				
159.90	1544	1710	78				
165.40	1522	1730	-				
169.90	1562	1780	49				
172.90	1538	1750	42				
178.00	1533	1780	77				
185.97	1535	1710	-				
190.50	1523	1670	37				
201.57	1518	1710	104				

Table 11.3 Physical properties for ODP Hole 709C at Site 709

Depth	V_p	ρ	Depth	V_p	ρ
(m)	(m/s)	(kg/m ³)	(m)	(m/s)	(kg/m ³)
70.90	1576	1670	137.07	1541	1700
70.98	1514	1640	156.48	1522	1490
80.60	1516	1630	167.29	1548	1720
90.20	1516	1670	167.48	1570	1730
90.32	1510	1660	196.40	1515	1620
98.37	1516	1680	244.78	1584	1870
98.45	1536	1660	274.37	1537	1750
109.48	1532	1650	289.32	1563	1780
119.10	1548	1760	346.11	1684	1940
128.52	1534	1700	350.57	1605	1690
128.67	1543	1730	352.91	1647	1680
136.89	1523	1700			

Table 11.4 Small-scale permeabilities, porosity and preconsolidation pressure for samples from ODP Hole 709C (Site 2).

Sample I-D	Depth	Permeability	f/f_c	Porosity	σ_{pc}
	(m)	(m ²)			(kPa)
3H-05-147	20.87	(2.54).10 ⁻¹⁴	0.233	0.70	300
5H-05-146	40.24	(6.21).10 ⁻¹⁵	0.057	0.68	400
7H-06-146	60.96	(1.92).10 ⁻¹⁵	0.018	0.65	400
10H-05-146	90.36	(1.28).10 ⁻¹⁵	0.012	0.62	400
13H-05-146	119.27	(1.05).10 ⁻¹⁵	0.010	0.60	800

Table 11.5 Averaged compressional velocity, shear velocity and density versus effective stress for samples from ODP Hole 709C

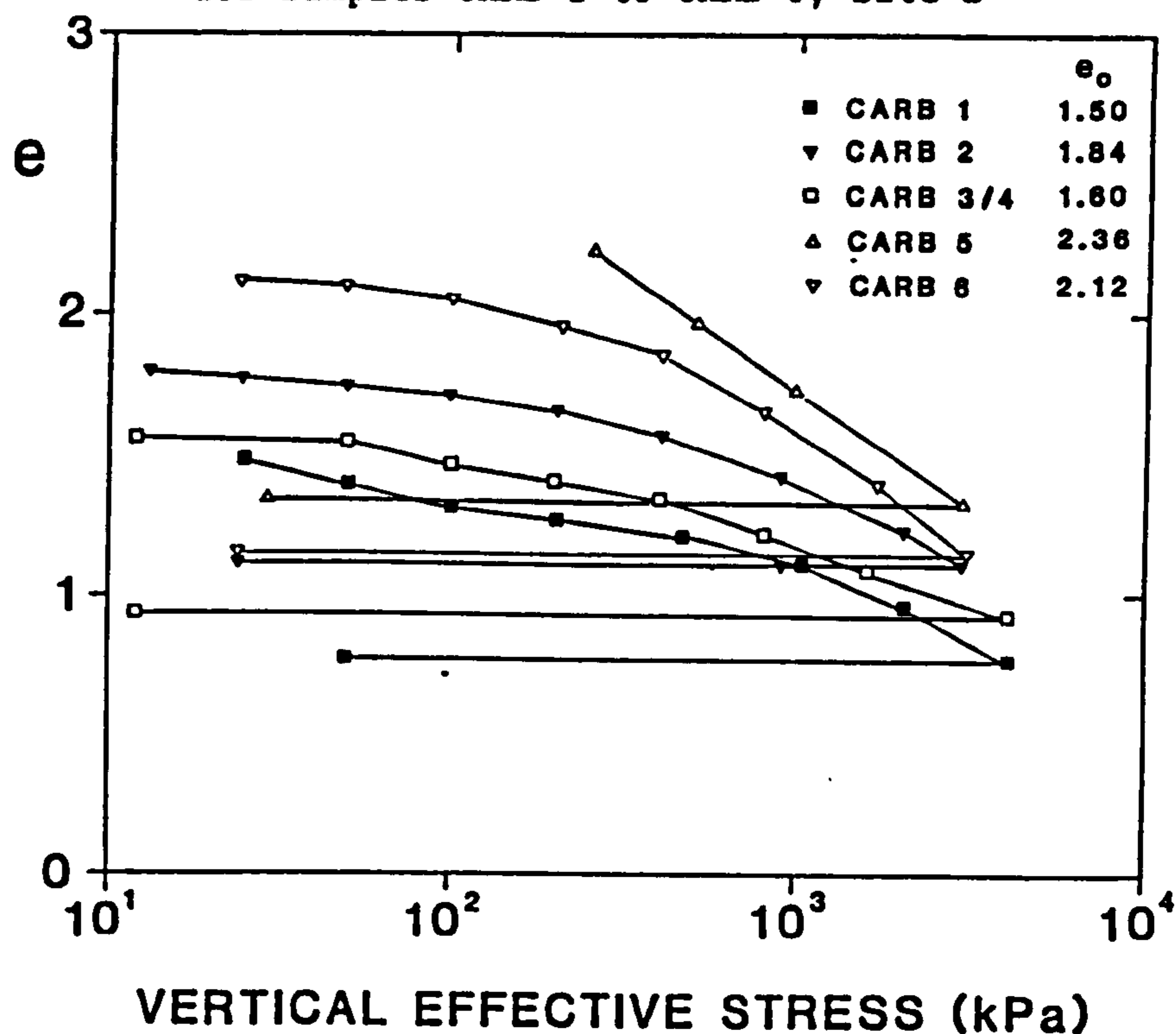
σ_{eff}	Depth	V_p	ρ	V_s
(kPa)	(m)	(m/s)	(kg/m ³)	(m/s)
12.5	2.03	1529	1635	110
25.0	4.06	1532	1642	116
50.0	8.13	1536	1645	124
100.0	16.25	1541	1655	137
200.0	32.50	1547	1669	156
400.0	65.00	1559	1693	182
800.0	130.00	1580	1740	220

11.2.3 Results from post-cruise laboratory geotechnical and acoustical experiments on sediments recovered from Site 2

A number of whole-core samples were brought back from Leg 115 for laboratory geotechnical and geoacoustical tests. Consolidation and permeability tests were carried out on five samples from different depths in the bore-hole using the procedures outlined in 4.2.3. Note, six samples were tested in all, but the permeability / consolidation test failed on one occasion. A summary of the void ratio versus vertical effective stress experimental results are shown in Figure 11.1. A summary of the direct-flow permeability data (obtained using the methods outlined in 4.4.1) are shown in Table 11.4. Compressional wave velocities and shear wave velocities were measured during the consolidation test using a modified back-pressured consolidation cell (similar to that described by Schultheiss, 1981). The results for the shear wave velocity versus effective stress for the samples from Site 2 have already been presented and discussed in 5.4.4: averaged values of shear wave velocity and density at different effective stresses are shown in Table 11.5.

Some interesting observations can be made from Figure 11.1, where the e -log σ_{eff} curves for samples from Site 2 are plotted. The first is that there is negligible porosity rebound when the effective stress is reduced from 3000 kPa to 30 kPa. The second is that the pre-consolidation stress (σ_{pc}) is not well defined for any of the curves. Using Casagrande's method (Vickers, 1978), σ_{pc} , (which relates to the past maximum effective stress to which the sample has been subjected to) is given by the stress on the e -log σ_{eff} curve at which the gradient becomes linear. Interpreted σ_{pc} values for the five samples are given in Table 11.4. The important point to note is that these values should increase in a step-wise fashion with increasing sample depth; but this is not obvious due to the insufficient resolution of the e -log σ_{eff} curves.

Figure 11.1 Experimental void ratio versus effective stress for samples CARB 1 to CARB 6, Site 2



The third observation from Figure 11.1 is that the e -log σ_{eff} curves do not tend to the same asymptote at high effective stresses. This means that a sample from 60 mbsf subjected to a stress of 3000 kPa (say) has a different void ratio to a sample from 40 mbsf (say) at the same stress. Such high effective stresses far exceed the σ_{pc} for these two samples, and it might be expected that both samples would tend to the same void ratio. In practice, the sample from 40 mbsf has a lower void ratio at 3000 kPa than the sample from 20 mbsf. This suggests that there is some other processes (e.g. cementation - reprecipitation) which makes the sample from 40 mbsf act in a fundamentally different way to the sample from 20 mbsf. The upshot of this is that an unrealistic void ratio effective stress profile would be obtained if only data from one sample were considered. However, the e -log σ_{eff} profile for the sample from 60 mbsf appears to give some kind of average representation of the suite of samples. As a simple compromise, this profile is used to characterise the e -log σ_{eff} relationship for Site 2.

The experimental results for compressional wave velocity versus effective stress for the five samples tested are generally of a poor quality exhibiting a large amount of experimental scatter, and a best line fit was put through all the data. Any inherent differences in the V_p versus σ_{eff} profiles - which may have existed for the samples from different depths - were masked by the scatter in the data. The V_p values obtained from this best-fit line were corrected to in-situ depths. First, effective stresses were converted to depths using the empirical equation given in 11.2.2. Then velocities were corrected to in-situ temperature and pressure conditions by multiplying them by the ratio $V_{in-situ}/V_{lab}$, where V_{lab} is the velocity of sea-water in laboratory and $V_{in-situ}$ is the sea-bottom water velocity. Here $V_{lab} = 1526$ m/s, and $V_{in-situ}$ is 1485 m/s (from Tables from Wilson, 1960, for a water depth of 1500 m and bottom water temperature of 3°C and salinity 35 ppt.). These in-situ corrected V_p results are shown in Table 11.5, along with average shear wave velocities obtained from Figure 5.8, and density values from Figure 11.1. The density values are simply calculated from the void ratio data taken for the sample from 60 mbsf and using a grain density of 2720 kg/m³.

11.3 A geoacoustical model of Site 2 based on ship-board measurements and comparisons between measured and predicted values of V_p

A geoacoustic model for Site 2 based upon ship-board laboratory measurements can be defined by Tables 11.1-11.3 and 11.6. In Table 11.6, k_a is an average value for calcareous foraminiferal and nannofossil oozes (after Silva et al., 1981). Using this k_a value in equation 6.1 gives $f/f_c = 0.1$. Dispersion effects are apparent at $f/f_c > 0.1$ (Figure 7.1), therefore some dispersion may be present in the laboratory V_p measurements, but it will only be significant if the true micro-permeabilities of these sediments are greater than $(1.2) \cdot 10^{-14}$ m².

Table 11.6 Physical parameters characterising carbonate sediments for geoacoustical models for Site 2 - data set CARB_M3/M4

1. Wet-bulk density	Tables 11.1 to 11.3 and 11.5
2. Fluid density	1024 kg/m ³
3. Grain density	2677 to 2734 kg/m ³
4. Fluid modulus	(2.39).10 ⁹ Pa
5. Grain modulus	(6.3).10 ¹⁰ Pa
6. Dynamic viscosity	0.001 Pa.s
7. Circular frequency	2 π .10 ⁶ Hz
8. Shear modulus	$\rho.V_s^2$ Pa
9. Frame bulk modulus	2.17 G
10. Permeability	(8).10 ⁻¹⁵ m ²
11. Pore radius	(3.3).10 ⁻⁷ m
12. Tortuosity	1.2

1,8	Tables 11.1 to 11.3 and 11.5
2,5,6	Ogushwitz (1985)
3,7,12	measured
9	from Silva (1981)
10	from Table 11.4
11	equation 4.5

Additional information: $V_{in-situ}/V_{lab} = 1485/1526$

Effective stress - depth relationship: σ_{eff} (kPa) = 6.16z (m)

The zero and infinite frequency Biot velocity limits (V_Z and V_I) were calculated for the measurements given in Tables 11.1 - 11.3 and 11.6. The error in this V_Z prediction (ΔV_Z) was also calculated, assuming the following errors in the input parameters; $\Delta\phi = 0.05\phi$, $\Delta K_b = 0.25K_b$, $\Delta G = 0.25G$, $\Delta K_s = 0.21K_s$, $\Delta K_f = 0.01K_f$, $\Delta\rho_f = 0.01\rho_f$, $\Delta\rho_s = 0.07\rho_s$ (for ODP Site 707) and $\Delta\rho_s = 0.03\rho_s$ (for ODP Site 709). Smooth curves were drawn through the $V_Z + \Delta V_Z$ and $V_Z - \Delta V_Z$ predictions, which are plotted in Figures 11.2 and 11.3, along with the experimental ship-board velocity data from Site 2. and the V_I predictions.

Figure 11.2 V_p experimental measurements and predictions, with uncertainties, versus porosity, for ODP Site 707 using data set CARB_M3 (Site 2 Ship-board model)

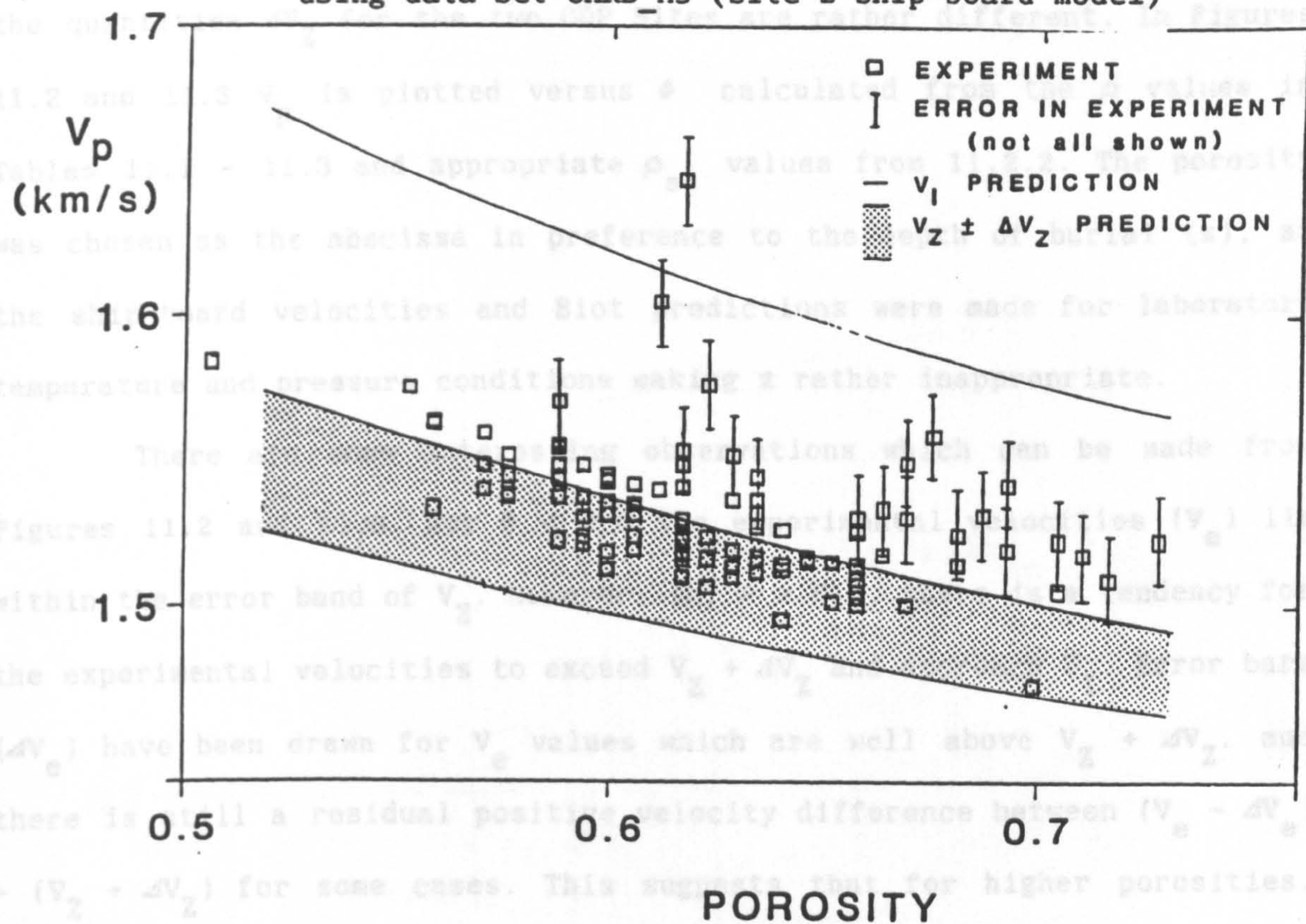
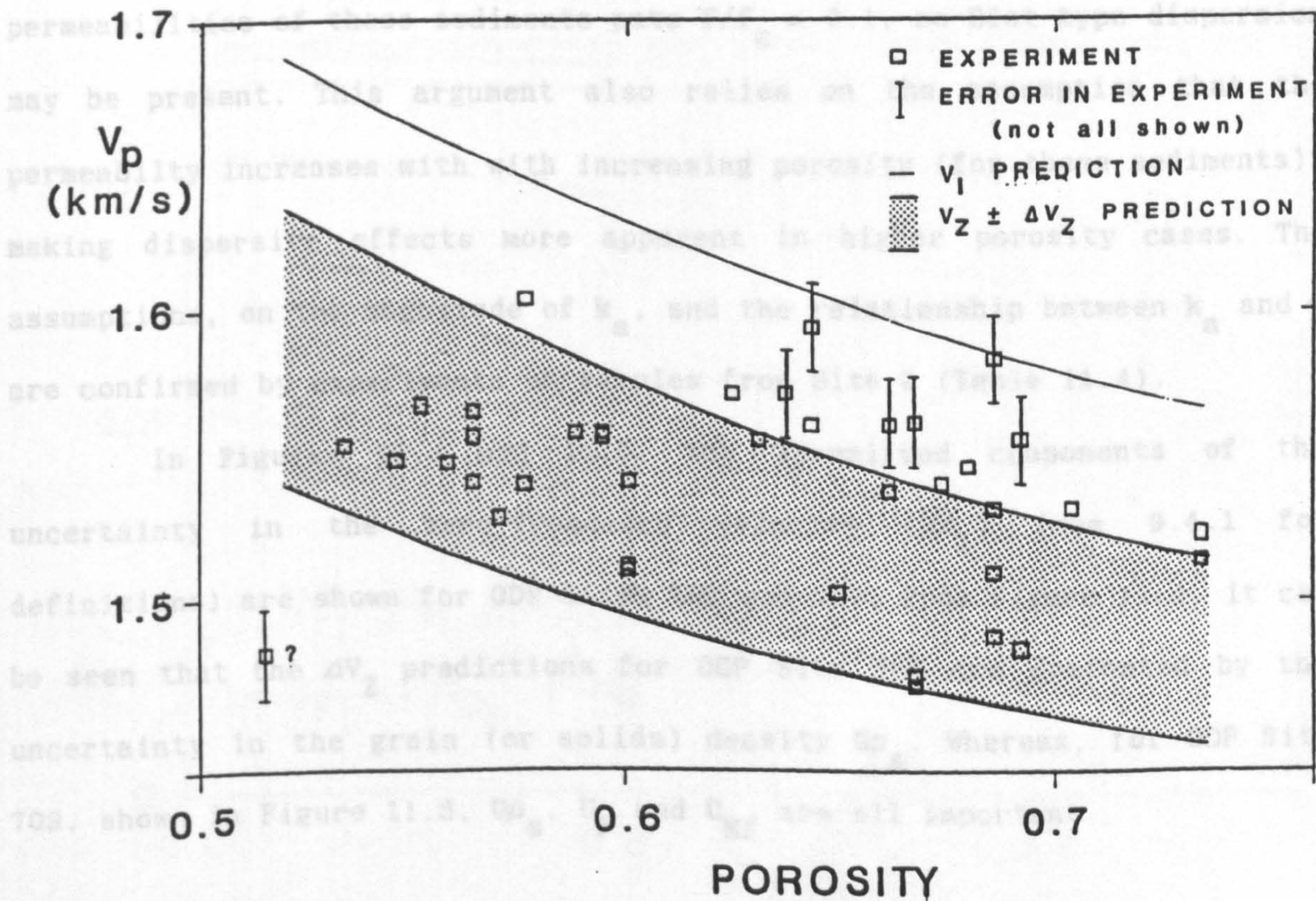


Figure 11.3 V_p experimental measurements and predictions, with uncertainties, versus porosity, for ODP Site 709 using data set CARB_M3 (Site 2 Ship-board model)



The Site 2 data have been split up into ODP Sites 707 and 709, as the quantities ΔV_Z for the two ODP Sites are rather different. In Figures 11.2 and 11.3 V_p is plotted versus ϕ calculated from the ρ values in Tables 11.1 - 11.3 and appropriate ρ_s values from 11.2.2. The porosity was chosen as the abscissa in preference to the depth of burial (z), as the ship-board velocities and Biot predictions were made for laboratory temperature and pressure conditions making z rather inappropriate.

There are some interesting observations which can be made from Figures 11.2 and 11.3. For $\phi < 0.6$ the experimental velocities (V_e) lie within the error band of V_Z . However, for $\phi > 0.6$, there is a tendency for the experimental velocities to exceed $V_Z + \Delta V_Z$ and approach V_I . Error bars (ΔV_e) have been drawn for V_e values which are well above $V_Z + \Delta V_Z$, and there is still a residual positive velocity difference between $(V_e - \Delta V_e) - (V_Z + \Delta V_Z)$ for some cases. This suggests that for higher porosities, there is an additional (dispersive) contribution to the experimental velocities which is not lost in the uncertainties in measurements and predictions. This would appear to make some sense, as the assumed permeabilities of these sediments puts $f/f_c \simeq 0.1$, so Biot type dispersion may be present. This argument also relies on the assumption that the permeability increases with increasing porosity (for these sediments), making dispersive effects more apparent in higher porosity cases. The assumptions, on the magnitude of k_a , and the relationship between k_a and ϕ are confirmed by experiments on samples from Site 2 (Table 11.4).

In Figures 11.4 and 11.5, the normalised components of the uncertainty in the zero-frequency velocity (ΔV_Z) (see 9.4.1 for definitions) are shown for ODP Sites 707 and 709. From Figure 11.4, it can be seen that the ΔV_Z predictions for ODP Site 707 are dominated by the uncertainty in the grain (or solids) density $U\rho_s$. Whereas, for ODP Site 709, shown in Figure 11.5, $U\rho_s$, $U\phi$ and U_{Kf} are all important.

Figure 11.4 Normalised V_z uncertainty components versus porosity
ODP Site 707 - (Site 2 Ship-board model)

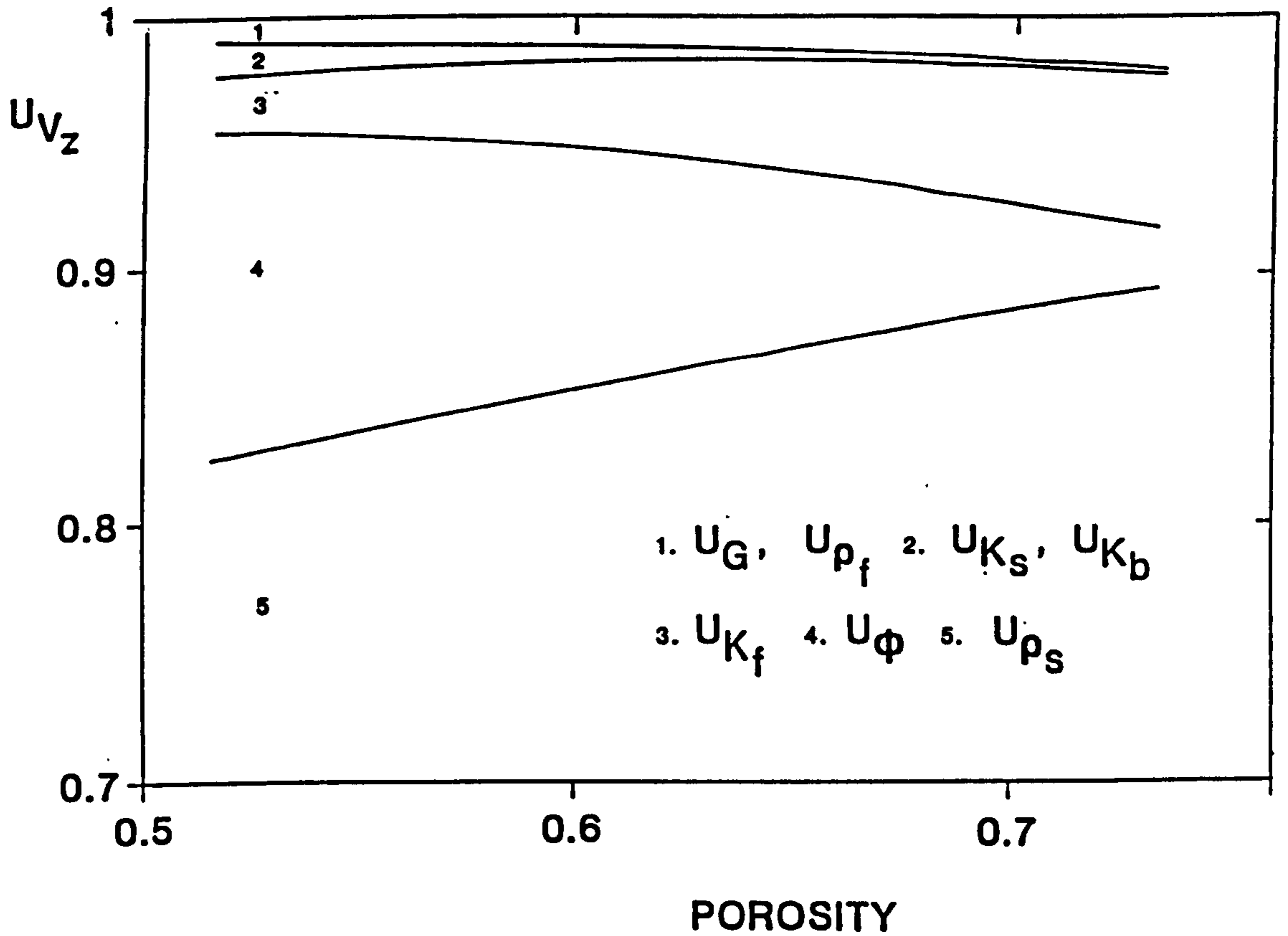
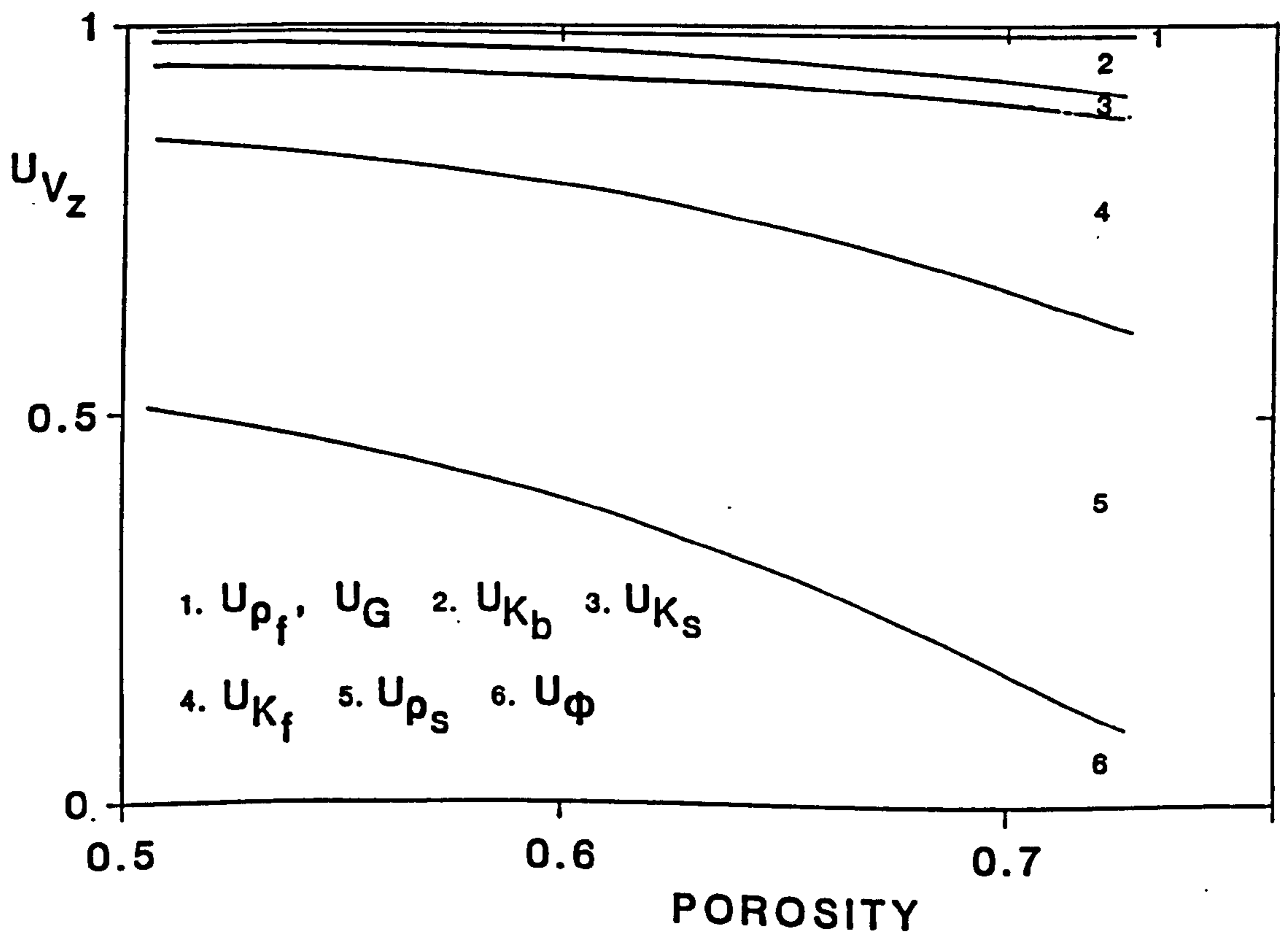


Figure 11.5 Normalised V_z uncertainty components versus porosity
ODP Site 709 - (Site 2 Ship-board model)



The differences between Figures 11.4 and 11.5 are due mainly to the difference between the values of ρ_s and $\Delta\rho_s$ used for the predictions: $\rho_s = 2670 \text{ kg/m}^3$ with $\Delta\rho_s = 200 \text{ kg/m}^3$ was used for ODP Site 707 (Figure 11.4) and $\rho_s = 2730 \text{ kg/m}^3$ with $\Delta\rho_s = 70 \text{ kg/m}^3$ was used for ODP Site 709 (Figure 11.5). Two important points are illustrated by these differences. The first is that accurate laboratory determinations of the grain density are vital if the uncertainty introduced into V_z due to $\Delta\rho_s$ is to be minimised for these particular cases. The second point, is that it is not obvious which parameters will be most important in affecting the magnitude and break-down of ΔV_z , prior to sensitivity analysis for the particular case in question. This point is emphasised by looking at Figure 9.4, where the components UK_b and UG are dominant and $U\rho_s$ is only of minor importance. Therefore the magnitude and break-down of ΔV_z cannot be characterised by a simple rule of thumb.

As an example of the practical uses of the geoacoustical model developed for Site 2, a comparison between a synthetic seismogram and a field generated seismogram is shown in Figure 11.6 (from Hempel, personal communication). The impedance record at ODP Site 709 is generated from the measurements given in Tables 11.2 and 11.3, after the velocities and densities have been converted to in-situ conditions. The impedance-depth profile is then converted to an impedance-TWT profile, using the velocity-depth structure given in the model. The source wavelet (centred between 20-200 Hz) is convolved with the impedance profile to give a synthetic seismogram for ODP Site 709. Comparisons can be made between the major reflectors in synthetic and field records, allowing identification of the samples which cause these reflectors. Stratigraphical studies (Backman, Duncan et al., in press) give the ages of these samples and, hence, the reflectors can be associated with sediments of certain ages, allowing mapping of sediment isochrone from seismic records.

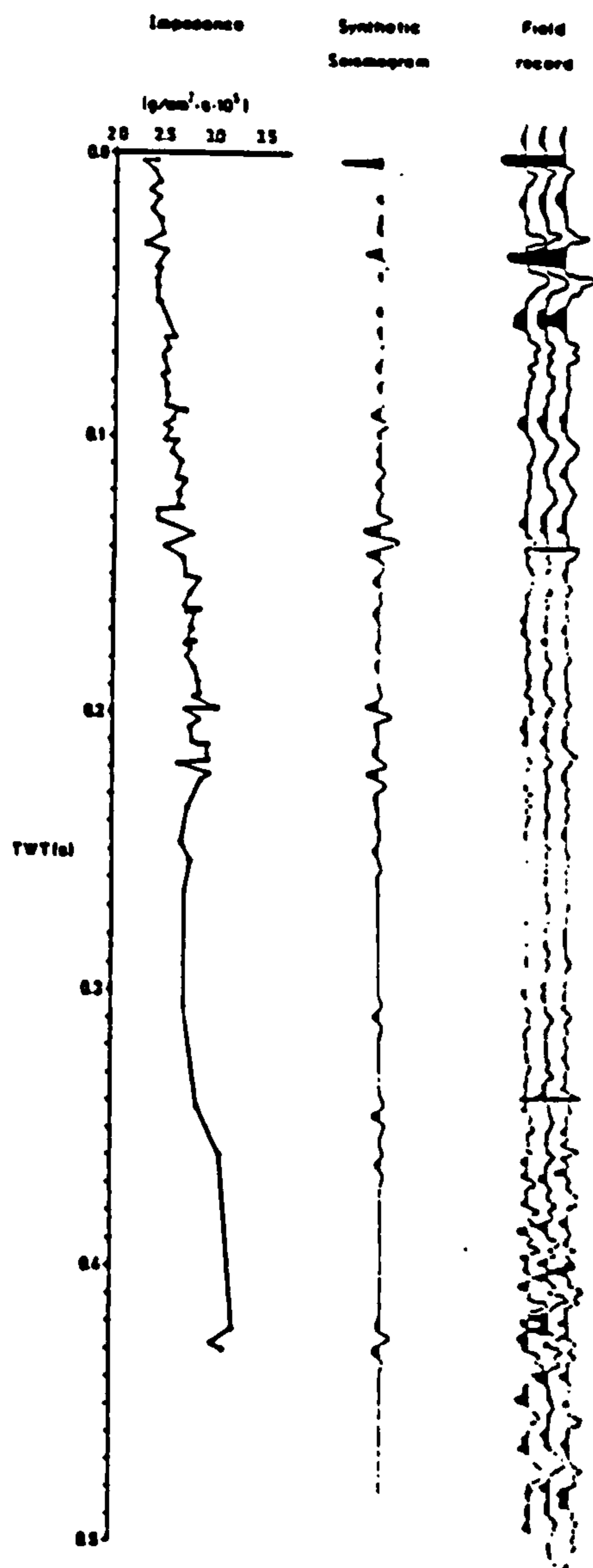


Figure 11.6 Synthetic and Field seismograms using a geoacoustical model for Site 2 (Hempel, personal comm.)

11.4 A geoacoustical model of Site 2 based on post-cruise measurements and comparisons between measured and predicted values of V_p

A simple geoacoustical model of Site 2 can be defined by the values given in Tables 11.5 and 11.6 from post-cruise experiments on a few samples. Here, experimental information on the subtle variations of velocities and density with depth (as given in Tables 11.1 - 11.3 and used in 11.3) is sacrificed in order to investigate the effect of the gradients of these properties with depth upon predicted fast wave velocities. The quantities $V_Z + \Delta V_Z$, $V_Z - \Delta V_Z$ and V_I are calculated from Tables 11.5 and 11.6 and the predictions are shown in Figure 11.7 along with the experimental velocities from Table 11.5.

Figure 11.7 V_p experimental measurements and predictions, with uncertainties, versus depth, for post-cruise model

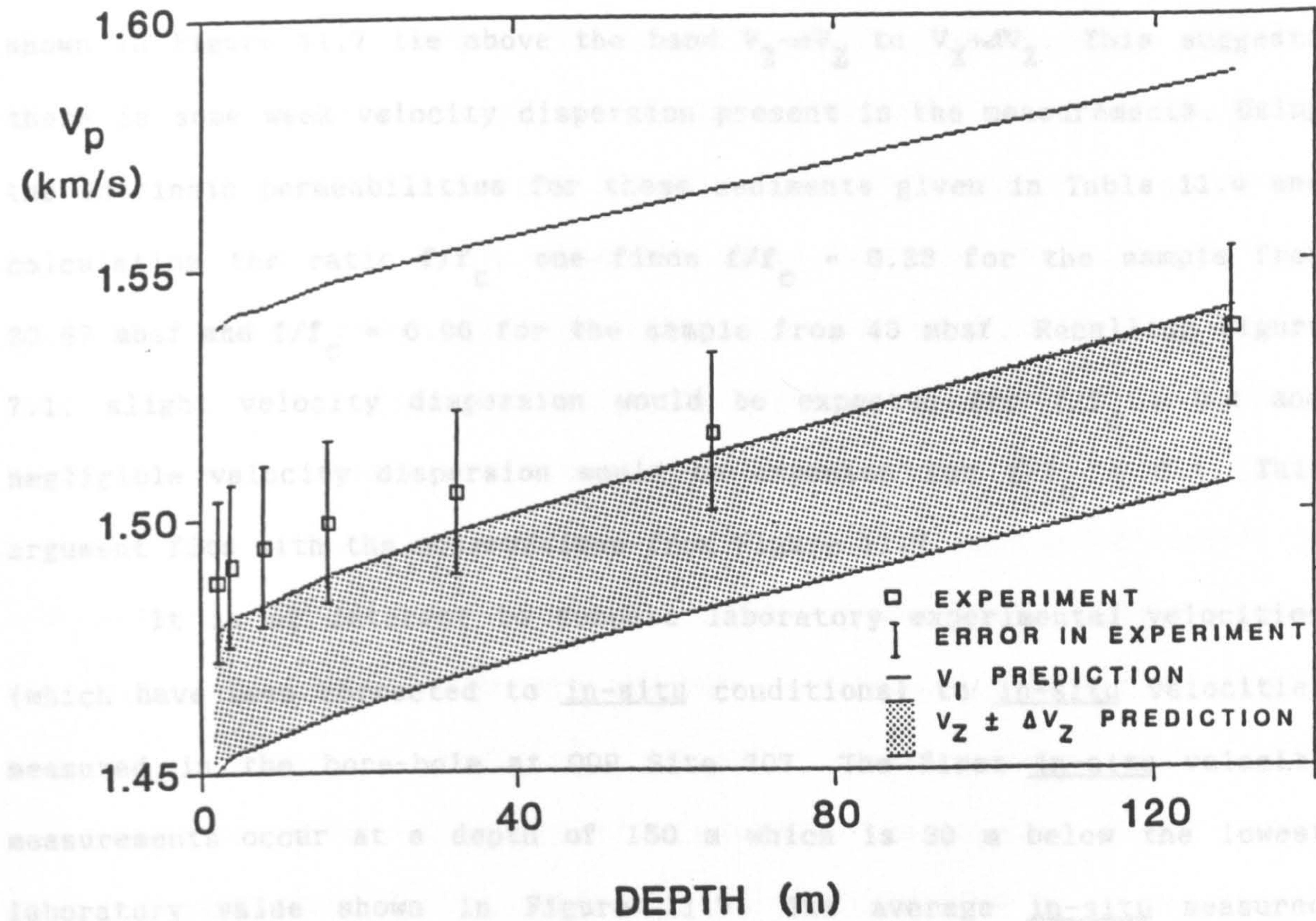
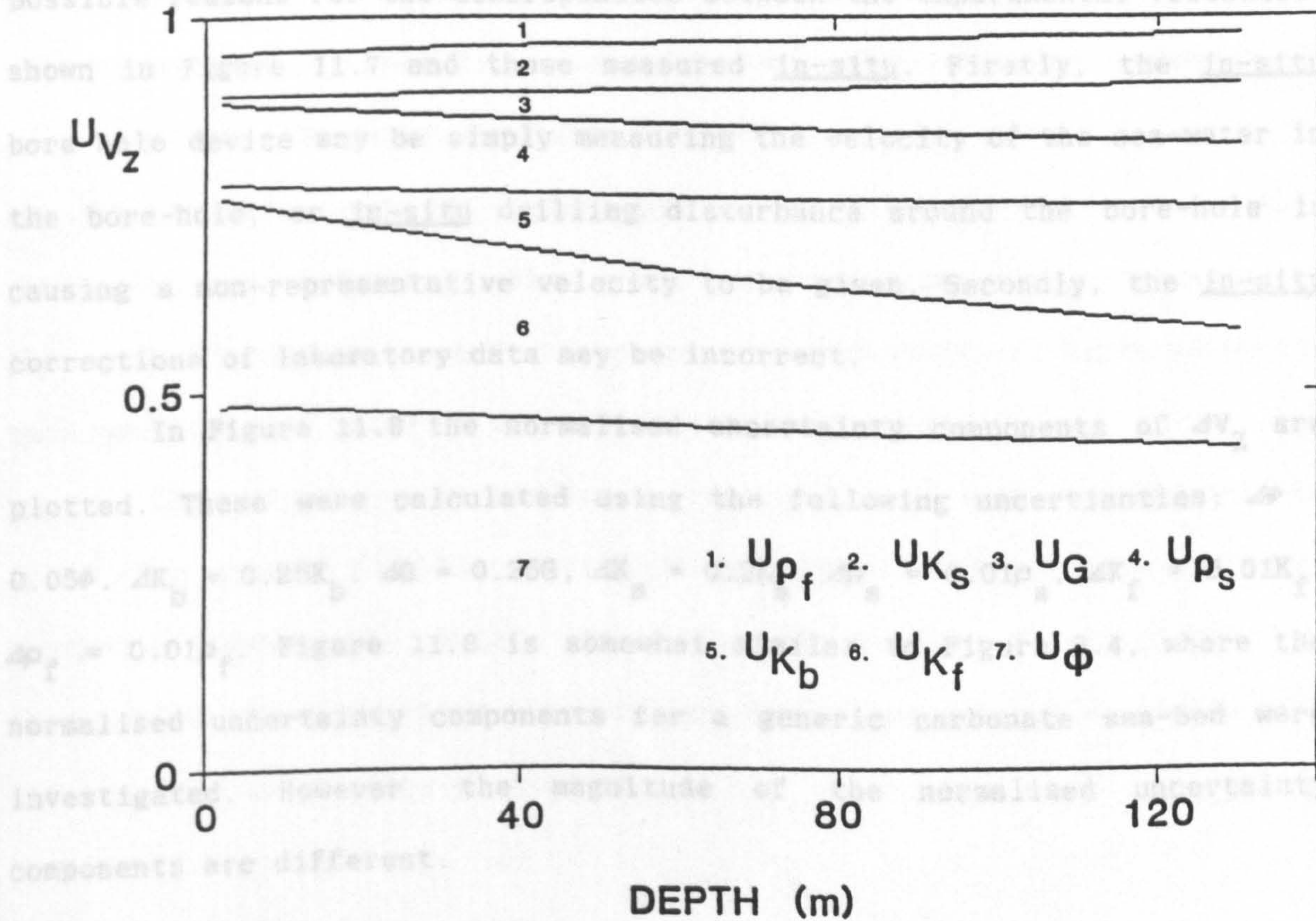


Figure 11.8 Normalised V_z uncertainty components versus depth for post-cruise model, Site 2



At depths of less than 30 metres, the experimental velocities shown in Figure 11.7 lie above the band $V_Z - \Delta V_Z$ to $V_Z + \Delta V_Z$. This suggests there is some weak velocity dispersion present in the measurements. Using the intrinsic permeabilities for these sediments given in Table 11.4 and calculating the ratio f/f_c , one finds $f/f_c = 0.23$ for the sample from 20.87 mbsf and $f/f_c = 0.06$ for the sample from 40 mbsf. Recalling Figure 7.1, slight velocity dispersion would be expected for $f/f_c > 0.1$ and negligible velocity dispersion would be expected for $f/f_c < 0.1$. This argument fits with the observations from Figure 11.7.

It is of interest to compare laboratory experimental velocities (which have been corrected to in-situ conditions) to in-situ velocities measured in the bore-hole at ODP Site 707. The first in-situ velocity measurements occur at a depth of 150 m which is 30 m below the lowest laboratory value shown in Figure 11.7. The average in-situ measured velocity is 1495 m/s for the interval 150-250 m. This is only 10 m/s above the velocity of the sea-water at the surface of the sea-bed. There are two possible reasons for the discrepancies between the experimental velocities shown in Figure 11.7 and those measured in-situ. Firstly, the in-situ bore-hole device may be simply measuring the velocity of the sea-water in the bore-hole, or in-situ drilling disturbance around the bore-hole is causing a non-representative velocity to be given. Secondly, the in-situ corrections of laboratory data may be incorrect.

In Figure 11.8 the normalised uncertainty components of ΔV_Z are plotted. These were calculated using the following uncertainties; $\Delta \phi = 0.05\phi$, $\Delta K_b = 0.25K_b$, $\Delta G = 0.25G$, $\Delta K_s = 0.2K_s$, $\Delta \rho_s = 0.01\rho_s$, $\Delta K_f = 0.01K_f$, $\Delta \rho_f = 0.01\rho_f$. Figure 11.8 is somewhat similar to Figure 9.4, where the normalised uncertainty components for a generic carbonate sea-bed were investigated. However, the magnitude of the normalised uncertainty components are different.

11.5 A discussion on the usefulness of geoacoustic models of Site 2 and whether or not Biot-type dispersion is verified by them

The large amount of data used in the geoacoustical model of Site 2 based on ship board measurements (11.3), allows small-scale variations in physical properties to be characterised. This is useful, as the variations in density and compressional wave velocity can be used to create detailed impedance profiles, from which synthetic seismograms can be formed (Figure 11.6 Hempel, personal communication). However, there are some disadvantages in using this large data set which was collected rapidly in a ship-board laboratory environment. Firstly, the errors associated ~~the~~ with ^{the} ship-board experiments are greater than those collected in stable post-cruise laboratory conditions. Secondly, the ship-board experimental data were collected at atmospheric pressure and require a subsequent pressure correction. Thirdly, the data set is incomplete as no ship-board permeability tests were conducted on the samples.

The geoacoustical model based on post-cruise measurements (11.4) has the advantage of using high quality data: carefully conducted accurate measurements of permeability, compressional wave velocity, shear wave velocity and density measurements were made on the same samples; experiments were conducted under appropriate effective stresses so this correction is not required. This model has the disadvantage of missing out the small-scale variations in the parameters with depth as captured by the geoacoustic model based on the ship-board measurements.

Clearly, for many studies a combination of both models would be ideal (for example for the creation of in-situ effective stress corrected synthetic seismograms). Such a combination has not been attempted here, as the problem of ascertaining whether Biot type dispersion is validated with these models is of primary interest.

For the results from the ship-board geoacoustical model (Figures 11.2 and 11.3) it would appear that Biot dispersion possibly occurs for high porosity samples (see 11.3) with many experimental velocity values lying between the low frequency asymptote and the high frequency asymptote. This observation (of possible dispersion in high porosity samples) is somewhat backed-up by the results from the post-cruise geoacoustical model (Figure 11.7); with the experimental velocities for samples at shallow depths (hence high porosities) lying between the high and low frequency asymptotes. Looking at Figures 11.2, 11.3 and 11.7, for both ship-board and post-cruise geoacoustic models, the uncertainties associated with the experimental and low frequency asymptotic velocities are rather large. This means that Biot's theory would not be very effective if used in an inverse way. For example, permeabilities obtained by matching experimental and predicted velocities would have considerable errors associated with them. It is interesting to note that when such a matching is carried out, the permeabilities obtained are some two orders of magnitude greater than the direct-flow permeabilities measured on samples from Site 2 (Table 11.4). A similar observation was made in Chapter 4 for the sediments from Site 1 (see Figure 4.9), and it was concluded that the larger magnitude micro-permeability controlled Biot dispersion as opposed to the lesser small-scale values. Therefore, there are grounds to not consider Biot dispersion for practical geoacoustical models, bearing in mind the difficulty in determining the micro-permeability of sediments.

If Biot dispersion is dropped from these geoacoustic models (along with the slow wave and the fast wave attenuation - Chapter 9) there becomes no distinction between Biot's theory and the simple poroelastic theory of Gassmann (Chapter 2). If this approach is adopted, then the experimental velocities should fall within the low-frequency velocity

uncertainty band. If the velocities lie outside this band (which they do in Figures 11.2, 11.3 and 11.7) then a possible explanation is that an inappropriate values for the shear modulus and frame bulk modulus have been used for the predictions. This argument could be applied to similar observations from Figures 7.3, 7.4, 7.6, 7.7, 10.2 and 10.3. Hamilton et al. (1982), in discussion of the data of Johnson et al. (1977), (which are shown in Figure 7.3), use the non-dispersive version of Biot's theory. To obtain a good fit between predicted and experimental velocities, their analysis requires extremely high values of the frame bulk modulus (Hamilton, 1971), which are not consistent with the limited results presented in Chapter 5. It is not possible to show if the non-dispersive high frame modulus (K_b) approach of Hamilton et al. (1982) is any more correct than the dispersive (high) micro-permeability (k_a) approach presented here, as both K_b and k_a are extremely difficult to experimentally determine (Chapters 4, 5 and 7).

11.6 Summary

A case study has been conducted for Site 2, located in the W Indian Ocean, defined by the area of sediments between ODP Sites 707 and 709. Biot's theory was applied to two geoacoustical models of the sea-bed, one based upon ship-board measurements and the other upon post-cruise measurements. For both models, predicted compressional wave velocities were compared with experimental values and the role of Biot-type dispersion was assessed.

Site 2 consists of a thick sequence of ooze-chalk carbonate sediments, whose physical and acoustical properties were comprehensively determined (at atmospheric pressures) by ship-board laboratory measurements. A number of samples were taken for post-cruise laboratory measurements, and experiments were performed to give the shear velocity,

permeability, compressional wave velocity and density as a function of effective stress. Two geoacoustic models were constructed from these two sets of data.

For the geoacoustical model based upon ship-board measurements, predicted compressional wave velocities were compared to experimental velocities. It was found that, for porosities exceeding 60%, there was some evidence for Biot-type dispersion, as experimental velocities lay well above the non-dispersive prediction uncertainty band. This argument fits with the observation that higher porosity carbonate sediments have higher permeabilities (note, this observation does not extend to high porosity clays), hence exhibit greater dispersion. The magnitude and break-down of the uncertainty in the non-dispersive prediction was studied; revealing that the uncertainty in the grain density was the important controlling parameter.

For the geoacoustical model based upon post-cruise measurements, the experimental velocities were fairly close to the non-dispersive prediction. There was some evidence to suggest Biot-type dispersion being greater for shallow sediments, which fits the observation that shallower sediments have greater permeability. The uncertainty in the non-dispersive velocity (ΔV_z) was dominated by the uncertainties in the fluid modulus, the frame bulk modulus and the grain density.

Geoacoustical models based on data from post-cruise and ship-board experiments, were used to investigate Biot dispersion in the carbonate sediments of Site 2, in addition to other related problems. The following conclusions were drawn from these studies:

- 1 The errors associated with performing experiments in a ship-board environment - especially the grain-density determination - mean that the existence^e of Biot-type dispersion can not be simply verified.

- 2 Small-scale permeability measurements, obtained from careful post-cruise laboratory permeability experiments, were too small to account for Biot-type dispersion (the argument touched on in Chapter 4, that the micro-permeability is the appropriate parameter for Biot-dispersion, was recalled).
- 3 The combination of data from ship-board and post-cruise geoacoustical models can be usefully applied to other problems: such as the creation of synthetic seismograms for stratigraphical studies.

12.1 The findings of this thesis

There have been few attempts to apply Biot's theory to models of sea-bed sediments. This has been due to conceptual problems in implementing the theory and/or technical problems in measuring the appropriate sediment physical properties for the models. The studies described in this thesis have clarified the following conceptual and technical points:

(1) The permeability of deep-sea turbidite sediments has been shown to vary over 7 orders of magnitude due to technique dependent and intrinsic reasons.

(2) In-situ determinations of the shear modulus of turbidite sediments are up to a factor of 4 greater than those obtained from laboratory techniques.

(3) Using the resonant column method as a standard, bender transducer methods have been shown to give good determinations of the shear velocity of sediments, and there is little evidence for dispersion.

(4) Longitudinal low frequency forced and resonance methods for determining the extensional elastic and anelastic properties of sediments and rocks have been shown to be experimentally problematic, yielding unreliable results.

(5) Currently available techniques for accurately assessing the micro-geometry and size of pore space and inter-pore space are inadequate.

(6) Through Biot's theory, a new solution has been developed for the magnitude of tidally-induced pore-pressures in the sea-bed.

(7) Biot's propagative slow wave has been argued to be a fluid and not a frame wave, induced at free-flow boundaries, and must be difficult to measure.

(8) A quantified verification of Biot-type fast wave dispersion has been shown for high porosity/permeability carbonate sediments.

(9) Sensitivity analysis has allowed identification of the physical properties which influence the magnitude of the uncertainty in Biot velocity predictions at low frequencies.

(10) A qualitative verification of Biot-type fast wave attenuation has been shown for some sandstones and unconsolidated sands.

12.2 Applications of the findings of this thesis

The points outlined in 12.1 are all of great importance to the various problems of defence, exploration, design and pollution control. which were introduced in 1.1. Some of the points are of particular significance to the individual problems:

For naval defence requirements, points (7) and (8) are important for calculating high frequency reflection coefficients from the sea-bed: (7) will reduce reflection coefficients, while (8) contributes to an increases in reflection coefficients for high porosity/permeability sediments. Additionally, points (4) and (9) contribute to the understanding of low-frequency sound wave propagation through sea-bed sediments.

For oil exploration problems, points (1), (5), (8) and (10) are of high significance: (1) (5) and (10) show that ultrasonic (and other) techniques for probing the size and shape of the pore-space (where the oil resides!) do not give fool-proof results, for intrinsic and technique-dependent reasons; point (8) is important for tying down discrepancies between high frequency bore-hole and laboratory compressional velocities, and the lower frequency seismic results.

For geotechnical design purposes, points (1) to (4) are especially important: (1) is crucial in deciding which permeability to use in design calculations; points (2) to (4) show the "pros and cons" of laboratory

testing techniques for evaluating the dynamic moduli of sea-bed sediments.

For sea-bed radio-active waste disposal, points (1) and (6) are significant: (6) is of interest in obtaining an inverse determination of the in-situ large-scale permeability of the sea-bed sediments; (1) is of interest in allowing comparisons of small-scale laboratory determined permeabilities with in-situ predictions, as a correct in-situ permeability is needed to calculate flow rates of contaminated pore-fluids.

12.3 A statement on the problems involved with the successful application of Biot's theory to sea-bed sediments

This thesis has focussed on the following problem: can a numerical model of the sea-bed (based on measurements of sediment physical properties) be used as input into Biot's theory to allow predictions of the response of the sea-bed when it is subjected to dynamic stresses? There is not a straightforward all-embracing answer to this problem: the quality of the prediction will strongly depend upon the accuracy of the experimental determinations of the appropriate input and output parameters. However, the findings outlined in 12.1 allow some useful guide-lines to be drawn-up for simple models, which can be used with a simple version of Biot's theory, as a practical predictive tool.

Points (1) to (5) in 12.1 highlight the difficulties in experimentally determining the input parameters to Biot's theory. Point (4) shows it is not possible to characterise the anelastic properties of sediments: this means that the simpler Biot (1956 a,b) poroelastic theory should be used in preference to Biot's (1962 a,b) poro-anelastic theory. Point (4) also means that a relationship between shear and frame bulk moduli has to be estimated (such as $K_b = 2.17G$). Point (5) indicates the problem in assessing the size of inter-pore connections: this means that Biot's (1956b) frequency correction cannot be applied to predictions (made

with Biot's, 1956a theory), with confidence. Point (1) shows that the permeability used/predicted in/by Biot's (1956a) theory will be a "micro-permeability", which will be greater than "small-scale" direct-flow laboratory permeabilities.

Points (7) and (10) show that fast wave attenuation and the propagating slow wave are difficult to measure or predict with confidence. This means these phenomena will not need to be considered for simple practical models of the sea-bed. Point (9) shows that the uncertainties in K_b , G and the solids density (ρ_s) are important in controlling the magnitude of the uncertainty in the predicted low frequency velocity, whereas the uncertainty introduced through the solids bulk modulus (K_s) is minimal, allowing K_s to be safely estimated. Point (10) shows that the tortuosity (T) and micro-permeability (k_a) of sediments control the fast wave dispersion.

For a simple geoacoustical model of the sea-bed, which can be used along with Biot's (1956a) theory as a predictive tool, the following parameters are required: measurements of G , T , k_a , ρ_s and V_p (fast wave velocity at a frequency f); values for the fluid modulus (K_f), density (ρ_f) and viscosity (η) found from tables, and the estimates $K_b = 2.17G$ and $K_s = \infty$. Using these parameters, Biot's (1956a) theory can be used to predict V_p at any frequency. Alternatively, the theory can be used in an inverse way to predict any one of the other parameters using measurements of V_p . Such a simplified approach will lack many of the requirements of sophisticated problems of acoustical interactions with sea-bed sediments, but will act as a good base to start any such investigations.

For a simple hydrodynamic model, which can be used along with Biot's (1956a) theory, less parameters are required: measurements of G , k_a , ρ_s and the dynamic tidal pore-pressure (p_p); K_f , ρ_f , η , K_b and K_s estimated or from tables. These parameters can be used along with a new

tidally-induced pore-pressure solution (Point 9 in 12.1) to predict the in-situ dynamic pore-pressure. Alternatively, using measurements of p_p , inverse in-situ predictions of any of the other parameters can be made. Such predictions will be gross estimates - due to the simplicity of the model and solution - but will yield valuable in-situ estimates of the geotechnical properties of the sea-bed. This is especially important for G and k_a , which are difficult to measure in-situ.

12.4 The way forward

Biot's (1956 a,b) gives an over-simplified view of stress waves in sediments and rocks. The theoretical developments since (Biot, 1962 a,b, Cleary, 1980, McCann and McCann, 1985, Berryman and Thigpen, 1987) have lead to a better conceptual understanding of the manner of stress wave propagation in sediments. Such theoretical developments may continue, but a wider acceptance of Biot's ideas requires significant experimental progress. Only through accurate experimental determination of the appropriate physical parameters of sediments will satisfactory Biot-type predictions be made. The simplified models given in 12.3, using Biot's (1956a) theory, are the virtual practical limit today.

The key input parameters which require measurement are the frame bulk moduli (K_b and G) and the variables controlling the microscopic flow of pore-water (k_a , T and a). Measurements of the fast wave attenuation and velocity at different frequencies are required for comparison with the output parameters. Improved dynamic pore-pressures measurements (for hydrodynamic models) and also measurements of the slow wave velocity would be useful.

The resonant column method for determining K_b and G should be pursued. A redesign of the system described in Chapter 5 may overcome the inability to make reliable K_b measurements. The end-compliance problems of

low-frequency shaker experiment described in Chapter 6 need to be overcome to yield sensible data relating to the longitudinal anelastic properties of sedimentary rocks. Of course, such laboratory determinations of K_b and G are second-best to in-situ measurements. There are many good current methods for measuring shear modulus in-situ - through shear wave experiments - but there is no simple way to measure K_b in this way. Laboratory tests have to therefore be pursued along side an in-situ field experiment program.

Improved methods to characterise the pore-space variables k_a and a are more difficult to visualise. The best route is probably through SEM image analysis. This is rather undesirable, as it requires new technical advances and it would be not be practical for routine studies. Furthermore, this technique relies on laboratory measurements, which again brings up the question of the in-situ applicability of laboratory derived data. Perhaps more effort is needed to establish better empirical relationships (along the lines of the Kozeny equation), relying on proven (if not crude) experimental techniques. Incidentally, one is probably safe in measuring the tortuosity from electrical conductivity measurements.

Measurements of fast wave attenuation and dispersion over many orders of magnitude are required. This could be achieved by extension of the frequency band of the "low-frequency shaker" experiment described in Chapter 8. Measurements of the slow wave in unlithified sediments may be possible through the use of a dynamic pore-pressure sensor as discussed in Chapter 6. Lastly, improving the piezometer PUPPI by using a longer probe with a greater number of pore-pressure ports would significantly help for the hydrodynamic modelling studies.

The predictive powers of Biot's theory are great: they allow elastic and anelastic deformations of sediments (and any other porous material) to be characterised over the entire spectrum of frequencies.

The potential of Biot's thoery will only be realised through an increased awareness of the relative importance of the different input and output parameters and how to attempt to accurately experimentally measure those parameters. Good luck if you intend to contribute to this area of science!

APPENDIX 1 Elasticity theory

A1.1 Introduction

The classical theory of elasticity is a basic component of all theories concerning the deformation of solids. The following precis is based upon a number of standard text books (Kolsky, 1963, Norwick and Berry, 1972, Nye, 1979, Bourne and Kendall, 1979 and White, 1983).

A1.2 The state variables and co-ordinate system

A1.2.1 The Cartesian axes system

The principle Cartesian axes are defined as three mutually perpendicular vectors (Ox_i) of unit length originating from a fixed point O. Standard Cartesian vector and tensor notation is adopted (see Bourne and Kendall, 1977).

A1.2.2 The stress tensor

The stress at any point P in a material is defined by the second rank tensor $[\sigma_{ij}]$. The stress tensor describes the forces acting on the faces of an infinitesimally small cube surrounding P. There are three normal stress components ($i=j$) and six shear stress components ($i \neq j$).

A1.2.3 The Strain tensor

When stresses are applied to a material it will deform, and the distances between adjacent points will change. The variation of displacement (u_i) with position (x_i) can be used to define nine components of an antisymmetrical tensor $[e_{ij}]$:

$$e_{ij} = \frac{\partial u_i}{\partial x_j} \quad (i, j = 1, 2, 3) \quad \text{A1.1}$$

The three components $i=j$, represent extensions per unit length parallel to the three principal axes (Ox_i). The six other components $i \neq j$, represent the following rotations: e_{12} is the rotation of a line element parallel to Ox_2 , about Ox_3 , towards Ox_1 ; e_{21} is the rotation of a line element parallel to Ox_1 , about Ox_3 , towards Ox_2 , etc.

The strain tensor $[\epsilon_{ij}]$ is defined as the symmetrical part of $[e_{ij}]$:

$$\epsilon_{ij} = \frac{1}{2} \cdot (e_{ij} + e_{ji}) \quad \text{A1.2}$$

A1.3 The fundamental relationship between state variables

A1.3.1 The constitutive equation

The stress tensor is related to the strain tensor through the constitutive equation:

$$\sigma_{ij} = M_{ijkl} \cdot \epsilon_{kl} \quad \text{A1.3}$$

M_{ijkl} is a fourth rank tensor with 81 coefficients. Due to symmetry considerations, the number of coefficients can be reduced to 36 (Nye, 1979). For an isotropic material only two independent elastic constants, denoted λ and G , are required to calculate the remaining coefficients. Using these elastic constants it is possible to rewrite the constitutive relationship in the more familiar way as Hooke's law, where ϵ is the dilatation:

$$\sigma_{ij} = 2G\epsilon_{ij} + \delta_{ij}\lambda\epsilon \quad (\delta_{ij}=1, i=j; \delta_{ij}=0, i \neq j) \quad \text{A1.4}$$

$$\epsilon = \epsilon_{11} + \epsilon_{22} + \epsilon_{33} \quad \text{A1.5}$$

A1.3.2 The elastic constants

The two elastic constants λ and G , completely describe the behaviour of an isotropic material. However, for convenience, five interrelated constants are used: Young's modulus (E), Poissons's ratio (ν), the bulk modulus (K), the shear modulus (G) and the constrained modulus (D). The definitions and a table of all the interrelationships between these elastic constants are summarised by White (1983). Some of the relationships are:

$$D = K + \frac{4}{3}G = \lambda + 2G = \frac{E - \nu E}{1 - \nu - 2\nu\nu} \quad A1.6$$

A1.4 Static and dynamic deformations

A1.4.1 The equilibrium of the stress field

Neglecting body forces, if all parts of a body are in static equilibrium, then the stress field is zero:

$$\sum_j \frac{\partial \sigma_{ij}}{\partial x_i} = 0 \quad A1.7$$

Neglecting body forces, if dynamic stresses act upon the body, inertial forces have to be considered, and the stress field becomes:

$$\sum_j \frac{\partial \sigma_{ij}}{\partial x_i} = \rho \cdot \frac{\partial^2 u_i}{\partial t^2} \quad A1.8$$

A1.4.2 Classification of dynamic responses

If periodic stresses of angular frequency (ω), are applied to a body, then the ratio ω/ω_r , where ω_r is the resonant angular frequency of the body, controls the type of dynamic response induced. The following responses are defined:

$\omega \ll \omega_r$ - subresonance; $\omega \approx \omega_r$ - resonance, and $\omega \gg \omega_r$ - suprreresonance.

If the dynamic force F_a acts on the body, there will be a restoring force F_s , due to the displacement of the mass (m_s) of the body. The restoring force must enter the stress equilibrium equation, which can be re-written as the equation of motion for the body:

$$F_a - F_s = m \cdot \frac{\partial^2 u_i}{\partial t \partial t} \quad A1.9$$

This equation can be simply solved for each dynamic response (e.g. Norwick and Berry, 1972) using the following simplifications: for subresonance the presence of the inertia of the body is not important ($F_a \approx F_s$); for resonance, the force applied to the body is not important ($F_a \approx 0$) and at suprreresonance the restoring force is not important ($F_s \approx 0$). The solutions show that for subresonance, the response is simply governed by the constitutive relationship; for resonance the resonant frequency is given by:

$$\omega_r^2 = C \cdot M_{ijkl} \quad A1.10$$

where C is a constant depending on the shape and dimensions of the body. Lastly, for suprreresonance, the solutions describe the propagation of stress waves in the body.

A1.5 The wave equations

A1.5.1 The wave equation for compressional deformations

For suprreresonance deformations the equations A1.4 and A1.7 can be combined to give the three-dimensional equations of motion:

$$\rho \cdot \frac{\partial^2 u_i}{\partial t \partial t} = (G + \lambda) \cdot \frac{\partial \epsilon}{\partial x_i} + G \nabla^2 u_i \quad A1.11$$

$$\nabla^2 = \sum_1^1 \frac{\partial^2}{\partial x_1^2} \quad \text{A1.12}$$

Differentiating A1.11 and summing on i gives the wave equation for the propagation of the dilatation ϵ (Equation A1.13). If harmonic solutions are assumed, then it is straightforward to show that the dilatation propagates with a velocity V_p :

$$\rho \cdot \frac{\partial^2 \epsilon}{\partial t \partial t} = (2G + \lambda) \cdot \nabla^2 \epsilon \quad \text{A1.13}$$

$$V_p = \left[\frac{2G + \lambda}{\rho} \right]^{1/2} \quad \text{A1.14}$$

A1.5.2 The wave equation for shear deformations

The wave equation for shearing deformations can be found by using the rotation (Ω_{ij}), which is defined:

$$\Omega_{ij} = \frac{1}{2} \cdot (e_{ij} - e_{ji}) \quad \text{A1.15}$$

Differentiating the equations of motion (Equation A1.11) with respect to directions perpendicular to i , gives three pairs of coupled equations for the antisymmetrical strain components e_{ij} , with $i \neq j$. Using the definition for the rotation (Equation A1.15) and subtracting one equation from the other in each pair gives the wave equation for shearing deformations (Equation A1.16). If harmonic solutions are assumed then the rotational deformation propagates with a velocity V_s :

$$\rho \cdot \left[\frac{\partial^2 e_{ij}}{\partial t \partial t} - \frac{\partial^2 e_{ji}}{\partial t \partial t} \right] = G \cdot \nabla^2 \cdot (e_{ij} - e_{ji}) \quad \text{A1.16}$$

$$V_s = \left[\frac{G}{\rho} \right]^{1/2} \quad \text{A1.17}$$

APPENDIX 2 Anelastic theory

A2.1 Introduction

In practice all real materials are never completely elastic, but are non-elastic in some fashion. Materials which do not obey Hooke's law are non-elastic. Of the various types of non-elastic behaviour anelastic theory is the most straightforward to use and the most applicable for small strain amplitude deformations of rocks and sediments. The following precis is based mainly on Norwick and Berry (1972).

A2.2 Quasi-static anelastic deformations

Anelastic deformations are not instantaneous but are time (hence frequency) dependent. Over long periods of time (e.g. days or years) it is most convenient to work in the time domain, while the opposite is true for higher frequency deformations.

If a static stress is applied to an anelastic material, then its strain response will be quasi-static, and creep will occur after the initial elastic deformation. Conversely, if a static strain is applied to an anelastic material, stress relaxation will occur after the initial elastic deformation. In the latter case, the modulus given by Hooke's law (equation A1.3), can be allowed to become time dependent: relaxing with increasing time (see Figure A2.1).

In Figure A2.1, the decay of the modulus from its "unrelaxed" state (M_u), to its "relaxed" state (M_r), is some function of time, the simplest case being an exponential decay characterised by a single relaxation time constant τ ;

$$M(t) = M_r + (M_u - M_r) \cdot e^{-(t/\tau)} \quad \text{A2.1}$$

$$M_u = M(0), \quad M_r = M(\infty) \quad \text{A2.2}$$

A2.3 Dynamic anelastic deformations

It is useful to treat dynamic anelastic deformations in the frequency domain. In a similar way as for classical elastic deformations (see A1.4.2), anelastic deformations can be classified into subresonant, resonant and supresonant divisions, depending upon the frequency of the deformations.

For subresonant deformations, a complex frequency dependent dynamic modulus $\hat{m}(\omega)$ can be defined for a harmonic strain disturbances (ϵ). With reference to Figure A2.2, if a harmonic stress (σ) is applied to an anelastic material at a frequency ω , then the strain (ϵ) induced in the material will lag behind the stress by an angle ϕ , known as the loss angle. The complex dynamic modulus is defined by the ratio of the stress to the strain:

$$\hat{m}(\omega) = \frac{\sigma_0 \cdot e^{i\omega t}}{\epsilon_0 \cdot e^{i(\omega t - \phi)}} = |m(\omega)| \cdot e^{i\phi} \quad \text{A2.3}$$

The complex dynamic modulus can be simply divided into real and imaginary components ($m_r(\omega)$ and $m_i(\omega)$), for which the following relationships hold for small ϕ :

$$\hat{m}(\omega) = m_r(\omega) + im_i(\omega) \quad \text{A2.4}$$

$$|m|^2 = m_r^2 + m_i^2 \quad \text{A2.5}$$

$$\tan(\phi) = m_i/m_r \approx \phi \quad \text{A2.6}$$

$$\hat{m}(\infty) = M_u, \quad \hat{m}(0) = M_r \quad \text{A2.7}$$

In a similar way, complex dynamic anelastic moduli \hat{G} , \hat{E} , \hat{K} and \hat{D} can be defined after the elastic moduli G , E , K and D . Note, the convention of dropping from upper case for time-domain moduli, to lower case for frequency dependent moduli (e.g. M to \hat{m}) is not adopted for \hat{G} , \hat{E} , \hat{K} and \hat{D} .

A2.6 Experimental methods for characterising dynamic anelasticity

Extensional-mode experiments can yield the longitudinal anelastic properties (denoted by the subscript E) of materials. Torsional-mode experiments can give the shearing anelastic properties (denoted by the subscript S). Analysis is presented for the extensional case. However, similar analysis hold for shearing deformations.

At subresonant frequencies anelastic properties of materials can be determined from applying a known stress (σ) to the material and measuring the resultant strain (ϵ). If σ is plotted versus ϵ as in Figure A2.3, then a hysteresis curve will be produced. The gradient of the major axis of the curve will give $|m|$, while a good approximation for the loss angle can be found by the shape of the curve. Hardin et al. (1967). If A_t is the area of the shaded triangle in Figure A2.3 and A_1 is the area inside the hysteresis loop then a good approximation for the extensional damping ratio D_E is given by:

$$D_E \approx \frac{A_1}{4\pi \cdot A_t} \approx \phi/2 \quad \text{A2.8}$$

At resonant frequencies (ω_r), $|m|$ can be found if the dimensions and shape of the anelastic body are known (see Equation A1.10). At resonance, two methods can be used to determine parameters which are related to the loss angle. For the first method, the extensional specific

attenuation ($1/Q_E$) is deduced from width of the "Lorentzian" resonance peak ($\Delta\omega$) at $1/\sqrt{2}$ the maximum displacement amplitude at ω_r (Norwick and Berry, 1972, White, 1983). For the second method, the logarithmic decrement is determined from amplitude of the displacement of two successive cycles (A_n and A_{n+1}) as the body is allowed to relax freely from resonance

$$1/Q_E \approx 2\Delta\omega/\omega_r \approx \phi_E \quad \text{A2.9}$$

$$\delta_E \approx \ln(A_n/A_{n+1}) \approx \pi \cdot \phi_E \quad \text{A2.10}$$

A2.7 Anelastic wave propagation

A2.7.1 The anelastic wave equation

The three dimensional elastic wave equation for the dilatation ϵ (Equation A1.13) can be simply extended for an anelastic material:

$$\rho \cdot \frac{\partial^2 \epsilon}{\partial t \partial t} = \hat{D} \cdot \nabla^2 \epsilon \quad \text{A2.11}$$

$$\hat{D} = 2\hat{G} + \hat{\lambda} \quad \text{A2.12}$$

$$\epsilon = \epsilon_0 \cdot e^{i(\omega t + \mathbf{k} \cdot \mathbf{x})} \quad \text{A2.13}$$

The dilatation travels with a complex wave number $\hat{\mathbf{k}}$, which is related to the real and imaginary components of the modulus \hat{D} , as well as to the velocity (V_p) and attenuation coefficient a_p of the wave. It is straightforward to show that the following relations exist (e.g. Norwick and Berry, 1972):

$$\hat{\mathbf{k}} = \mathbf{k}_r + i\mathbf{k}_i \quad \text{A2.15}$$

$$k_r = \omega \cdot \left[\frac{\rho}{D_r} \right]^{1/2} \quad \text{A2.16}$$

$$k_i = \frac{D}{2D_r} \cdot \left[\frac{\rho}{D_r} \right]^{1/2} \quad \text{A2.17}$$

$$v_p = \omega / k_r \quad \text{A2.18}$$

$$a_p = k_i \approx \frac{\omega \phi}{2v_p} \quad \text{A2.19}$$

here, a_p is in Nepers per unit length. The attenuation coefficient may also be expressed in decibels per unit length:

$$a_p \text{ (dB/m)} = 8.686 a_p \text{ (Np/m)} \quad \text{A2.20}$$

Figure A2.1 Time dependent anelastic modulus relaxation

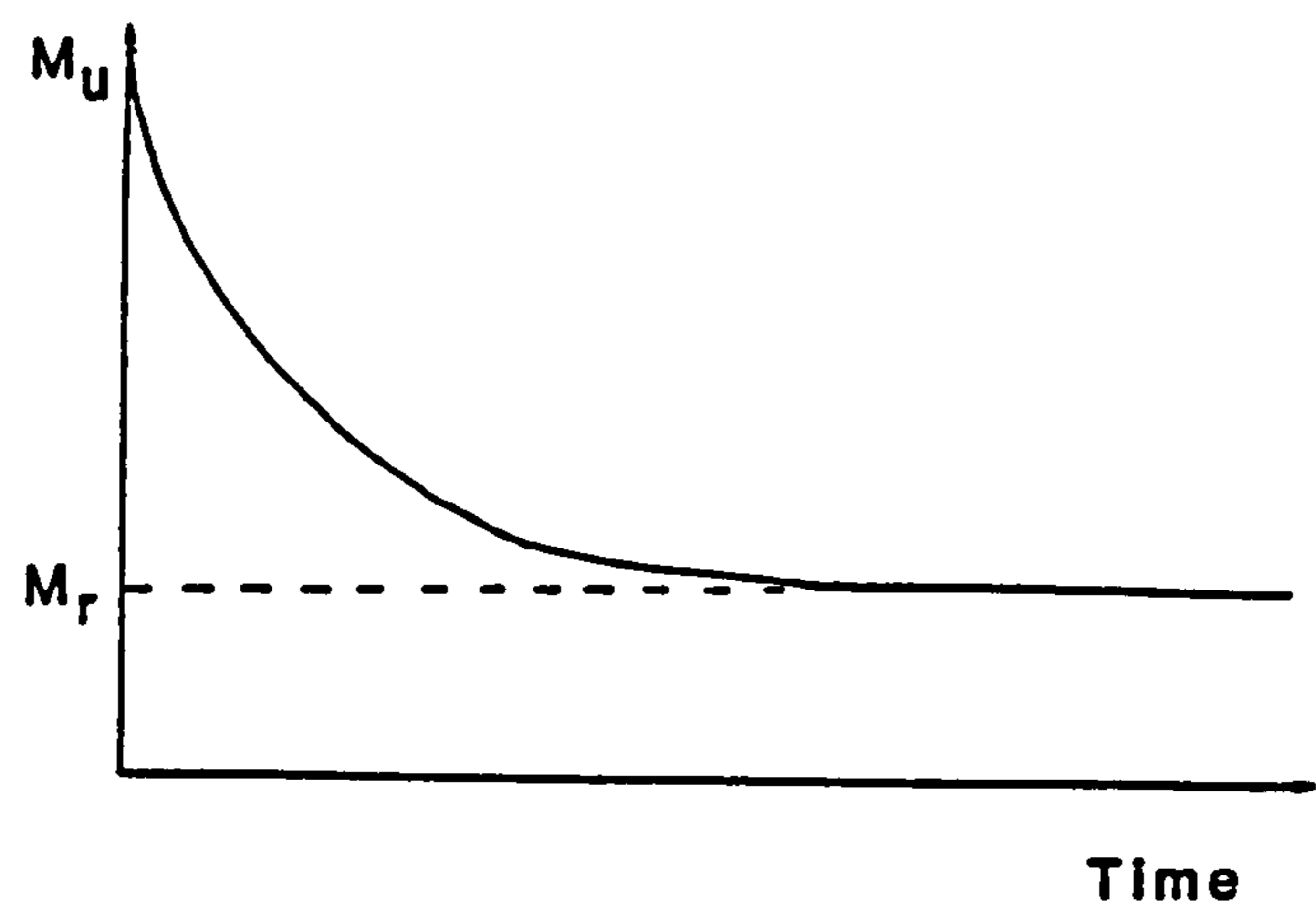


Figure A2.2 Anelastic modulus complex phase diagram

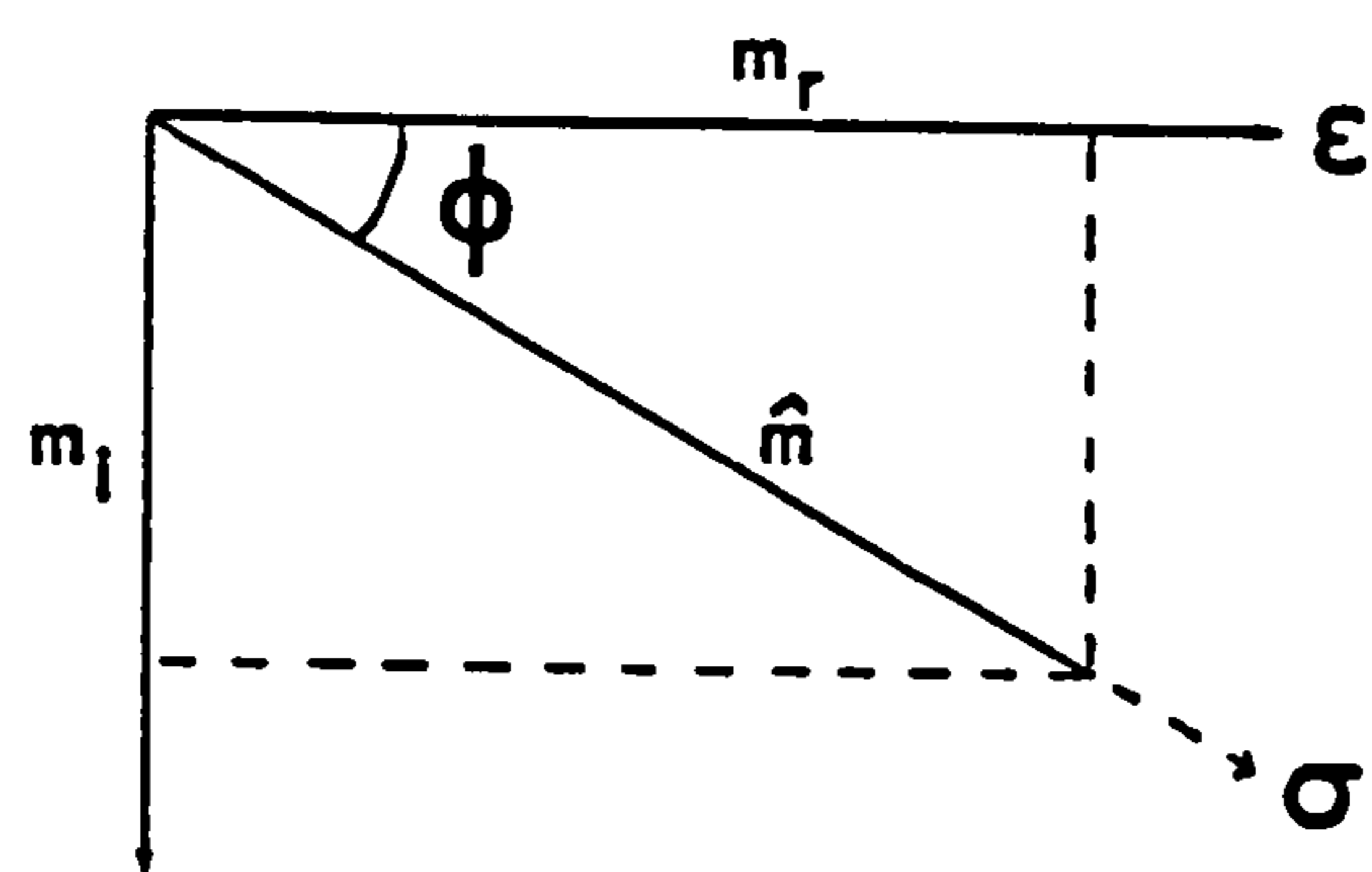
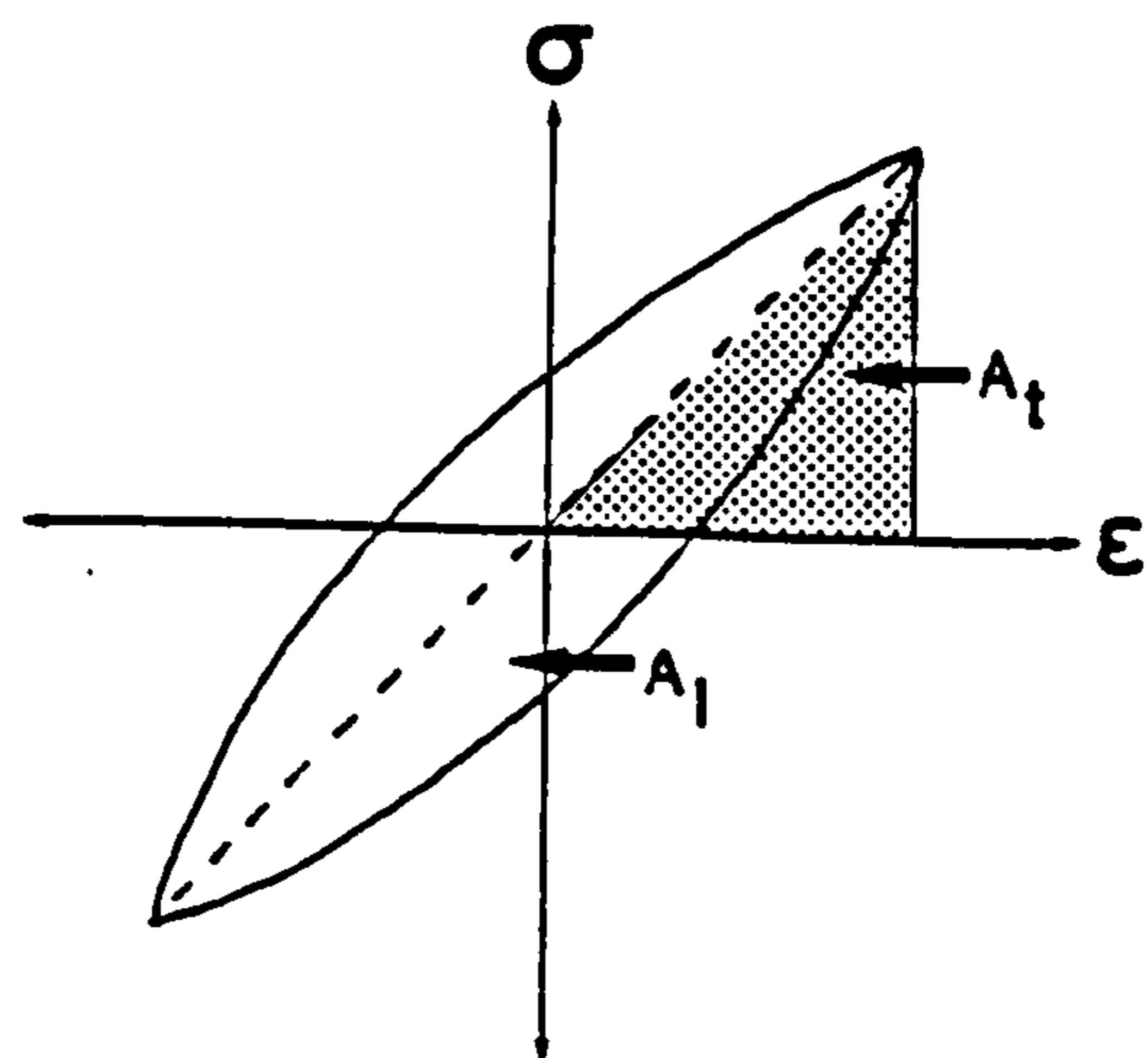


Figure A2.3 Stress - strain hysteresis loop



APPENDIX 3 Description and geographical location of data sets and samples

Table titles:

- A3.1 Description and location of data sets used in Biot's theory
- A3.2 Description and location of samples used for resonant column tests (Sites 1 and Site 4).
- A3.3 Description and location of samples used for consolidation / permeability tests at site 1 (after Schultheiss and Gunn, 1985)
- A3.4 Description and location of samples used for consolidation, permeability, V_p and V_s tests at Site 2
- A3.5 Location of PUPPI deployments at Site 1

Table A3.1 Description and location of data sets used in Biot's theory

Data set	Sediment type	Site	Table	Reference
TURB_M1	Clay/carbonate turbidite	1	3.1	
TURB_M2	Turbidite	1	4.3	Hydrodynamic model Site 1
TURB_M3	Turbidite	1	10.2	Geoacoustical model Site 1
CARB_M1/M2	Carbonate ooze	3	7.1,7.2	Johnson <u>et al.</u> (1977)
CARB_M3/M4	Carbonate ooze	2	11.1-11.6	Geoacoustical models Site 2
SILT_M1	Fine silt	4	6.5	Hamdi and Taylor-Smith (1982)
SAND_M1	Beach sand	4	5.1	
SAND_M2	Sand	-	6.2	Wingham (1985)
SAND_M3	Sand	-	6.3,6.4	Bedford <u>et al.</u> (1982)
SAND_M4	Glass beads	-	6.6	McCann and McCann (1985)

Table A3.2 Description and location of samples used for resonant column tests (Sites 1 and Site 4).

Sample No./ Sample code	Sediment type	Sub-bottom depth (m)	Latitude N	Longitude W	Site	Water depth (m)
D11174/11/70 TURB 2	turbidite ^{*1} (nanno marl)	15.7	31° 26' .5	24° 49' .6	1	5439
D11174/06/80 TURB 3	turbidite (nanno marl)	8.3	31° 26' .5	24° 49' .6	1	5439
D11174/11/120 TURB 4	turbidite (nanno marl)	16.2	31° 26' .5	24° 49' .6	1	5439
D11192/03/40 CARB	carbonate (nanno ooze)	3.4	31° 29' .1	24° 03' .8	1	5378
D11192/07/90 CLAY	red clay (nanno ooze)	9.9	31° 29' .1	24° 03' .8	1	5378
Newborough sand (SAND)	marine sand ^{*2}	surface	Newborough, Anglesey, U.K.			

*1 see Weaver and Rothwell (1987) for further description

*2 see Bennell et al. (1984) for further description

Table A3.3 Description and location of samples used for consolidation / permeability tests, Site 1 (after Schultheiss and Gunn, 1985)

Sample No.	Sediment type	Sub-bottom depth (m)	Latitude N	Longitude W	Site	Water depth (m)
D10695/6/28	turbidite ^{*1} (nanno marl)	7.94	31° 23' .7	24° 46' .3	1	5433
D10695/2/14	turbidite (nanno marl)	1.68	31° 23' .7	24° 46' .3	1	5433
D10695/3/28	turbidite (nanno marl)	3.90	31° 23' .7	24° 46' .3	1	5433
D10325/7	pelagic (foram nanno marl)	0.44	30° 22' .9	24° 05' .8	1	5407
S126/4-5	turbidite (nanno marl)	1.02	31° 31' .7	24° 25' .3	1	5446
S126/4-4	turbidite (nanno marl)	0.74	31° 31' .7	24° 25' .3	1	5446
S126/4-10	turbidite (nanno marl)	3.44	31° 31' .7	24° 25' .3	1	5446
S126/2-3	pelagic (foram nanno marl)	0.62	31° 32' .2	24° 50' .5	1	5446

*1 see Weaver and Rothwell (1987) for further descriptions

Table A3.4 Description and location of samples used for consolidation, permeability, V_p and V_s tests at Site 2

Sample No./ Sample code	Sediment type	Sub-bottom depth (m)	Latitude N	Longitude W	Site	Water depth (m)
115 709C 13H 05 147 CARB 1	(nanno ooze)	119.27	3° 54' .7	60° 33' .2	2	3048
115 709B 7H 06 144 CARB 2	(nanno ooze)	60.96	3° 54' .7	60° 33' .2	2	3048
115 709C 10H 05 144 CARB 3	(nanno ooze)	90.36	3° 54' .7	60° 33' .2	2	3048
115 709C 10H 05 147 CARB 4	(nanno ooze)	90.39	3° 54' .7	60° 33' .2	2	3048
115 709C 03H 05 146 CARB 5	(nanno ooze)	20.87	3° 54' .7	60° 33' .2	2	3048
115 709C 05H 05 144 CARB 6	(nanno ooze)	40.24	3° 54' .7	60° 33' .2	2	3048

Table A3.5 Location of PUPPI deployments at Site 1

Station No.	Longitude N	Latitude W
CD6/1	31° 17' .6	25° 19' .8
CD6/2	31° 18' .2	25° 18' .7
CD6/3	31° 18' .9	25° 18' .5
CD9B/8	31° 30' .2	25° 03' .6
CD9B/11	31° 26' .7	24° 53' .8
CD9B/28	31° 31' .7	25° 53' .0
D11317	30° 43' .8	24° 29' .3
D11320	31° 21' .4	25° 25' .1
D11329	31° 20' .7	25° 27' .1
D11381	31° 20' .9	25° 25' .7
D11382	31° 20' .8	25° 25' .8
D11388	31° 27' .9	26° 17' .8
D11391	31° 20' .9	25° 25' .8

APPENDIX 4 BASIC code for solving Biot's characteristic equation

```

20 PRINT "***** "
30 PRINT
40 PRINT "          Program  BIOT_FRQ.BAS "
50 PRINT " This program calculates the velocity and attenuation from the"
60 PRINT " Biot theory as a function of frequency. The file containing "
70 PRINT " the input and output file names, and the default parameter "
80 PRINT " values is specified by the user. "
90 PRINT
100 PRINT " Note.   1.  set CAPITALS LOCK on. "
110 PRINT "        2.  use BASIC/D (double precision basic) only "
120 PRINT
130 PRINT
140 PRINT
150 PRINT "          M.T. Hurley "
160 PRINT
170 PRINT "          August 1987 "
180 PRINT
190 PRINT "***** "
200 PRINT
210 REM
220 REM          Notes
230 REM
240 REM      a. Geertsma and Smit approximation will break down if the
250 REM          Biot frequency correction function is used. Set F1=1 and
260 REM          F0=0 for approximate analysis.
270 REM      b. Infinite frequency asymptote is subject to the same
280 REM          limitations as stated in a., as it is calculated after
290 REM          Geertsma and Smit
300 REM
310 REM      1.0  Wait to start
320 REM
330      GOSUB 4810
340 REM
350 REM      1.1  Dimension and define variables
360 REM
370      DEFDBL A-E :DEFDBL X-Y
380      PI=3.14159265E : E=2.7182818E
390      DIM IN(30.2) :DIM O1(20):DIM O0(20)
400      DIM NP(40) :DIM A(40) :DIM VR(40) :DIM VS(40)
410 REM
420 REM      1.2  Set input parameters and model type
430 REM
440      GOSUB 4110 :REM GET INPUT FILE NAME FROM USER
450      GOSUB 4200 :REM READ INPUT PARAMETERS FROM FILE
460      GOSUB 4380 :REM SET PROGRAM VARIABLES
470      GOSUB 4510 :REM DISPLAY MODEL TYPE ON MONITOR
480      GOSUB 4880 :REM READ DATA FROM FILE
490      GOSUB 4960 :REM RESET PROGRAM VARIABLES
500 REM
510 REM      2.0  SOLVE FREQUENCY EQUATION
520 REM
530      GOSUB 680: REM - SWEEP PARAMETER ADJUST
540      GOSUB 780: REM - SET VARIABLES AND PRINTER
550      GOSUB 940: REM - PORE SIZE SPECTRUM
560      GOSUB 1560: REM - FREQ CORRECTION FUNCTION
570      GOSUB 2090: REM - VISCOELASTIC COMPLEX MODULI
580      GOSUB 2400: REM - VISCOELASTIC COEFFICIENTS
590      GOSUB 2710: REM - SOLVE QUADRATIC

```

```

600      IF MS(2)<>" " THEN 550
610      GOSUB 3690: REM - ASYMPTOTIC SOLUTIONS
620      GOSUB 5160: REM - OUTPUT RESULTS
630      IF MS(5)="D" THEN 650
640      IF SWEEPS<>"DONE" THEN 530
650      IF MS(6)<>" " THEN 480
660      STOP
670      REM
680      REM      3.0   Adjust parameters for sweep
690      REM
700      REM      3.1.1 Frequency sweep
710      REM
720      IF MS(5)<>"A" THEN RETURN
730      F=10^FPOW
740      IF FPOW>FMAX THEN SWEEPS="DONE"
750      FPOW=FPOW+1/FINC
760      RETURN
770      REM
780      REM      3.1.2 Set variables
790      REM
800      W=2*PI*F :DT=N*DF+(1-N)*DS
810      FC=(NU*N)/(2*PI*DF*K)
820      FT=NU*PI/(16*DF*A^2)
830      IF SWEEP<>0 THEN 870
840      FCP=FC :FTP=FT :AP=A
850      KP=K :DP=D
860      REM
870      REM      3.1.3 Calculate frame modulus
880      REM
890      IF MS(9)<>"YES" THEN 920
900      SIG=POIS
910      KB1=2*G1*(1+SIG)/(3*(1-2*SIG))
920      RETURN
930      REM
940      REM      3.2   Pore size spectrum
950      REM
960      REM      3.2.1 SET PORE DISTRIBUTION
970      REM
980      REM      3.2.1.1 LEES DISTRIBUTION
990      REM
1000     IF MS(2)="N" THEN 1180
1010     IF MS(2)<>"L" THEN RETURN
1020     IF S>0 THEN 1310
1030     A(0)=1 :A(1)=.414 :A(2)=.225 :A(3)=.175
1040     A(4)=.117 :VS(0)=0! :VS(1)=.0525
1050     VS(2)=.017 :VS(3)=.032 :VS(4)=.011
1060     VR(0)=.2595 :VR(1)=.207 :VR(2)=.19
1070     VR(3)=.158 :VR(4)=.149
1080     FOR I=0 TO 4 :A(I)=A(I)*D :NEXT I
1090     FOR I=1 TO 8
1100     FOR J=1 TO 4
1110     A(4*I+J)=A(4*I+J-1)*A(J)/A(J-1)
1120     VS(4*I+J)=VR(4*I+J-1)*VS(J)/VR(J-1)
1130     VR(4*I+J)=VR(4*I+J-1)-VS(4*I+J)
1140     NEXT J
1150     NEXT I
1160     GOTO 1310
1170     REM
1180     REM      3.2.1.2 NORMAL MODAL DISTRIBUTION
1190     REM

```

```

1200      NP(1)=.4772 :NP(2)=.4641 :NP(3)=.4452
1210      NP(4)=.4192 :NP(5)=.3849 :NP(6)=.3413
1220      NP(7)=.2881 :NP(8)=.2258 :NP(9)=.1554
1230      NP(10)=.0793 :NP(11)=0
1240      FOR I= 1 TO 10
1250      A(11-I)=AMOD+AMOD*2*I/30 :VR(0)=1
1260      A(10+I)=AMOD-2*AMOD*I/30
1270      VS(I)=(NP(I)-NP(I+1))
1280      VS(21-I)=(NP(I)-NP(I+1))
1290      NEXT I
1300      REM
1310      REM      3.2.2 INTEGRAL PORE SIZE SOLUTIONS
1320      REM
1330      IF S<3 THEN 1370
1340      VD=V(1)-V(0):V(0)=V(1)
1350      IF VD<>0 THEN 1370
1360      FIN=1
1370      IF FIN=0 THEN 1420
1380      V1A=V1A+V(1)*(1-TVS)
1390      V2A=V2A+V(2)*(1-TVS)
1400      AC1A=AC1A+AC(1)*(1-TVS)
1410      AC2A=AC2A+AC(2)*(1-TVS):GOTO 1470
1420      V1A=V1A+V(1)*VS(S)/VR(0)
1430      V2A=V2A+V(2)*VS(S)/VR(0)
1440      TVS=TVS+VS(S)/VR(0)
1450      AC1A=AC1A+AC(1)*VS(S)/VR(0)
1460      AC2A=AC2A+AC(2)*VS(S)/VR(0)
1470      AC(1)=AC1A :AC(2)=AC2A
1480      S=S+1:K=A(S)^2*N/(8*2) :A=A(S)
1490      IF FIN<>1 THEN 1530
1500      V(1)=V1A :V(2)=V2A
1510      Q(1)=W/(2*V(1)*AC(1))
1520      SWEEPS="DONE" :GOTO 620
1530      IF K<>0 THEN RETURN
1540      FIN=1:GOTO 1360
1550      REM
1560      REM      3.3      FREQUENCY CORRECTION FUNCTION
1570      REM
1580      REM      3.3.1 FREQUENCY RANGE
1590      REM
1600      FC=(NU*N)/(2*PI*DF*K)
1610      IF MS(8)=" " THEN F1=1 AND F0=0 :GOTO 2070
1620      FT=NU*PI/(16*DF*A^2)
1630      IF F<FT THEN F1=1: F0=0 :GOTO 2070
1640      IF X=((W*DF/NU)^.5)*A/2 THEN 2070
1650      X=((W*DF/NU)^.5)*A/2
1660      BERP=0 : BEIP=0 : BERN=0 : BEIN=0
1670      IF X>5 THEN 1850
1680      REM
1690      REM      3.3.2 BESSEL FUNCTIONS FOR X<5
1700      REM
1710      FOR I=0 TO 10
1720      GOSUB 5230: IFAC=FAC: I=I+1: REM - CALC I!
1730      GOSUB 5230: JFAC=FAC: I=I-1: REM - CALC (I+1)!
1740      TRMO=((-1)^I*(-1)+1)/2
1750      TRME=((-1)^(I)+1)/2
1760      EXPO=X^(2*I+1)
1770      EXPE=X^(2*I)
1780      SIGN=(-1)^(INT(I/2)+1)
1790      BERP=BERP+(TRMO*SIGN*EXPO/(IFAC*JFAC))

```

```

1800      BEIP=BEIP-(TRME*SIGN*EXPO/(IFAC*JFAC))
1810      BERN=BERN-(TRME*SIGN*EXPE/(IFAC^2))
1820      BEIN=BEIN-(TRMO*SIGN*EXPE/(IFAC^2))
1830      NEXT
1840      GOTO 1950
1850  REM
1860  REM      3.3.3 BESSEL FUNCTIONS FOR X>5
1870  REM
1880      TS1=.7071*X^2 : TS2=.3927
1890      TS3=1.1701 : TS4=1.9635
1900      BERN=SIN(TS1+TS3)+(SIN(TS1+TS2))/(16*X)
1910      BEIN=SIN(TS1-TS2)+(SIN(TS1-TS3))/(16*X)
1920      BERP=SIN(TS1+TS4)-(SIN(TS1+TS3))/(16*X/3)
1930      BEIP=SIN(TS1+TS2)-(SIN(TS1-TS2))/(16*X/3)
1940  REM
1950  REM      3.3.4 COMPLEX CORRECTION
1960  REM
1970      X1=BERP : X2=BEIP : X3=BERN : X4=-BEIN
1980      GOSUB 5300 : REM COMPLEX *
1990      Y1=X5 : Y2=X6 : Y3=(X3*X3)+(X4*X4)
2000      T1=Y1/Y3 : T0=Y2/Y3
2010      X1=-X*T0/2 : X2=X*T1/2
2020      X3=-T1/X : X4=(T0/X)-1
2030      GOSUB 5300 : REM COMPLEX *
2040      Y1=X5 : Y2=X6 : X1=X3 : X2=-X4
2050      GOSUB 5300 : REM COMPLEX *
2060      Y3=X5 : Y4=X6 : F1=Y1/Y3 : F0=Y2/Y3
2070      RETURN
2080  REM
2090  REM      3.4      FREQ DEPENDENT COMPLEX MODULI
2100  REM
2110      IF M$(3)="Q" THEN 2260
2120      IF M$(3)<>"Z" THEN RETURN
2130  REM
2140  REM      3.4.1 STANDARD VISCOELASTIC SOLID
2150  REM
2160      TS1=VSR : TS2=QSR : TS3=STOR
2170      GOSUB 2200 : G1=M1 : G0=M2
2180      TS1=VER : TS2=QER : TS3=ETOR
2190      GOSUB 2200 : KB1=M1 : KB0=M2 : RETURN
2200      VR=TS1/(1+(1/(2*TS2)))
2210      K1=VR^2*DT : K2=2*K1/TS2
2220      TS4=W*TS3/(1+(W*TS3)^2)
2230      M1=K1*(1+K2*W*TS3*TS4/K1)^2 : M2=K2*TS4
2240      RETURN
2250  REM
2260  REM      3.4.2 BAND LIMITED CONSTANT "Q"
2270  REM
2280      TS1=VSL : TS2=QSL*2*PI : GOSUB 2140
2290      G1=M1 : G0=M2
2300      TS1=VEL : TS2=QEL*2*PI : GOSUB 2140
2310      KB1=M1 : KB0=M2 : RETURN
2320      TS4=W*(S2-S1) : TS5=W^2+S1*S2
2330      TS6=S2^2*(S1^2+W^2) : TS7=S1^2*(S2^2+W^2)
2340      TS8=S2^2*(S1^2+W^2) : TS9=S1^2*(S2^2+W^2)
2350      VR=TS1/(1+(1/TS2)*LOG(TS8/TS9))
2360      M1=VR^2*DT*(1+(1/TS2)*LOG(TS6/TS7))
2370      M2=VR^2*DT*4*(ATN(TS4/TS5))/TS2
2380      RETURN
2390  REM

```

```

2400 REM 3.5 COMPLEX VISCOELASTIC COEFFICIENTS
2410 REM
2420 REM 3.5.1 "P"
2430 REM
2440 X1=(1-N-KB1/KS)*KS*(1-N)+(N*KS*KB1/KF)
2450 X2=-KB0*(N-1)+(N*KS*KB0/KF)
2460 X3=(1-N+N*KS/KF-KB1/KS)
2470 X4=KB0/KS
2480 GOSUB 5300 : REM COMPLEX *
2490 Y1=X5 :Y2=X6 :TS1=X1 :X1=X3 :X2=-X4
2500 GOSUB 5300 : REM COMPLEX *
2510 Y3=X5 :Y4=X6 :GE=G1
2520 PE=TS1/X3+4*GE/3
2530 P1=Y1/Y3+4*G1/3
2540 P0=Y2/Y3+4*G0/3
2550 REM
2560 REM 3.5.2 "Q"
2570 REM
2580 X1=(1-N-KB1/KS)*KS*N :X2=-N*KB0
2590 GOSUB 5300 : REM COMPLEX *
2600 Y1=X5 :Y2=X6 :QE=X1/X3
2610 Q1=Y1/Y3 :Q0=Y2/Y3
2620 REM
2630 REM 3.5.3 "R"
2640 REM
2650 X1=N^2*KS :X2=0
2660 GOSUB 5300 : REM COMPLEX *
2670 Y1=X5 :Y2=X6 :RE=X1/X3
2680 R1=Y1/Y3 :R0=Y2/Y3
2690 RETURN
2700 REM
2710 REM 3.6 SOLVE QUADRATIC
2720 REM
2730 REM 3.6.1 MASS AND INERTIAL TERMS
2740 REM
2750 B=N^2*NU/K
2760 TS1=-(T-1)*N*DF-F0*B/W
2770 TS2=(1-N)*DS-TS1
2780 TS3=N*DF-TS1 :TS4=B*F1/W
2790 REM
2800 REM 3.6.2 NORMALISE COEFFICIENTS
2810 REM
2820 H=PE+2*QE+RE
2830 Y(1,1,1)=P1/H :Y(1,1,0)=P0/H
2840 Y(1,2,1)=Q1/H :Y(1,2,0)=Q0/H
2850 Y(2,2,1)=R1/H :Y(2,2,0)=R0/H
2860 X(1,1,1)=TS2/DT :X(1,1,0)=TS4/DT
2870 X(1,2,1)=TS1/DT :X(1,2,0)=-TS4/DT
2880 X(2,2,1)=TS3/DT :X(2,2,0)=TS4/DT
2890 REM
2900 REM 3.6.3 QUADRATIC COEFFICIENTS A,B,C
2910 REM
2920 REM 3.6.3.1 COEFFICIENT A
2930 REM
2940 A1=0 :B1=0 :C1=0
2950 A0=0 :B0=0 :C0=0
2960 FOR I=1 TO 2
2970 X1=X(1,I,1) :X2=X(1,I,0)
2980 X3=X((3-I),2,1) :X4=X((3-I),2,0)
2990 GOSUB 5300 : REM COMPLEX *

```

```

3000      A1=A1+(X5*(-1)^(I+1)) :A0=A0+(X6*(-1)^(I+1))
3010      NEXT I
3020      REM
3030      REM      3.6.3.2 COEFFICIENT B
3040      REM
3050          FOR I=1 TO 3
3060      Z1=1 :Z2=1 :Z3=2 :Z4=2 :IF I=1 THEN 3090
3070      Z1=2 :Z2=2 :Z3=1 :Z4=1 :IF I=2 THEN 3090
3080      Z1=1 :Z2=2 :Z3=1 :Z4=2 :IF I=3 THEN 3090
3090      TS1=((Z1-Z2)*3+1)
3100      X1=X(Z1,Z2,1)*TS1 :X2=X(Z1,Z2,0)*TS1
3110      X3=Y(Z3,Z4,1) :X4=Y(Z3,Z4,0)
3120      GOSUB 5300 : REM COMPLEX *
3130      B1=B1+X5 :B0=B0+X6
3140      NEXT I
3150      REM
3160      REM      3.6.3.3 COEFFICIENT C
3170      REM
3180          FOR I=1 TO 2
3190      X1=Y(1,I,1) :X2=Y(1,I,0)
3200      X3=Y((3-I),2,1) :X4=Y((3-I),2,0)
3210      GOSUB 5300 : REM COMPLEX *
3220      C1=C1+(X5*(-1)^(I+1)) :C0=C0+(X6*(-1)^(I+1))
3230      NEXT I
3240      REM
3250      REM      3.6.4 PARTIAL QUADRATIC SOLUTION
3260      REM
3270      X1=B1 :X3=B1 :X2=B0 :X4=B0
3280      GOSUB 5300 : REM COMPLEX *
3290      Y1=X5 :Y2=X6 :X1=A1
3300      X2=A0 :X3=C1 :X4=C0
3310      GOSUB 5300 : REM COMPLEX *
3320      E1=Y1-4*X5 :E0=Y2-4*X6
3330      TS1=(E1+SQR(E1*E1+E0^2))
3340      IF TS1>0 THEN 3370
3350      K=A(S-1)^2*N/(8*2)
3360      A=A(S-1):FIN=1:RETURN
3370      D1=SQR((E1+SQR(E1*E1+E0^2))/2)
3380      D0=E0/(2*D1)
3390      REM
3400      REM      3.6.5 VELOCITY AND ATTENUATION SOLUTIONS
3410      REM
3420          FOR I=1 TO 2
3430      X1=B1-((-1)^I*D1) :X2=B0-((-1)^I*D0)
3440      X3=A1 :X4=-A0 :TS1=2*(A1^2+A0^2)
3450      GOSUB 5300 : REM COMPLEX *
3460      E1=X5/TS1 : E0=X6/TS1
3470      TS1=(E1+SQR(E1^2+E0^2))
3480      IF TS1>0 THEN 3510
3490      K=A(S-1)^2*N/(8*2)
3500      A=A(S-1):FIN=1:RETURN
3510      C(I,1)=SQR((E1+SQR(E1^2+E0^2))/2)
3520      C(I,0)=E0/(2*C(I,1))
3530      TS1=C(I,1)/(C(I,1)^2+C(I,0)^2)
3540      TS2=-C(I,0)/(C(I,1)^2+C(I,0)^2)
3550      K(I,1)=((DT/H)^.5)*W*TS1
3560      K(I,0)=((DT/H)^.5)*W*TS2
3570      V(I)=W/K(I,1) :AC(I)=K(I,0)*8.686001
3580      Q(I)=W/(2*V(I)*AC(I)) :D(I)=PI/Q(I)
3590      TS1=AC(I)

```

```

3600 REM      IF TS1<0 THEN K=A(S-1)^2*N/(8*2)
3610 REM      IF TS1<0 THEN A=A(S-1):FIN=1:GOTO 1420
3620          NEXT I
3630          RETURN
3640      REM
3650      REM      3.7      ASYMPTOTIC APPROXIMATIONS
3660      REM
3670      REM      3.7.1  NON DISSIPATIVE STIFF FRAME
3680      REM
3690          FOR I=1 TO 2
3700              TS1=DT*X(1,1,1) :TS2=DT*X(1,2,1)
3710              TS3=DT*X(2,2,1) :TS4=PE*RE-QE^2
3720              DELT=PE*TS3+RE*TS1-2*QE*TS2
3730              TS5=TS1*TS3-TS2^2
3740              TS6=SQR(DELT^2-4*TS4*TS5)
3750              VE(I)=SQR((DELT-((-1)^I*TS6))/(2*TS5))
3760          NEXT I
3770      REM
3780      REM      3.7.2.1 WHITE LOW FREQUENCY SLOW WAVE
3790      REM
3800          TS1=N/KF+(1-N)/KS-KB1/(KS^2)
3810          TS2=(1-KB1/KS)^2: K1=KB1+TS2/TS1
3820          TS1=(KB1+G1*4/3)/(K1+G1*4/3)
3830          TS2=(N/KF+(1-N)/KS-KB1/(KS^2))
3840          KA=TS1/TS2: VA(1)=(2*W*K*KA/NU)^.5
3850          ARG0=W*.019/VA(1)
3860      REM
3870      REM      3.7.2.2 BIOT LOW FREQUENCY SLOW WAVE
3880      REM
3890          VC=(H/DT)^.5 :X1=C1 :X2=C0
3900          X3=X(1,2,1)+X(2,2,1)
3910          X4=-X(1,2,0)-X(2,2,0)
3920          GOSUB 5300 : REM COMPLEX *
3930          Y1=X5 :Y2=X6 :X1=X3 :X2=-X4
3940          GOSUB 5300 : REM COMPLEX *
3950          VA(2)=VC*((2*F*Y1/(FC*X5))^.5)
3960      REM
3970      REM      3.8      Geertsma and Smit Approximation
3980      REM
3990          KE=PE-2*G1-(QE^2)/RE :ME=RE/N^2
4000          LE=N*(QE+RE)/RE :HE=KE+LE^2*ME+2*G1
4010          DC=DT*X(2,2,1)/N^2 :GL=DF/DT
4020          GC=DC/DT :SK=LE*ME/HE :SL=ME/HE
4030          WCG=F1*NU/((GC-GL^2)*K*DT)
4040          TS1=GC+SL-2*GL*SK :TS2=GC-GL^2
4050          V1Z=(HE/DT)^.5
4060          V1I=((HE*TS1)/(DT*TS2))^.5
4070          TS1=(WCG/W)^2 :TS2=V1I^2 :TS3=V1Z^2
4080          V1G=SQR((TS2^2+TS3^2*TS1)/(TS2+TS3*TS1))
4090          RETURN
4100      REM
4110      REM      4.0      Get file name from user
4120      REM
4130          CLS : PRINT : PRINT : PRINT
4140          PRINT SPC(10) "Input set file name (eg A:289C_SET.DAT)";
4150          INPUT SETS : PRINT : PRINT SPC(10) "Set file is "SETS
4160          PRINT SPC(10) "Hit R to re-enter, anything else to continue"
4170          GOS=INKEYS :IF GOS="" THEN 4170
4180          IF GOS="R" THEN 4130
4190          RETURN

```

```

4200 REM
4210 REM 4.1 Set model type and open files
4220 REM
4230 OPEN SETS FOR INPUT AS £1
4240 FOR J=1 TO 2
4250 FOR I=0 TO 29
4260 INPUT£1, IN(I,J)
4270 NEXT I
4280 NEXT J
4290 FOR I=1 TO 9:INPUT£1, MS(I): NEXT I
4300 CLOSE £1
4310 IF MS(6)=" " THEN 4330
4320 OPEN MS(6) FOR INPUT AS £1
4330 IF MS(7)=" " THEN 4350
4340 OPEN MS(7) FOR OUTPUT AS £2
4350 RETURN
4360 REM
4370 REM 4.2 Reset parameters
4380 REM
4390 N=IN(1,1) :KF=IN(2,1) :KS=IN(3,1) :T=IN(4,1)
4400 G1=IN(5,1) :GO=IN(6,1) :KB1=IN(7,1) :KBO=IN(8,1)
4410 DF=IN(9,1) :D=IN(10,1) :DS=IN(11,1) :A=IN(12,1)
4420 NU=IN(13,1) :K=IN(14,1) :F=IN(15,1) :POIS=IN(16,1)
4430 S2=IN(17,1) :S1=IN(18,1) :VSL=IN(19,1) :VEL=IN(20,1)
4440 QSL=IN(21,1) :QEL=IN(22,1) :VSR=IN(23,1) :VER=IN(24,1)
4450 STOR=1/IN(25,1) :ETOR=1/IN(26,1) :FPOW=IN(17,2)
4460 FINC=IN(18,2) :FMAX=IN(19,2) :SIG=IN(20,2)
4470 SMAX=IN(21,2) :SINC=IN(22,2)
4480 RETURN
4490 REM
4500 REM 4.3 Display selected program mode
4510 REM
4520 TS1=VAL(MS(1))
4530 IF TS1<4 THEN DS(1)="BIOT POROELASTIC"
4540 IF TS1=4 THEN DS(1)="BIOT-GARDNER ROD WAVES"
4550 IF TS1=5 THEN DS(1)="ASYMPTOTIC POROELASTIC SOLUTIONS"
4560 IF MS(2)<>" " THEN DS(2)="YES"
4570 IF MS(3)<>" " THEN DS(3)="YES"
4580 IF MS(4)<>" " THEN DS(4)="YES"
4590 IF MS(5)="A" THEN DS(5)="FREQUENCY"
4600 IF MS(5)="B" THEN DS(5)="POISSON'S RATIO"
4610 IF MS(5)="C" THEN DS(5)="CONVERGENCE"
4620 DS(6)=MS(6) :DS(7)="PRINTER"
4630 IF MS(7)<>"P" THEN DS(7)=MS(7)
4640 IF MS(8)<>" " THEN DS(8)="YES"
4650 IF MS(9)<>" " THEN DS(9)="YES"
4660 CLS :PRINT :PRINT
4670 PRINT SPC(12) "Selected program mode read from ";SETS
4680 PRINT :PRINT
4690 PRINT SPC(10)"MODEL : "DS(1)
4700 PRINT SPC(10)"PORE SIZE DISTRIBUTION : "DS(2)
4710 PRINT SPC(10)"VISCOELASTIC COEFFICIENTS : "DS(3)
4720 PRINT SPC(10)"KOZENY-CARMAN PERMEABILITY : "DS(4)
4730 PRINT SPC(10)"SWEEP : "DS(5)
4740 PRINT SPC(10)"FILE INPUT : "DS(6)
4750 PRINT SPC(10)"FILE OUTPUT : "DS(7)
4760 PRINT SPC(10)"FREQUENCY CORRECTION : "DS(8)
4770 PRINT SPC(10)"CALCULATE FRAME MODULUS : "DS(9)
4780 PRINT :PRINT
4790 PRINT SPC(12) "Edit SET file to alter mode"

```

```

4800 PRINT SPC(12) "Press any key to continue"
4810 GOS=INKEY$ :IF GOS="" THEN 4810
4820 CLS:PRINT:PRINT:PRINT:PRINT:PRINT
4830 PRINT SPC(16) "PROGRAM BIOT_FRQ.BAS IN OPERATION": PRINT
4840 PRINT SPC(14) "(note this program is quite slow)"
4850 RETURN
4860 REM
4870 REM 4.4 Read data from disc
4880 REM
4890 IF MS(6)="" THEN RETURN
4900 N=(DT-DS)/(DF-DS)
4910 G1=DT*VSHEAR^2
4920 V(1)=0:INC=.1
4930 RETURN
4940 REM
4950 REM 4.5 Reset program variables
4960 REM
4970 S=0 :AMOD=A :W=2*PI*F : SWEEP$="" :CONVS=""
4980 FPOW=IN(17,2) :FINC=IN(18,2)
4990 SIG=IN(20,2) :SINC=IN(22,2)
5000 IF MS(5)="C" THEN SINC=.1
5010 S=0 :V1A=0 :V2A=0 :TVS=0
5020 AC1A=0 :AC2A=0 :FIN=0
5030 V(1)=0 :V(2)=0 :AC(1)=0 :AC(2)=0
5040 V(0)=0 :VD=0 :AC(0)=0 :AMOD=IN(12,2)
5050 REM
5060 REM 4.5.1 Kozeny Carman permeability
5070 REM
5080 IF MS(4)<>"D" THEN 5110
5090 A=D*N/((1-N)*3)
5100 K=A^2*N/(8*T)
5110 IF MS(4)<>"A" THEN 5130
5120 K=A^2*N/(8*T)
5130 RETURN
5140 REM
5150 REM 4.6 Output results to disc
5160 REM
5170 PRINT DEPTH;VMEAS;V(1);V1G;VC;VE(1);V1I;F/FC
5180 WRITE £2, DEPTH;VMEAS;V(1);V1G;VC;VE(1);V1I;F/FC
5190 RETURN
5200 REM
5210 REM 5.0 Trivial mathematical subroutines
5220 REM
5230 REM 5.1 Calculate I factorial
5240 REM
5250 FAC=1
5260 FOR J=1 TO I :FAC=J*FAC: NEXT
5270 RETURN
5280 REM
5290 REM 5.2 Multiply two complex numbers
5300 REM
5310 X5=(X1*X3)-(X2*X4)
5320 X6=(X1*X4)+(X2*X3)
5330 RETURN

```

APPENDIX 5 BASIC code for uncertainty in Biot's Vz prediction

```

20 PRINT "*****"
30 PRINT
40 PRINT "          Program  BIOT_ERR.BAS"
50 PRINT " This program calculates the errors in velocity due to the"
60 PRINT " errors in the input parameters in the Biot model."
70 PRINT
80 PRINT " Note,   1.  set CAPITALS LOCK on."
90 PRINT "         2.  use BASIC/D (double precision basic) only"
100 PRINT
110 PRINT "          August 1987"
120 PRINT
130 PRINT "          M.T. Hurley"
140 PRINT
150 PRINT "*****"
160 PRINT
170 REM
180 REM   1.0  Wait to start
190 REM
200 GOSUB 5480
210 REM
220 REM   1.1  Dimension and define variables
230 REM
240 DEFDBL A-E :DEFDBL X-Y
250 PI=3.14159265E : E=2.7182818E
260 DIM IN(30.2) :DIM O1(20):DIM O0(20)
270 DIM NP(40) :DIM A(40) :DIM VR(40) :DIM VS(40)
280 REM
290 REM   1.2  Set input parameters and model type
300 REM
310 GOSUB 4780 :REM GET INPUT FILE NAME FROM USER
320 GOSUB 4870 :REM READ INPUT PARAMETERS FROM FILE
330 GOSUB 5050 :REM SET PROGRAM VARIABLES
340 GOSUB 5180 :REM DISPLAY MODEL TYPE ON MONITOR
350 GOSUB 5540 :REM READ DATA FROM FILE
360 GOSUB 5640 :REM RESET PROGRAM VARIABLES
370 REM
380 REM   2.0  Set coefficients
390 REM
400 GOSUB 480: REM - Calculate variables
410 GOSUB 640: REM - Complex coefficients
420 GOSUB 950: REM - Elastic-density coefficients
430 GOSUB 1120: REM - Error analysis
440 GOSUB 5990: REM - Output results
450 IF MS(6)<>" THEN 350
460 STOP
470 REM
480 REM   2.1  Frequency variables
490 REM
500 W=2*PI*F :DT=N*DF+(1-N)*DS
510 FC=(NU*N)/(2*PI*DF*K)
520 FT=NU*PI/(16*DF*A^2)
530 IF SWEEP<>0 THEN 570
540 FCP=FC :FTP=FT :AP=A
550 KP=K :DP=D
560 REM
570 REM   2.2  Calculate frame modulus
580 REM
590 IF MS(9)<>"YES" THEN 620

```

```

600      SIG=POIS
610      KB1=2*G1*(1+SIG)/(3*(1-2*SIG))
620      RETURN
630      REM
640      REM      2.3      COMPLEX VISCOELASTIC COEFFICIENTS
650      REM
660      REM      2.3.1      "P"
670      REM
680      X1=(1-N-KB1/KS)*KS*(1-N)+(N*KS*KB1/KF)
690      X2=-KB0*(N-1)+(N*KS*KB0/KF)
700      X3=(1-N+N*KS/KF-KB1/KS)
710      X4=KB0/KS
720      GOSUB 6130 : REM COMPLEX *
730      Y1=X5 :Y2=X6 :TS1=X1 :X1=X3 :X2=-X4
740      GOSUB 6130 : REM COMPLEX *
750      Y3=X5 :Y4=X6 :GE=G1
760      PE=TS1/X3+4*GE/3
770      P1=Y1/Y3+4*G1/3
780      P0=Y2/Y3+4*G0/3
790      REM
800      REM      2.3.2      "Q"
810      REM
820      X1=(1-N-KB1/KS)*KS*N :X2=-N*KB0
830      GOSUB 6130 : REM COMPLEX *
840      Y1=X5 :Y2=X6 :QE=X1/X3
850      Q1=Y1/Y3 :Q0=Y2/Y3
860      REM
870      REM      2.3.3      "R"
880      REM
890      X1=N^2*KS :X2=0
900      GOSUB 6130 : REM COMPLEX *
910      Y1=X5 :Y2=X6 :RE=X1/X3
920      R1=Y1/Y3 :R0=Y2/Y3
930      RETURN
940      REM
950      REM      2.4      SET ELASTIC AND MASS COEFFICIENTS
960      REM
970      REM      2.4.1      MASS AND INERTIAL TERMS
980      REM
990      B=N^2*NU/K
1000     TS1=-(T-1)*N*DF-F0*B/W
1010     TS2=(1-N)*DS-TS1
1020     TS3=N*DF-TS1 :TS4=B*F1/W
1030     REM
1040     REM      2.4.2      NORMALISE COEFFICIENTS
1050     REM
1060     H=PE+2*QE+RE
1070     X(1,1,1)=TS2
1080     X(1,2,1)=TS1
1090     X(2,2,1)=TS3
1100     RETURN
1110     REM
1120     REM      3.0      ERROR ANALYSIS
1130     REM
1140     REM      3.1      P.D. of coefficients w.r.t. porosity
1150     REM
1160     REM      3.1.1      P.D. of P w.r.t. POROSITY (dP/dN)
1170     REM
1180     V1=N: V2=KS:V3=KS*((KB1/KS)+(KB1/KF)-2)
1190     V4=KS-KB1 :V5=1-(KB1/KS) :V6=(KS/KF-1)

```

```

1200      U1=(V3+2*V2*V1)/(V5+V6*V1)
1210      U2=(V6*(V4+V3*V1+V2*V1*V1))/((V5+V6*V1)^2)
1220      DPDN=U1-U2
1230      REM
1240      REM      3.1.2  p.d. of Q w.r.t. POROSITY (dQ/dN)
1250      REM
1260      V1=N :V2=KS-KB1 :V3=KS :V4=1-KB1/KS :V5=(KS/KF)-1
1270      U1=(V2-2*V1*V3)/(V4+V1*V5)
1280      U2=(V5*(V1*V2-V1*V1*V3))/((V4+V1*V5)^2)
1290      DQDN=U1-U2
1300      REM
1310      REM      3.1.3  p.d. of R w.r.t. POROSITY (dR/dN)
1320      REM
1330      V1=N :V2=1-KB1/KS :V3=KS/KF-1 :V4=KS
1340      U1=2*V1*V4/(V2+V3*V1)
1350      U2=V1*V1*V4*V3/((V2+V1*V3)^2)
1360      DRDN=U1-U2
1370      REM
1380      REM      3.1.4  p.d. of mass-terms w.r.t. POROSITY
1390      REM
1400      DD11DN=T*DF-DS-DF
1410      DD12DN=DF-T*DF
1420      DD22DN=T*DF
1430      REM
1440      REM      3.2    p.d. of coefficients w.r.t. SOLID MODULUS
1450      REM
1460      REM      3.2.1  P.D. OF P W.R.T. SOLID MODULUS (dP/dKS)
1470      REM
1480      V1=KS: V2=(1-N)^2+N*KB1/KF :V3=-KB1*(1-N)
1490      V4=1-N :V5=KB1 :V6=N/KF
1500      U1=V2/(V4-(V5/V1)+V6*V1)
1510      U2=(V1*V2+V3)*(V5/(V1^2)+V6)
1520      U3=(V4-V5/V1+V6*V1)^2
1530      DPDKS=U1-U2/U3
1540      REM
1550      REM      3.2.2  P.D. OF Q W.R.T. SOLID MODULUS (dQ/dKS)
1560      REM
1570      V1=KS :V2=N*(1-N) :V3=1-N
1580      V4=N/KF :V5=KB1 :V6=-N*KB1
1590      U1=V2/(V3+V1*V4-V5/V1)
1600      U2=(V1*V2+V6)*(V4+V5/(V1*V1))/((V3+V1*V4-V5/V1)^2)
1610      DQDKS=U1-U2
1620      REM
1630      REM      3.2.3  P.D. OF R W.R.T. SOLID MODULUS (dR/dKS)
1640      REM
1650      V1=KS :V2=N*N :V3=1-N :V4=N/KF :V5=KB1
1660      U1=V1*V2 :U2=V3+V1*V4-V5/V1
1670      DU1DKS=V2 :DU2DKS=V4+V5/(V1*V1)
1680      DRDKS=(DU1DKS/U2)-(U1*DU2DKS)/(U2*U2)
1690      REM
1700      REM      3.3    p.d. of coefficients w.r.t. FRAME MODULUS
1710      REM
1720      REM      3.3.1  P.D. OF P W.R.T. FRAME MODULUS (dP/dKB1)
1730      REM
1740      V1=KB1 :V2=N*KS/KF+N-1 :V3=KS*((1-N)^2)
1750      V4=1-N+N*KS/KF :V5=KS
1760      U1=V2/(V4-V1/V5)
1770      U2=(V1*V2+V3)/((V5)*((V4-V1/V5)^2))
1780      DPDKB1=U1-U2
1790      REM

```

```

1800 REM      3.3.2 P.D. OF Q W.R.T. FRAME MODULUS (dQ/dKB1)
1810 REM
1820 V1=KB1 :V2=N*KS*(1-N) :V3=N
1830 V4=1-N+N*KS/KF :V5=KS
1840 U1=-V3/(V4-V1/V5)
1850 U2=(V2-V1*V3)/((-V5)*(V4-V1/V5)^2)
1860 DQDKB1=U1-U2
1870 REM
1880 REM      3.3.3 P.D. OF R W.R.T. FRAME MODULUS (dR/dKB1)
1890 REM
1900 V1=KB1 :V2=N*N*KS :V3=1-N+N*KS/KF :V4=KS
1910 DRDKB1=V2*(-1/V4)/((V3-V1/V4)^2)
1920 REM
1930 REM      3.4 p.d. of coefficients w.r.t. FLUID MODULUS
1940 REM
1950 REM      3.4.1 P.D. OF P W.R.T. FLUID MODULUS (dP/dKF)
1960 REM
1970 V1=KF :V2=KS*KB1*N :V3=KS*(1-N)^2-KB1*(1-N)
1980 V4=1-N-KB1/KS :V5=N*KS
1990 U1=V2/V1+V3 :U2=V4+V5/V1
2000 DU1DKF=-V2/(V1*V1) :DU2DKF=-V5/(V1*V1)
2010 DPDKF=(DU1DKF/U2)-(U1*DU2DKF/(U2*U2))
2020 REM
2030 REM      3.4.2 P.D. OF Q W.R.T. FLUID MODULUS (dQ/dKF)
2040 REM
2050 V1=KF :V2=(1-N-KB1/KS)*N*KS
2060 V3=1-N-KB1/KS :V4=N*KS
2070 DQDKF=V2*V4/(((V3+V4/V1)^2)*V1*V1)
2080 REM
2090 REM      3.4.3 P.D. OF R W.R.T. FLUID MODULUS (dR/dKF)
2100 REM
2110 V1=KF :V2=N*N*KS :V3=1-N-KB1/KS :V4=N*KS
2120 DRDKF=V2*V4/(V1*V1*(V3+V4/V1)^2)
2130 REM
2140 REM      3.5.1 P.D. OF P W.R.T. SHEAR MODULUS (dP/dG1)
2150 REM
2160 DPDG1=4/3
2170 REM
2180 REM      3.5.2 P.D. mass-terms w.r.t. FLUID DENSITY
2190 REM
2200 DD11DDF=-N+T*N
2210 DD22DDF=T*N
2220 DD12DDF=N-T*N
2230 REM
2240 REM      3.5.3 P.D. mass-terms w.r.t. SOLID DENSITY
2250 REM
2260 DD11DDS=1-N
2270 REM
2280 REM      3.5.4 P.D. mass-terms w.r.t. TORTUOSITY
2290 REM
2300 DD11DT=N*DF
2310 DD22DT=N*DF
2320 DD12DT=-N*DF
2330 REM
2340 REM      4.1 Error in zero velocity asymptote
2350 REM
2360 REM      4.1.1 P.D. of Vz w.r.t elastic coefficeints
2370 REM
2380 H1=P1+R1+2*Q1
2390 DT=X(1,1,1)+X(2,2,1)+2*X(1,2,1)

```

```

2400      TS1=.5*(H1/DT)^(-.5)
2410      DVZDP=TS1/DT :DVZDQ=TS1*2/DT :DVZDR=TS1/DT
2420      REM
2430      REM      4.1.2 P.D. of Vz w.r.t mass coefficeints
2440      REM
2450      DVZDD11=-TS1*H/(DT^2)
2460      DVZDD12=-TS1*2*H/(DT^2)
2470      DVZDD22=-TS1*H/(DT^2)
2480      REM
2490      REM      4.1.3 P.D. of Vz w.r.t porosity
2500      REM
2510      TS1=DVZDP*DPDN :TS2=DVZDQ*DQDN :TS3=DVZDR*DRDN
2520      TS4=DVZDD11*DD11DN :TS5=DVZDD12*DD12DN :TS6=DVZDD22*DD22DN
2530      DVZDN=TS1+TS2+TS3+TS4+TS5+TS6
2540      REM
2550      REM      4.1.4 P.D. of Vz w.r.t elastic constants
2560      REM
2570      TS1=DVZDP*DPDKS :TS2=DVZDQ*DQDKS :TS3=DVZDR*DRDKS
2580      DVZDKS=TS1+TS2+TS3
2590      TS1=DVZDP*DPDKF :TS2=DVZDQ*DQDKF :TS3=DVZDR*DRDKF
2600      DVZDKF=TS1+TS2+TS3
2610      TS1=DVZDP*DPDKB1 :TS2=DVZDQ*DQDKB1 :TS3=DVZDR*DRDKB1
2620      DVZDKB1=TS1+TS2+TS3
2630      REM
2640      REM      4.1.5 P.D. of Vz w.r.t mass constants
2650      REM
2660      TS1=DVZDD11*DD11DDS :TS2=DVZDD12*DD12DDS :TS3=DVZDD22*DD22DDS
2670      DVZDDS=TS1+TS2+TS3
2680      TS1=DVZDD11*DD11DDF :TS2=DVZDD12*DD12DDF :TS3=DVZDD22*DD22DDF
2690      DVZDDF=TS1+TS2+TS3
2700      TS1=DVZDD11*DD11DT :TS2=DVZDD12*DD12DT :TS3=DVZDD22*DD22DT
2710      DVZDT=TS1+TS2+TS3
2720      REM
2730      REM      4.1.6 Delta Vz
2740      REM
2750      TS1=DVZDN^2*IN(1,2)^2 :TS2=DVZDKF^2*IN(2,2)^2
2760      TS3=DVZDKS^2*IN(3,2)^2 :TS4=DVZDT^2*IN(4,2)^2
2770      TS5=DVZDG1^2*IN(5,2)^2 :TS6=DVZDKB1^2*IN(7,2)^2
2780      TS7=DVZDDF^2*IN(9,2)^2 :TS8=DVZDDS^2*IN(11,2)^2
2790      DELVZ=(TS1+TS2+TS3+TS4+TS5+TS6+TS7+TS8)^.5
2800      VZ=(H1/DT)^.5
2810      REM
2820      REM      4.2 Error in Vi
2830      REM
2840      REM      4.2.1 P.D. of Vi w.r.t P
2850      REM
2860      U1=R1*X(1,1,1)-2*Q1*X(1,2,1) :U2=U1 :U4=Q1*Q1
2870      U5=X(1,1,1)*X(2,2,1)-X(1,2,1)*X(1,2,1) :U3=U5
2880      V1=(P1*X(2,2,1)+U2)^2 :V2=4*U3*(P1*R1-U4)
2890      V3=(V1-V2)^.5 :V4=P1*X(2,2,1)+U1
2900      DV1DP=2*(P1*X(2,2,1)+U2)*X(2,2,1)
2910      DV2DP=4*U3*R1 :DV4DP=X(2,2,1)
2920      DV3DP=.5*(DV1DP-DV2DP)*(V1-V2)^(-.5)
2930      TS1=.5*((V4+V3)/(2*U5))^(-.5)
2940      TS2=(DV4DP+DV3DP)/(2*U5)
2950      DVIDP=TS1*TS2
2960      REM
2970      REM      4.2.2 P.D. of Vi w.r.t R
2980      REM
2990      U1=P1*X(2,2,1)-2*Q1*X(1,2,1) :U2=U1 :U4=Q1*Q1

```

```

3000      U5=X(1,1,1)*X(2,2,1)-X(1,2,1)*X(1,2,1) :U3=U5
3010      V1=(R1*X(1,1,1)+U2)^2 :V2=4*U3*(P1*R1-U4)
3020      V3=(V1-V2)^.5 :V4=R1*X(1,1,1)+U1
3030      DV1DR=2*(R1*X(1,1,1)+U2)*X(1,1,1)
3040      DV2DR=4*U3*P1 :DV4DR=X(1,1,1)
3050      DV3DR=.5*(DV1DR-DV2DR)*(V1-V2)^(-.5)
3060      TS1=.5*((V4+V3)/(2*U5))^(-.5)
3070      TS2=(DV4DR+DV3DR)/(2*U5)
3080      DVIDR=TS1*TS2
3090      REM
3100      REM      4.2.3 P.D. of Vi w.r.t Q
3110      REM
3120      U1=R1*X(1,1,1)+P1*X(2,2,1) :U2=U1 :U4=P1*R1
3130      U5=X(1,1,1)*X(2,2,1)-X(1,2,1)*X(1,2,1) :U3=U5
3140      V1=(-2*Q1*X(1,2,1)+U2)^2 :V2=4*U3*(U4-Q1*Q1)
3150      V3=(V1-V2)^.5 :V4=-2*Q1*X(1,2,1)+U1
3160      DV1DQ=2*(-2*Q1*X(1,2,1)+U2)*(-2*X(1,2,1))
3170      DV2DQ=-8*U3*Q1 :DV4DQ=-2*X(1,2,1)
3180      DV3DQ=.5*(DV1DQ-DV2DQ)*(V1-V2)^(-.5)
3190      TS1=.5*((V4+V3)/(2*U5))^(-.5)
3200      TS2=(DV4DQ+DV3DQ)/(2*U5)
3210      DVIDQ=TS1*TS2
3220      REM
3230      REM      4.2.4 P.D. of Vi w.r.t d11
3240      REM
3250      U1=P1*X(2,2,1)-2*Q1*X(1,2,1) :U2=U1 :U4=P1*R1-Q1*Q1
3260      U5=X(1,2,1)*X(1,2,1) :U3=U5
3270      V1=(R1*X(1,1,1)+U2)^2 :V2=4*U4*(X(1,1,1)*X(2,2,1)-U3)
3280      V3=(V1-V2)^.5 :V4=2*X(1,1,1)*X(2,2,1)-2*U5
3290      V5=R1*X(1,1,1)+U1 :V6=(V5+V3)/V4
3300      DV1DD11=2*(R1*X(1,1,1)+U2)*R1
3310      DV2DD11=4*U4*X(2,2,1)
3320      DV3DD11=.5*(DV1DD11-DV2DD11)*(V1-V2)^(-.5)
3330      DV4DD11=2*X(2,2,1) :DV5DD11=R1
3340      DV6DD11=((DV5DD11+DV3DD11)/V4)-DV4DD11*(V5+V3)/(V4*V4)
3350      DVIDD11=.5*V6^(-.5)*DV6DD11
3360      REM
3370      REM      4.2.5 P.D. of Vi w.r.t d22
3380      REM
3390      U1=R1*X(1,1,1)-2*Q1*X(1,2,1) :U2=U1 :U4=P1*R1-Q1*Q1
3400      U5=X(1,2,1)*X(1,2,1) :U3=U5
3410      V1=(P1*X(2,2,1)+U2)^2 :V2=4*U4*(X(1,1,1)*X(2,2,1)-U3)
3420      V3=(V1-V2)^.5 :V4=2*X(1,1,1)*X(2,2,1)-2*U5
3430      V5=P1*X(2,2,1)+U1 :V6=(V5+V3)/V4
3440      DV1DD22=2*(P1*X(2,2,1)+U2)*P1
3450      DV2DD22=4*U4*X(1,1,1)
3460      DV3DD22=.5*(DV1DD22-DV2DD22)*(V1-V2)^(-.5)
3470      DV4DD22=2*X(1,1,1) :DV5DD22=P1
3480      DV6DD22=((DV5DD22+DV3DD22)/V4)-DV4DD22*(V5+V3)/(V4*V4)
3490      DVIDD22=.5*V6^(-.5)*DV6DD22
3500      REM
3510      REM      4.2.6 P.D. of Vi w.r.t d12
3520      REM
3530      U1=P1*X(1,1,1)+R1*X(2,2,1) :U2=U1 :U4=P1*R1-Q1*Q1
3540      U5=X(1,1,1)*X(2,2,1) :U3=U5
3550      V1=(-Q1*2*X(1,2,1)+U2)^2 :V2=4*U4*(-X(1,2,1)*X(1,2,1)+U3)
3560      V3=(V1-V2)^.5 :V4=-2*X(1,2,1)*X(1,2,1)+2*U5
3570      V5=-2*Q1*X(1,2,1)+U1 :V6=(V5+V3)/V4
3580      DV1DD12=2*(-2*Q1*X(1,2,1)+U2)*(-2*Q1)
3590      DV2DD12=-8*U4*X(1,2,1)

```

```

3600      DV3DD12=.5*(DV1DD12-DV2DD12)*(V1-V2)^(-.5)
3610      DV4DD12=-4*X(1,2,1) :DV5DD12=-2*Q1
3620      DV6DD12=((DV5DD12+DV3DD12)/V4)-DV4DD12*(V5+V3)/(V4*V4)
3630      DVIDD12=.5*V6^(-.5)*DV6DD12
3640      REM
3650      REM      4.2.7 P.D. of Vi w.r.t porosity
3660      REM
3670      TS1=DVIDP*DPDN :TS2=DVIDQ*DQDN :TS3=DVIDR*DRDN
3680      TS4=DVIDD11*DD11DN :TS5=DVIDD12*DD12DN :TS6=DVIDD22*DD22DN
3690      DVIDN=TS1+TS2+TS3+TS4+TS5+TS6
3700      REM
3710      REM      4.2.8 P.D. of Vi w.r.t elastic constants
3720      REM
3730      TS1=DVIDP*DPDKS :TS2=DVIDQ*DQDKS :TS3=DVIDR*DRDKS
3740      DVIDKS=TS1+TS2+TS3
3750      TS1=DVIDP*DPDKF :TS2=DVIDQ*DQDKF :TS3=DVIDR*DRDKF
3760      DVIDKF=TS1+TS2+TS3
3770      TS1=DVIDP*DPDKB1 :TS2=DVIDQ*DQDKB1 :TS3=DVIDR*DRDKB1
3780      DVIDKB1=TS1+TS2+TS3
3790      REM
3800      REM      4.2.9 P.D. of Vi w.r.t mass constants
3810      REM
3820      TS1=DVIDD11*DD11DDS :TS2=DVIDD12*DD12DDS :TS3=DVIDD22*DD22DDS
3830      DVIDDDS=TS1+TS2+TS3
3840      TS1=DVIDD11*DD11DDF :TS2=DVIDD12*DD12DDF :TS3=DVIDD22*DD22DDF
3850      DVIDDDF=TS1+TS2+TS3
3860      TS1=DVIDD11*DD11DT :TS2=DVIDD12*DD12DT :TS3=DVIDD22*DD22DT
3870      DVIDT=TS1+TS2+TS3
3880      REM
3890      REM      4.2.10 Delta Vi
3900      REM
3910      TS1=DVIDN^2*IN(1,2)^2 :TS2=DVIDKF^2*IN(2,2)^2
3920      TS3=DVIDKS^2*IN(3,2)^2 :TS4=DVIDT^2*IN(4,2)^2
3930      TS5=DVIDG1^2*IN(5,2)^2 :TS6=DVIDKB1^2*IN(7,2)^2
3940      TS7=DVIDDF^2*IN(9,2)^2 :TS8=DVIDDS^2*IN(11,2)^2
3950      DELVI=(TS1+TS2+TS3+TS4+TS5+TS6+TS7+TS8)^.5
3960      REM
3970      REM      4.3 Gassmann error analysis
3980      REM
3990      REM      4.3.1 p.d. of V0 w.r.t KF
4000      REM
4010      G=G1
4020      U1=4*G/3+KB1 :U2=(1-KB1/KS)^2 :U3=N
4030      U4=(1-N)/KS-KB/(KS^2) :U5=N*DF+(1-N)*DS
4040      V1=U1/U5 :V2=U2 :V3=U5*(U3/KF+U4) :V4=V1+V2/V3
4050      DV3DKF=-U5*U3/KF^2 :DV4DKF=-V2*DV3DKF/V3^2
4060      DVODKF=.5*DV4DKF*V4^(-.5)
4070      REM
4080      REM      4.3.2 p.d. of V0 w.r.t KS
4090      REM
4100      U1=4*G/3+KB1 :U2=KB1 :U3=N/KF
4110      U4=(1-N) :U5=KB1 :U6=N*DF+(1-N)*DS
4120      V1=U1/U6 :V2=(1-U2/KS)^2
4130      V3=U6*(U3+U4/KS-U5/KS^2) :V4=V1+V2/V3
4140      DV2DKS=(U2/KS^2)*2*(1-U2/KS)
4150      DV3DKS=(-U6*U4/KS^2)+(2*U5*U6/KS^3)
4160      DV4DKS=DV2DKS/V3-DV3DKS*V2/V3^2
4170      DVODKS=.5*DV4DKS*V4^(-.5)
4180      REM
4190      REM      4.3.3 p.d. of V0 w.r.t KB1

```

```

4200 REM
4210 U1=4*G/3 :U2=KS :U3=N/KF+(1-N)/KS
4220 U4=KS^2 :U5=N*DF+(1-N)*DS
4230 V1=(KB1+U1)/U5 :DV1DKB1=1/U5
4240 V2=(1-KB1/U2)^2 :DV2DKB1=-2*(1-KB1/U2)/U2
4250 V3=U5*(U3-KB1/U4) :DV3DKB1=-U5/U4
4260 V4=V1+V2/V3 :DV4DKB1=DV1DKB1+DV2DKB1/V3-DV3DKB1*V2/(V3^2)
4270 DV0DKB1=.5*DV4DKB1*V4^(-.5)
4280 REM
4290 REM 4.3.4 p.d. of V0 w.r.t G
4300 REM
4310 U1=N*DF+(1-N)*DS :U2=KB1 :U3=(1-KB1/KS)^2
4320 U4=(N/KF+(1-N)/KS-KB1/KS^2)
4330 DV0DG=(2/(3*U1))*(4*G/(U1^3)+U2/U1+U3/(U1*U4))^(-.5)
4340 REM
4350 REM 4.3.5 p.d. of V0 w.r.t N
4360 REM
4370 U1=KB1+4*G/3 :U2=(1-KB1/KS)^2 :U3=KF
4380 U4=KS :U5=1/KS-KB1/KS^2
4390 M1=-(1/U3-1/U4) :M2=U2
4400 M3=(N/U3-N/U4+U5)^2
4410 DMDN=M1*M2/M3 :DDDND=DF-DS
4420 M=U1+U2/(N/U3-N/U4+U5) :D=N*DF+(1-N)*DS
4430 V1=M/D :DV1DN=DMDN/D-DDDN*M/D^2
4440 DV0DN=.5*DV1DN*V1^(-.5)
4450 REM
4460 REM 4.3.6 p.d. of V0 w.r.t DS
4470 REM
4480 U1=KB1+4*G/3 :U2=N*DF :U3=(1-N)
4490 U4=(1-KB1/KS)^2 :U5=N/KF+(1-N)/KS-KB1/KS^2
4500 U6=N*DF :U7=(1-N)
4510 V1=U2+U3*DS :DV1DS=U3
4520 V2=U5*(U6+U7*DS) :DV2DS=U5*U7
4530 V3=U1/V1+U4/V2 :DV3DS=-DV1DS*U1/V1^2-DV2DS*U4/V2^2
4540 DV0DS=.5*DV3DS*V3^(-.5)
4550 REM
4560 REM 4.3.7 p.d. of V0 w.r.t DF
4570 REM
4580 U1=KB1+4*G/3 :U2=(1-N)*DS :U3=N
4590 U4=(1-KB1/KS)^2 :U5=N/KF+(1-N)/KS-KB1/KS^2
4600 U6=(1-N)*DS :U7=N
4610 V1=U2+U3*DF :DV1DF=U3
4620 V2=U5*(U6+U7*DF) :DV2DF=U5*U7
4630 V3=U1/V1+U4/V2 :DV3DF=-DV1DF*U1/V1^2-DV2DF*U4/V2^2
4640 DV0DF=.5*DV3DF*V3^(-.5)
4650 REM
4660 REM 4.3.8 Delta V0
4670 REM
4680 TS1=DV0DN^2*IN(1,2)^2 :TS2=DV0DKF^2*IN(2,2)^2
4690 TS3=DV0DKS^2*IN(3,2)^2 :TS4=DV0DT^2*IN(4,2)^2
4700 TS5=DV0DG^2*IN(5,2)^2 :TS6=DV0DKB1^2*IN(7,2)^2
4710 TS7=DV0DF^2*IN(9,2)^2 :TS8=DV0DS^2*IN(11,2)^2
4720 DELV0=(TS1+TS2+TS3+TS4+TS5+TS6+TS7+TS8)^.5
4730 SUM=DELV0^2
4740 DELN=TS1/SUM :DELKF=TS2/SUM :DELKS=TS3/SUM :DELT=TS4/SUM
4750 DELG=TS5/SUM :DELDT=TS6/SUM :DELDF=TS7/SUM :DELDS=TS8/SUM
4760 RETURN
4770 REM
4780 REM 5.0 Get file name from user
4790 REM

```

```

4800      CLS :PRINT :PRINT :PRINT
4810      PRINT SPC(10) "Input set file name (e.g.289C_SET.DAT)";
4820      INPUT SET$ :PRINT :PRINT SPC(10) "Set file is "SET$
4830      PRINT SPC(10) "Hit R to re-enter, anything else to continue"
4840      GOS=INKEY$ :IF GOS="" THEN 4840
4850      IF GOS="R" THEN 4800
4860      RETURN
4870  REM
4880  REM      5.1      Set model type and open files
4890  REM
4900      OPEN SET$ FOR INPUT AS #1
4910      FOR J=1 TO 2
4920      FOR I=0 TO 29
4930      INPUT#1, IN(I,J)
4940      NEXT I
4950      NEXT J
4960      FOR I=1 TO 9:INPUT#1, MS(I): NEXT I
4970      CLOSE #1
4980      IF MS(6)="" THEN 5000
4990      OPEN MS(6) FOR INPUT AS #1
5000      IF MS(7)="" THEN 5030
5010      MS(7)=MID$(MS(7),1,5)+"ERR.DAT"
5020      OPEN MS(7) FOR OUTPUT AS #2
5030      RETURN
5040  REM
5050  REM      5.2      Reset parameters
5060  REM
5070      N=IN(1,1) :KF=IN(2,1) :KS=IN(3,1) :T=IN(4,1)
5080      G1=IN(5,1) :G0=IN(6,1) :KB1=IN(7,1) :KB0=IN(8,1)
5090      DF=IN(9,1) :D=IN(10,1) :DS=IN(11,1) :A=IN(12,1)
5100      NU=IN(13,1) :K=IN(14,1) :F=IN(15,1) :POIS=IN(16,1)
5110      S2=IN(17,1) :S1=IN(18,1) :VSL=IN(19,1) :VEL=IN(20,1)
5120      QSL=IN(21,1) :QEL=IN(22,1) :VSR=IN(23,1) :VER=IN(24,1)
5130      STOR=1/IN(25,1) :ETOR=1/IN(26,1) :FPOW=IN(17,2)
5140      FINC=IN(18,2) :FMAX=IN(19,2) :SIG=IN(20,2)
5150      SMAX=IN(21,2) :SINC=IN(22,2)
5160      RETURN
5170  REM
5180  REM      5.3      Display selected program mode
5190  REM
5200      TS1=VAL(MS(1))
5210      IF TS1<4 THEN DS(1)="VELOCITY ERROR ANALYSIS"
5220      IF TS1=4 THEN DS(1)="BIOT-GARDNER ROD WAVES"
5230      IF TS1=5 THEN DS(1)="ASYMPTOTIC POROELASTIC SOLUTIONS"
5240      IF MS(2)<>" " THEN DS(2)="YES"
5250      IF MS(3)<>" " THEN DS(3)="YES"
5260      IF MS(4)<>" " THEN DS(4)="YES"
5270      IF MS(5)="A" THEN DS(5)="FREQUENCY"
5280      IF MS(5)="B" THEN DS(5)="POISSON'S RATIO"
5290      IF MS(5)="C" THEN DS(5)="CONVERGENCE"
5300      DS(6)=MS(6) :DS(7)="PRINTER"
5310      IF MS(7)<>"P" THEN DS(7)=MS(7)
5320      IF MS(8)<>" " THEN DS(8)="YES"
5330      IF MS(9)<>" " THEN DS(9)="YES"
5340      CLS :PRINT :PRINT
5350      PRINT SPC(12) "Selected program mode read from ";SET$
5360      PRINT :PRINT
5370      PRINT SPC(10)"MODEL                                : "DS(1)
5380      PRINT SPC(10)"PORE SIZE DISTRIBUTION                : "DS(2)
5390      PRINT SPC(10)"VISCOELASTIC COEFFICIENTS              : "DS(3)

```

```

5400 PRINT SPC(10)"KOZENY-CARMAN PERMEABILITY : "DS(4)
5410 PRINT SPC(10)"SWEEP : "DS(5)
5420 PRINT SPC(10)"FILE INPUT : "DS(6)
5430 PRINT SPC(10)"FILE OUTPUT : "DS(7)
5440 PRINT SPC(10)"FREQUENCY CORRECTION : "DS(8)
5450 PRINT SPC(10)"CALCULATE FRAME MODULUS : "DS(9)
5460 PRINT :PRINT
5470 PRINT SPC(12) "Edit SET file to alter mode"
5480 PRINT SPC(12) "Press any key to continue"
5490 GOS=INKEY$ :IF GOS="" THEN 5490
5500 CLS:PRINT:PRINT:PRINT:PRINT:PRINT
5510 PRINT SPC(16) "PROGRAM BIOT_ERR.BAS IN OPERATION": PRINT
5520 RETURN
5530 REM
5540 REM 5.4 Read data from disc
5550 REM
5560 IF MS(6)="" THEN RETURN
5570 INPUT E1,DEPTH,VMEAS,DT,VSHEAR
5580 N=(DT-DS)/(DF-DS)
5590 G1=DT*VSHEAR^2
5600 REM A=(DIA*.000001)/2
5610 V(1)=0:INC=.1
5620 RETURN
5630 REM
5640 REM 5.5 Reset program variables
5650 REM
5660 S=0 :AMOD=A :W=2*PI*F : SWEEPS="" :CONVS=""
5670 FPOW=IN(17,2) :FINC=IN(18,2)
5680 SIG=IN(20,2) :SINC=IN(22,2)
5690 IF MS(5)="C" THEN SINC=.1
5700 S=0 :V1A=0 :V2A=0 :TVS=0
5710 AC1A=0 :AC2A=0 :FIN=0
5720 V(1)=0 :V(2)=0 :AC(1)=0 :AC(2)=0
5730 V(0)=0 :VD=0 :AC(0)=0 :K=IN(14,1) :AMOD=IN(12,2)
5740 REM
5750 REM 5.5.1 Kozeny Carman permeability
5760 REM
5770 IF MS(4)<>"D" THEN 5800
5780 A=D*N/((1-N)^3)
5790 K=A^2*N/(8*T)
5800 IF MS(4)<>"A" THEN 5850
5810 A=D*N/((1-N)^3)
5820 REM
5830 REM 5.5.2 Errors in G1, KB1 and N
5840 REM
5850 DELDT=DT*.05: U=DS-DT :V=DS-DF :DNDDS=1/V-U/V^2
5860 DNDDF=U/V^2 : DNDDT=-1/V :TS1=IN(11,2)^2*DNDDS^2
5870 TS2=DELDT^2*DNDDT^2 :TS3=IN(9,2)^2*DNDDS^2
5880 IN(1,2)=(TS1+TS2+TS3)^.5
5890 DELVS=VSHEAR*.1 :DGDVS=2*VSHEAR*DT :DGDDT=VSHEAR^2
5900 TS1=DELVS^2*DGDVS^2 :TS2=DELDT^2*DGDDT^2
5910 IN(5,2)=(TS1+TS2)^.5
5920 SIG=POIS :U=2*G1*(1+SIG) :V=3*(1-2*SIG)
5930 DUDSIG=2*G1:DVDSIG=-6
5940 DKBDSIG=DUDSIG/V-DVDSIG*U/V^2 :DKBDG=U/(V*G1)
5950 TS1=IN(5,2)^2*DKBDG^2 :TS2=IN(16,2)^2*DKBDSIG^2
5960 IN(7,2)=(TS1+TS2)^.5
5970 RETURN
5980 REM
5990 REM 5.6 Output results to disc

```

```

6000    REM
6010    PRINT DELN;DELKF;DELKS;DELT;DELG;DELDT;DELDF;DELDS;DELVO;VZ
6020    WRITE £2, DELN;DELKF;DELKS;DELT;DELG;DELDT;DELDF;DELDS;DELVO;VZ
6030    RETURN
6040    REM
6050    REM      6.0      Trivial mathematical subroutines
6060    REM
6070    REM      6.1      Calculate I factorial
6080    REM
6090    FAC=1
6100    FOR J=1 TO I :FAC=J*FAC: NEXT
6110    RETURN
6120    REM
6130    REM      6.2      Multiply two complex numbers
6140    REM
6150    X5=(X1*X3)-(X2*X4)
6160    X6=(X1*X4)+(X2*X3)
6170    RETURN

```

REFERENCES

- Akal, T., 1980, Sea floor effects on shallow water acoustic propagation, in Bottom interacting ocean acoustics, Kuperman, W.A. and F.B. Jensen, eds., Plenum, New York, 557-576.
- Akal, T. and J.M. Berkson (eds.), 1986, Ocean seismo acoustics, Plenum, New York, pp. 907.
- Archie, G.E., 1942, The electrical resistivity log as an aid in determining some resevoir characteristics, Trans. Am. Inst. Mining and Met. Eng., 146, 54-62.
- Attenborough, K., 1982, Acoustical characteristics of porous materials, Phys. Reps., 82, 179-227.
- Backman, J., R. Duncan, et al., in press, Proceedings of the Ocean Drilling Program, Volume 115, Part A, Texas A and M University.
- Bear, J., 1972, Dynamics of fluids in porous media, Elsevier, New York, pp. 746.
- Bedford, A., G.L. Ellis, K.P. Elliott, S.K. Mitchell and D.J. Shirley, 1982, Acoustical properties of sediments, Applied Research Labs., Texas, ARL-TR-82-47, pp. 66.
- Bennell, J.D., D. Taylor-Smith, A.M. Davis, 1984, Resonant column testing of marine sediments, Oceanology Int. 84. 1.9., pp. 19.
- Bennett, R.H., H. Li, P.J. Valent, J. Lipkin and M.I. Esrig, 1985, In-situ undrained shear strengths and permeabilities derived from piezometer measurements, in Strength testing of marine sediments: laboratory and in-situ measurements, A.S.T.M. Special Technical Publication 883, 83-100.
- Berryman, J.G., 1980, Confirmation of Biot's theory, Appl. Phys. Lett., 37, 382-384.
- Berryman, J.G., 1986, Elastic wave attenuation in rocks containing fluids, Appl. Phys. Lett., 49, 552-554.

- Berryman, J.G. and S.C. Blair, 1986, Use of digital image analysis to estimate fluid permeability of porous materials: application of two-point correlation functions, *J. Appl. Phys.*, 60, 1930-1938.
- Berryman, J.G. and L. Thigpen, 1987, Extensions of Biot's theory of poroelasticity to complex porous media, Lawrence Livimore National Laboratory, CA, Report, pp. 20.
- Biot, M.A., 1941, General theory of three-dimensional consolidation, *J. Appl. Phys.*, 12, 155-164.
- Biot, M.A., 1956a, Theory of propagation of elastic waves in a fluid saturated porous solid, I. Low frequency range, *J. Acoust. Soc. Am.*, 28, 168-178.
- Biot, M.A., 1956b, Theory of propagation of elastic waves in a fluid saturated porous solid, II. High frequency range, *J. Acoust. Soc. Am.*, 28, 179-191.
- Biot, M.A., 1956c, General solutions of the equations of elasticity and consolidation for a porous material, *J. Appl. Mech.*, 78, 91-96.
- Biot, M.A., 1962a, Mechanics of deformation and acoustic propagation in porous media, *J. Appl. Phys.*, 33, 1482-1489.
- Biot, M.A., 1962b, Generalised theory of acoustic propagation in porous dissipative media, *J. Acoust. Soc. Am.*, 34, 1254-1264.
- Biot, M.A. and D.G. Willis, 1957, The elastic constants of the theory of consolidation, *J. Appl. Mech.*, 24, 594-601.
- Bourne, D.E. and P.C. Kendall, 1977, Vector analysis and Cartesian tensors, Nelson, London, pp. 256.
- Boyce, R.E., 1976, Definition and laboratory techniques of compressional sound velocity parameters and wet-water content, wet-bulk density, and porosity parameters by gravimetric and gamma ray attenuation techniques, in Schlanger, S.O. and E.D. Jackson, et al., Initial Reports D.S.D.P., 33, Washington (U.S Govt. Printing Office), 931-958.

- Brown, R.J.S., 1980, Connection between formation factor for electrical resistivity and fluid-solid coupling factor in Biot's equations for acoustic waves in fluid-filled porous media, *Geophysics*, 45, 1269-1275.
- Chandler, R.N. and D.L. Johnson, 1981, The equivalence of quasi-static flow in fluid saturated porous media and Biot's slow wave in the limit of zero frequency, *J. Appl. Phys.*, 52, 3391-3395.
- Chatzis, I. and F.A.L. Dullien, 1977, Modelling pore structure by 2-D and 3-D networks with application to sandstones, *J. Can. Powder Tech.*, January-March, 97-108.
- Cleary, M.P., 1980, Wave propagation in fluid infiltrated porous media - some review and analysis, *Reports of Research in Mechanics and Materials*, Massachusetts Institute of Technology, NH, pp. 133.
- Davis, A.M. and J.D. Bennell, 1986, Dynamic properties of marine sediments, in *Ocean seismo-acoustics*, Akal, T. and J.M. Berkson, (eds.), Plenum, New York, 501-510.
- Davis, A.M. and P.J. Schultheiss, 1980, Seismic signal processing in engineering site investigations - a case history, *Ground Engineering*, 13, 44-48.
- De Alba, P., K. Baldwin, V. Janoo, G. Roe and B. Celikkol, 1984, Elastic wave velocities and liquefaction potential, *Geotechnical Testing Journal*, GTJODJ, 7, 77-87.
- Deresiewicz, H and J.T. Rice, 1962, The effect of boundaries on wave propagation in a liquid filled porous solid: III. Reflection of plane waves at a free plane boundary (general case), *Bull. Seis. Soc. Am.*, 52, 595-626.

- Drnevich, V.P., J.R. Hall, Jr. and F.E. Richart, Jr., 1967, Effect of amplitude of vibration on the shear modulus of sand, in, Proceedings of the international symposium on wave propagation and dynamic properties of earth materials, Albuquerque, NM, USA. 189-199.
- Dunn, K-J., 1986, Acoustic attenuation in fluid-saturated porous cylinders at low frequencies, J. Acoust. Soc. Am., 79, 1709-1721.
- Dyvik, R. and C. Madshus, 1986, Lab measurements of G_{max} using bender elements, Norwegian Geotechnical Insititute Publication 161, pp 7.
- Gardner, G.H.F., 1962, Extensional waves in fluid-saturated porous cylinders, J. Acoust. Soc. Am., 34, 36-40.
- Gassmann, F., 1951, Ueber die elastizitat poroser medien, Vierteljahrschrift de Naturforschenden Gesellschaft, Zurich, 96, 1-22.
- Geertsma, J. and D.C. Smit, 1961, Some aspects of elastic wave propagation in fluid-saturated porous solids, Geophysics, 16, 169-181.
- Goldsberry, S.L., 1985, The determination of permeability in, In-situ marine-floor sediments, SACLANT publication S.M.-185, La Spezia, Italy, pp. 35.
- Hamdi, F. and D. Taylor-Smith, 1982, The influence of permeability on compressional wave velocity in marine sediments, Geophys. Prosp., 30, 622-640.
- Hamilton, E.L., 1971, Predictions of in-situ acoustic and elastic properties of sediments, Geophysics, 36, 226-284.
- Hamilton, E.L., 1972, Compressional wave attenuation in marine sediments, Geophysics, 37, 620-645.
- Hamilton, E.L., 1976a, Variations of density and porosity with depth in deep sea sediments, J. Sed. Petrol., 46, 280-300.

- Hamilton, E.L., 1796b, Shear wave velocity versus depth in marine sediments: A review, *Geophysics*, 41, 985-996.
- Hamilton, E.L., 1980, Geoacoustic modeling of the sea-floor, *J. Acoust. Soc. Am.*, 68, 1313-1340.
- Hamilton, E.L., R.T. Bachman, W.H. Berger, T.C. Johnson and L.A. Mayer, 1982, Acoustic and related properties of calcareous deep-sea sediments, *J. Sed. Petrol.*, 52, 733-753.
- Hardin, B.O., 1978, The nature of stress-strain behaviour for soils, in *Proceedings of American Society of Civil Engineers, Specialty Conference on Earthquake Engineering and Soil Dynamics*, Pasadena, Cal., 1, 3-90.
- Hardin, B.O. and W.L. Black, 1968, Vibration modulus of normally consolidated clay, *J. Soil. Mech. and Found. Div.*, ASCE, 94, 353-368.
- Hardin, B.O. and V.P. Drnevich, 1971, Shear modulus and damping in soils: design equations and curves, *J. Soil. Mech. Found. Div.*, ASCE, 98, 667-693.
- Haumeder, M., 1986, Low-frequency anomalies in the reflection behaviour of marine sediments, in *Ocean seismo-acoustics*, Akal, T. and J.M. Berkson, (eds.), Plenum, New York, 445-454.
- Hovem, J.M. and G.D. Ingram, 1979, Viscous attenuation of sound in marine sediments, *J. Acoust. Soc. Am.*, 66, 1807-1812.
- Hurley, M.T. and P. Hempel, in press, Physical properties: O.D.P. Sites 705 to 715, in Backman, J., R. Duncan, et al., *Proceedings of the Ocean Drilling Program, Volume 115, Part A*, Texas A and M University.
- Jackson, P.D., D. Taylor-Smith and P.N. Stanford, 1978, Resistivity - porosity - particle shape relationships for marine sands, *Geophysics*, 43, 1250-1268.

- Johnson, D.L., 1982, Elastodynamics of gels, J. Chem. Phys., 77, 1531-1539.
- Johnson, D.L., J. Koplik and R. Dashen, 1987, Theory of dynamic permeability and tortuosity in fluid-saturated porous media, J. Fluid Mech., 176, 379-402.
- Johnson, D.L. and T.J. Plona, 1982, Acoustic slow waves and the consolidation transition, J. Acoust. Soc. Am., 72, 556-564.
- Johnson, T.C., E.L. Hamilton and W.H. Berger, 1977, Physical properties of calcareous ooze: control by dissolution at depth, Marine Geol., 24, 259-277.
- Kjartansson, E., 1979, Constant Q-wave propagation, J. Geophys. Res., 84, 4737-4749.
- Kolsky, H., 1963, Stress waves in solids, Dover Publ. Inc., New York, pp. 213.
- Lee, H.J., 1985, Laboratory determination of the strength of marine soils, in Strength testing of marine sediments: laboratory and in-situ measurements, ASTM Special Technical Publication 883, 181-250.
- Lees, G., 1970, Studies of inter-particle void characteristics, Q. J. Eng. Geol., 2, 287-229.
- Lovell, M.A., 1985, Thermal conductivity and permeability assessment by electrical resistivity measurements in marine sediments, Marine Geotechnology, 6, 205-240.
- Lovell, M.A. and P. Ogden, 1984, Remote assessment of permeability / thermal diffusivity fo consolidated clay sediments, E.E.C. Rpt., EUR 9206En (Brussels), pp. 95.
- Malahoff, A., 1974, Forward for Physics of sound in marine sediments, L Hampton (ed.), Plenum, New York, pp. 567.

- Manghnani, M.H., B.R. Lienert, M.T. Hurley and S.L. Webb, 1987, Low frequency attenuation and modulus measurements on marine sediments and sedimentary rocks, Progress Report, O.N.R. N00014-84-G-0159, University of Hawaii, H.I., pp. 42.
- Mayer, L.A., 1982, Physical properties of sediments recovered on D.S.D.P. Leg 68 with the hydraulic piston corer, in Prell, W.L., Gardner, J.V., et al., Init. Repts. D.S.D.P., 68: Washington (U.S. Govt. Printing Office), 365-382.
- McCann, C. and D.M. McCann, 1985, A theory of compressional wave attenuation in noncohesive sediments, Geophysics, 50, 1311-1317.
- McPhail, S.D. and P.J. Schultheiss, 1986, PUPPI - A free-fall seabed piezometer for geotechnical studies, in Ocean science and Offshore Engineering, 6, Oceanology, Graham and Trotman Ltd, 249-258.
- McQuillin, R., M. Bacon and W. Barclay, 1984, An introduction to seismic interpretation, Graham and Trotman, pp. 287.
- Mei, C.C. and M.A. Foda, 1981, Wave-induced responses in a fluid-filled poro-elastic solid with a free interface - a boundary layer theory, Geophys. J. R. Astr. Soc., 66, 579-631.
- Mengi, Y. and H.D. McNiven, 1976, Response of fluid filled porous media to a transient input, J. Acoust. Soc. Am., 61, 84-94.
- Muir-Wood, A.M., 1980, Opening address in Offshore site investigation, Society of Underwater Technology, Graham and Trotman Ltd, pp. 291
- Murphy, W.F., 1982, Effects of partial water saturation on attenuation in Massillon sandstone and Vycor porous glass, J. Acoust. Soc. Am., 71, 1458-1468.
- Murphy, W.F., K.W. Winkler and R.L. Kleinberg, 1986, Acoustic relaxation in sedimentary rocks: dependence on grain contacts and fluid saturation, Geophysics, 51, 757-766.

- Nickerson, C.R., 1978, Consolidation and permeability characteristics of deep sea sediments, M.S. Thesis, Worcester Polytechnic Institute, Massachusetts, pp. 212.
- Norwick, A.S. and B.S. Berry, 1972, Anelastic relaxation in crystalline solids, Academic Press, New York, pp. 378.
- Nye, J.F., 1979, Physical properties of crystals, Oxford Univ. Press, pp. 322.
- Ogushwitz, P.R., 1985, Applicability of the Biot theory. III. Wave speeds versus depths in marine sediments, J. Acoust. Soc Am., 77, 453-464.
- Okusa, S., 1985, Wave-induced stresses in unsaturated submarine sediments, Geotechnique, 35, 517-532.
- Olson, R.E. and D.E. Daniel, 1979, Field and laboratory measurements of the permeability of saturated and partially saturated fine-grained soils, Geotechnical Engineering Report GE79-1, University of Texas, Austin, pp. 78.
- Patterson, N.R., 1956, Seismic wave propagation in porous granular media, Geophysics, 21, 691-714.
- Plona, T.J., 1980, Observation of a second bulk compressional wave in a porous medium at ultrasonic frequencies, Appl. Phys. Lett., 36, 259-261.
- Rice, J.R. and M.P. Cleary, 1976, Some basic stress-diffusion solutions for fluid-saturated elastic porous media with compressible constituents, Rev. Geophys., 14, 227-241.
- Riley, J.P. and G. Skirrow, 1965, Chemical Oceanography, Academic Press, London, pp. 467.
- Schultheiss, P.J., 1981, Simultaneous measurement of P and S wave velocities during conventional laboratory soil testing procedures, Marine Geotechnology, 4, 343-367.

- Schultheiss, P.J., 1985, Physical and geotechnical properties of sediments from the North West Pacific: D.S.D.P Leg 86, in Heath G.R. and Burkle L.H. et al., Init. Reps. D.S.D.P., 86: Washington (U.S. Govt. Printing Office), 701-722.
- Schultheiss, P.J. and D.E. Gunn, 1985, The permeability and consolidation of deep-sea sediments, Institute of Oceanographic Sciences Report 201, pp. 94.
- Schultheiss, P.J. and S.D. McPhail, 1985, Direct indication of pore-water advection from pore-pressure measurements in Madeira abyssal plain sediments, *Nature*, 320, 348-350.
- Schultheiss, P.J. and S.D. McPhail, in press, An automated P-wave logger (PWL) for recording fine-scale compressional wave velocity structures in sediments, in Proceedings of the Ocean Drilling Program, Volume 108, Part B, Texas A and M University.
- Searle, R.C., P.J. Schultheiss, P.P.E. Weaver, M. Noel, R.B. Kidd, C.L. Jacobs and Q.J. Huggett, 1985, Great Meteor East (distal Madeira abyssal plain): geological studies of its suitability for disposal of heat-emitting radioactive wastes, Institute of Oceanographic Sciences, Report, 193, pp. 162.
- Shirley, D.J. and L.D. Hampton, 1978, Shear wave measurements in laboratory sediments, *J. Acoust. Soc. Am.*, 63, 607-613.
- Silva, A.J., J.R. Hetherman and D.I. Calnan, 1981, Low-gradient permeability testing of fine-grained marine sediments, in Permeability and ground water contamination transport, A.S.T.M. S.T.P. 746, 121-136.
- Soderberg, L.O., 1962, Consolidation theory applied to foundation pile time effects, *Geotechnique*, 12, 217-225.
- Spencer, J.W., 1981, Stress relaxation at low frequencies in fluid-saturated rocks: attenuation and modulus dispersion, *J. Geophys. Res.*, 96, 1803-1812.

- Stoll, R.D., 1974, Acoustic waves in saturated sediments, in Physics of sound in marine sediments, L. Hampton (ed.), Plenum, New York, 19-39.
- Stoll, R.D., 1985, Marine sediment acoustics, J. Acoust. Soc. Am., 77, 1789-1798.
- Stoll, R.D. and G.M. Bryan, 1970, Wave attenuation in saturated sediments, J. Acoust. Soc. Am., 47, 1440-1447.
- Stoll, R.D. and T.K. Kan, 1981, Reflection of acoustic waves at a water-sediment interface, J. Acoust. Soc. Am., 70, 149-156.
- Taylor-Smith, D., 1974, Acoustic and mechanical loading of marine sediments, in Physics of sound in marine sediments, L. Hampton (ed.), Plenum, New York, 41-61.
- Taylor-Smith, D., 1986, Geotechnical characteristics of the sea-bed related to seismo-acoustics, in Ocean-seismo acoustics, Akal, T. and J.M. Berkson, (eds.), Plenum, New York, 480-500.
- Toksoz, M.N. and D.H. Johnson, 1981, Preface to Seismic wave attenuation, Geophysical Reprint Series No. 2., D.H. Johnson and M.N. Toksoz (eds.), Society of Exploration Geophysics, Tulsa, pp. 459.
- Vickers, B., 1978, Laboratory work in civil engineering: soil mechanics, Granada, London, pp. 148.
- Wardlaw, N.C. and M. McKeller, 1981, Mercury porosimetry and the interpretation of pore geometry in sedimentary rocks and artificial models, Powder Technology, 29, 127-143.
- Weaver, P.P.E. and P.J. Schultheiss, 1983a, Detection of repenetration and sediment disturbance in open barrel gravity cores, J. Sed. Petrol., 53, 649-654.
- Weaver, P.P.E. and P.J. Schultheiss, 1983b, Vertical open burrows in deep-sea sediments 2-m in length, Nature, 301, 329-331.

- Weaver, P.P.E. and R.G. Rothwell, 1987, Sedimentation on the Madeira Abyssal Plain over the last 300 000 years, in Geology and Geochemistry of Abyssal Plains, eds. P.P.E. Weaver and J. Thompson, Blackwell Scientific, London, 71-86.
- White, J.E., 1983, Underground sound, Elsevier, New York, pp. 368.
- White, J.E., 1986, Biot-Gardner theory of extensional waves in porous rods, Geophysics, 51, 742-745.
- Whitmarsh, R.B. and R.C. Lilwall, 1982, A new method for the determination of in-situ shear wave velocity in deep-sea sediments, Oceanology Int. 82., 4.2, pp. 21.
- Williams, S.R.J., 1987, Faulting in abyssal plain sediments, Great Meteor East, Madeira abyssal plain, in Geology and geochemistry of abyssal plains P.P.E. Weaver and J. Thompson (eds.), Blackwell Scientific, London, 87-104.
- Wilson, W.D., 1960, Speed of sound in sea water as a function of temperature, pressure and salinity, J. Acoust. Soc. Am., 32, 641-644.
- Wingham, D.J., 1985, The dispersion of sound in sediment, J. Acoust. Soc. Am., 78, 1757-1760.
- Winkler, K.W., 1983, Frequency dependent ultrasonic properties of high porosity sandstones, J. Geophys. Res., 88, 9493-9499.
- Winkler, K.W., 1985, Dispersion analysis of velocity and attenuation in Berea sandstone, J. Geophys. Res., 90, 6793-6800.
- Wood, A.B., 1941, A textbook of sound, G. Bell, London, pp. 578.
- Yamamoto, T., H.L. Koning, H. Sellmeier and E.V. Hijum, 1978, On the response of a poro-elastic sea-bed to water waves, J. Fluid Mech., 87, 193-206.
- Zienkiewicz, O.C., C.T. Chang, and P. Bettess, 1980, Drained, undrained, consolidating and dynamic behaviour assumptions in soils, Geotechnique, 30, 385-395.

Znidarcic, D., P. Croce, V. Pane, H-Y. Ko, H.W. Olsen and R.L. Schiffman, 1984, The theory of one-dimensional consolidation of saturated clays: III. Existing testing procedures and analyses, Geotechnical Testing Journal, GTJODJ, 7, 123-133.